Ab initio study of free and deposited transition metal clusters

Dissertation

zur Erlangung des Grades
Doktor der Naturwissenschaften

an der Fakultät für Physik
der Universität Duisburg-Essen

von
Frau Sanjubala Sahoo
aus Odisha, Indien

Referent: Prof. Dr. Peter Entel
Korreferent: Prof. Dr. Hubert Ebert
Tag der mündlichen Prüfung: 15.08.2011

Contents

List of Figures

List of Tables

Abstract

Transition metal (TM) clusters occupy an important role in the class of materials projected for nano applications. In addition to the unusual properties due to their cluster form, TM clusters have the advantage of developing magnetic moments. The goal of this thesis is to study the properties of clusters and cluster related phenomena. Physical properties of clusters are suitable platform to study quantum effects, which becomes prominent at such low dimensions. Thus, it is essential to study the properties of clusters using first-principles methods because they cannot be easily handeled by empirical approaches. The present thesis deals with the density functional theory total energy formalism through the Kohn-Sham approach. The many-body correlation effects are accounted for the generalized gradient approximation (GGA) which has been successful in describing the properties of materials, especially metals.

The ground state structure of various sizes of elemental and binary TM clusters is studied. One of the main observation is that the icosahedron is one of the most stable geometries for 13-atom elemental (Fe, Co, Ni) clusters. For large Fe clusters with regular icosahedron geometry, the core of the cluster relaxes towards the cuboctahedral geometry. For all sizes, after geometrical optimization, we find slight structural distortions. This is associated with the physics of Jahn-Teller effect. We observe that the Jahn-Teller effect is more prominent in Fe clusters as compared to Ni and Co clusters. Also, the evolution of magnetic moment with cluster size is studied. The clusters show enhanced magnetic moment which is inversely related to the cluster size. The magnetic moment versus cluster size obtained from calculations match very well with the experimental results.

One of the main goals of studying binary cluster is to understand the site-specific occupation of atomic species in a multi-component (here binary) cluster. This is achieved this by studying the competition between chemical ordering and segregation for binary Fe-(Co, Ni, Pt) and Co-(Pt, Mn) icosahedral clusters. The energetically favorable distribution of constituent elements in binary cluster is examined for different compositions. Using the lowest energy structure so obtained, the composition-dependent mixing energy is studied. It is observed that the qualitative behavior of mixing energy with respect to composition for 13-atom Fe-Ni clusters is very similar to that of the bulk alloy. It is found that Ni atoms tend to occupy the surface sites on a cluster (segregation tendency) for Fe-rich and Ni-rich compositions. This appears to be a common trend which has been verified for both 13- and 55-atom clusters. Owing to heavy computational demand, we have verified the trend at some specific compositions for 55-atom clusters.

Magnetic properties like the orbital magnetic moment and the magnetic anisotropy are studied for free

and deposited clusters. 13- and 55-atom icosahedral clusters of Fe, Ni and Co are deposited on the substrates like Pt(111) and Pt(001) for these studies. Both the free clusters and the deposited clusters are observed to exhibit large magnetic anisotropy as compared to that of the respective bulk metals. The angle (angle between magnetization and the spin-quantization axis) dependent anisotropy energy is calculated from DFT and then fitted to the classical Heisenberg model containing an anisotropy term. Large values of magnetic anisotropy energy are found for relaxed clusters as compared to perfect clusters because of the structural symmetry-breaking.

In addition to its structural and magnetic properties, transition metal clusters are attractive candidates for catalysis. In principle, the catalysis can be studied by estimating the activation energy barrier of various paths of a reaction by nudged elastic band method. There are studies in literature of the catalytic properties of TM clusters (for example Fe and Pt) for the oxidation of carbon monoxide to carbon-dioxide on graphene surface. We have attempted to study the oxidation of carbon monoxide on graphene surface. The goal is to understand the role of TM clusters in reducing the activation barrier of the chemical reaction and to derive the possible reaction paths. Presently, the proper site for adsorption of CO molecule on free and graphene-supported TM clusters are identified within the accuracy of GGA.

From another aspect, we tried to extrapolate the magnetic properties of clusters to finite temperature using the exact diagonalization technique. We have only studied the magnetic properties of 4- and 13-atom clusters. The exact diagonalization method is applied to the quantum Heisenberg Hamiltonian with nearest-neighbor spin-interactions. The role of dipolar interaction and local uniaxial anisotropy terms in the Heisenberg Hamiltonian are taken into account which has non-negligible contribution for clusters. We observe discontinuities in the magnetization with change in external magnetic field for clusters with antiferromagnetic interactions, which is unlike for clusters with ferromagnetic interaction. The ground state and the temperature-dependent spin-spin correlation functions are also studied.

The findings of these studies for elemental and binary clusters like the size-dependent structural and magnetic properties, the composition-dependent atomic distributions of multi-component clusters (segregation), magnetic anisotropy of free and supported TM clusters are expected to shed light on the understanding of physics of clusters in general and may be helpful for experimentalists.

Zusammenfassung

Übergangsmetallcluster nehmen einen wichtigen Platz in der Klasse der Materialien für Anwendungen im Nanobereich ein. Übergangsmetallcluster besitzen, zusätzlich zu weiteren ungewöhnlichen Eigenschaften aufgrund ihrer Cluster-Form, den Vorteil magnetische Momente zu entwickeln. Das Ziel dieser Arbeit ist die Eigenschaften von Clustern und der damit zusammenhängenden Phänomene zu untersuchen. Die physikalischen Eigenschaften von Clustern sind eine geeignete Grundlage um Quanteneffekte zu studieren, die in niedrigen Dimensionen dominieren. Da sich die Eigenschaften der Cluster nicht mit empirischen Ansätzen einfach beschreiben lassen ist es notwendig, parameterfreie *first-principles* Methoden zu verwenden. In dieser Arbeit kommt der Dichtefunktional Gesamtenergieformalismus im Rahmen des Kohn-Sham-Ansatzes zum Einsatz. Die Vielteilchen-Korrelationseffekte werden im Rahmen der verallgemeinerten Gradienten Approximation (GGA) behandelt, die sehr erfolgreich für die Beschreibung von Materialien, insbesondere Metalle, eingesetzt wird.

Im Rahmen dieser Arbeit wurden die Grundzustandsstrukturen von elementaren und binären Übergangsmetallclustern verschiedener Größen untersucht. Eine der wichtigsten Beobachtungen ist hierbei, dass die ikosaedrische Geometrie eine der stabilsten Formen für elementare 13-Atom (Fe, Co, Ni) Cluster ist. Für alle untersuchten Größen sind leichte strukturelle Verzerrungen präsent, die auf dem Jahn-Teller-Effekt beruhen. Dieser tritt stärker in Fe-Clustern als in Ni- und Co-Clustern auf. Für größere Fe-Cluster mit regelmäßiger ikosaedrischer Geometrie relaxiert der Kern des Clusters in Richtung einer kuboktaedrischen Geometrie. Ebenfalls untersucht wurde die Entwicklung des magnetischen Momentes mit der Clustergröße. Die Cluster besitzen ein erhöhtes magnetisches Moment, dessen Größe sich umgekehrt zur Clustergröße verhält. Der berechnete Zusammenhang stimmt gut mit experimentellen Resultaten überein.

Ein weiteres wichtiges Ziel der Untersuchung binärer Cluster ist das Verständnis der gitterplatzspezifischen Besetzung der atomaren Spezies in mehrkomponentigen (hier binären) Clustern. Dazu wurde die Konkurrenz zwischen chemischer Ordnung und Segregation in binären Fe-(Co, Ni, Pt) und Co-(Pt, Mn) Clustern mit ikosaedrischer Struktur untersucht. Für verschiedene Zusammensetzungen wurde die energetisch günstigste Verteilung der konstituierenden Elemente berechnet. Aufbauend auf der so bestimmten Struktur mit der niedrigsten Energie, wurde das zusammensetzungsabhängige Mischungsverhalten der Elemente untersucht. Das qualitative Verhalten der Mischungsenergie eines 13-Atom Fe-Ni-Clusters stellt sich in Bezug auf die Zusammensetzung als sehr ähnlich zu dem des Festkörpers heraus. Dabei zeigt sich, dass Ni zur Besetzung der Oberflächenplätze (Segregationstendenz) im Fe-reichen wie auch im Ni-reichen Zusammensetzungsbereich tendiert. Das erscheint als

allgemeiner Trend, der in dieser Arbeit für 13- und 55-Atom-Cluster verifiziert werden konnte.

Ebenfalls untersucht wurden magnetische Eigenschaften wie das Bahnmoment und die magnetische Anisotropie für freie und deponierte Cluster. Hierzu wurden, ikosaedrische Cluster mit 13 und 55 Atomen bestehend aus Fe, Ni und Co auf Pt(111) und Pt(001) Substraten deponiert. Sowohl die freien, wie auch die deponierten Cluster zeichnen sich durch eine große magnetische Anisotropie im Vergleich zu den entsprechenden Festkörper-Materialien aus. Die winkelaufgelöste Anisotropie-Energie (gemeint ist der Winkel zwischen Magnetisierung und Spin-Quantisierungsachse) wurde im Rahmen der DFT berechnet. An diese Ergebnisse wurden die Parameter eines klassischen Heisenberg-Modells mit Anisotropieterm gefittet. Für relaxierte Cluster werden im Vergleich zu perfekten Strukturen aufgrund der strukturellen Symmetriebrechung große Anisotropie-Energien gefunden.

Abgesehen von ihren strukturellen und magnetischen Eigenschaften sind Übergangsmetallcluster attraktive Kandidaten für katalytische Anwendungen. Im Prinzip können die katalytischen Eigenschaften durch Bestimmung der Aktivierungsbarriere für verschiedene Reaktionspfade im Rahmen der Nugded-elastic-band-Method untersucht werden. In der Literatur existieren Studien der katalytischen Eigenschaften von Übergangsmetallclustern (z.B. Fe oder Pt) im Bezug auf die Oxidation von Kohlenmonoxid zu Kohlendioxid. Im Rahmen dieser Arbeit wird die Oxidation von Kohlenmonoxid auf Graphen mit dem Ziel untersucht, die Rolle der Übergangsmetallcluster im Hinblick auf eine Reduzierung der Aktivierungsbarriere der chemischen Reaktion zu verstehen und mögliche Reaktionspfade abzuleiten. Bislang konnte der Adsoptionsplatz eines CO-Moleküls auf freien und Graphen-unterstützten Clustern im Rahmen der Genauigkeit der GGA bestimmt werden.

Um die magnetischen Eigenschaften bei endlichen Temperaturen besser zu verstehen, wurden vier bis 13-Atom Cluster im Rahmen des quantenmechanischen Heisenbergmodells mit nächster-Nachbar-Spin-Wechselwirkung exakt diagonalisiert. Die Rolle der Dipolwechselwirkung und radialer Anisotropieterme, die nicht vernachlässigbare Beiträge für Cluster haben, wurden im Heisenberg-Hamiltonian berücksichtigt. Für antiferromagnetische Cluster wurden - im Gegensatz zu ferromagnetische wechselwirkenden Clustern - Unstetigkeiten in der Magnetisierung als Funktion des externen Magnetfeldes gefunden. Zusätzlich wurden für diese Cluster Grundzustand und temperaturabhängige Spin-Spin-Korrelationsfunktionen berechnet.

Die Ergebnisse dieser Arbeit für elementare und binäre Cluster, wie die Größenabhängigkeit struktureller und magnetischer Eigenschaften, die zusammensetzungsabhängige Verteilung der Atome in mehrkomponentigen Clustern (Segregation), magnetische Anisotropie freischwebender und deponierter Übergangsmetallcluster können beitragen, das Verständnis der Clusterphysik im Allgemeinen voranzubringen und Hilfestellungen für experimentelle Arbeiten bieten.

1 Introduction

1.1 Magnetism in low dimensional systems

Magnetism is a relatively old topic, but still attracts lot of scientific attention. Phenomenas associated with magnetism can be classified as many-body problems and quantum mechanics has been successful in interpreting them [1]. The scope of the present thesis is understanding the structure and magnetism of some pure and mixed transition metal clusters. Clusters provide the unique opportunity to study the development of a physical property from the atom towards the solid, i.e., from a “zero”-dimensional to a three-dimensional system. This concerns the formation of an electronic band structure or the development of many-electron phenomena, such as solid state magnetism or superconductivity. Like the corresponding atoms these small particles have significant spin and orbital contributions to their magnetic moment. This is in contrast to the respective solids, where the orbital moment is almost completely quenched by crystal fields and where in most cases the exchange energy that could be gained by spin alignment is exceeded by the increase in kinetic energy that according to the Pauli principle is required to promote the electrons to empty orbitals. Most solids therefore are non-magnetic. When the energy band width is small and correspondingly the density of states $D(E_F)$ is large at the Fermi energy, like in some d- and f- metals, there is a gain in exchange energy at the expense of kinetic energy and then magnetism survives. This corresponds to the Stoner criterion, which states that for a material to be magnetic the product of the exchange integral I and $D(E_F)$ needs to be larger than one. Experimentally, the magnetic moments of metal clusters are usually studies by in-flight molecular beam Stern-Gerlach experiment. In the experiment, a magnetic field gradient induces small deflections of a beam of magnetic clusters traveling through a high vacuum channel. The tiny deflections are only a fraction of millimeters in magnitude, but can be measured with very accurate precision by a position-sensitive time of flight (TOF) technique [2]. From the magnitude of these deflections the magnetic moments of the clusters can be determined. Another advanced method for characterization of magnetic moments is the technique of X-ray magnetic circular dichroism (XMCD). The advantage of XMCD is that one can make a distinction between spin and orbital contributions to the magnetic moment when clusters are soft landed on the substrate [3].

The following is a short recapitulation of the basic properties of clusters [4]. Clusters have very different and often very individual physical and chemical properties. For example, the chemical reactivity can change by orders of magnitude from one cluster size to the next. Therefore, clusters may form specific material selective catalysts. Clusters have structures with five-fold symmetry (possibly also

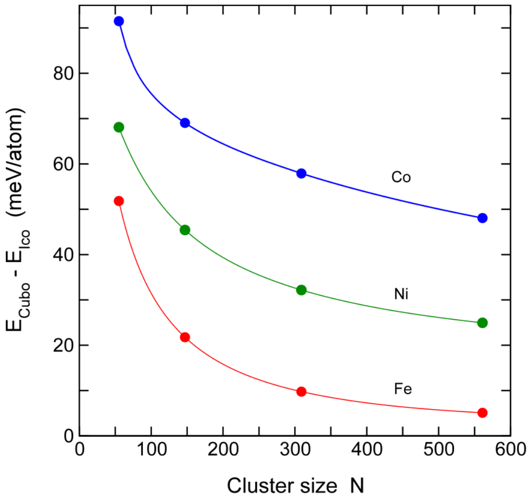

Figure 1.1: The variation of energy differences between cuboctahedra and icosahedra for Co, Ni and Fe as a function of the cluster size calculated by *ab initio* methods. The lines are guide to the eye [7].

seven-fold symmetry) like that of the icosahedral geometry structures which have their own individual growth patterns. Due to their five-fold symmetry axes they cannot grow into periodic lattice structures. Clusters are characterized by a large surface to volume ratio, that is, a large fraction of the constituents occupies low coordinated surface sites. For example, for a cluster with 2000 atoms, a fraction of ~ 30 % atoms is still at the surface. The number of surface atoms in a cluster is inversely proportional to the mean cluster radius R. The large fraction of surface atoms makes the clusters sensitive for chemical reactions. The large number of surface atoms in clusters also have consequences in magnetism since the surface atoms are low-coordinated as compared to the bulk. Therefore, they have a more atom-like character than the interior atoms. As a result, magnetic properties of clusters are very sensitive to their chemical environment. On one hand magnetism in clusters may be quenched, e.g. by charge transfer into empty d-states, on the other hand, it is also possible to even increase the magnetic moment of a cluster. It has been recently shown that even gold nanoparticles can be remanently magnetized, when capped with thiol ligands, even at room temperature [5]. This sensitivity also has implications for deposited clusters. The systematics of cluster physics can be given by expressing the binding energy as a function of cluster size N [6, 7],

$$E(N) = aN + bN^{2/3} + cN^{1/3} + d. \tag{1.1}$$

Where, a, b, c and d signify the contributions arising from the cluster volume, facets, edges, and vertices, respectively. The volume and surface (facets, edges and vertices) contributions compete with each other. These coefficients show a dependence on the type and shape of the cluster. Fig. 1.1 shows a comparison of the energy differences between the icosahedra and cuboctahedra geometries of Fe, Co and Ni clusters [7], which shows that the icosahedral structures are more favorable for Co and Ni with larger energy difference in contrast to Fe.

1.2 Origin of magnetism in atoms: Hund's rules

There exists a close relationship between angular momentum and magnetism [8]. Each electron in an atomic orbital contributes to spin and orbital magnetic moment. The addition of these contributions is within the scope of the vector model of atomic magnetism. In the **LS** coupling, also known as Russell-Saunders coupling scheme, the total orbital momentum $\mathbf{L} = \Sigma_i \mathbf{l}_i$ and the total spin momentum $\mathbf{S} = \Sigma_i \mathbf{s}_i$ combine to yield the total momentum $\mathbf{J} = \mathbf{L} + \mathbf{S}$. The moments obey the matrix-operator rules, such as $\mathbf{S}^2 = S(S+1)$, $\mathbf{L}^2 = L(L+1)$, and $\mathbf{J}^2 = J(J+1)$. In heavy elements, due to the large nuclear charges, spin-orbit interactions are larger than spin-spin interactions or orbit-orbit interactions. This situation is described by the **jj** coupling, where, $\mathbf{J} = \Sigma_i \mathbf{J}_i = \Sigma_i \left(\mathbf{L}_i + \mathbf{S}_i\right)$.
Hund's rules can be summarized by three rules.

- For an electronic configuration, the spin configuration with maximum multiplicity has the lowest energy. The multiplicity is given by $2S$+1, which is maximum when S is maximum. This is possible because of the Pauli exclusion principle which states that two electrons cannot share the same set of quantum numbers.

- For a given multiplicity, the configuration with the largest value of L has the lowest energy. This rule deals with reducing the repulsion between electrons.

- For a given atom with the outermost subshell half-filled or less, the configuration with the lowest value of J is the lowest in energy. If the outermost shell is more than half-filled, the configuration with the highest value of J is the lowest in energy. This rule takes into consideration the energy shifts due to spin-orbit coupling, and is valid for the case where the spin-orbit coupling is weak compared to the residual electrostatic interaction.

Any degeneracy beyond the Hund's rules is removed by interactions such as Zeeman coupling and interatomic exchange. This is of importance for the temperature dependence of magnetic anisotropy.

1.3 Cluster magnetism

Magnetism is sensitive to many factors such as the symmetry, atomic coordination and interatomic distances in the cluster. These characteristics are interrelated [9]. Let us consider the case of free atoms. Fe, Co and Ni have eight, nine and ten valence electrons, respectively and are distributed in the $3d$ and $4s$ shells. Hund's rules require the spin to be a maximum and this leads to electronic configurations $3d{\uparrow}^5\ 3d{\downarrow}^1\ 4s^2$ for Fe, $3d{\uparrow}^5\ 3d{\downarrow}^2 4s^2$ for Co, and $3d{\uparrow}^5\ 3d{\downarrow}^3 4s^2$ for Ni, where the $3d{\uparrow}$ and $3d{\downarrow}$ subshells are separated by the exchange interaction. Since the spin magnetic moment of an electron is 1 μ_B, and these atoms have non-zero spins, the atoms possess substantial moments. The magnetic moment is given by the difference in the number of spin ↑ and spin ↓ 3*d* electrons per atom, which is $n_d(\uparrow) - n_d(\downarrow) = 4, 3, 2$ for Fe, Co and Ni, respectively. When the atoms come together in a cluster, the overlap between the atomic orbitals of neighbor atoms gives rise to energy bands. The levels corresponding to 4*s* electrons produce a free electron-like band, while the *d* electrons stay localized on the atomic sites. The crystal potential stabilizes the *d* and *s* states by different amounts. Together with the crystal potential, *spd* hybridization leads to charge transfer from *s* to *d* states, and the number of *s* electrons for systems other than the atom is close to 1. Assuming that the 3*d* orbitals are atomic-like, the Hund's rules require the majority $3d\uparrow$ sub-band to be fully occupied with five electrons per atom while the minority $3d\downarrow$ sub-band has two, three and four electrons per atom in Fe, Co and Ni respectively. The difference in the number of spin ↑ and spin ↓ 3*d* electrons per atom is $n_d(\uparrow) - n_d(\downarrow) = 3, 2, 1$ for Fe, Co and Ni respectively, and the magnetic moments per atom are 3 μ_B, 2 μ_B and 1 μ_B for Fe, Co and Ni, respectively. These values are quite close to the magnetic moments of very small clusters. The bulk moments per atom for Fe (2.2 μ_B), Co (1.7 μ_B) and Ni (0.6 μ_B) are smaller, and their noninteger values originate because of the partial delocalization of the 3*d* electrons. This also leads to the mutual alignment of the moments, which is known as itinerant exchange.

1.4 Magnetism in bulk

The main characteristic of bulk is that the energy levels are classified as energy bands which can be delocalized [9]. In a one-electron picture, the electrons fill the available delocalized states up to the Fermi level. This explains the occurrence of noninteger magnetic moments in bulk transition metals. Nonmagnetic metals have two equally populated ↑ and ↓ spin subbands. With application of magnetic field, some electrons are transferred from the ↓ to the ↑ band. This type of behaviour of metals are characteristically known as Pauli paramagnetism. The corresponding spin polarization is small, usually less than 0.1%. In itinerant ferromagnets the corresponding one-electron energies of the bands, as represented by the band width, compete against intra-atomic exchange. As a result ferromagnetism is realized in narrow bands. The simplest model of itinerant ferromagnetism is the Bloch model, where the intra-atomic exchange is evaluated for the free electrons. A more sophisticated model is the Stoner model, which relates the onset of ferromagnetism with that of the DOS at the Fermi level. The density of states strongly depend on the crystal structure. This makes it difficult to predict the ferromagnetic moment of solids from their atomic composition. Itinerant magnets with approximately half-filled bands exhibit a strong tendency towards antiferromagnetism because the hybridization energy of half-filled ↑ and ↓ spin bands is lower than that of completely-filled ↑ bands. Magnetism in the iron-series transition metal elements is because of the itinerant electrons. The itinerant character is represented by the non-integer spin moments per atom, such as the 2.2 μ_B for Fe, 1.7 μ_B for Co, and 0.6 μ_B for Ni, as already discussed. The origin of non-integer values of magnetic moment cannot be accounted

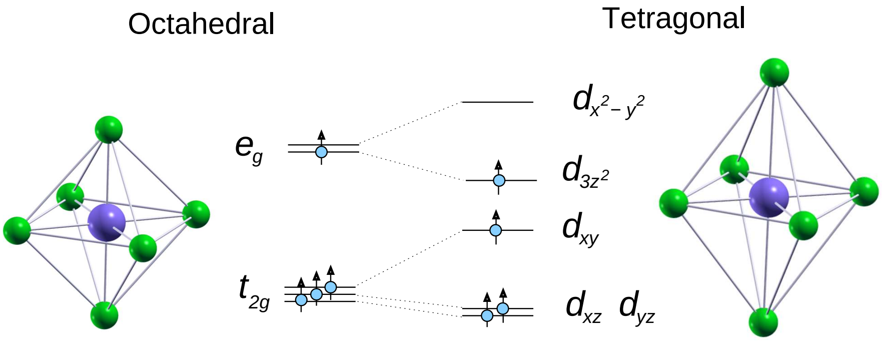

Figure 1.2: The Jahn-Teller effect for Mn^{3+} ($3d^4$). The left side indicates the Mn^{3+} ion (purple) placed at the center of an oxygen (green) octahedron. Due to structural distortion, the octahedral symmetry is converted to a tetragonal one (shown in the right side) and the energy of the d_{3z^2} orbital pointing along the z direction is lowered. Since the d_{3z^2} orbital is filled and the higher $d_{x^2-y^2}$ orbital is empty, the system can lower its energy. For details, see Ref. [10].

with the ionic nature, but reflect the interatomic hopping of the spin-polarized electrons. Itinerant magnetism also occurs in many alloys, such as $Fe_{1-x}Ni_x$, PtCo, and the low-T_c intermetallic $ZrZn_2$. On the other hand, magnetism in rare-earth $4f$ metals, heavy-fermion compounds such as $CeAl_3$ can only be explained from the localized picture. Rare-earth transition metal intermetallics such as $SmCo_5$ and Nd_2Fe_14B exhibit both itinerant ($3d$) and localized ($4f$) features.

In iron-series transition metals the delocalized electrons can be classified as two types, $4s$ electrons and $3d$ electrons. Both $4s$ and $3d$ electrons contribute to transport properties, such as electrical and thermal conductivities, but the magnetic moment largely originates from the $3d$ electrons. However, $4s$ help to realize a RKKY-type exchange [11–13] between the atomic moments. This is different from the rare-earth elements, where the metallic conductivity is due to delocalized $5d$ and $6s$ electrons but the magnetic moment originates from localized $4f$ electrons. As in other transition metal magnets, the orbital moment of the itinerant $3d$ electrons is largely quenched. Typical orbital moments of itinerant $3d$ electrons are of order 0.1 μ_B, so that the Landé g-factor is close to 2 and the moment is equal to the number of unpaired spins.

1.5 Jahn-Teller effect

The Jahn-Teller effect is an important physical effect whose role is more prominent in cluster physics. The Jahn-Teller theorem states that any non-linear molecule with a degenerate electronic ground state will undergo a geometrical distortion that removes the degeneracy, because the distortion lowers the overall energy of the complex [10, 14]. This implies that a system having a degenerate ground state will spontaneously deform to lower its symmetry. It mostly occurs in octahedral complexes of the transition metals. As an example, the mechanism of such effect has been shown for Mn^{3+} ion in

Fig 1.2. When the Mn^{3+} in high spin configuration is placed in the octahedral ligand field, it contains a single electron in the upper e_g state. The system lowers its energy by a tetragonal distortion, thereby causing a splitting in the energy levels. The total energy is lowered due to the lowering of the one of the e_g orbitals (d_{3z^2}) marked by the increased bond length along the z axis. This causes the filled d_{3z^2} orbital to drop in energy below the empty $d_{x^2-y^2}$ orbital. On the other hand, since both of the split t_{2g} states are filled and the center of gravity is preserved, the t_{2g} states donot contribute to the overall energy saving.

1.6 Other general aspects of clusters

The difference between cluster and bulk are manyfold. One of them is the number of surface atoms, which are significantly larger in the cluster. Another aspect of the difference is that the electrons are confined in a small volume of the potential well in clusters. As a result the electrons are filled in discrete levels instead of the band which is characteristic of bulk. Clusters provide the bridge between atoms, molecules and bulk. One of the important questions which is still lacking convincing answer is how many number of atoms are required for a cluster to mimic the bulk behaviour. Although the jellium model sucessfully explains the stability of clusters of nearly free electron metals, it has limitations in describing the structural properties of clusters, such as their geometry and atomic arrangements (for many elements in clusters). There are ample research going on studying clusters by rigorous molecular orbital calculations based on density-functional theory.
Clusters can be broadly classified into following categories based on the type of chemical bonding [4]. Accordingly, needs different experimental setups for synthesis and also different level of theory are necessary for studying the system.

- Van der Waals clusters

  The clusters are characterized by the weak van der Waals interaction. Due to the central force, the most stable clusters have a closed-packing of atoms. The weak binding leads to low melting and boiling points. Molecular clusters like $(I_2)_N$, $(N_2)_N$, $(CO_2)_N$, $(SF_6)_N$ belong to this class.

- Metal clusters

  One can sub-classify the metals clusters based on constituent like, simple metals (Na or Al with sp-valence electrons) and transition metals (Fe or Co, where the localized d electrons play an important role). Some polyvalent non-transition elements like Pb form a group in between. The clusters reflect these characteristics. The strength of the binding in metallic clusters ranges from moderate to strong (0.5 to 3 eV per atom). The main property of the clusters of the simple sp elements is the existence of electronic shell effects [15]. The delocalized character of the electronic states in sp elements allows for the occurence of collective electronic excitations at low energies. The presence of d electrons in transition metals make it more complex than the clusters of *sp* elements. One of the interesting effects of these clusters is their role in catalysis. Another interesting effect is the evolution of magnetic properties with the cluster size.

- Clusters of ionic materials

  The cohesion of such clusters can be described by potentials with an attractive part due to electrostatic monopole forces and a repulsive part from the overlap of the electronic clouds of ions with filled electronic shells. The structures of these clusters can have a rectangular shape cut from the solid.

- Network clusters

  In this case, the covalent bonding leads to the formation of atomic networks in clusters. Materials like Si, Ge and C belong to this catagory. The binding energy in network clusters is strong (1 to 4 eV per atom). Some of the example are the fullerene C_{60}, and water clusters.

1.7 Experimental techniques for synthesis of clusters

Depending on the physical or chemical properties of the clusters, different methods of synthesis techniques are used [16].

Clusters having low melting points can be produced through liquid metal ion source, where the metal cluster is heated in an oven and then distilled into a tungsten capillary needle. By applying high electric field between the tip of the capillary needle and an extraction electrode to the field emission of cluster ions of different size can be synthesized.

Ion bombardment is another method of generating clusters. Here a beam of inert gas ions with a high kinetic energy is directed towards the sample to produce the cluster ions. Charged cluster of noble metals and the Zn group elements have been obtained in this way. This method is applied to produce clusters with high boiling point like alkali halides.

Clusters have been synthesized using techniques like supersonic nozzle sources. The basic idea behind this method is the formation of clusters by condensation of an expanding gas of atoms. A highly compressed gas (typically under pressure of around 10 bar) with atoms of the material to be aggregated is allowed to expand through a small nozzle. The adiabatic expansion slows down the atoms up to a point at which binding between neighboring atoms becomes energetically favorable. This leads to a successive aggregation of the atoms to form clusters. Supersonic sources are often used for producing clusters of low melting metals like alkali metals. A furnace containing molten metal is heated to produce the metal vapor of pressure around 10-100 mbar. This vapor is mixed with a rare gas introduced into the source at a pressure of several bar. The hot mixture of metal vapor and rare gas is driven through the nozzle which expands after coming out of the nozzle. This pure vapor source is efficient to produce van der Waals clusters. In the case of metallic clusters it produces mainly small clusters, and some medium size clusters but with low abundances. This source is not suitable for the formation of large metallic clusters because the process of atom aggregation leaves the cluster in an excited state and the metal vapor must act also as a heat bath to cool the clusters.

Metal clusters can also be produced using gas aggregation sources, where the metal vapor exists in a supersaturated state for a short time. This leads to the formation of small clusters. But large clusters are formed with the increase of corresponding times in gas aggregation sources. In a gas aggregation source the metal vapor from the oven enters a condensation chamber, where it mixes with a stream of inert gas at pressure about 1 Torr. Cluster growth continues in the condensation chamber until the mixture of gas and clusters is discharged through an orifice into a sourrounding vacuum chamber. The distribution of cluster sizes is controlled by the temperatures of the oven and condensation chamber and by the gas flow rate. Experimental parameters can be adjusted to produce clusters up to sizes of 10^5 atoms.

Laser vaporization is another method of producing clusters. It can produce aggregates with up to 100 atoms or more of any substance which exists in the solid state. In this method of production of clusters, a pulsed laser beam is allowed to hit a metallic rod or disk placed in a tube. The laser pulse evaporates atoms producing an extremely hot plasma. This vapor is cooled by a stream of inert gas flowing through the tube and condensation of the vapor produces clusters of different sizes. The flowing inert gas carries the clusters to a vacuum chamber where the pressure difference induces a supersonic expansion of the beam. Collisions ocurring during the expansion cool the aggregates down to a low temperature. Both neutral and ionized clusters has been produced by this method.

1.8 Experimental characterization of clusters

After the production of clusters, it is analyzed to estimate the size distributions and varios other cluster properties. The size distribution is estimated with mass spectrometers. There are two main classes of experimental setups involving either time-dependent or time-independent electromagnetic fields. Typical devices with time-dependent fields are quadrupoles setup, ion cyclotron resonance systems and the widely used time of flight (TOF) set-up. TOF mass spectrometry [2] is a method of mass spectrometry in which ions are accelerated by an electric field of known strength. The velocity of the ion depends on the mass-to-charge ratio. The time that it subsequently takes for the particle to reach a detector at a known distance is measured. From this time and the known experimental parameters one can find the charge to mass ratio of the ion. The characterization discussed is valid for gas-phase synthesis of clusters as discussed above.

X-ray diffraction (XRD) and transmission electron microscopy (TEM) are often used for structure analysis. X-ray photoelectron spectroscopy (XPS) is useful for anlysing the chemical composition of the clusters. Magnetic characterization is commonly done using the superconducting quantum interference device (SQUID). The system is designed to measure the magnetic moment of a sample, from which the magnetization and magnetic susceptibility can be obtained. Temperature dependent magnetic properties can also be studied. X-ray absorption spectroscopy (XAS), which essentially measures the atomic composition of the material by analysing the element specific X-ray absorption process. This is complementary to XPS, which probes the emission spectra. One of the improtant experimental characterization techniques for measuring the spin and orbital magnetic moments separately is XMCD. In this case circularly polarized X-ray from a synchrotron source (which contains an angular momentum - the helicity) is incident on a sample. The XMCD is yielded by the difference of the absorption curves for both the helicities of X-ray. The XMCD effect is commonly described by a two step model [10], which distinguishes the generation of a spin and/or orbitally polarized photoelectron and the transfer of this photoelectron to free electron state of higher energy.

1.9 Outline of thesis

This thesis addresses mainly the structural and magnetic properties of TM clusters based on DFT. As TM clusters, Fe, Co, Ni, Pt and their combinations are mostly studied. TM clusters show enhanced stability at some particular sizes, known as magic numbers (13, 55, 147, 309, 561, 923, $\cdots$). Clusters with magic number of atoms usually have the geometry of a closed shell icosahedron, cuboctahedron and decahedron. As a result, the main focus is on 13 and 55 atom icosahedron and cuboctahedron. The structural stability and magnetic properties of isolated and deposited closed shell transition metal clusters are studied with much focus. Along with the elemental clusters, some of the binary clusters of (Fe-Co, Ni, Pt) are studied. The motivation for studying binary clusters is that the intermixing of different atomic species in clusters gives rise to more parameters to control the physical and chemical properties, those are different from the corresponding elemental clusters. After a short description of the DFT and specific settings used for the calculations in the second chapter, the elementary and binary clusters are discussed with emphasis on properties like segregation and mixing in clusters in the third chapter.

The magnetic clusters are projected as possible candidates for future recording media [17], where hypothetically, each cluster can store one bit of information by means of the magnetic configuration. For this purpose, magnetic anisotropy is a primary requirement. Since magnetism of small clusters is not stable due to superparamagnetism and thermal fluctuation is a major menace as size reduction of the storage devices, therefore, materials with large magnetic anisotropy are needed to block the thermal fluctuations. In chapter four, the magnetic anisotropy, spin moment and orbital moments of elemental and binary clusters are discussed. The studies on orbital magnetism and magnetic anisotropy needs the incorporation of spin-orbit interaction in the DFT Hamiltonian. The spin-orbit coupling in the present case is treated as a perturbation term in the scalar-relativistic Hamiltonian. Theoretical determination of magnetic anisotropy based on DFT is challenging, because of the very small energy differences. For example, the value of magnetocrystalline anisotropy in bulk is of the order of 10^{-6} eV. Thus, to determine the magnetic anisotropy for clusters, the energy tolerance to 10^{-10} eV is necessary which is a sensitive task [18]. Therefore, calculation of MAE requires much careful attention towards some facts like the proper convergence of energy and accuracy of the results.

Physical phenomena associated with surfaces and its interaction with molecules and clusters are currently much aspired research problems [19]. Chapter five discusses the structural stability and magnetic properties of clusters deposited on Pt surfaces. The magnetic anisotropy of deposited clusters are also discussed.

The use of TM clusters as catalysts is well known [20, 21]. Some studies on the catalytic activity of metal clusters are attempted and reported in the literature [23, 24]. (Fe, Co, Ni and Pt) $_{13,55}$ clusters on a pristine (defect free) and a five-member ring graphene (with defect) sheet are used as substrate to study the stability of clusters and the cluster-graphene interface. This topic is discussed in chapter six.

The cluster calculations have mostly been perfomed with a quantum mechanical package named as Vienna Ab initio simulation package (VASP) [25, 26]. It solves the Kohn-Sham equations of local density or spin-density functional theory, iteratively within a plane-wave basis-set. The interaction between ions and electrons is described by the projector-augmented wave (PAW) [27] method. In addition to the VASP calculations, we have used the SIESTA code [28] for a comparative study in chapter four. In a few case, the cluster calculations have been performed with the full potential FPLO code of the Dresden group [29], see chapter four. The consideration of catalytic reaction (oxidation of CO in different environments) in chapter six represents the first step in this important of research. Here, further calculations are needed, which are beyond the scope of the present thesis.

Thermodynamics of the cluster magnetism is done by the exact diagonalization method. In chapter seven, we discuss the Heisenberg spin Hamiltonian to which our cluster can be modeled and then study the thermodynamic properties by the exact diagonalization technique. We have treated the case of 13- and 4-atom clusters with spin-1/2 and spin-1 particles [30, 31].

2 Density functional theory

The DFT is a theory where the many-body problem is treated by the single-particle density through the Kohn-Sham equations. This was proposed by P. Hohenberg and W. Kohn in 1964 [32]. The total energy is a functional of the density. Thus all properties of the system can be considered to be unique functionals of the ground state density. The number of degrees of freedom is now significantly reduced allowing for quick computations in comparison to other quantum chemical methods. As a result DFT has become a primary tool for calculation of electronic structure in condensed matter and is increasingly important for quantitative studies of molecules and other finite systems. The formulation of DFT as we use today, comes from the classic work of W. Kohn and L. J. Sham [33] and has become the basis of much of present-day methods for treating electrons in atoms, molecules, clusters, surfaces, adsorbates and bulk. One of the landmark achievement of the DFT is the local-density approximation (LDA) as the exchange-correlation functional which is very successful in describing the material properties. Improvements over LDA, like generalized gradient approximation (GGA) is also mostly recommended in many cases. Below we present a brief theoretical description of the DFT following the description of Ref. [34]. For more detailed description one must refer to standard books and review articles.

2.1 Thomas-Fermi-Dirac model

The original DFT of quantum systems was proposed by Thomas [35] and Fermi [36] in 1927. Although their approximation is not accurate enough for present-day electronic structure calculations, the approach illustrates the way DFT works. In the original Thomas-Fermi method the kinetic energy of the system of electrons is approximated as an explicit functional of the density, idealized as non-interacting electrons in a homogeneous gas with density equal to the local density at any given point. However, in this case the exchange-correlation among the electrons is neglected. Later on in 1930, Dirac formulated the local approximation for exchange. This leads to the energy functional for electrons in an external potential $V_{\mathrm{ext}}(\mathbf{r})$

$$\begin{aligned} E_{\mathrm{TF}}[n] = C_1 \int d^3r\; n(\mathbf{r})^{5/3} + \int d^3r\; V_{\mathrm{ext}}(\mathbf{r}) n(\mathbf{r}) + C_2 \int d^3r\; n(\mathbf{r})^{4/3} \\ + \frac{1}{2} \int d^3r d^3r'\; \frac{n(\mathbf{r})n(\mathbf{r})'}{\mid \mathbf{r} - \mathbf{r}' \mid} \end{aligned} \tag{2.1}$$

where the first term is the local approximation to kinetic energy with $C_1 = \frac{3}{10}(3\pi^2)^{2/3}$ The ground state density and energy can be found by minimizing the functional $E_{TF}[n]$ in Eq. (2.1) and the number of electrons $n(\mathbf{r})$

$$\int d^3r\, n(\mathbf{r}) = N. \tag{2.2}$$

Using the Lagrange method, the solution can be found by an unconstrained minimization of the functional

$$\Omega_{\mathrm{TF}}[n] = E_{\mathrm{TF}}[n] - \mu\{\textstyle\int d^3r\, n(\mathbf{r}) - N\} \tag{2.3}$$

where the Lagrange multiplier μ is the Fermi energy. For small variations of the density $\delta n(\mathbf{r})$, the condition for a stationary point is

$$\int d^3r\, \{\Omega_{\mathrm{TF}}[n(\mathbf{r}) + \delta n(\mathbf{r})] - \Omega_{\mathrm{TF}}[n(\mathbf{r})]\} \rightarrow \int d^3r \left\{\frac{5}{3}C_1 n(\mathbf{r})^{2/3} + V(\mathbf{r}) - \mu\right\} \delta n(\mathbf{r}) = 0, \tag{2.4}$$

where $V(\mathbf{r}) = V_{\mathrm{ext}}(\mathbf{r}) + V_{\mathrm{Hartree}}(\mathbf{r}) + V_{\mathrm{x}}(\mathbf{r})$ is the total potential. Since Eq. 2.4 must be satisfied for any function $\delta n(\mathbf{r})$, it follows that the functional is stationary if and only if the density and potential satisfy the relation

$$\frac{1}{2}(3\pi^2)^{2/3} n(\mathbf{r})^{2/3} + V(\mathbf{r}) - \mu = 0. \tag{2.5}$$

DFT is attractive because in this case the equation for density is more simpler compared to the many-body Schrödinger equation that involves $3N$ degrees of freedom for N electrons. Thomas-Fermi approach has very crude approximations, which lacks the essential physics, unable to provide a useful description of electrons in matter.

2.2 The Hohenberg-Kohn theorems

The formulation of DFT by Hohenberg and Kohn applies to any system of interacting particles in an external potential $V_{\mathrm{ext}}(\mathbf{r})$, with the electrons and fixed nuclei. In this case, the Hamiltonian can be written as

$$\hat{H} = -\frac{\hbar^2}{2m_e}\sum_i \nabla_i^2 + \sum_i V_{\mathrm{ext}}(\mathbf{r}_i) + \frac{1}{2}\sum_{i\neq j}\frac{e^2}{\mid \mathbf{r}_i - \mathbf{r}_j \mid}. \tag{2.6}$$

DFT is based on two theorems proved by Hohenberg and Kohn [32], which is as follows.

- Theorem **I**: For any system of interacting particles in an external potential $V_{ext}(\mathbf{r})$, the potential $V_{\mathrm{ext}}(\mathbf{r})$ is uniquely determined, except for a constant, by the ground state particle density $n_0(\mathbf{r})$.

- Theorem **II**: A universal functional for the energy $E[n]$ in terms of the density $n(\mathbf{r})$ can be defined, which is valid for any external potential $V_{\text{ext}}(\mathbf{r})$. For any particular $V_{\text{ext}}(\mathbf{r})$, the exact ground state of the system is the global minimum value of this functional, and the density $n(\mathbf{r})$ which minimizes the functional is the exact ground state density $n_0(\mathbf{r})$.

2.3 The Kohn-Sham approach

The assumption made behind this approach is that the ground state density of the original interacting system is equal to that of a non-interacting system, which leads to independent particle equations of the non-interacting system that can be considered exactly soluble with all many-body terms incorporated into an exchange-correlation functional of the density. By solving the equations one finds the ground state density and energy of the original interacting system with the accuracy limited by the approximations in the exchange-correlation functional.

The Hamiltonian for the independent particle system has form

$$\hat{H}^{\sigma} = -\frac{1}{2}\nabla^2 + V^{\sigma}(\mathbf{r}) \tag{2.7}$$

For a system of N independent electrons with $N = N^{\uparrow} + N^{\downarrow}$ obeying this, the ground state has one electron in each of the N^{σ} orbitals ψ_i^{σ} with the lowest eigen values ε_i^{σ} of the Hamiltonian (Eq. 2.7). The density of the auxiliary system is given by sums of squares of the orbitals for each spin

$$n(\mathbf{r}) = \sum_{\sigma} n(\mathbf{r},\sigma) = \sum_{\sigma}\sum_{i=1}^{N^{\sigma}} |\ \psi_i^{\sigma}(\mathbf{r})\ |^2 \tag{2.8}$$

the independent-particle kinetic energy T_s is given by

$$T_s = -\frac{1}{2}\sum_{\sigma}\sum_{i=1}^{N^{\sigma}} \langle \psi_i^{\sigma} \mid \nabla^2 \mid \psi_i^{\sigma}\rangle = \frac{1}{2}\sum_{\sigma}\sum_{i=1}^{N^{\sigma}} |\ \nabla\psi_i^{\sigma}\ |^2, \tag{2.9}$$

and the classical Coulomb energy of the electron density $n(\mathbf{r})$ is defined as

$$E_{\text{Hartree}}[n] = \frac{1}{2}\int d^3r d^3r' \frac{n(\mathbf{r})n(\mathbf{r}')}{|\ \mathbf{r}-\mathbf{r}'\ |}. \tag{2.10}$$

The Kohn-Sham approach to the full interacting many-body problem is to rewrite the Hohenberg-Kohn expression of ground state energy functional in the form

$$E_{\text{KS}} = T_s[n] + \int d\mathbf{r} V_{\text{ext}}(\mathbf{r}) n(\mathbf{r}) + E_{\text{Hartree}}[n] + E_{\text{H}} + E_{\text{xc}}[n]. \tag{2.11}$$

Where, $V_{\text{ext}}(\mathbf{r})$ is the external potential due to the nuclei and other external fields (assumed to be independent of spin), E_H: the interaction among the nuclei.

Using expressions for $n^\sigma(\mathbf{r})$ and T_s from Eqs. 2.8 and 2.9 and the Lagrange multiplier method for the constraints, the Kohn-Sham Schrödinger-like equation is obtained. this has a form

$$(H_{\mathrm{KS}}^\sigma - \varepsilon_i^\sigma)\psi_i^\sigma(\mathbf{r}) = 0, \tag{2.12}$$

where ε_i are the eigenvalues, and H_{KS} is the effective Hamiltonian

$$H_{\mathrm{KS}}^\sigma(\mathbf{r}) = -\frac{1}{2}\nabla^2 + V_{\mathrm{KS}}^\sigma(\mathbf{r}), \tag{2.13}$$

where $V_{\mathrm{KS}}^\sigma(\mathbf{r})$ consists of three terms, i.e.,

$$V_{\mathrm{KS}}^\sigma(\mathbf{r}) = V_{\mathrm{ext}}(\mathbf{r}) + \frac{\delta E_{\mathrm{Hartree}}}{\delta n(\mathbf{r},\sigma)} + \frac{\delta E_{\mathrm{xc}}}{\delta n(\mathbf{r},\sigma)} = V_{\mathrm{ext}}(\mathbf{r}) + V_{\mathrm{Hartree}}(\mathbf{r}) + V_{\mathrm{xc}}^\sigma(\mathbf{r}). \tag{2.14}$$

The last three equations are the Kohn-Sham equations, with the electron density $n(\mathbf{r},\sigma)$ and total energy E_{KS} given in Eqs. 2.8 and 2.11. If the exact $E_{\mathrm{xc}}[n]$ functional is known, then the exact ground state density and energy can be calculated for the interacting system.

2.4 Exchange correlation functionals

2.4.1 Local density approximation (LDA)

In local density approximation (LDA) or more generally the local spin density approximation (LSDA), the exchange- correlation energy is an integral over all space with the exchange-correlation energy density at each point assumed to be the same as in a homogeneous electron gas with that density,

$$E_{\mathrm{xc}}^{LSDA}[n^\uparrow, n^\downarrow] = \int d^3r\, n(\mathbf{r})\varepsilon_{\mathrm{xc}}^{\mathrm{hom}}(n^\uparrow(\mathbf{r}), n^\downarrow(\mathbf{r})) \tag{2.15}$$

Here, the spin quantization axis is assumed to be the same at all points in space. The LSDA is the most common local approximation for exchange and correlation . In the case of unpolarized systems, the LDA is found by setting $n^\uparrow(\mathbf{r})$=$n^\downarrow(\mathbf{r})$=$n(\mathbf{r})/2$. In LDA,

$$\delta E_{\mathrm{xc}}[n] = \sum_\sigma \int d\mathbf{r} \left[\varepsilon_{\mathrm{xc}}^{\mathrm{hom}} + n\frac{\partial\varepsilon_{\mathrm{xc}}^{\mathrm{hom}}}{\partial n^\sigma}\right]_{\mathbf{r},\sigma} \delta n(\mathbf{r},\sigma) \tag{2.16}$$

Hence the exchange-correlation potential V_{xc}^σ can be expressed as

$$V_{\mathrm{xc}}^\sigma(\mathbf{r}) = \left[\varepsilon_{\mathrm{xc}}^{\mathrm{hom}} + n\frac{\partial\varepsilon_{\mathrm{xc}}^{\mathrm{hom}}}{\partial n^\sigma}\right]_{\mathbf{r},\sigma}, \tag{2.17}$$

Since $\varepsilon_x^{\mathrm{hom}}(n^\sigma)$ scales $(n^\sigma)^{-1/3}$, the LDA exchange terms are

$$V_{\mathrm{xc}}^\sigma(\mathbf{r}) = \frac{4}{3}\varepsilon_x^{\mathrm{hom}}(n(\mathbf{r},\sigma)). \tag{2.18}$$

2.4.2 Generalized-gradient approximation (GGA)

In generalized gradient approximation (GGA), the exchange-correlation potential is treated as a function of both electron density as well as the gradient of the density. The exchange-correlation functional in GGA has the form

$$\delta E_{\mathrm{xc}}[n] = \sum_{\sigma} \int d\mathbf{r} \left[\varepsilon_{\mathrm{xc}} + n\frac{\partial \varepsilon_{\mathrm{xc}}}{\partial n^{\sigma}} + n\frac{\partial \varepsilon_{\mathrm{xc}}}{\partial \nabla n^{\sigma}} \nabla \right]_{\mathbf{r},\sigma} \delta n(\mathbf{r},\sigma). \tag{2.19}$$

where, the term in the square brackets is the exchange-correlation potential.

$$\delta V^{\sigma}_{\mathrm{xc}}(\mathbf{r}) = \left[\varepsilon_{\mathrm{xc}} + n\frac{\partial \varepsilon_{\mathrm{xc}}}{\partial n^{\sigma}} + n\frac{\partial \varepsilon_{\mathrm{xc}}}{\partial \nabla n^{\sigma}} \nabla \right]_{\mathbf{r},\sigma}. \tag{2.20}$$

2.5 Basis sets

A basis set is a set of unknown functions through which the wavefunction is expanded. For a single electron, the wavefunction can be written as

$$\psi_i(\mathbf{r}) = \sum_{j=1}^{\infty} c_j \phi_j(\mathbf{r}) \tag{2.21}$$

where $\phi_j(\mathbf{r})$ are a complete set of functions. Any set of functions could be used as basis functions. In principle, the basis functions should have the same limiting behavior as the real wavefunction, for isolated atom or molecules they should decay to zero, and they should be computationally inexpensive.

2.5.1 Localized basis sets

The wavefunction exponentially decays to zero at large distances for isolated atoms and molecules. This means that the basis functions also should behave in a similar way. Atomic orbitals are the basis functions possessing this property and have two forms: Slater type orbitals (STO) and Gaussian type orbitals (GTO).

STOs have the following form in spherical coordinates [37]

$$\phi^{nlm\zeta}_{\mathrm{STO}}(r,\theta,\phi) = \alpha Y_{lm}(\theta,\phi) r^{n-1} e^{-\zeta r}$$

where α is a normalization constant, $Y_{lm}(\theta,\phi)$ is the spherical harmonic. l, m, and n are quantum numbers, and ζ determines the radius of the orbit. The exponential dependence on distance is the same as for the hydrogen atom.

GTOs in spherical coordinates have a form

$$\phi^{nlm\zeta}_{\mathrm{GTO}}(r,\theta\phi) = \alpha Y_{lm}(\theta,\phi) r^{(2n-2-l)} e^{-\zeta r^2}.$$

In both cases the angular dependence of the wavefunction is contained in the spherical harmonics, where the l, m values determine the type of orbital (e.g. $l = 0$ is a s type orbital, $l = 1$ a p orbital, etc). The main difference between STO and GTO is the power of r in the exponent. GTOs have a zero slope at the nucleus ($r = 0$) whereas STOs have a cusp. GTOs also fall off more rapidly with distance than STOs. These factors suggest that more GTOs are needed to form a suitable basis set than STOs, roughly three times as many are needed to achieve the same accuracy [37]. However, GTOs are computationally more efficient than STOs: the factor r in the exponent requires taking a square root ($r = \sqrt{x^2 + y^2 + z^2}$) which is computationally very slow. This computational efficiency compensates for the additional number of functions needed, hence GTOs are more commonly used in calculations. The size of the basis set has a large effect on the accuracy of the calculation. The smallest basis set possible is the minimum basis set which contains only enough functions to contain all the electrons in the neutral atoms. Increasing the number of basis functions improves the accuracy of the calculation.

2.5.2 Plane wave basis sets

The potential for a periodic system has the property

$$V(\mathbf{r} + n\mathbf{a}) = V(\mathbf{r}) \tag{2.22}$$

where $\mathbf{a}$ is a lattice vector and n is an integer. From Bloch's theorem [38], the wavefunction can be written as a product of a periodic and a wave-like part, i.e.,

$$\psi_i(\mathbf{r}) = e^{i\mathbf{k}\cdot\mathbf{r}}\phi_i(\mathbf{r}) \tag{2.23}$$

Because of periodicity, $f(\mathbf{r})$ can be expanded as a set of plane waves

$$\phi_i(\mathbf{r}) = \sum_{G} c_i, G e^{i\mathbf{G}\cdot\mathbf{r}} \tag{2.24}$$

where $\mathbf{G}$ are the reciprocal lattice vectors. Substituting Eq. 2.24 in Eq. 2.23, the wave function can be written as

$$\psi_i(\mathbf{r}) = \sum_{\mathbf{G}} c_{i,\mathbf{G}} e^{i(\mathbf{k}+\mathbf{G})\cdot\mathbf{r}} \tag{2.25}$$

The number of wavefunctions used is controlled by the largest wave vector in the expansion in Eq. 2.24. This is equivalent to a cut-off on the kinetic energy since the kinetic energy of an electron with wave vector $\mathbf{k}$ is given by

$$E_k = \frac{\hbar^2|\mathbf{k}|^2}{2m}. \tag{2.26}$$

Using the plane waves, the Kohn-Sham equations can be written as [39]

$$\left[\sum_{G'} \frac{\hbar^2}{2m}|\mathbf{k}+\mathbf{G}|^2\delta_{\mathbf{GG'}} + V_{en}(\mathbf{G}-\mathbf{G'}) + V_{ee}(\mathbf{G}-\mathbf{G'}) + V_{\mathrm{XC}}(\mathbf{G}-\mathbf{G'})\right] c_{i,\mathbf{k}+\mathbf{G'}} = c_{i,\mathbf{k}+\mathbf{G}}\varepsilon_i, \tag{2.27}$$

where $V_{\mathrm{en}}(\mathbf{G}-\mathbf{G'})$, $V_{\mathrm{ee}}(\mathbf{G}-\mathbf{G'})$ and $V_{\mathrm{XC}}(\mathbf{G}-\mathbf{G'})$ are the Fourier transforms of electron-nuclei, electron-electron, and exchange-correlation potentials.

The major advantages of using plane wave basis sets:

- it is very easy to calculate all kinds of matrix elements, where the fast-Fourier-transform techniques are of great help.
- the size of basis set can be increased systematically in a simple way.
- the same basis set can be used for all atomic species,
- convergence towards completeness can easily be tested,
- plane waves do not depend on nuclear positions so, unlike localized basis sets, correction terms are not needed for the calculation of forces.

The main disadvantage is that the basis sets become large very easily. For finite systems such as clusters and molecules in a plane wave approach, it is essential to construct a supercell in each dimension in which the system is localized. In order to neglect any interactions with the images, the supercell should be large enough. This means that a large number of plane waves should be used; nevertheless, this may be an effective way of solving the problem.

2.6 Pseudopotentials

The application of pseudopotentials in electronic structure is to replace the strong Coulomb potential on the nucleus and the effects of tightly bound core electrons by an effective ionic potential acting on the valence electrons. Since the core states remain unchanged, a pseudopotential can be generated and used to compute properties of valence electrons in the system. The advantage of ultrasoft or norm-conserving pseudopotentials has led to accurate calculations which are the basis for the development of new methods in electronic structure.

2.6.1 Norm-conserving pseudopotentials

The norm-conserving pseudo functions ψ^{PS} are normalized and are solutions of a model potential chosen to reproduce the valence properties of all-electron calculation. In the application of pseudopotential to molecules, clusters or solids, the valence pseudo functions must satisfy the orthonormality conditions, i.e.,

$$\langle \psi_i^{\sigma,PS} \mid \psi_j^{\sigma',PS} \rangle = \delta_{i,j}\delta_{\sigma,\sigma'} \tag{2.28}$$

so that the Kohn-Sham equations can be written as,

$$\left(H_{\mathrm{KS}}^{\sigma,PS}-\varepsilon_i^{\sigma}\right)\Psi_i^{\sigma,PS}(r)=0, \tag{2.29}$$

with the external potential given by the pseudopotentials.

The norm-conserving pseudopotentials must satisfy the following conditions, namely,

1. All-electron and pseudo valence eigenvalues must agree for the atomic reference configuration.
2. All-electron and pseudo valence wavefunctions must agree beyond the core radius R_c.
3. The logarithmic derivatives of the all-electron and pseudo wavefunctions must agree at R_c.
4. The integrated charge inside R_c for each wavefunction must agree (norm-conservation).
5. The energy derivative of the logarithmic derivatives of the all-electron and pseudo wavefunctions must agree at R_c.

Generation of a pseudopotential starts with the usual all-electron atomic calculation with each l, m states treated independently. The total potential is calculated self-consistently for the given approximation for exchange and correlation and for the given configuration of the atom.

Relativistic effects can be incorporated into the pseudopotentials, since they lead to finite effects in the interior of the atom very close to the nucleus. The relativistic effects incorporated in the valence electrons, like shifts due to scalar relativistic effects and spin-orbit interactions, could be easily carried into the molecular or solid-state calculations.

2.7 Projector augmented wave (PAW) method

The projector augmented wave (PAW) method [27], developed by Blöchl (1994) is a powerful method for performing pseudopotential electronic structure calculations within DFT. It retains the information about the correct nodal behavior of the valence electron wave functions and includes the upper core states in addition to valence states in the self-consistent iterations without significant additional computation. The problem of constructing the projector and basis functions needed for PAW technique is very similar to the problem of constructing local and nonlocal pseudopotentials. The PAW method starts with a self-consistent all-electron atomic structure calculation within the framework of DFT. The projector and basis functions are derived from the eigenstates of the all-electron atomic Hamiltonian. They are determined iteratively solving radial differential equations. A detailed description of the PAW method can be found in Ref [40].

2.8 Noncollinear magnetism

In the collinear case of a spin polarized system, for spin up and spin down there are always two densities $[n^{\uparrow}(\mathbf{r}), n^{\downarrow}(\mathbf{r})]$ and potentials $[V_{\text{xc}}^{\uparrow}(\mathbf{r}), V_{\text{xc}}^{\downarrow}(\mathbf{r})]$. Since the spin axis can vary in space, i.e., the non-collinear case [41], the electron density at every point is represented by a vector giving the direction.

The local spin density matrix has a form

$$\rho^{\alpha\beta}(\mathbf{r}) = \sum_i \phi_i \psi_i^{\alpha\star}(\mathbf{r})\psi_i^{\beta}(\mathbf{r}), \tag{2.30}$$

The Kohn-Sham Hamiltonian becomes a 2 × 2 matrix

$$H_{\text{KS}}^{\alpha\beta}(\mathbf{r}) = -\frac{\hbar^2}{2m_e}\nabla^2 + V_{\text{KS}}^{\alpha\beta}(\mathbf{r}), \tag{2.31}$$

where the only part of $V_{\text{KS}}^{\alpha\beta}$ that is non-diagonal in $\alpha\beta$ is $V_{\text{xc}}^{\alpha\beta}$.

Although this looks like a major complication, the real difficulty is in the nature of the functional $\varepsilon_{\text{xc}}^{\alpha\beta}$. In LDA it is given by finding the local axis of spin quantization and using the same functional form $\varepsilon_{\text{xc}}^{\text{hom}}(n^{\uparrow}(\mathbf{r}), n^{\downarrow}(\mathbf{r}))$, whereas the gradient of spin axis is taken into account for the modifications of GGA expressions.

2.9 Spin-orbit coupling

The spin-orbit coupling involves the interaction between electron spin with its orbital motion. It plays an significant role in determining the magnetic properties such as the magnetocrystalline anisotropy, magnetostriction and magneto-optical effects. The spin-orbit coupling can be included as a perturbation in the scalar relativistic LSDA Hamiltonian (Eq. 2.13) with a self-consistent treatment of spin-orbit contribution at each variational step.

$$\hat{H} = \hat{H}_0 + \hat{H}_{\text{SO}} \tag{2.32}$$

where, H_0 is the scalar relativistic Hamiltonian and H_{SO} is the spin-orbit Hamiltonian, which has a form

$$\hat{H}_{\text{SO}} = \frac{\hbar^2}{2M^2c^2}\frac{1}{r}\frac{dV}{dr}\mathbf{L}\cdot\sigma = \xi\mathbf{L}\cdot\sigma, \tag{2.33}$$

$\xi = \frac{\hbar^2}{2M^2c^2}\frac{1}{r}\frac{dV}{dr}$ and is the spin-orbit coupling strength.

For 3d transition metals, the H_{SO} alters charge density, spin density, and spin moment negligibly [42]. While for heavy elements like 4d or 5d elements, H_{SO} has to be included in the self-consistence loop for the solution of the Kohn-Sham equations.

2.10 Methods for the determination of magnetocrystalline anisotropy

The determination of magnetocrystalline anisotropy energy (E_{MAE}) form first-principles is a great challenge. It is known that spin-orbit coupling is the origin of magnetocrystalline anisotropy, which is the fully relativistic total energy difference between two separate magnetization directions. There are three different methods to calculate the MAE; (i) the force theorem [43–45], (ii) the total energy [46], (iii) the torque method [45, 47]. There are evidences of achieving similar results for most of the $3d$ systems.

The calculation of MAE through force theorem includes the difference in the band energies of the two different magnetization directions with spin-orbit coupling included in the Kohn-Sham equation in the presence of the same self-consistent scalar-relativistic potential [43, 44]. It has a the following form

$$E_{MAE} = E(90^\circ) - E(0^\circ) \approx \sum_{occ'} \varepsilon_i(90^\circ) - \sum_{occ'} \varepsilon_i(0^\circ). \tag{2.34}$$

Where, ε_i are the band energies which are summed up to the occupied bands. In order to restrain the numerical fluctuations, a large number of k points are required.

On the other hand, the calculation of MAE from total energies not only deals with large number of k points but also a well-converged charge density or potential.

The torque method [47] involves the calculation of the expectation values of the angular derivative of H^{SOC} (spin-orbit coupling term) at some particular angle (θ_m and ϕ_m). The prime in the wave function denotes the consideration of SOC.

$$E_{\mathrm{MAE}} = \sum_{i\varepsilon occ} \langle \Psi_i'(\theta_m, \phi_m) \mid \frac{\partial H^{\mathrm{SOC}}}{\partial \theta} \mid \Psi'(\theta_m, \phi_m) \rangle. \tag{2.35}$$

θ_m and ϕ_m can be found from the symmetry of the crystal lattice. However, it gives reliable results with few k-points.

2.11 Electronic structure calculations

2.11.1 Single point energy calculations

In a single point energy (SPE) calculation, the wavefunction and charge density, and hence the energy of an arrangement of nuclei is calculated self-consistently. The total energy functional of a system of electrons and nuclei can be written as

$$E[\rho(\mathbf{r_i}), \mathbf{R}_I] = T_e[\rho(\mathbf{r_i})] + T_n + E_{en}[\rho(\mathbf{r}_i), \mathbf{R_I}] + E_{ee}[\rho(\mathbf{r_i})] + E_{nn}(\mathbf{R_I}) \tag{2.36}$$

where $T_e[\rho(\mathbf{r_i})]$ is the electronic kinetic energy, T_n is the nuclear kinetic energy, E_{en} is the electron-nuclei interaction, E_{ee} is the electron-electron interaction and E_{nn} is the nuclei-nuclei interaction. E_{ne} is described using pseudopotentials, while for a fixed set of nuclear positions T_n is zero and E_{nn} is a constant. Therefore, a SPE calculation is reduced to finding the charge density that minimizes the total energy functional by solving the Kohn-Sham equations.

The total energy minimization can be done in several ways. One method is through direct diagonalization of the matrix equation 2.27. Starting from an initial trial density E_{ee} is calculated and inserted into 2.27. A new density is then calculated by inverting the matrix equation 2.27. If the change in energy between iterations is smaller than a given tolerance, it is then inserted into the total energy functional and the energy calculated. Otherwise this new density is used to calculate a new E_{ee}. This is repeated until the density and potential are consistent with each other within a given tolerance.

The matrix diagonalization method has the disadvantage that the computational cost of matrix diagonalization scales as the cube of number of plane waves. An alternative method is to minimize the energy functional directly [48], where the energy is a functional of the density, which is determined by the expansion coefficients $c_{i,\mathbf{k}+\mathbf{G}}$. The ground state density is found from the set of $c_{i,\mathbf{k}+\mathbf{G}}$ that minimize the energy functional. Several standard functional optimization methods [49] can then be used to find the minima of the total energy functional. One of such techniques is the method of Steepest Descents (SD) [49]. The SD method produces a series of points $\{\mathbf{P}_i\}$

$$\mathbf{P}_{i+1} = \mathbf{P}_i + \lambda_i \mathbf{h}_i \tag{2.37}$$

where

$$\mathbf{h}_i = -\nabla f(\mathbf{P}_i).$$

Here, $\mathbf{P}_i$ are sets of plane wave expansion coefficients and $f(\mathbf{P})$ is the energy functional. λ_i (a scalar) is the distance along the direction $\mathbf{h}_i$ from $\mathbf{P}_i$ that a minima is located. The SD method proceeds by moving in the steepest downhill direction from a point $\mathbf{P}_i$ until a minima along that direction is located at point $\mathbf{P}_{i+1}$. The steepest downhill direction from $\mathbf{P}_{i+1}$ is then determined ($-\nabla f(\mathbf{P}_{i+1})$) and the minima located along that direction is found. This is repeated until the change in the function is lower than a preset tolerance. The speed at which the SD method will find a minima is limited as at each step only the information at that point is taken into account. It is easy to think of examples where this will lead to slow convergence. A better method is the Conjugate Gradients (CG) method [48, 49]]. It differs from the SD method in that each search direction is conjugate to the last one. In CG method the function has a quadratic form

$$f(\mathbf{x}) \approx \frac{1}{2}\mathbf{x}.\mathbf{A}.\mathbf{x} \tag{2.38}$$

where $\mathbf{A}$ is the Hessian and is given by

$$A_{ij} = \left.\frac{\partial^2 f}{\partial x_i \partial x_j}\right|_{\mathbf{x}=\mathbf{x}_0}. \tag{2.39}$$

Using the quadratic form Eq. 2.38 the step needed to get to the minima in the direction $\mathbf{h}_i$ is given by [49]

$$\lambda_i = \frac{\mathbf{h}_i.\mathbf{g}_i}{\mathbf{h}_i.\mathbf{A}.\mathbf{h}_i}. \tag{2.40}$$

This however can be found from a one-dimensional minimization along $\mathbf{h}_i$, i.e. without explicitly calculating the Hessian. As the Hessian is an $N \times N$ matrix, for DFT calculations with $N = 10^5 - 10^6$ plane waves the CG method has a large advantage over methods that explicitly use the Hessian. The CG method will find a minimum of an N dimensional function in N iterations. For CG and SD methods to minimize the total energy functional, the wavefunctions have to be orthonormal which is an additional constraint on the minimization. The number of iterations required can be substantially reduced by preconditioning the function [48].

2.11.2 Geometry optimization

The aim of geometry optimization is to generate the lowest energy structure of a molecule or cluster from any arbitrary starting state. Since using the Born-Oppenheimer approximation, the motion of the nuclei and the electrons can be separated, hence a geometry optimization consists of a set of single point energy calculations. For the initial starting geometry, a SPE calculation is performed. The forces on the nuclei are calculated from the wavefunction using the Hellmann-Feynman theorem [50]. The force in this case is given by

$$\mathbf{F}_I = -\left\langle \frac{\partial E}{\partial \mathbf{R}_I} \right\rangle \tag{2.41}$$

where E is the energy, R_I is the position of the nucleus. This force can be used to find the ground state positions of the atoms. As the forces point towards a local minimum in the energy integrating the equations of motion for the nuclei will move the nuclei towards an equilibrium structure. Alternatively, functional optimization techniques like SD or CG methods may be used. However the Hessian based methods [49] may also be used for this purpose.

Two points should be made about the above method. Firstly, if the basis set is incomplete, an error is introduced into the Hellman-Feynman forces, known as the Pulay force [51]. However, for a plane wave basis set the wavefunctions do not depend on the nuclear positions, hence this error is zero, as long as the electronic system has converged to the ground state. For situations where the cell shape changes analogous Pulay stresses arise. Secondly, the above procedure will find the nearest point in the configuration space at which the forces are zero. Hence, if a poor starting point is chosen it may find a local rather than a global minimum in the potential energy surface or if the starting point is an energy maximum it may stay there. This procedure can also be rather time consuming with many SPE calculations needed to find the minima. Thus it is common to perform an initial energy minimization using molecular mechanics calculations to get to the vicinity of a minima and then perform a full *ab initio* geometry optimization.

3 Structure and magnetism in transition metal clusters

3.1 Introduction

One of the important quest in the physics of transition metal clusters is to understand how the properties of clusters vary with change in morphology and size. The physical and chemical properties of clusters, such as magnetic properties and chemical reactivity can be determined by analyzing their geometry and electronic structures. For instance, the magnetic properties of TM clusters depend on various parameters like bond lengths, structural geometry, cluster size, d-band filling (TM type), atomic distributions (for binary clusters) and surrounding environment (deposited clusters). Therefore it is essential to study the physics of clusters by an *ab initio* approach, where all type of interactions are modeled through more fundamental electron-electron interactions and correlations.

Transition metal clusters of Fe, Co and Ni have been the main topic of research both experimentally [52–55] and theoretically [56, 57]. Experimental studies based on Stern-Gerlach setup [52] for magnetic properties of Fe_N, Co_N and Ni_N clusters show enhancement of the average magnetic moment for small clusters relative to bulk. With increase in cluster size, upto few hundreds of atoms, the average magnetic moment are still higher but slowly approaches towards the corresponding bulk value in a non monotonous way. The convergence of magnetic moment towards the bulk limit are faster for Ni and Co in comparison to Fe. There exist various experimental [52, 53] and theoretical [56, 58–60] studies for the structure and magnetism of Ni and Fe clusters. For example, the geometry of small Ni_N, $3 \leq N \leq 28$, clusters have been studied by Parks *et al.* [61, 62] through molecular adsorption and have reported different atomic packings with respect to cluster sizes. Using the classical molecular dynamics and molecular orbital theory, Reddy et al. [63] have studied the morphology, energetics, electronic structure and vertical ionization potential and magnetic properties of Ni clusters up to 21 atoms (N = 21). Through the self-consistent tight-binding model, Aguilera-Granja *et al.* [64] have studied the variation of the magnetic moments of nickel clusters for $5 \leq \mathrm{N} \leq 60$. Reuse and Khanna [65] have performed studies on the geometry, electronic and magnetic properties of nickel clusters using the linear combination of atomic orbitals. They have found a number geometries and spin multiplicities for Ni_N (N = 2-6, 8, 13) clusters. A study of the electronic structure and magnetic properties of Ni_N (N= 2-39 and 55) clusters was also performed by Duan *et al.* [58] using LSDA. Futschek *et al.* [66] have studied the structural and magnetic properties of Ni clusters through the fixed spin moment calculations within the GGA based on DFT. Experimental studies related to structure of Fe clusters are still limited [67–69]. The bond lengths for Fe dimer on neon [67] and argon matrix [68] are predicted to be 2.02 ± 0.02 Å and 1.87 ± 0.13 Å, respectively, through extended X-ray absorption fine structure (EXAFS) analysis. For a Fe trimer (N = 3), Raman spectroscopy measurements by Haslett *et al.* [70] have proved a Jahn-Teller distorted ground state. For Fe clusters larger than three atoms, no direct experimental results are available regarding the structural stability. However, experimentally, there exists results for electron affinity and ionization potential [71–74] of Fe clusters up to 100 atoms. Theoretical studies on structure and magnetism of Fe clusters are many, which are mainly based on tight-binding techniques [60, 75] or first-principles approach [76–79]. LSDA calculations for small Fe clusters containing up to 5 atoms have shown enhanced stabilities for higher-dimensional clusters [76, 77]. For instance, among several isomers for Fe_4, the tetrahedral geometry is more preferable over the square and linear geometry. Using density functional tight binding and DFT, Bobadova *et al.* [80] have evaluated the potential energy surface as well as the magnetic properties of Fe clusters up to 19 atoms. Diéguez *et al.* [79] have performed LSDA calculations to study the structures and magnetic moments of Fe clusters up to 17 atoms. There have been studies on the optimal geometries, binding energies, bond dissociation energies, ionization potentials and electron affinities of neutral and charged iron clusters up to 5 atoms using the nonlocal spin density method [81].

The literature survey discussed above mainly deals with the properties of clusters based on collinear treatment of spins, where a global spin quantization axis is assumed for the whole system. One must note that spin spiral states exist in bulk fcc Fe [82]. On the other hand, triangular lattice structures of bulk Mn and Cr leads to the spin frustration. This shows the importance of non-collinear magnetism occurring in clusters. There are already reports for the noncollinear magnetic configurations for small clusters of Fe, Cr and Mn studied within the LSDA [83–85].

3.2 Elemental clusters

In order to determine the equilibrium geometries, we have considered several isomers (same cluster size but different structural geometry) for each cluster size. Since the number of isomers increase rapidly with cluster size, it is nearly impossible to scan all the isomers in the potential energy surface of each cluster. Therefore, the starting geometry is constructed according to certain educated geuss backed from literature. After structural optimization, all isomers of Ni_N and Fe_N are found to be distorted from their regular geometries. These structural deformations can be attributed to Jahn-Teller (JT) [14] distortions. Jahn-Teller distortions are characterized by structural distortions in finite systems like molecules and clusters, which is accompanind by removal of any degeneracy of electronic energy levels near the Fermi level by breaking the symmetry and there by lowering the energy of the system.

3.2.1 Ni_N clusters

Using the linear combination of atomic and molecular orbitals Reuse *et al.* [65] have reported a bond length of 1.76 Å and corresponding binding energy of 1.61 eV/atom for Ni-dimer. Our studies based on GGA for Ni_2 also gives a ferromagnetic ground state, however we obtain slightly larger bond length of 2.08 Å. We have obtained the binding energy as 1.41 eV/atom, which is slightly smaller. This difference is due to the degree of approximations used in the calculations. We believe that GGA gives a much better value and our obtained results also agree very well with other calculations done in GGA [56, 66]. Baden *et al.* [86] have presented results on binding energy calculated using various functionals and the binding energy is shown to vary from 1.15 to 1.25 eV/atom. The experimentally obtained bond length and binding energy of Ni_2 is reported to be 2.15 Å and 1.02 eV/atom, respectively [87]. One observes that the bond length of Ni_2 is shorter than the nearest-neighbour distance of bulk fcc Ni (2.49 Å). We have obtained a magnetic moment of 1.0 μ_B/atom for Ni_2.

The equilibrium geometry for Ni_3 is a distorted triangle with an average bond length of 2.20 Å. The total magnetic moment is found to be 0.733 μ_B/atom and a binding energy is 1.84 eV/atom. It must be compared with results obtained by Castro *et al* [56], where they have obtained a regular equilateral triangle as the ground state structure. The value of bond length, magnetic moment and the binding energy are howerver comparable to the values obtained from our calculations, on the other hand the binding energy reported by Futschek *et al.* [66] is slightly lower. The reason for obtaining a low binding energy can be accounted from the structural optimization which they have performed within fixed-spin constraints. Our calculations, however, are done with fully unconstrained relaxation also allowing for noncollinear magnetic moments. LSDA values of bond length, magnetic moment and binding energy reported by Reuse *et al.* [65] agrees very well with our results obtained from GGA.

For Ni_4, a JT distorted tetrahedron is found to be the minimum energy structure. The average bond length is 2.28 Å (the exreme values of bond length are 2.20 and 2.33 Å), total magnetic moment is 0.86 μ_B/atom and the binding energy is 2.14 eV/atom. The above results match well with those obtained by Bienati *et al.* [88]. Castro *et al.* have also predicted a Jahn-Teller distorted structure with a large variation of bond length (from 2.21 Å to 2.41 Å). The value of binding energy reported is 2.33 eV/atom, which is larger as compared to ours. It must be noted that unlike Ni_3, they obtain distorted structure for Ni_4. Reuse *et al.* [65] on the other hand, have obtained the distorted tetrahedron and square as structures with degenerate energies for Ni_4 cluster. This is unlike the energy trend obtianed by us for the two structures.

A JT-distorted trigonal bipyramid with three atoms in a triangular ring and two atoms occupying the apex sites is found to be the stable structure for Ni_5 with variation in bond length between 2.25 Å to 2.34 Å. The total magnetic moment and binding energy are calculated to be 0.77 μ_B/atom and 2.39 eV/atom, respectively. The obtained minimum energy structure is in agreement with Castro *et al* [56], Reuse *et al* [65] and Michelini *et al.* [89]. LSDA calculations [65, 89] predict a larger binding energy for Ni_5 compared to the present GGA calculations. The calculated total spin moment, howevr, agrees well with the LSDA calculations.

For Ni_6 cluster, a Jahn-Teller distorted octahedral cluster is obtained as the ground state structure with a bond length range between 2.29 Å-2.35 Å. Similar structure is predicted as the lower in energy by Reuse *et al.* [65] and Michelini *et al.* [89]. The calculated values of bond length variations, magnetic moment (1.1 μ_B/atom) and binding energy (2.61 eV/atom) agree with those of Michelini *et al.* [89]. On the other hand, Reuse *et al.* have obtained a relatively large value of binding energy $\sim$ 3.30 eV/atom, which might be due to the small variation of bond lengths in their results. They have obtained a distorted octahedral Ni_6 cluster with bond length variation (2.32-2.35 Å) as low energy strcuture. The total mangnetic moment obtained in our calculations for Ni_6(1.10 μ_B/atom) agrees well with the experimental obtained values of 1.33 μ_B/atom [54].

A distorted pentagonal bipyramidal structure is determined as the stable structure for Ni_7 obtained from our calculations. Using embeded atoms potentials, Böyükata *et al.* [90] have obtained a similar structure as the minimum energy structure. The emperical many body potential and molecular dynamics simulations by Nayak *et al.* [91] have also shown such a structure having the lowest energy. However, LSDA calculations by Desmarais *et al.* shows a capped octahedron as the stable structure for Ni_7 [92]. They have also predicted a distorted pentagonal bipyramid structure as energetically close to the ground state structure. The calculated value of binding energy (2.71 eV/atom) is almost comparable to the corresponding result in Ref. [90].

We have found the lowest energy structure for Ni_8 as a distorted bidisphenoid structure with the bond lengths varying from 2.27 to 2.39 Å. Such a structure is also predicted by Desmarais *et al.* [92]. Our calculated binding energy, 2.84 eV/atom is slightly less as compared to their values, this is because of the different exchange-correlation functional used in the calculations. They have used LSDA, while our calculations are in GGA. The energetically favorable structures for Ni_9-Ni_{11} are observed to be of polytetrahedral geometry. The binding energies for Ni_9, Ni_{10} and Ni_{11} are calculated to be 2.95, 2.98 and 3.05 eV/atom, respectively, and their magnetic moments are 0.86 (Ni_9), 0.8 (Ni_{10}) and 0.75 μ_B/atom (Ni_{11}). The equilibrium geometries and binding energies obtained in our calculations agree with the results Refs. [90, 91]. Form Ni_{12} onwards, the icosahedral-like geometry is more favorable. For instance, the Ni_{13} cluster is a JT-distorted icosahedron, with average center to shell distance of 2.32 Å and a total spin moment of 0.61 μ_B/atom, which is close to the corresponding bulk value of fcc Ni (0.6 μ_B/atom).

The equilibrium geometries obtained for Ni_N clusters are illustrated in Fig 3.1. The calculated value of magnetic moments for Ni_N clusters are compared with the available theoretical and experimental results in Fig 3.2. It shows that theoretically obtained values of magnetic moments are lower compared to that of the experimental ones. Our calculations show a good qualitative agreement with Ref. [63]. The strong fluctuations in the moments of small cluster sizes may be due to the different equilibrium structures predicted from various approximations. From $N = 6$ onwards, almost a linear decrease in the magnetic moment is observed until $N = 14$. This trend is supported by other theoretical results [58, 63, 64] and also from experiment [54]. There is a discrepancy in the theoretical results for clusters larger than $N = 14$. We must stress that the present calculation is consistent with the experimental

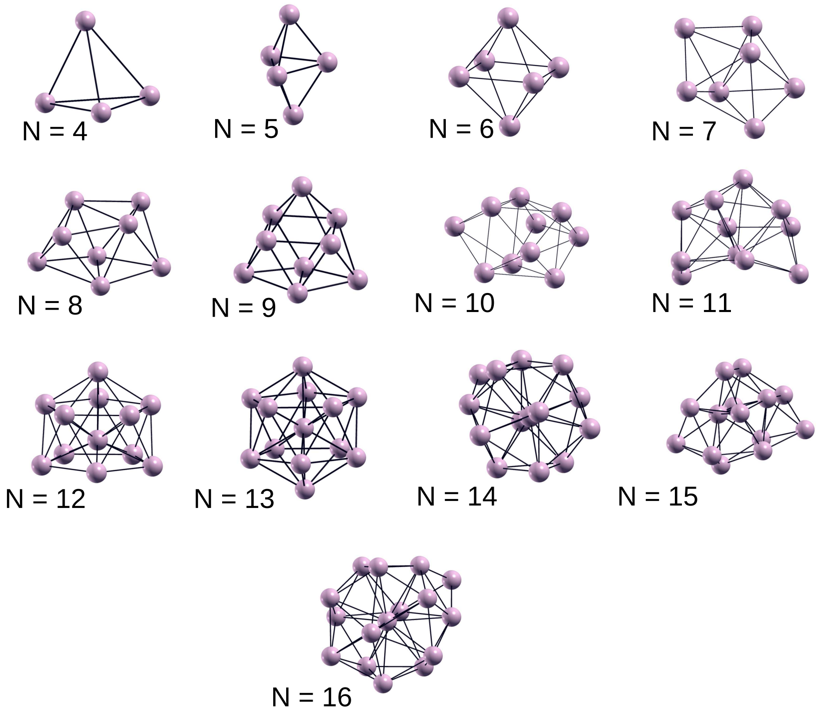

Figure 3.1: The equilibrium geometries of Ni_N clusters.

values [54]. The magnetic moment for Ni_6 cluster obtained experimentally is smaller than for Ni_5 cluster. This is not supported either by our calculations or other theoretical calculations [58, 63], except that of Aguilera *et al.* [64].

3.2.2 Fe_N clusters

The minimum energy morphologies for Fe_N clusters obtained in our calculation are consistent with previous DFT calculations [56, 78, 79] with slight difference in the structural parameters. The ground state geometries of Fe_N clusters are found to show Jahn-Teller distortion, like Ni_N clusters.

For Fe_2, we found a bond length of 1.98 Å which is in agreement with that of the experimentally obtained value of 2.02 Å on neon [67] and 1.87 Å on argon [68] matrices. Several DFT studies based on LSDA have obtained a similar value of 1.95 Å [56] and 1.96 Å [79]. The binding energy for Fe dimer is calculated to be 1.5 eV/atom, which is larger than the experimental value of 0.65 eV/atom. LSDA calculations even report a more larger value of binding energy [76, 79, 81] based on the LSDA calculations. Such an overestimation of binding energy in LSDA calculations mainly occurs due to the error in the atomic energy. However, the calculated value of total magnetic moment 2.82 μ_B/atom agrees well with the experimental [93] results as well as the DFT calculations [76, 79, 81].

For Fe_3 cluster, a JT-distorted triangle with average bond length 2.22 Å (varying from 2.07 Å to 2.32 Å) is found to be the ground state structure. with a magnetic moment of 2.98μ_B/atom and the

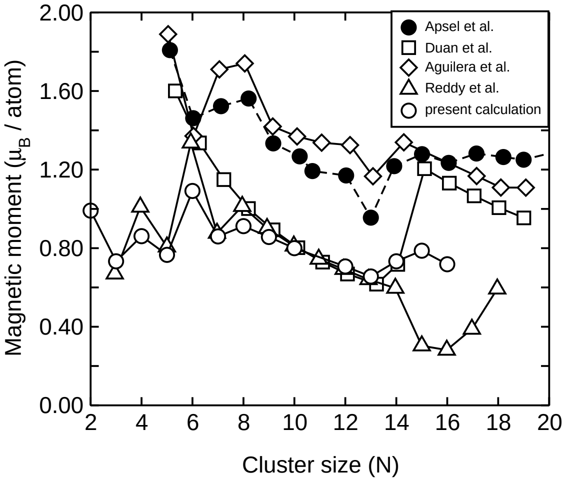

Figure 3.2: The variation of magnetic moment per atoms as a function of cluster size for Ni_N clusters. The curves show a comparison of magnetic moment of several theoretical calculations (☐ [58], ◇ [64], △ [63] and ◯: Present calculation) with the experimental results [54] (filled circle).

binding energy 1.94 eV/atom. The average bond length for Fe_3 agrees well with the corresponding results from previous DFT calculations [76, 79, 81]. In addition, the calculated magnetic moment per atom for this cluster is in agreement with the experimentally [93] obtained value of 2.7 μ_B/atom.

There are several predictions for the ground state structure of Fe_4. For instance, DFT calculations by Chen *et al.* [76] and Castro *et al.* [81] report an ideal tetrahedron as the minimum energy structure with total magnetic moment 3.0 μ_B/atom. On the other hand, in Refs. [78, 79, 83], a distorted tetrahedron was predicted as the most stable structure. This is in agreement with the present results, where a JT-distorted tetrahedral structure with a bond length varying from 2.16 Å to 2.38 Å is obtained. The binding energy and average magnetic moment for this cluster are calculated to be 2.36 eV/atom and 3.06 μ_B/atom, respectively.

A distorted trigonal bipyramid is predicted as the ground state structure for Fe_5 cluster with bond lengths varying from 2.28 Å-2.37 Å and an average magnetic moment 3.20 μ_B/atom. A similar geometry was also reported as the minimum energy structure in Refs. [78, 79, 81, 83]. The value of average magnetic moments obtained in our calculations are in agreement with Refs [79, 81]. For this structure, a non-collinear magnetic configuration is obtained, where the magnetic moments of the apical atoms are tilted by 31° in opposite directions [94]. Such a non-collinear ground state for Fe_5 has been previously reported by Oda *et al.* [83] and Hobbs *et al.* [84] through LSDA calculations. They have obtained an average magnetic moment for Fe_5 cluster as 2.9 μ_B/atom, which is relatively small compared to that of the present calculations.

For Fe_6 cluster, a distorted octahedron is found to be the ground state structure with varying bond lengths between 2.30 Å to 2.70 Å. A total magnetic moment of 3.00 μ_B/atom and binding energy

2.85 eV/atom. LSDA calculations by Diéguez *et al.* [78, 79] have predicted such a structure to be more favorable for Fe_6. Our calculated value of magnetic moment for the octahedron is slightly less than that of Diéguez *et al.*, who have obtained 3.33 μ_B/atom. The ground state structure for Fe_7 is a distorted pentagonal bipyramid with a bond length range between 2.28 Å-2.56 Å, which agrees with the results in Refs. [78, 79]. The calculated value of magnetic moment 2.88 μ_B/atom is lowered by 0.26 μ_B compared to Ref. [79].

The ground state structures obtained for Fe_8, Fe_9 and Fe_{10} are similar to the corresponding findings of Diéguez *et al.* [79], who have found a bidispenoid for Fe_8, a tricapped trigonal prism for Fe_9 and a bicapped square anti prism for Fe_{10} with relatively larger value of binding energies (4.12 eV/atom, 4.19 eV/atom and 4.27 eV/atom for Fe_8, Fe_9 and Fe_{10}, respectively). The binding energy obtained from our calculations are 3.17, 3.21 and 3.27 eV/atom which have a lower value compared to those obtained in LSDA calculations. The average magnetic moments obtained in our calculations are 2.77, 2.69 and 2.63 μ_B/atom for Fe_8, Fe_9 and Fe_{10} clusters, respectively.

From $N = 11$ onwards, the stable structures exhibit icosahedral-like strucutres. In particular, for Fe_{13} cluster we obtain a JT-distorted closed shell icosahedron [18, 95] with everage center to shell distance of 2.39 Å and an average magnetic moment 3.02 μ_B/atom with binding energy 3.45 eV/atom. LSDA studies also predict a distorted icosahedron as the ground state structure for Fe_{13} [96, 97]. The calculated value of average magnetic moment for this cluster is comparable with the experimental value of 2.6±0.4 μ_B as obtained from the cluster beam deflection experiments [98]. The collinear fixed spin moment calculations for Fe_{13} suggest the existence of two spin states. The high spin state with total magnetic moment 44 μ_B (all spins parrell) is lower in energy compared to the low spin state of 34 μ_B where the central spin is reversed with respect to the surrounding atoms. Figure 3.3 shows the total energies obtained for each spin moment of Fe_{13} icosahedral cluster using the fixed spin moment method [99], where the total energy is calculated by fixing the total magnetic moment of the cluster. It shows that both LDA and GGA yield the same result with the high spin state as the more favorable in energy as compared to the low spin state. Our findings for GGA calculation of Fe_{13} agrees with Ref. [97].

Figures 3.4, 3.5 and 3.6 shows a comparison of the evolution of cluster properties with respect to cluster size for the minimum energy structures of Ni_N and Fe_N clusters. The variation of binding energy as a function of cluster size for both cluster species are illustrated in Fig. 3.4. The variation of binding energies for Ni_N and Fe_N clusters show monotonically increasing trends with increasing cluster size. However, no anomalous feature is observed towards the existence of magic numbers previously reported for alkali metal clusters.

In Fig. 3.5, the total magnetic moment per atom as a function of cluster size are plotted for Fe_N and Ni_N clusters, which shows oscillatory behavior for both clusters with increase in the number of atoms in a cluster. Both clusters show magnetic moment enhancements relative to the corresponding values of bulk bcc Fe (2.22 μ_B/atom) and fcc Ni (0.6 μ_B/atom). However, such an enhancement for Ni_N is found to be weak compared to Fe_N. It is observed that the magnetic moment in Fe clusters increases

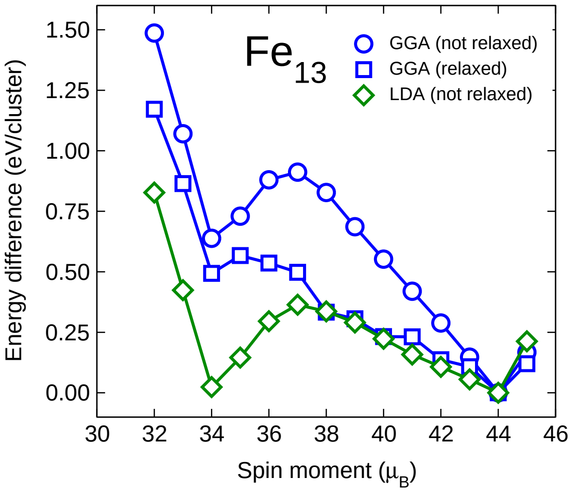

Figure 3.3: The variation of total energy with respect to the spin moments obtained from fixed spin moment calculations for Fe_{13} icosahedron. The black, blue curves represent the GGA results and the green curve represent the LDA results. The energy difference is with respect to the minimum energy corresponding to each curve. We observe a low-spin state (with the center spin reversed with respect to the surface spins and a high spin state with all spins parallel to each other).

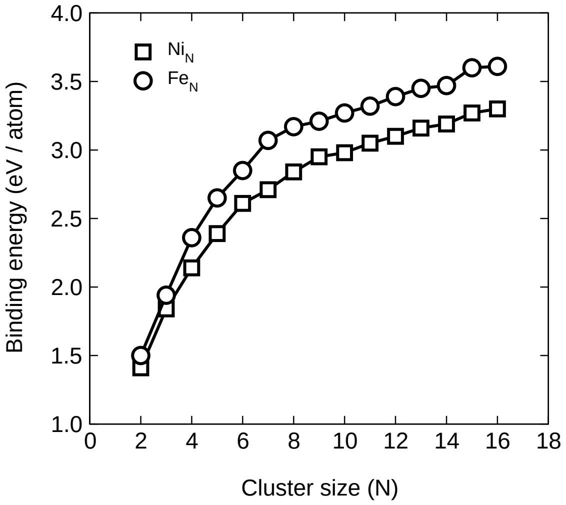

Figure 3.4: The binding energy per atom for Ni_N (square) and Fe_N (circle) clusters as a function of cluster size.

steadily from Fe_2 to Fe_5 and then shows a regular decrease until Fe_{10} and a similar oscillatory trend thereafter, the magnetic moment enhancement in nickel clusters is abrupt and varies sharply with increase of cluster size, especially for small clusters. It is observed that Ni_6 has the highest enhanced magnetic moment followed by Ni_2. A comparison with Fe clusters show that Fe_{13} has the maximum

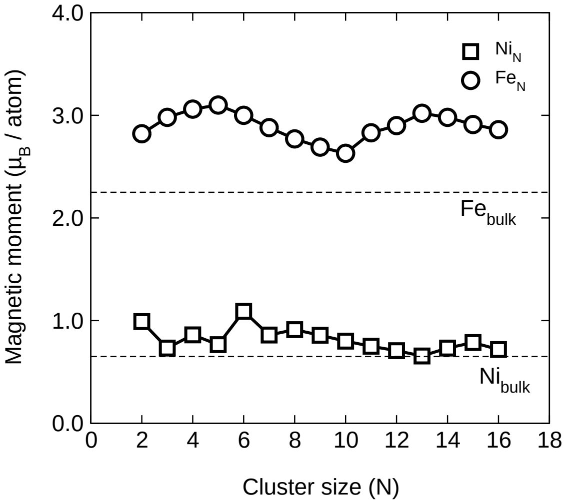

Figure 3.5: The variation of magnetic moment per atom for Ni_N (square) and Fe_N (circle) clusters as a function of cluster size, N. The dashed lines represent the values of magnetic moment per atom for bulk bcc Fe and bulk fcc Ni.

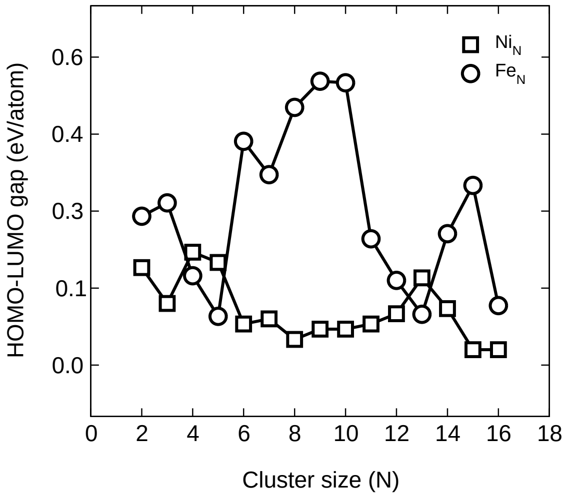

Figure 3.6: The variation of HOMO-LUMO gap for Ni_N (square) and Fe_N (circle) clusters with respect to cluster size.

enhanced moment, whereas Ni_{13} has the minimum enhanced moment, inspite of the similar structures. It should be noted that the ground states structures of Ni_N and Fe_N clusters have a collinear arrangements of atomic spins with ferromagnetic coupling.

Besides the total magnetic moment, the HOMO-LUMO gap (highest occupied molecular orbital-lowest unoccupied molecular orbital) is calculated for these clusters and plotted in Fig. 3.6 as a function of cluster size. The HOMO-LUMO gap indicates the stability of the electronic distribution for a system. A large HOMO-LUMO gap generally corresponds to a closed-shell electronic configuration which indicates the absence of low-energy excitations in the system. In the present calculations, a large energy gap is obtained for Ni_4, Ni_5 and Ni_{13} clusters with 0.22 eV, 0.19 eV and 0.17 eV, respectively, which indicates an enhanced stability for these clusters. On the other hand, the energy gap for Fe_5 clusters show large fluctuations in particular, for Fe_5 and Fe_{13}, a lower gap is observed. Our calculations of HOMO-LUMO gap for Ni clusters (marked by squares in Fig. 3.6) show a good agreement with Ref. [63] from $N \geq 7$. Some discrepancies appear for small clusters. The origin of such discrepancies can be due to the different treatment of the electronic structure as well as the use of model potentials to optimize the geometries. However, our results are more reliable because of the high-precision calculations performed with the PAW method and a large basis set with an energy cut-off of 270 eV.

3.3 Size dependence of the magnetic moments

The variation of the average magnetic moment as a function of the cluster size is not smooth in general. The overal decay is due to the increasing number of nearest neighbors, an effect that enhances the itinerant character of the *d* electrons. On the surface of the clusters the number of neighbors is still low compared to the bulk, so only when the number of surface atoms becomes small compared to the total number of atoms in the cluster, then the cluster magnetic moment converges towards the bulk moment. Furthermore, small clusters have structures that are not simple fragments of the crystal. All these ingredients affect the detailed broadening of the electronic levels to form the *d* bands. So the exchange splitting between ↑ and ↓ *d* sub-bands, the charge transfer from the *s* to the *d* band and the *sd* hybridization depend on the cluster size *N*, and control the evolution of magnetic moments.

The magnetic moments of Fe, Co and Ni clusters with sizes up to 700 atoms have been measured [52, 54, 55] under conditions where the clusters follow superparamagnetic behavior, for low cluster temperatures (vibrational temperature $T_{vib} = 120K$ for Fe clusters and 78 K for Ni and Co clusters). The results are shown in Fig. 3.7. The magnetic moment per atom decreases with increasing cluster size and converges to the bulk value for a few hundred atoms; this convergence is faster for the Ni clusters. However, in the three cases weak oscillations are superimposed to the global decrease of average magnetic moments. The size dependent magnetic moments has been studied for Fe clusters up to 641 atoms using DFT [100]. Figure 3.8 shows the energetics (left panel) and the corresponding magnetic moments (right panel) for Fe clusters (for details, see Ref. [100]). For each cluster size, the Fe clusters with bcc, fcc, and Mackay transformed (discussed in Section 4.4.2) geometries are structurally optimized. It shows that the for small clusters of 13 atoms, the Jahn-Teller distorted Fe_{13} cluster shows enhanced stability, whereas with increase in cluster size (clusters containing more than 100 atoms), the Fe clusters with bcc symmetry are found to show more stability compared to the Jahn-Teller distorted or Mackay transformed ones. Concerning the magnetic moments for all clusters (shown in the right panel of Fig. 3.8), it slowly approaches towards the bulk limit with increase in cluster size, the Mackay transformed and bcc Fe clusters show a better agreement with the experimental results [53, 55].

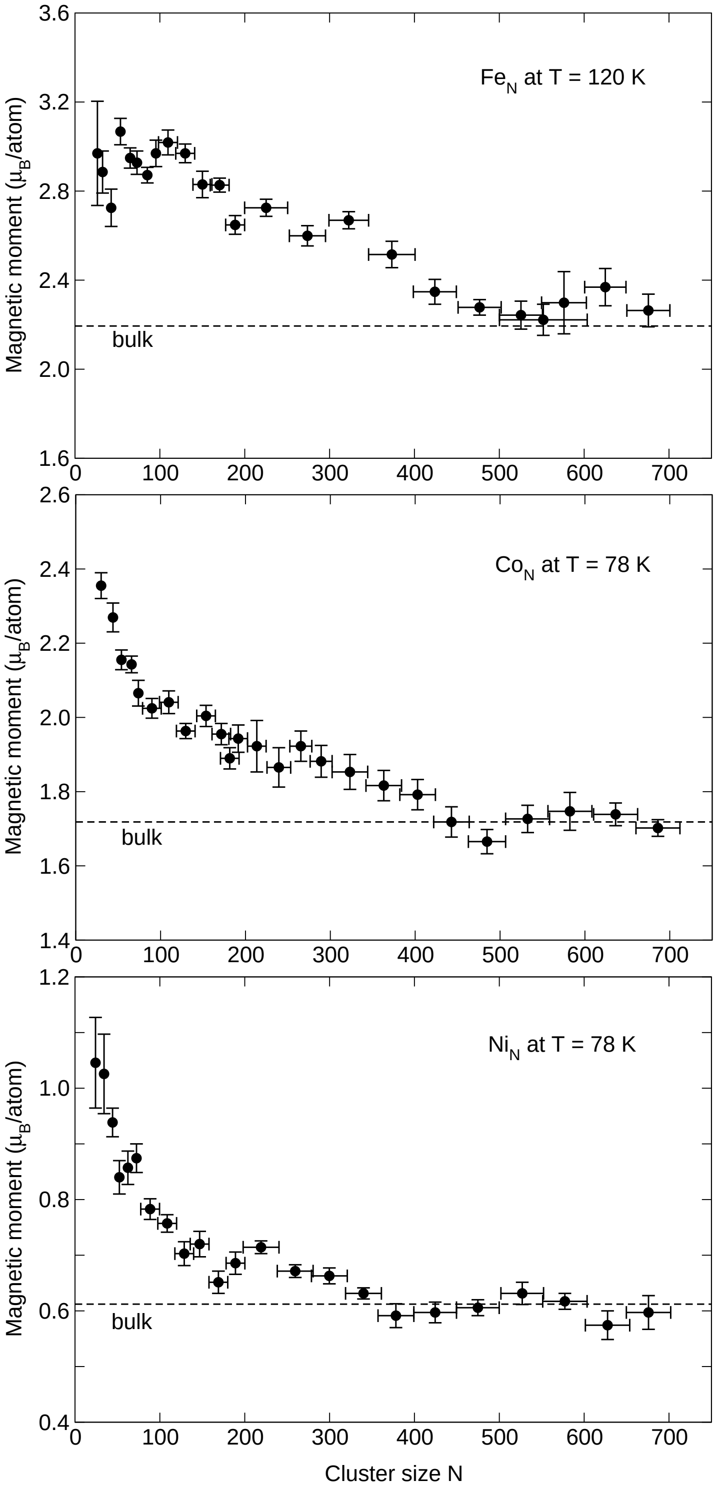

Figure 3.7: The variation of magnetic moments per atom of Fe_N, Co_N and Ni_N clusters as a function of cluster size [52]. The dashed lines indicate the bulk values of magnetic moment for bcc Fe (top), fcc Co (middle) and fcc Ni (bottom).

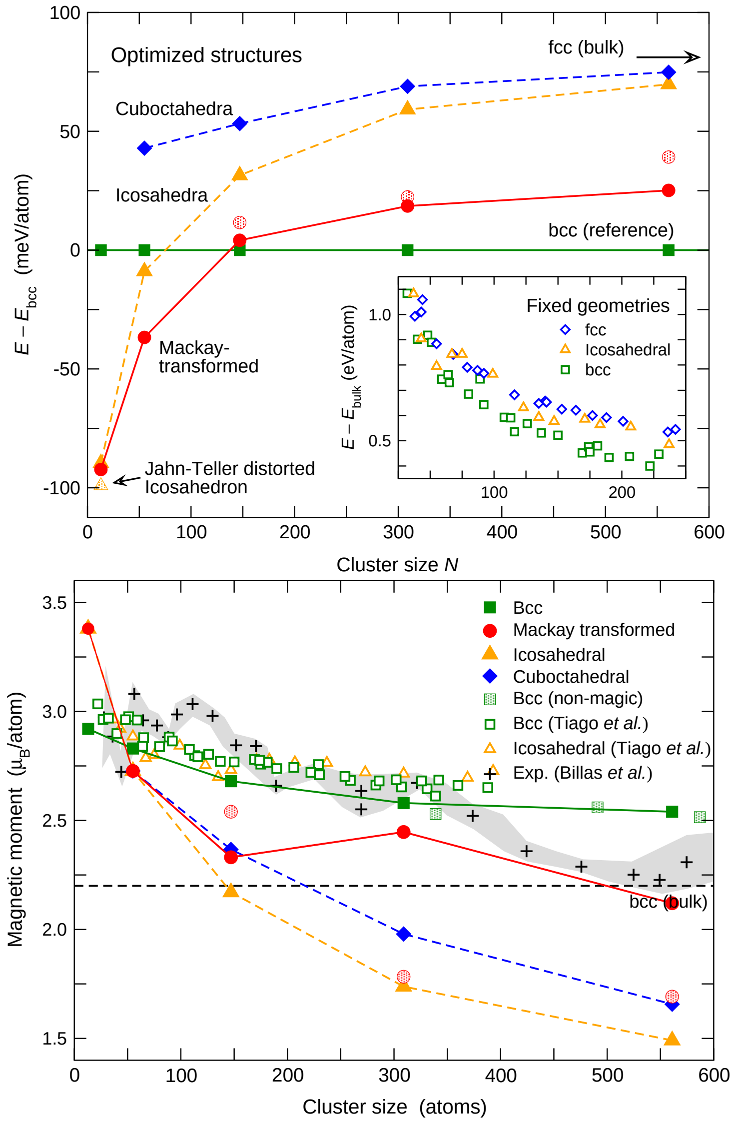

Figure 3.8: Top: The energy differences with respect to bcc structure as a function of Fe$_N$ cluster size. The energy of bcc structure is considered as the reference. The circles, triangles and the diamonds denote the shellwise Mackay-transformed, icosahedral and the cuboctahdral structures, respectively. The shaded circles indicate the Mackay-transformed clusters with different magnetic structures. The energy of the fcc bulk Fe is included for comparison. The inset shows the size dependence of the total energies for various geometries evaluated at the experimental bcc lattice constant. Bottom: The magnetic moments as a function of cluster size for Fe$_N$ clusters. The filled symbols such as squares, circles, triangles, diamonds denote the moments for bcc, Mackay transformed, icosahedral and cuboctahedral clusters, respectively. The shaded circles denote the shellwise Mackay transformed structures with magnetic configuration higher in energy and the shaded squares represent the relaxed bcc clusters. The crosses denote the experimental data [53, 55] and the bcc bulk data are taken from Ref. [101]. The solid region are the extension of error bars. Figure is taken from [100]. Lines are only guide to the eyes.

Experiments performed on 4*d* and 5*d* transition metal clusters show that clusters develop a magnetic moment unlike bulk which is nonmagnetic. Rh clusters with less than 60 atoms show magnetic moments, but larger clusters are nonmagnetic. Clusters with about ten atoms have magnetic moments $\overline{\mu} \approx 0.8\mu_B$, and $\overline{\mu}$ decays quickly between N=10 and 20, showing, oscillations that produce large moments for Rh_{15}, Rh_{16} and Rh_{19}. Rhodium was the first case in which magnetism was observed in clusters of a nonmagnetic metal. This behavior is different from that shown by clusters of the 3*d* elements Fe, Co and Ni, where the variation of average magnetic moment extends over a much wider range of cluster sizes. In contrast to Rh, Ruthenium and Palladium clusters with 12 to more than 100 atoms are reported nonmagnetic.

3.4 Binary clusters: Segregation and mixing

In addition to elemental clusters, we have studied the ground state properties of multi-component clusters. One of the main features of the multi-component clusters is that their properties can be tuned by changing the chemical ordering and composition [102–108]. As a result, they show physical and chemical properties different from their constituent elemental clusters as well as bulk. Several studies have been carried out on the structure and chemical ordering as well as magnetic properties of bimetallic transition metal clusters [109–114]. Experimentally, Rousset *et al.* have performed TOF mass spectrometry and photo fragmentation techniques for free and supported Pd-Pt bimetallic clusters, where they observed the segregation tendency of Pd for both free and supported cases [115]. Yasuda *etal*. [116] have studied the alloying and phase stability for Au-Sn binary clusters using transmission electron microscopy and have observed an enhanced solubility of Sn atoms into Au clusters. Theoretical studies based on EAM method for Cu-Ni and Cu-Pd bimetallic clusters have shown the surface segregation of Cu atoms for Cu-Ni clusters, and the coexistance of both segregation and ordering for the Cu-Pd clusters [117]. The studies on the growth of for Ag-Pd and Ag-Cu core-shell clusters by Baletto *et al.* [118] have shown well-defined single-layer shells of Ag atoms on Pd at low temperatures and on Cu at high temperatures.

Another aspect is to study the magnetism in binary clusters, which is one of our prime interest. It has been observed that alloying among 3*d* elements as well as 3*d* with 4*d* or 5*d* element gives rise to novel magnetic properties. For instance, enhancements of magnetic moments have been observed experimentally for binary clusters such as Fe-(Co, Ni) [119], Co-Rh [120], Ni-Pd [121] and Fe-Pt [122]. The enhancements of of magnetic moments for these systems [123–127] are also confirmed by theoretical calculations.

In this chapter, the segregation and magnetic properties of binary Fe-Ni, Fe-Co, Fe-Pt, Co-Pt and Co-Mn clusters are discussed for closed-shell icosahedra consisting of 13 atoms in the whole concentration range. In order to check wheather the properties observed in small clusters still persist for larger clusters, the binary clusters consisting of 55 atoms are studied. Unlike the case of 13-atom binary clusters, few compositions for 55-atom binary clusters are considered due to the existence of

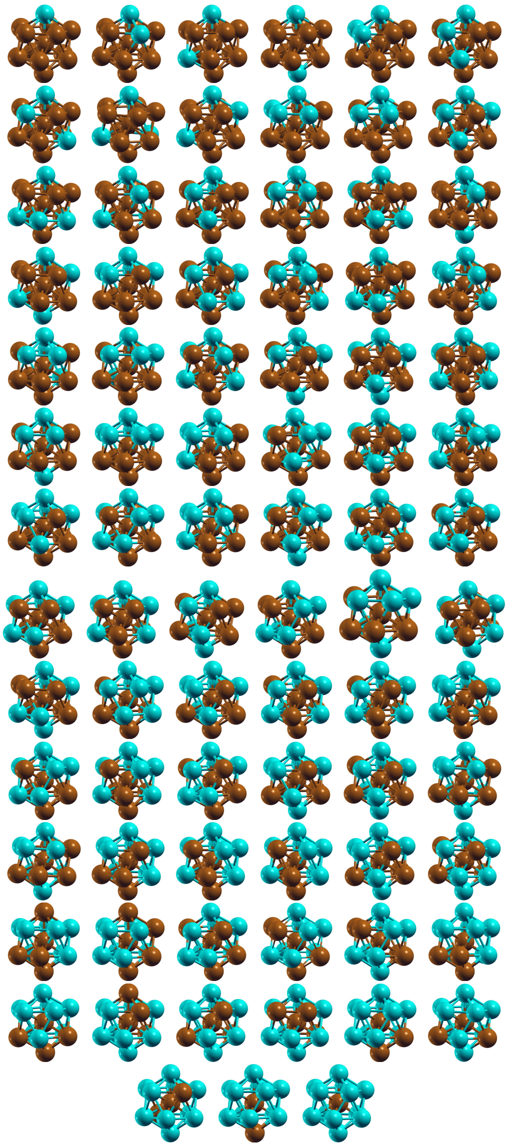

Figure 3.9: 81 possible distributions of atoms on the surface shell of 13-atom icosahedral binary cluster [128]. The distributions concerning the central atom are not shown here. For the case of Fe-Ni and other binary clusters, the energy of these clusters have been calculated.

large number of distributions ($\sim 10^{14}$ configurations) of each atomic species. For 13-atom binary clusters with icosahedral geometry, there are 164 possibilities of distributing two kinds of atomic species. In Fig. 3.9 the possible distributions of two atomic species on the surface of the icosahedral shell are displayed.

The mixing energy is calculated for the binary clusters, which measures the stability of the heterogeneous system with respect to its composition. For clusters, it is defined as the difference in energy to construct the binary cluster from the identical configurations of its elemental constituents. The mixing energy per atom of a bimetallic cluster is given by,

$$E^{Mix} = \frac{1}{N}\left[E_{A_nB_{(N-n)}} - \frac{n}{N}E_{A_n} - \frac{(N-n)}{N}E_{B_N}\right] \tag{3.1}$$

where, E^{Mix} : Mixing energy per atom. A, B: Different species of atoms in the cluster. N: Total number of atoms in the bimetallic cluster. n: Number of atoms of species A. $E_{A_nB_{(N-n)}}$: Total energy of the bimetallic cluster.

3.4.1 Fe-Ni

Binary Fe-Ni systems are important from many respects, one of them is the Invar property, where the alloy of Fe-Ni with 65 % Fe and 35 % Ni shows a low linear expansion for a wide range of temperature [129]. The Invar anomaly has been predicted for Fe-Ni nanoparticles with upto $\sim$ 8600 atoms using molecular dynamics simulation, where the average nearest neighbour distance is observed to vary slowly for a range of temperature and then rises linearly with temperature as expected for higher temperature [130]. Therefore, studying the nature of chemical ordering or segregation in such system is of immense interest.

The structural stability of $Fe_{13-n}Ni_n$ clusters have been studied for all compositions. For each cluster composition of $Fe_{13-n}Ni_n$, several isomers with different distributions of Fe and Ni atoms were relaxed without any constraints of symmetry. The lowest energy isomers for each cluster composition are illustrated in Fig. 3.10. We observe some degree of distortion for all clusters deviating from their symmetric geometry. However, the distortions are large for compositions in the Fe-rich part. This is expected, as elemental Fe_{13} shows large degree of distortion compared to Ni_{13} [95].

The most favorable configurations in the whole Ni concentration range are characterized by the surface occupancy of Ni atoms on the icosahedron. In spite that Ni atoms occupy the surface sites, different trends appear for the arrangement of Ni atoms at different range of compositions [131]. For instance, the composition with two Ni atoms,i.e., for $Fe_{11}Ni_2$, the energetically preferable structure is characterized by two Ni atoms occupying the nearest-neighbour positions of the surface shell of icosahedral cluster. A detailed study regarding the possible distributions and energetics for this cluster has been carried out in Ref. [95]. In order to confirm the tendency for the occupancy of Ni atoms in the low Ni concentration range, we have considered a cluster composition $Fe_{13}Ni_2$, where the energetics are studied by capping two Ni atoms at several positions on the Fe_{13} icosahedron. The energetics and magnetic moments for all possible arrangements of two Ni atoms are reported in Fig. 3.11. We observe that the energetically favorable structure corresponds to the nearest neighbour occupancy of Ni atoms on the surface of Fe_{13} icosahedron with maximization of Ni-Ni bonds. For $Fe_{11}Ni_3$, the lowest energy configuration corresponds to the Ni atoms occupying the nearest neighbour sites in the surface shell of the icosahedral cluster as observed for $Fe_{11}Ni_2$.

With increasing number of Ni atoms, different trends appear regarding the distribution of Ni atoms in the cluster. For instance, for clusters having 4 to 7 Ni atoms, instead of the nearest-neighbour occupancy, Ni atoms prefer a ring-like arrangement with a maximization of Fe-Ni bonds. Such distribution trends of Ni atoms has been described for Fe_8Ni_5 in Ref. [132], which is a suitable candidate for the study of Invar anomalies [133] in $Fe_{13-n}Ni_n$ clusters primarily found in *fcc* bulk Fe-Ni alloy with 65% Fe and 35% Ni. For clusters with $n = 8$ onwards, i.e., in the Ni rich part, the minimum energy structures possess large number of Fe-Ni bonds. Figure 3.12 and Table 3.1 depicts the number of Fe-Fe, Fe-Ni and Ni-Ni bonds for the low energy compositions of these clusters.

Figure 3.13 shows a comparison of mixing energies as a function of Ni concentration for clusters and bulk alloy of Fe-Ni in the left and right panel, respectively. The mixing energy per atom for the lowest energy isomers of $Fe_{13-n}Ni_n$ clusters with respect to Ni concentration is plotted in the left panel of Fig. 3.13 [131]. The nonlinear mixing energy curve indicates various degree of mixing in the same system depending on the composition of the binary components. Out of the minimum energy distributions for all compositions, it is observed that Fe_3Ni_{10} has gained higher stability due to the lower value of mixing energy in comparison to other compositions. A comparison of the mixing energy plot for $Fe_{13-n}Ni_n$ clusters with the fcc Fe-Ni bulk alloy [134] (right panel of Fig. 3.13), shows similar qualitative trends with respect to the composition. Both the plots show clear indications of two overlapping parabola occurring at two different compositions. Both the parabola seem to meet at a composition of 30% Ni, which is near to the composition of the Invar alloy in bulk Fe-Ni alloy with 35% Ni. In addition, we have studied the mixing energies of small $(Fe\text{-}Ni)_N$ clusters with $N = 3,.., 6$. For $N = 3$, 4, 5 and 6, the triangular, tetrahedral, trigonal bipyramidal and octahedral geometries are chosen, respectively, which are predicted as the stable geometries for the elemental Fe and Ni clusters. Figure 3.14 and 3.15 illustrate the mixing energies for these clusters as a function of Ni concentration. For all cases, the lowest energy structures for each composition are found to be distorted. For 5- (see top panel of Fig. 3.14) and 6-atom Fe-Ni clusters (see Fig. 3.15), the Fe atoms prefer to be at the basal triangle of the trigonal bipyramidal structure and basal square part of the octahedron, respectively.

A ferromagnetic ordering is found to be stable for the lowest energy structures of each composition of $Fe_{13-n}Ni_n$ clusters. With increasing number of Ni atoms, the magnetic moment show a decreasing trend.

In order to investigate the segregation and mixing properties for 55 atom Fe-Ni clusters, we have opted for the compositions in two extreme regions; in the Fe rich part: $Fe_{43}Ni_{12}$ and in the Ni rich part: $Fe_{12}Ni_{43}$. For every composition, several random distributions of atoms are optimized. The energetically favorable isomers obtained for $Fe_{43}Ni_{12}$ and $Fe_{12}Ni_{43}$ are shown in Fig. 3.16. For the Fe-rich composition, the preferrable structure corresponds to the occupancy of 12 Ni atoms on the most exposed sites (the vertex positions) on the surface of cluster creating a maximum number of Fe-Ni bonds. On the other hand, for the Ni-rich composition, 43 Ni atoms occupy the surface shell with 12 Fe atoms positioned towards the interior of the cluster and form a core-shell type arrangement. The occupancy of Ni atoms on the surface is due to the fact that Ni has a lower surface energy compared to Fe [139]. Such site-selected distribution of atoms in a binary cluster clearly indicate the segregation behavior in clusters which is observed primarily in bulk binary alloys.

Table 3.1: The nearest neighbour bonds for the lowest energy configurations of $Fe_{13-n}Ni_n$ clusters in the whole range.

Cluster	Fe – Fe	Ni – Ni	Fe – Ni
Fe_{13}	42		
$Fe_{12}Ni_1$	36	0	6
$Fe_{11}Ni_2$	31	1	10
$Fe_{10}Ni_3$	27	3	12
Fe_9Ni_4	21	3	18
Fe_8Ni_5	16	4	22
Fe_7Ni_6	12	6	24
Fe_6Ni_7	9	9	24
Fe_5Ni_8	7	13	22
Fe_4Ni_9	4	16	22
Fe_3Ni_{10}	2	20	20
Fe_2Ni_{11}	1	25	16
Fe_1Ni_{12}	0	30	12
Ni_{13}		42	

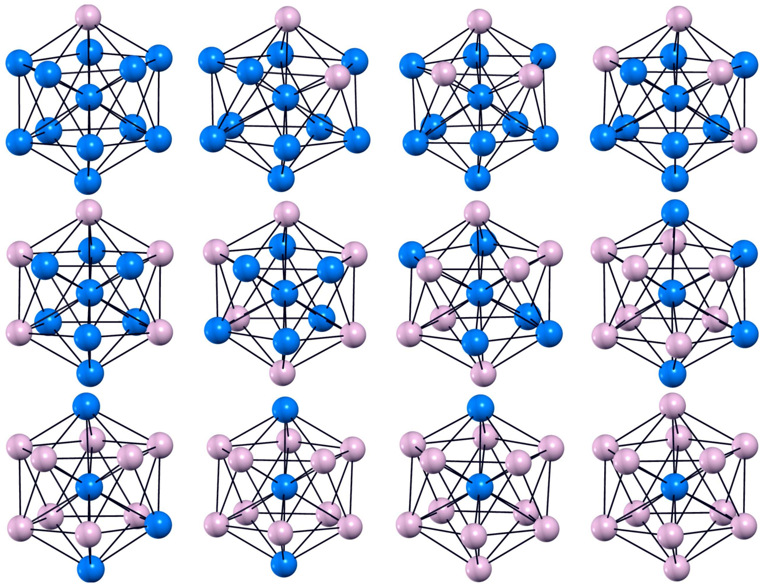

Figure 3.10: The lowest energy structures for $Fe_{13-n}Ni_n$ clusters. The blue and pink spheres denote Fe and Ni atoms, respectively. The mixing energy is calculated for these structures.

An antiferromagnetic ordering of atomic spin moments with the magnetic moment of central Fe atom aligned in the opposite direction is found to be stable for $Fe_{43}Ni_{12}$, whereas, for $(Fe_{12}Ni_{43})$, a ferromagnetic ordering is more favorable.

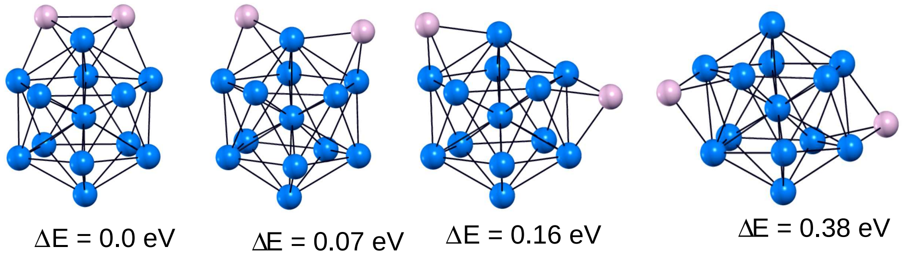

Figure 3.11: Energetics of $Fe_{13}Ni_2$ clusters. Blue and pink balls denote the Fe and Ni atoms, respectively. A ferromagnetic ordering is favored for all isomers with magnetic moment 2.93 μ_B/atom for each case.

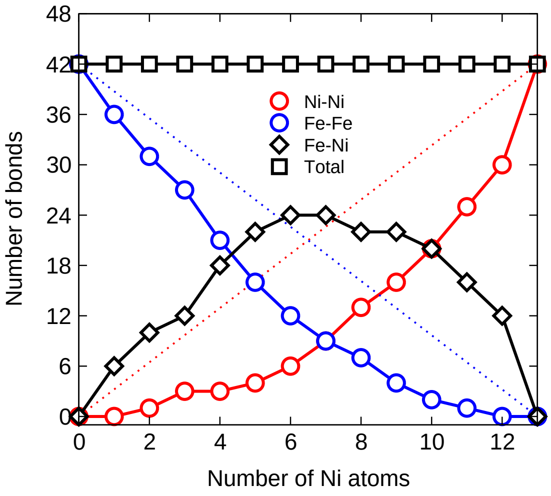

Figure 3.12: The number of nearest neighbour bonds with respect to the number of Ni atoms for the lowest energy structures of $Fe_{13}Ni_{13-n}$ cluster. Fe-Fe: Blue, Ni-Ni: Red and Fe-Ni: Diamond and the total number of bonds: square for the $Fe_{13}Ni_{13-n}$ cluster.

3.4.2 Fe-Co

The lowest energy structures for each composition of $Fe_{13-n}Co_n$ clusters are illustrated in Figure 3.17. The preferrable isomers for every composition of $Fe_{13-n}Co_n$ clusters corresponds to distorted icosahedrons with the occupation of Co atoms at the center position of cluster. The tendency of occupancy of Co atom at center position of $Fe_{13-n}Co_n$ icosahedron has been reported in a previous DFT study [135]. In our studies, the segregation tendency is found to be more pronounced in the Co-poor concentrations, with the formation of maximum Fe-Fe bonds on the surface. On the other hand, in the Co-rich concentrations, the mixing tendency is more dominant, where Fe atoms prefer to be far apart from each other and thus minimizing the number of Fe-Fe bonds. For the intermediate range of compositions, however, there is a competition between segregation and mixing. For this case, a ring-like

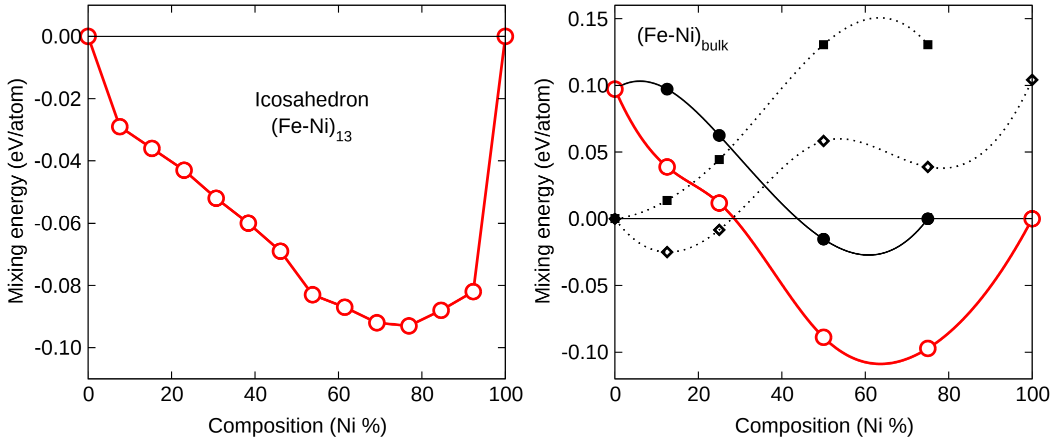

Figure 3.13: Left: The variation of mixing energy with respect to the composition for the lowest energy structures of $Fe_{13-n}Ni_n$ clusters. Right: Mixing energy for bulk Fe-Ni alloy as a function of Ni concentration [134]. The red curve in the right panel should be compared with the mixing energy curve of clusters.

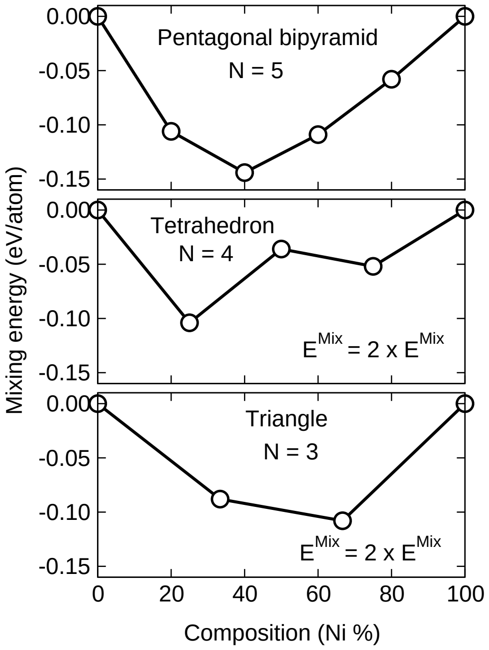

Figure 3.14: The variation of mixing energy in eV/atom with respect to Ni composition for (Fe-Ni)$_{3,4,5}$ clusters. The top, middle and bottom panels are the mixing energies for 5-, 4- and 3-atom Fe-Ni clusters, respectively.

arrangement of Co atoms is more favorable with maximum number of Fe-Co bonds. This is marked from Table 3.2 and Fig. 3.18 (left panel), where the total number of Fe-Fe, Co-Co and Fe-Co bonds for the lowest energy structures are plotted.

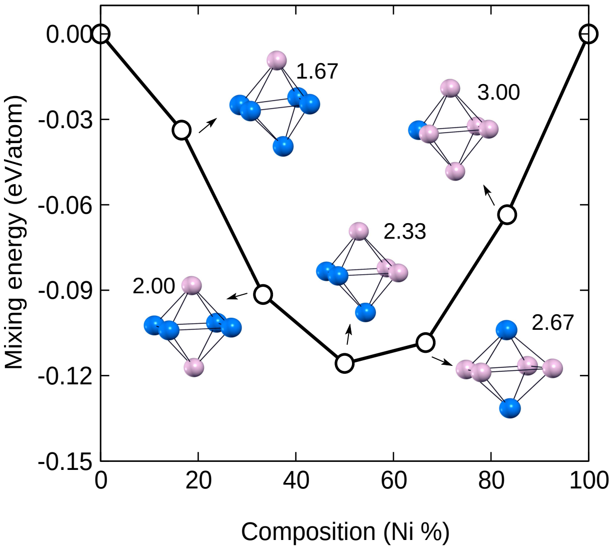

Figure 3.15: The mixing energy per atom for $Fe_{6-n}Ni_n$ octahedron as a function of Ni concentration. The average magnetic moments for the binary clusters are in units of μ_B/atom. Blue and pink balls represent Fe and Ni atoms, respectively.

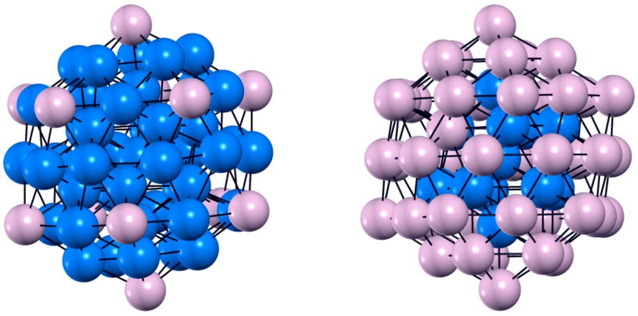

Figure 3.16: Energetically preferrable structures for $Fe_{43}Ni_{12}$ and $Fe_{12}Ni_{43}$ clusters. The blue and pink spheres are marked by Fe and Ni atoms.

The mixing energies for the lowest energy strucutres of $Fe_{13-n}Co_n$ clusters are plotted as a function of Co concentration in Fig. 3.18 This suggests an enhanced stability for the nearly equiatomic Fe_7Co_6 cluster. It should be noted that the mixing energy shows oscillatory trend in the Invar concentration range with with $60 \leq x \leq 100$ for bulk $Fe_{100-x}Co_x$.

A ferromagnetic ordering is found to be stable for the lowest energy structures of all compositions for $Fe_{13-n}Co_n$ clusters. In Table 3.3, the average magnetic moment on each atomic species and the total magnetic moment for the clusters are presented. The total magnetic moment per cluster shows a monotonically decreasing trend with increasing number of Co atoms, as reported in Table 3.3. Such a decreasing order can occur because of the substitution of Fe by Co atoms. However, for the Co-rich compositions, the average local magnetic moments are observed to have larger values both for Fe

(M_{Fe}) and Co (M_{Co}) sites as shown in Table 3.3. It is also observed that Fe gains maximum magnetic moment while surrounded by Co atoms. This suggests the important role of Co in enhancing the magnetism of Fe. Our studies agree well with previous theoretical studies [123]. However, such finding is in contrary to experimental results [136] for Fe or FeCo monolayers on W(110) substrate, where maximum magnetic moment is found on pure Fe compared to FeCo monolayers.

Table 3.2: The nearest neighbour Fe-Fe, Co-Co and Fe-Co bonds for the favorable structures of all compositions of $Fe_{13-n}Co_n$ clusters.

Cluster	Fe – Fe	Co – Co	Fe – Co
Fe_{13}	42		
$Fe_{12}Co_1$	30	0	12
$Fe_{11}Co_2$	25	1	16
$Fe_{10}Co_3$	21	3	18
Fe_9Co_4	16	4	22
Fe_8Co_5	12	6	24
Fe_7Co_6	9	9	24
Fe_6Co_7	6	12	24
Fe_5Co_8	4	16	22
Fe_4Co_9	2	20	20
Fe_3Co_{10}	1	25	16
Fe_2Co_{11}	0	30	12
Fe_1Co_{12}	0	36	6
Co_{13}		42	

Concerning the $(Fe\text{-}Co)_{55}$ atom clusters we have chosen $Fe_{43}Co_{12}$ and $Fe_{12}Co_{43}$ clusters for the investigations. For Fe-rich composition, i.e., $Fe_{43}Co_{12}$, the energetically favorable structure is characterized by the occupancy of Fe atom at the center and the outermost-shell of the cluster. The 12 Co atoms, however prefer the inner shell. This indicates the coexistence of both surface segregation and ordering. From the phase diagram of Fe-Co alloy [137, 138], the existence of ordering phase at low temperature region for Fe-rich compositions also shows such behavior. On the other hand, for $Fe_{12}Co_{43}$, 12 Fe atoms segregate towards the surface of the icosahedron cluster being far away from each other, as observed for 13-atom clusters in the Co-rich side with $8 \leq n \leq 11$. This suggests a dominant role of segregation over ordering for this composition. Both compositions have a ferromagnetic alignment of magnetic moments.

3.4.3 Fe-Pt

The energetically favorable structures for $Fe_{13-n}Pt_n$ clusters in the whole range of compositions are shown in Fig. 3.19. We observe that the ground state structure for all compositions are dependent on the distribution of atoms in such a way that Fe atoms tend to bond among itself more favorably than Pt. The icosahedral structure is found to be stable only for the low and high concentrations of Pt

Table 3.3: The average magnetic moments (μ_B/atom) on Fe (M_{Fe})and Co (M_{Co}) atoms for the lowest energy structures of $Fe_{13-n}Co_n$ clusters. M_{tot}: The total cluster magnetic moment in μ_B/cluster.

Cluster	M_{Fe}	M_{Co}	M_{tot}
Fe_{13}			44.00
$Fe_{12}Co_1$	3.08	1.77	39.00
$Fe_{11}Co_2$	3.09	1.88	38.00
$Fe_{10}Co_3$	3.09	1.95	37.00
Fe_9Co_4	3.10	1.95	36.00
Fe_8Co_5	3.03	1.86	34.00
Fe_7Co_6	3.05	1.87	33.00
Fe_6Co_7	3.11	1.91	32.00
Fe_5Co_8	3.08	1.93	31.00
Fe_4Co_9	3.17	1.99	31.00
Fe_3Co_{10}	3.17	2.03	30.00
Fe_2Co_{11}	3.22	2.05	29.00
Fe_1Co_{12}	3.17	2.07	28.00
Co_{13}			31.00

Table 3.4: The nearest neighbour Fe-Fe, Pt-Pt and Fe-Pt bonds for the favorable structures of all composition of $Fe_{13-n}Pt_n$ clusters.

Cluster	Fe – Fe	Pt – Pt	Fe – Pt
Fe_{13}	42		
$Fe_{12}Pt_1$	36	0	6
$Fe_{11}Pt_2$	30	0	12
$Fe_{10}Pt_3$	27	0	12
Fe_9Pt_4	20	2	20
Fe_8Pt_5	18	2	17
Fe_7Pt_6	12	0	24
Fe_6Pt_7	11	0	22
Fe_5Pt_8	7	6	20
Fe_4Pt_9	5	8	20
Fe_3Pt_{10}	0	18	18
Fe_2Pt_{11}	1	25	16
Fe_1Pt_{12}	0	30	12
Pt_{13}		42	

with Fe atom occupying the center position. At intermediatory compositions, for n = 4 to 10, there is a competition, as a result the structure is now deformed completely from the icosahedral geometry exhibiting maximum number of Fe-Pt bonds as listed in Table 3.4. The structural deformation is understandable from Fig. 3.20, where, the number of nearest neighbor bonds for homo, hetero species

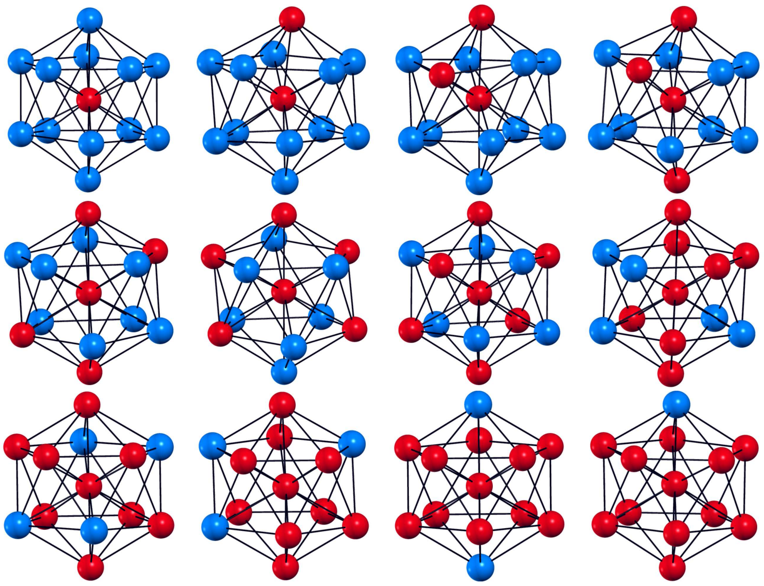

Figure 3.17: Lowest energy structures of $Fe_{13-n}Co_n$ clusters. Blue and red balls denote the Fe and Co atoms, respectively.

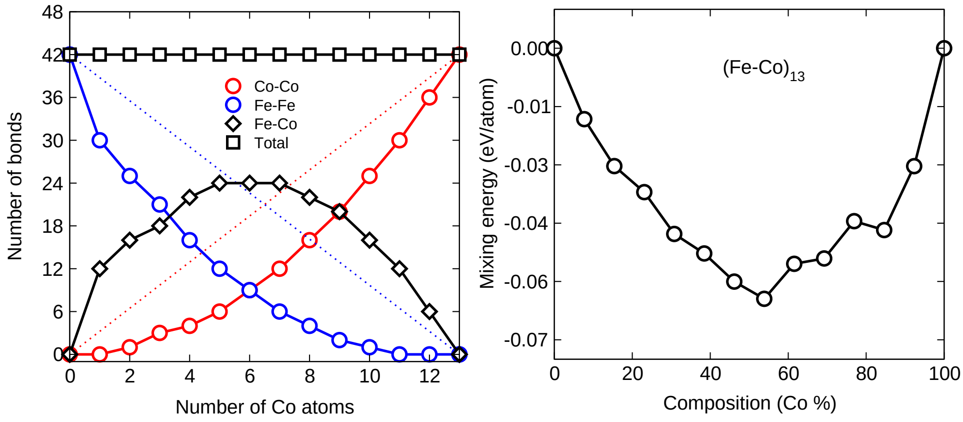

Figure 3.18: Left: The variation of nearest neighbour Co-Co (red circle), Fe-Fe (blue circle), Fe-Co (diamond) and total number of bonds (square) in the cluster with respect to the number of Co atoms. Right: The variation of mixing energy (eV/atom) with respect to Co composition for the low energy structures of $Fe_{13-n}Co_n$ clusters.

and total number of bonds are plotted with respect to the number of Pt atoms. The dotted lines indicate the linear variation of the corresponding quantities in the infinite system. Due to the structural deformation, the total number of bonds (black square) is not constant with respect to the number of Pt atoms. As a consequence of strong structural deformation for the intermediatory compositions, the oscillatory trends appear for the nearest neighbour bonds of Fe-Fe, Pt-Pt and the Fe-Pt, whereas for $Fe_{13-n}Co_n$ and $Fe_{13-n}Ni_n$, these fluctuations in the nearest neighbour bonds are not observed due

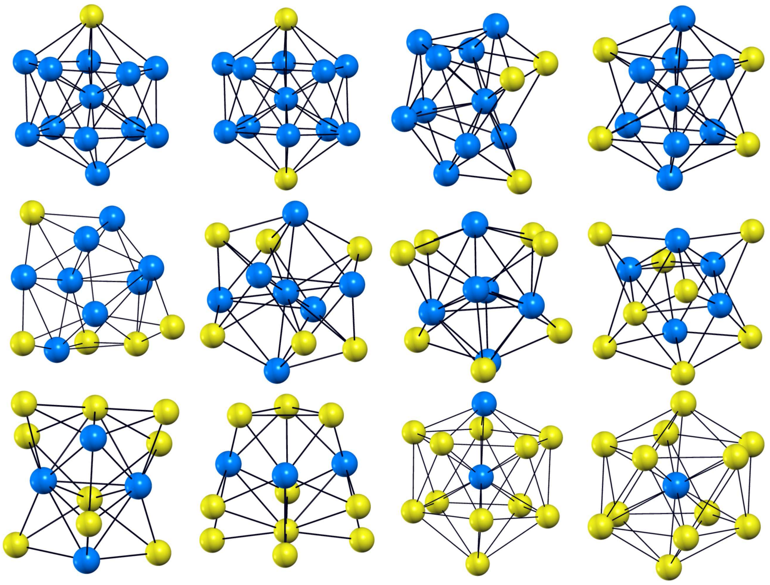

Figure 3.19: Lowest energy structures of $Fe_{13-n}Pt_n$ clusters. Blue and yellow balls denote the Fe and Pt atoms, respectively.

to the stability of icosahedral structures (see Fig. 3.18 and 3.12 for the nearest neighbour bonds of $Fe_{13-n}Co_n$ and $Fe_{13-n}Ni_n$, respectively).

The variation of mixing energy for the lowest energy structures of Fe-Pt clusters as a function of Pt composition is shown in the right panel of Fig. 3.20, which shows more stability for the nearly equiatomic compositions of Fe-Pt clusters. Like the case of Fe-Co clusters, the mixing energy shows oscillations in the Invar concentration range, which is from 30% to 60% of Pt concentration.

Now we discuss the magnetic properties of Fe-Pt clusters. The absolute value of average magnetic moment on Fe and Pt along with the total magnetic moment of the cluster are listed in Table 3.5. A ferromagnetic ordering is found to be more stable for all compositions of Fe-Pt cluster. Due to the presence of Fe atoms, there is induced moment on Pt atoms, which is a consequence of intermixing among the Fe 3*d* and Pt 5*d* orbitals. For the Fe-rich compositions, the hybridization between Fe-Fe orbitals results in slight decrease in magnetic moment compared to that of the atomic moment, while for the Pt-rich compositions, the local moment on Fe atoms retain their atomic-like character. For the intermediate compositions, enhancement of magnetic moment for both Fe and Pt atoms is observed, due to the strongly deformed structures, as a result, each atom possess low coordination and a hybridization between the Fe and Pt *d*-orbitals.

Concerning the $Fe_{55-n}Pt_n$ clusters, we have investigated $Fe_{43}Pt_{12}$ and $Fe_{12}Pt_{43}$ clusters. Out of several configurations, the energetically favorable structure for both compositions corresponds to the Pt segregation towards the surface with the Fe atom occupying the center position of the icosahedron. This trend is also observed for small $Fe_{13-n}Pt_n$ clusters. The segregation of Pt atoms on the surface is a consequence of its lower surface energy compared to that of Fe [139]. For the Fe-rich composition,

Table 3.5: The average magnetic moments (μ_B/atom) on Fe M_{Fe} and Pt M_{Pt} sites for the lowest energy structures of $Fe_{13-n}Pt_n$ clusters. M_{tot}: The total cluster magnetic moment in units of μ_B/cluster.

Cluster	M_{Fe}	M_{Pt}	M_{tot}
Fe_{13}			44.00
$Fe_{12}Pt_1$	2.86	0.39	34.70
$Fe_{11}Pt_2$	2.82	0.37	31.70
$Fe_{10}Pt_3$	2.95	0.56	31.14
Fe_9Pt_4	2.89	0.42	27.62
Fe_8Pt_5	3.01	0.41	26.15
Fe_7Pt_6	3.09	0.50	24.60
Fe_6Pt_7	3.17	0.52	22.64
Fe_5Pt_8	3.21	0.57	20.62
Fe_4Pt_9	3.30	0.41	16.90
Fe_3Pt_{10}	3.34	0.33	13.32
Fe_2Pt_{11}	3.10	0.31	9.62
Fe_1Pt_{12}	3.15	0.54	9.70
Pt_{13}		0.15	1.93

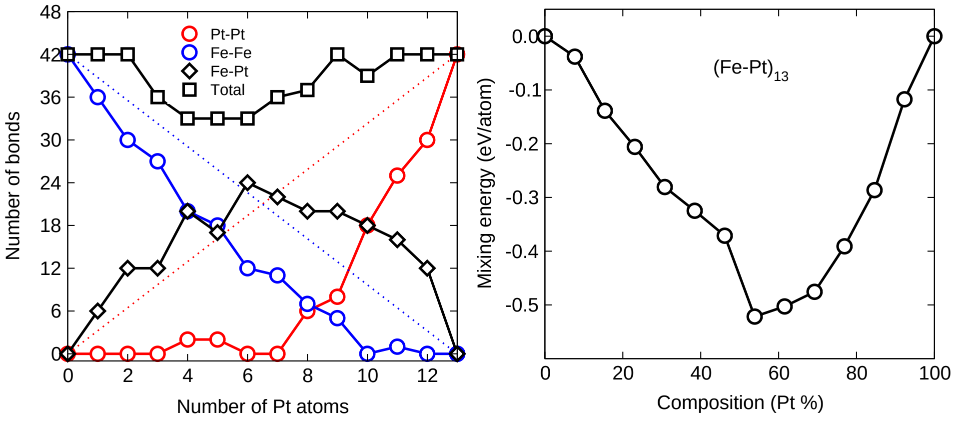

Figure 3.20: Left: The variation of nearest neighbour Pt-Pt (red circle), Fe-Fe (blue circle), Fe-Pt (diamond) and total number of bonds (square) in the cluster with respect to the number of Pt atoms. Right: The variation of mixing energy (eV/atom) with respect to Pt composition for the low energy structures of $Fe_{13-n}Pt_n$ clusters.

12 Pt atoms prefer the six-coordinated vertex sites with a minimization of Pt-Pt bonds, while in the Pt-rich composition, a core-shell structure is more favorable with Fe as the core and Pt as the outer-shell. Experimental observations through high resolution transmission electron micrographs (HRTEM) have confirmed the existence of such core-shell structures for icosahedral Fe-Pt nanoparticles with Pt segregation on the surface [140].

Different magnetic orderings are observed at two extreme compositions of $Fe_{55}Pt_n$ clusters in contrary to 13-atom clusters of Fe-Pt. The $Fe_{43}Pt_{12}$ favors an antiferromagnetic ordering with the moment of center atom aligned opposite to the surrounding atoms, while for $Fe_{12}Pt_{43}$, a ferromagnetic ground state with all moments in parallel direction is more stable. The reason for different magnetic behavior is related to the interlayer relaxation effects.

3.4.4 Co-Pt

The lowest energy structures for $Co_{13-n}Pt_n$ clusters show similar behavior as observed for Fe-Pt system for all compositions. In this case, the minimum energy structures for each composition form maximum Co-Co bonds as observed for Fe-Pt clusters. For the Co-rich and Pt-rich compositions, the Pt occupancy on the surface is more favorable with distorted icosahedral-like structure. However, for the intermediate compositions, the icosahedral structure is found to be completely deformed exhibiting a different symmetry, which results in maximization of Co-Pt bonds. The different structural trends can be marked from the oscillations appearing in the mixing energy for the favorable structures of each composition, plotted in Fig. 3.21.

Like Fe-Pt clusters, all lowest energy structures correspond to a ferromagnetic ground state. The total magnetic moment of the binary clusters decrease with increasing number of Co atoms. The presence of Co atoms leads to induced moment on Pt atoms, as depicted in Table 3.6.With increase in Pt atoms, the average moment on Co as well as the induced moment on Pt increases as a consequence of the orbital hybridization between the Co 3*d* and Pt 5*d* states.

For the $Co_{55-n}Pt_n$ clusters, both the Co-rich and Pt-rich compositions prefer the segregation of Pt atoms on the surface with Co being at the center. Due to the lower surface energy of Pt compared to Co, Pt segregation occurs on the surface of the cluster. However, unlike $Fe_{55-n}Pt_n$, the ground state structures for these clusters are observed to have ferromagnetic ordering for both compositions.

3.4.5 Co-Mn

The structural relaxation of $Co_{13-n}Mn_n$ clusters for all compositions of the cluster results in Jahn-Teller distorted icosahedral structures. For the lowest-energy isomers, Mn atom prefer to occupy the central position of the icosahedral shell with the remaining Mn atoms being far away from each other. However, $Co_{11}Mn_2$ is an exception to such trend, where two Mn atoms occupy the surface shell being in opposite positions of the icosahedron. For a detailed description, see Ref. [141]. The mixing energies as a function of Mn concentration for the lowest energy configurations of $Co_{13-n}Mn_n$ clusters are shown in Fig. 3.22. The negative values of E_{mix} over the whole range of compositions indicate the favorable solubility of the components. It also shows enhanced stability for the isomers having approximately equal amount of Co and Mn atoms.

Figure 3.23 shows the magnetic moment per atom for the lowest energy configurations of $Co_{13-n}Mn_n$ clusters. It shows that for the Co-rich compositions up to Co_6Mn_7, an increasing trend of the total magnetic moment is observed clusters increases with increase in number of Mn atoms. This agrees

Table 3.6: The average magnetic moments in μ_B/atom on Co $M_{\mathrm{Co}}$and Pt M_{Pt} atoms for the lowest energy structures of $\mathrm{Co}_{13-n}\mathrm{Pt}_n$ clusters. $\mathrm{M}_{\mathrm{tot}}$: The total cluster magnetic moment in μ_B/cluster.

Cluster	M_{Co}	M_{Pt}	$\mathrm{M}_{\mathrm{tot}}$
Co_{13}	2.23		29.00
$\mathrm{Co}_{12}\mathrm{Pt}_1$	1.76	0.34	21.43
$\mathrm{Co}_{11}\mathrm{Pt}_2$	1.83	0.28	20.65
$\mathrm{Co}_{10}\mathrm{Pt}_3$	1.88	0.26	19.62
$\mathrm{Co}_9\mathrm{Pt}_4$	1.97	0.40	19.34
$\mathrm{Co}_8\mathrm{Pt}_5$	1.97	0.34	17.49
$\mathrm{Co}_7\mathrm{Pt}_6$	1.93	0.26	15.10
$\mathrm{Co}_6\mathrm{Pt}_7$	2.13	0.61	17.03
$\mathrm{Co}_5\mathrm{Pt}_8$	2.13	0.47	14.41
$\mathrm{Co}_4\mathrm{Pt}_9$	2.12	0.36	11.70
$\mathrm{Co}_3\mathrm{Pt}_{10}$	2.26	0.37	10.47
$\mathrm{Co}_2\mathrm{Pt}_{11}$	2.17	0.44	9.22
$\mathrm{Co}_1\mathrm{Pt}_{12}$	2.10	0.32	6.00
Pt_{13}		0.15	1.93

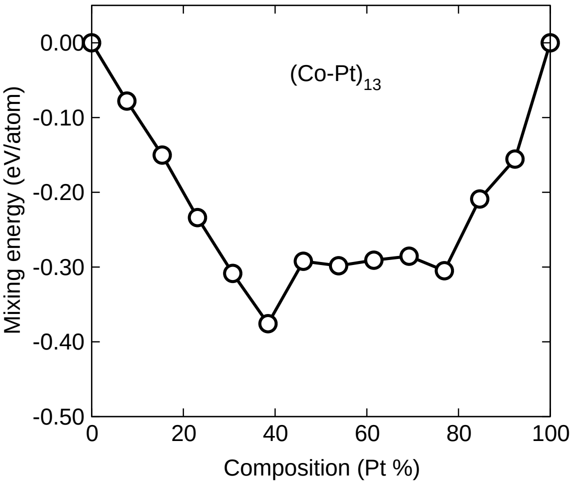

Figure 3.21: Mixing energy (eV/atom) with respect to Pt composition for the lowest energy structures of $\mathrm{Co}_{13-n}\mathrm{Pt}_n$ clusters.

with the experimental results [142, 143] through Stern-Gerlach molecular beam deflection technique. Such increase in magnetic moment with Mn concentration is found to be opposite to that of bulk Co-Mn alloy, where with increasing Mn concentration the magnetic moment shows a decreasing behavior [144].

The replacement of a Co atom by Mn at the center of the icosahedron results in a reduction in the magnetic moment by $8\mu_B$, which occurs for the bulk Co-Mn in the low Mn concentrations. However,

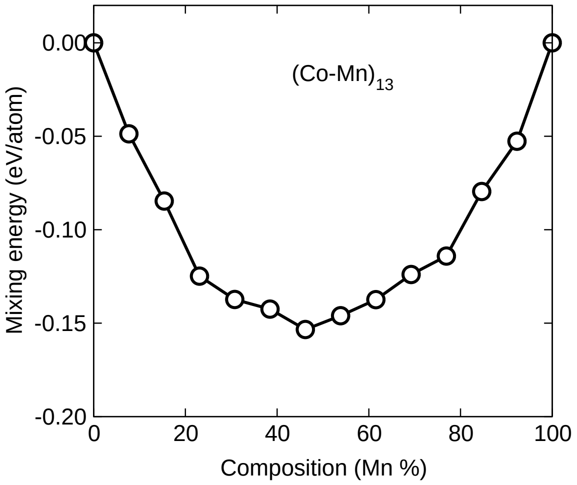

Figure 3.22: Mixing energy in eV/atom with respect to Mn concentration for the lowest energy configurations of $Co_{13-n}Mn_n$ clusters.

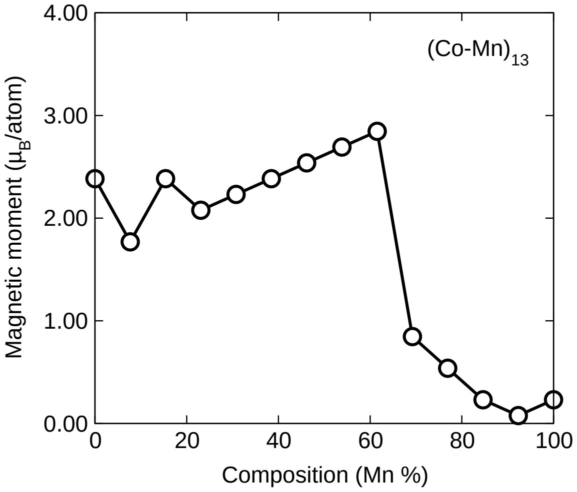

Figure 3.23: The variation of magnetic moments for the corresponding configurations as shown in Fig. 3.22 for $Co_{13-n}Mn_n$ clusters.

irrespective of the central atomic species, the substitution of a Co by a Mn atom at the surface increases the total cluster magnetic moment by $2\mu_B$, up to $n \leq 8$. This is in agreement with the behavior of Co-Mn clusters of different sizes observed experimentally [142].

For Co_5Mn_8, a crossover form ferro to antiferro-like ordering of magnetic moments occurs for the surface atoms. This is due to the different spin alignments of the corresponding elemental clusters. For example, Co_{13} has a ferromagnetic alignment of moments, on the other hand Mn_{13} has six of the surface atoms aligned opposite to the rest atoms, thereby exhibiting a small magnetic moment of 3 μ_B/cluster. Replacing few Mn atoms by Co, still does not change the antiferromagnetic-like ordering.

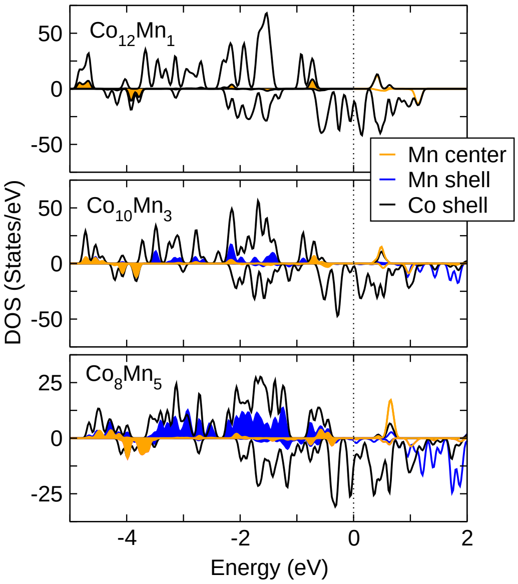

Figure 3.24: The site projected density of states (DOS) for $Co_{12}Mn_1$, $Co_{10}Mn_3$, and Co_8Mn_5 clusters. The DOS are calculated with a Gaussian broadening parameter 0.05 eV. The Fermi level is fixed at zero.

This agrees well with the theoretical calculations by Gutsev *etal*. [145] on elemental Mn clusters, where the ferro to antiferromagnetic-like transition was observed for Mn_5, which is not present in 13 atom Co-Mn clusters with less than 8 Mn atoms.

The absolute values of the local moments of the surface Mn atoms in Mn_{13} as well as in mixed clusters retain their atomic-like moments with values 4.1 μ_B, which is 1.5 μ_B larger than that of Co atoms in Co_{13}. This is shown in Fig. 3.24, where the change of the electronic structure of the lowest-energy isomers with the number of Mn atoms is displayed. The magnetic moment of the central atom is reduced for all isomers, resulting together with a decrease in the moment of the surrounding Co atoms. The surface Mn atoms couple ferromagnetically with the Co atoms. Their large magnetic moments arise due to the 3*d* spin-majority states, which are located between -3 to -1 eV below the Fermi level. However, due to the large exchange splitting, the corresponding minority spin states are unoccupied, which lie $\sim$ 4 eV higher.

We have studied 55-atom Co-Mn clusters in the low Mn concentration range with up to twelve Mn atoms due to the availability of experimental [142] data for the magnetic moments, where all possible configurations for $Co_{54}Mn_1$ (4) and $Co_{53}Mn_2$ (31) are investigated, while for $Co_{52}Mn_3$ to $Co_{43}Mn_{12}$ ten randomly chosen configurations are taken into account. Figure 3.25 depicts the magnetic moments and mixing energies of the 177 optimized structures. For the lowest-energy configurations of each composition, most of the Mn atoms prefer to occupy the outermost shell of the cluster being far away from each other, thereby maximizing the number of Co-Mn bonds. For some compositions, there is occupancy of Mn atom in the cluster center, in spite that the corresponding energy gain is

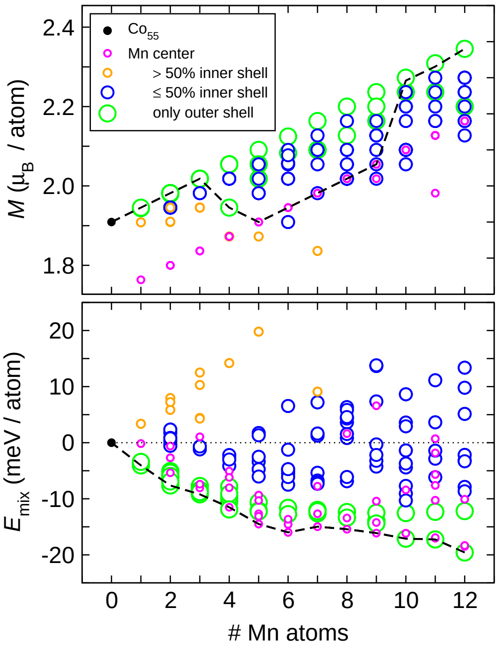

Figure 3.25: Top panel: Magnetic moments with respect to the number of Mn atoms for (Co-Mn)$_{55}$ clusters. Bottom panel: The corresponding mixing energies. The dashed line in both panels connects the quantities for the lowest energy isomers.

relatively small. On the other hand, occupation of the inner shell with many Mn atoms results in highly unfavorable structures.

The magnetic properties of the 55-atom cluster are found to be nearly similar to 13-atom clusters. Except some configurations that are energetically not relevant, the moments of all isomers lie in a 10μ_B-wide stripe. Replacing a Co atom at the center by Mn for the isomers with only Co atoms in the inner shell results in a decrease of magnetic moment by 8μ_B, which again mimics the bulk trend. Though it happens for some of the lowest-energy isomers, the overall increase in moment by 2μ_B per Mn atom is clearly recognized and is consistent with experimental results.

Figure 3.26 shows the magnetic moments and the mixing energies for all configurations of some more 13-atom binary clusters. Substituting Co by Ni, a same magnetic trend is observed like the case of Co-Mn clusters, with a slight increase in the slope of the magnetic moment (from 2 μ_B to 3 μ_B), as a function of Mn concentration. This is due to the difference in the atomic numbers of Mn and Ni. Like Co-Mn clusters, the most favorable structures are characterized by the occupancy of Mn atoms on the surface of Ni-Mn clusters. In addition, a crossover to antiferro-like magnetic ordering is also observed for this case, which is shown in Fig. 3.26. For Fe-Mn clusters(the results are illustrated also in Fig. 3.26), the results are more complicated due to the antiferromagnetic tendencies of the system. However, in comparison with Co-Mn and Ni-Mn, the mixing energy is found to be very small for these clusters.

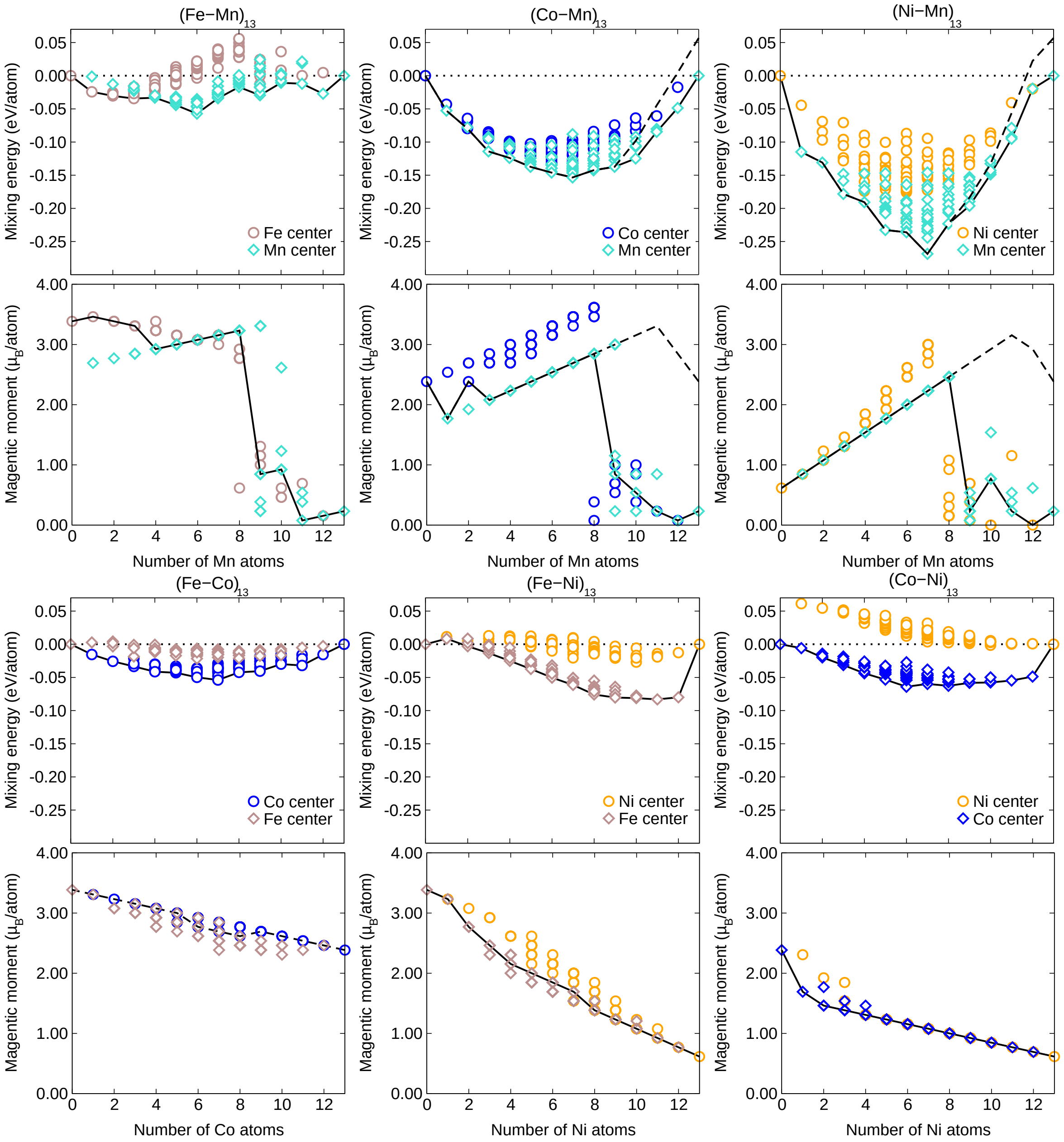

Figure 3.26: Variation of magnetic moments (top panel) and mixing energies (bottom panel) for all configurations of 13-atom binary clusters. Black solid lines denote the properties of the lowest-energy isomers found for each composition. For each system, the quantities are divided into two groups according to the element occupying the central position of the icosahedron [141].

4 Magnetic anisotropy of clusters

4.1 Introduction

One of the major obstacle in the miniaturization of magnetic storage devices is to overcome the thermal fluctuation of magnetic information which has attracted much attention in current research. Out of various factors that can help to overcome the obstacle, one of the main strategies is to enhance the magnetic anisotropy by artificial material manipulation. As an example, for a disk shaped sample, one can identify two main anisotropy directions: External field acting in the plane of the disk and external field acting perpendicular to the plane of the disk. This type of anisotropy is popularly called the shape anisotropy. For a ferromagnetic material the direction of the magnetization depends on the shape of the material due to the shape anisotropy. Besides shape of the material, the non-isotropic environment of atoms (in multi-component alloys, for example) in a crystal is another source of magneto-crystalline anisotropy.

Experimentally, there has been many ways to tailor magnetic anisotropies of nanostructured materials especially by manipulating lattice strains, compositions, capping layers, growth procedures, and surface adsorbates etc. [146–148]). Density-functional calculations have been extensively used to explore and understand the underlying mechanism at the electronic structure level [42, 149, 150]. The reliable determination of MAE for any material requires very accurate electronic structures calculations and proper treatment of the spin-orbit coupling because the energy we are dealing with are sometimes several orders of μeV, which can very easily superimpose with the numerical noise. The spin-orbit coupling term is usually omitted in most of the DFT calculations with the assumption that it does not play a major role in the chemical bonding and also for quick computations. In DFT the spin-orbit interaction is treated through the scalar-relativistic or semi-relativistic [151] approaches. The magnetic anisotropy is studied using the force theorem (for details, see Sec. 3.10). Such calculations involve a large number of k points to deal with the numerical fluctuation [43]. Several improvements are proposed, like broadening techniques [152], and the state-tracking and the torque schemes, to overcome this problem. The evaluation of E_{MAE} can also be done through the torque method. For a detail description, see Sec. 3.10. In all our studies on MAE we have adopted the former method, i.e. calculating the magnetic anisotropy energy using the magnetic force theorem method.

4.1.1 Magnetoelasticity

There exists a different magnetic phenomena, due to the strain dependence of the MAE, known as magnetostriction or magnetoelastic anisotropy, which is the deformation of the material in response to a change in its direction of magnetization through the application of a magnetic field [9]. Magnetoelastic anisotropy is caused by the mechanical strain which yields substantial anisotropy contributions in a material. It has long been exploited in iron-based magnets, such as carbon steels and related alloys (Fe-Cr, Fe-Co). It is also important in soft magnets, for example in permalloy-type magnets ($Fe_{100-x}Ni_x$), where the cubic anisotropy is small and the magnetoelastic contribution easily dominates the total anisotropy. The main source of magnetoelasticity is magnetocrystalline anisotropy. Magnetoelasticity is closely related to magnetostriction, where the mechanical strain is created by the rotation of the magnetization direction. Subjecting cubic magnets to uniaxial mechanical strain yields a uniaxial anisotropy contribution. Uniaxial magnetoelasticity is defined as

$$\frac{E_{ME}}{V} = -\frac{\lambda_s E}{2}(3cos^2\theta - 1)\varepsilon + \frac{E}{2}\varepsilon^2 - \varepsilon\sigma \tag{4.1}$$

where σ is the uniaxial stress, ε is the elongation along the stress axis and is equal to $\Delta l/l$, E is the Young's modulus and θ is the angle between the magnetization and strain axes. λ_s is the saturation magnetostriction that describes the strength of magnetoelastic coupling. Putting σ and θ = 0 and minimizing the magnetoelastic energy with respect to ε in Eq. 4.1 yields the elongation $\varepsilon = \lambda_s$, which means that λ_s is the spontaneous magnetostriction in the magnetization direction. A magnet that has a spherical shape in the paramagnetic state becomes a prolate ferromagnet for $\lambda_s > 0$ and an oblate ferromagnet for $\lambda_s < 0$. Since λ_s is very small in most compounds, moderate stress $\sigma = E\varepsilon$ outweighs the spontaneous magnetostriction, which yields the magnetoelastic anisotropy energy density

$$\frac{E_{ME}}{V} = -\frac{\lambda_s \sigma}{2}(3cos^2\theta - 1) \tag{4.2}$$

and the magnetoelastic contribution K_1= $3\lambda_s\sigma/2$. A crystal-field phenomenon occurring in highly symmetric crystals and requiring a degenerate ground state is the Jahn-Teller effect. Jahn-Teller ions can lower their energy by spontaneously distorting the surrounding lattice. This energy gain is small but proportional to ε, as compared to the elastic energy, which is proportional to ε^2. Minimizing the total energy results in a finite lattice distortion [8]. However, besides the crystal-field analogy, the Jahn-Teller effect is not related to magnetocrystalline anisotropy.

4.1.2 Magnetic anisotropy in thin films and wires

The origin of large uniaxial magnetic anisotropies in thin films are the surface interface effects and lattice strains arising because of lattice mismatches and presence of step edges [147, 153]. The contributions from surface and interface strongly depend on the atomic relaxations, chemisorptions, and growth morphologies. Therefore, the calculation of E_{MAE} through DFT requires geometrically op-

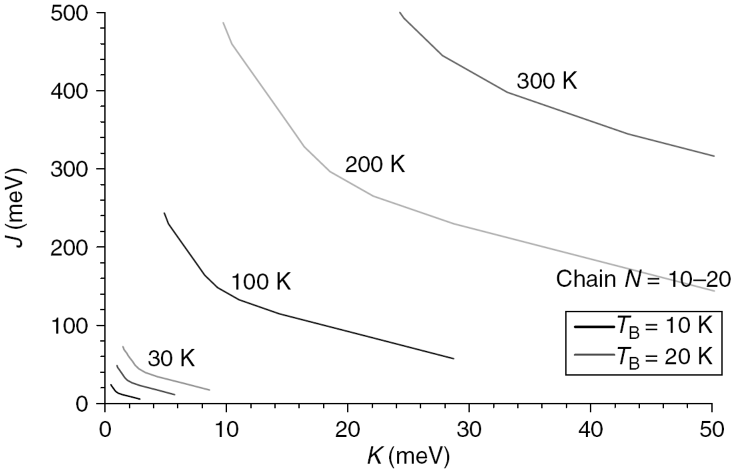

Figure 4.1: The phase diagram for a free-standing chain of 10-atoms using classical Monte Carlo simulations [45].

timized structures. Though GGA improves the results of atomic structures for 3*d* transition metals over LSDA, it overestimates the volume of 4*d* and 5*d* elements as well as oxides. A complete understanding of complex magnetic films requires the analysis of the electronic origin of the E_{MAE} for a free-standing magnetic monolayer.

There have been many calculations to study the effects of metal substrates or capping layers on the E_{MAE} of ultrathin magnetic thin films [42, 150]. The values of K for magnetic films can be determined through DFT calculations with suitable accuracy. Interestingly, E_{MAE} of Fe, Co and Ni films can be tuned by surface chemisorptions of O, CO, and H [154–158], and the underlying electronic mechanism has been actively explored through theory and experiment interplays.

The smallest possible magnetic recording units, such as monoatomic chains, are grown on substrates [159] or built by Scanning Tunneling Microscope (STM) tip manipulation [160] for 100-1000 TB in.$^{-2}$. The major problem of nanomagnets is the thermal fluctuation, which produces superparamagnetism [161] at finite temperature. Therefore, a high anisotropy energy barrier is required in order to maintain the ferromagnetic ordering. Experimentally, Jamet *et al.* have studied the magnetic anisotropy in a 3-nm Co cluster embedded in a niobium matrix and found the dominating role of atoms on the cluster surface [162–164]. Giant MAEs of Co particles on Pt(111) [3, 165] was found by Gambardella *et al.*. They have also found an oscillation of MAE and the coercive field as a function of the transverse width of the Co wires on Pt(997). The experimental studies by Rusponi *et al.* [166] for Co patches deposited on Pt(111) has predicted the dominant role of edge Co atoms in the perpendicular uniaxial anisotropy. Pratzer *et al.* have studied the Fe stripes on stepped W(110) and found an extremely narrow domain wall, ($\approx$ 6 Å), which might be due to large MAE [167, 168]. Figure 4.1 shows the magnetic phase diagram for a 10-atom monatomic chain, obtained through classical Monte Carlo simulations. In order to achieve a high blocking temperature (300K), below which the magnetization of each atom aligns along the easy axis and thereby forming a ferromagnetic structure, stringent conditions are required, such as, J= 320-420 meV and K= 30-50 meV/atom. Such a large E_{MAE} cannot be achieved in nano-entities only with 3*d* elements. For the free-standing or supported Co monatomic chains, E_{MCA} is still a few tenths meV/atom [169]. For Co chains deposited on Pt(111), Lazarovits *et al.* have found the easy axis to be perpendicular to the surface and independent of the length of the chains [170]. There are also studies on the growth of Fe_n chains on Cu(001), Cu(111) as well as embedded in the bulk Cu [169]. Shick *et al.* found that a quasi-one-dimensional Co chain at the Pt(111) step edge has an easy axis at an odd angle of 20° toward the Pt step [171, 172]. In addition, the spin and orbital magnetic moments are noncollinear. The relationship between MAE and the anisotropy of the orbital moment, that is adopted for measuring the E_{MAE} through the X-ray magnetic circular dichroism technique, was also examined for several systems [149, 173]. Large K values upto 30-50 meV have been found through DFT calculations. Model calculations for 3*d*-5*d* trimers (FeOsFe and FeIrFe) showed a large value of E_{MAE} up to 108 meV, which is due to the high spin polarization of Fe and the strong SOC from the 5*d* atoms. Giant values of 30-60 meV/atom were also reported for Ru or Rh wires by Mokrousov *et al.* through FLAPW calculations [174].

4.2 Spin moments, orbital moments and magnetic anisotropy for clusters

DFT successfully calculates several physical and chemical properties of clusters. While calculating the magnetic properties such as spin and orbital moments as well as the MAE of small clusters, from computational point of view, two cases should be taken into account, namely, the non-collinear magnetization density (the magnetization vector varies smoothly with respect to the position) and the spin-orbit coupling (the interaction between electron spin and its orbital motion). For Both cases, the spin-up and spin-down states are mixed together [175, 176]. It has been observed that TM clusters give rise to novel magnetic anisotropic properties compared to the bulk. For example, XMCD studies by Gambardella *et al.* [3] predict a large MAE of a single Co atom (9.0 meV/atom) deposited on Pt(111) surface. Experimentally, Balashov *et al.* [177] through inelastic tunnelling spectroscopy have found very large value of MAE for Fe and Co clusters up to 3 atoms compared to bulk. Theoretically there exists abundant studies for MAE of clusters deposited on substrates [178–184], however studies related to MAE of gas phase clusters are still limited [185–188]. Most of them are based on semiempirical techniques. For example, using tight binding technique, Pastor *et al.* [185] have calculated the MAE of small Fe clusters up to 7 atoms, where they have found large MAEs for clusters relative to the corresponding bulk as well as thin films. Using the same method, Xie *et al.* [189] and Guirado-Lopeź *et al.* [186] have calculated the MAE for Co nanoparticles. They have also obtained large MAEs for Co clusters relative to bulk. As an example, Figure 4.2 shows the MAE of Co clusters obtained from tight binding calculations [189]. Calculation of MAE for isolated clusters based on *ab initio* methods are mostly for TM dimers [188, 190, 191]. For larger clusters, there exists very few reports [192, 193].

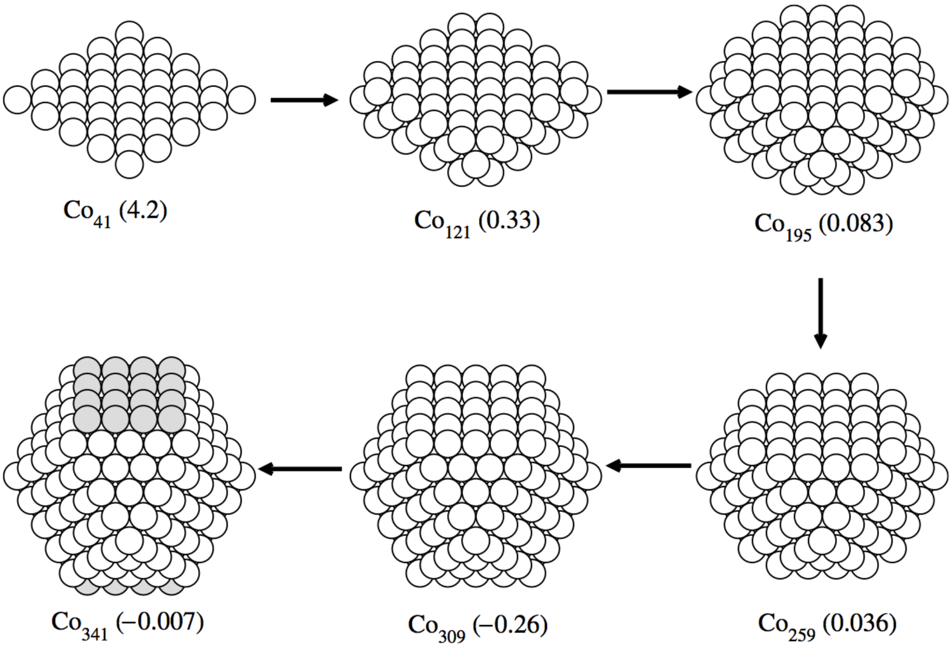

Figure 4.2: The magnetic anisotropy (E_{001} - E_{100}) in meV/atom of Co_N clusters with 1, 3, 5, 7, 9 and 11 layers for 41, 121, 195, 259 and 341 atoms. For Co_{309}, the MAE is calculated as the difference between (E_{111} - E_{001}) in μeV/atom [189].

Using DFT, Kortus *et al.* [192] have calculated the MAE of 5- and 13-atom Co and Fe clusters, where they have obtained the MAEs for Fe_5, Co_5 and Fe_{13} as 0.2, 0.1 and 0.27 meV/atom, respectively. However, for Co_{13}, they obtain nearly zero MAE. Hong *et al.* [193] have calculated the the orbital moments and MAE for small Co clusters up to six atoms using the full potential linearized augmented plane wave method, where they have obtained significantly enhanced value of orbital moment relative to the hcp bulk Co, but, the value of MAE calculated by them for Co clusters is less ($<$ 1 meV/atom).

In this respect, binary 3*d*-5*d* clusters can be a challenging material, since the alloying of non magnetic bulk 4*d* and 5*d* elements like Rh, Pt and Au with magnetic 3*d* transition metals result in enhanced magnetic moments [119, 194–196]. In the present work, we have studied the spin moments, orbital moments and MAE of elemental M_{13} (M = Fe, Co, Ni) clusters and the effect of capping them with Pt atoms. We have chosen the closed-shell icosahedral geometry for the M_{13} clusters, which are known to show enhanced stability for such cluster size. The following results are discussed in Ref. [18].

4.3 Computational details

The DFT calculations are performed using the VASP code [25, 26], within the GGA. The parameterization by Perdew and Wang (PW91) was used for the exchange and correlation functional [197].

VASP uses the projector augmented wave (PAW) method [26, 27] and a plane wave basis set. Periodic boundary conditions were imposed onto a sufficiently large cubic cell with an edge length of 15 Å for M_{13} clusters and 20 Å for $M_{13}Pt_n$ clusters which is large enough to minimize the interaction between the replicated cluster images. Only the Γ point was used for the Brillouin-zone sampling for the cluster calculations. Gaussian broadening for the discrete energy levels of 0.05 eV, a plane-wave cutoff of 270 eV, and a Fourier grid spacing of 0.05 $Å^{-1}$ were applied for all calculations except for the MAE calculations. The energy convergence criterion for the self-consistency was set to 10^{-10} eV. In order to compute the equilibrium lattice constants for bulk bcc Fe, fcc Ni, and fcc Co, a k-mesh of $(11\times11\times11)$ and Gaussian broadening as in the cluster calculations was used. The local magnetic moments were obtained by integration of the magnetization density over atom-centered spheres with radii of 1.302 Å (Fe, Co), 1.286 Å (Ni) and 1.455 Å (Pt).

It is known that the MAE for cubic bulk transition metals is of the order of 1 μ eV/atom. Thus, calculation of MAE requires much careful attention in order to overcome minute computational noise, which can easily interfere with the estimated quantities. Therefore, one must have a very refined convergence of charge density as well as proper choice of energy cutoff and a large Fourier mesh. For our studies on MAE of the clusters, we have used a Gaussian broadening parameter of 0.01 eV for the energy levels and a very high value of plane-wave cut-off of 1000 eV with a 0.046 $Å^{-1}$ Fourier grid spacing. The MAE is defined as the maximum energy difference between different settings of the spin moment with respect to the atoms framework.

For the sake of comparison and for the validation of the results on clusters, some calculations have been performed using a local-orbitals code, SIESTA (Spanish Initiative for Electronic Simulations with Thousands of atoms) [28] within GGA. SIESTA uses localized atom-centered basis functions of “double-ζ with polarization orbitals” quality and triple-ζ for $3d$ functions have been constructed according to the standard scheme of SIESTA method [198], version 1.4.13, with the “Energy Shift” parameter, which controls the localization of basis functions taken 0.01 Ry. Norm-conserving pseudopotentials of Troullier and Martins [199]. The treatment of the spin-orbit coupling was included as described by Fernandez-Seivane *et al.* [200].

For additional verification, few calculations have been done for the binary clusters with another first-principles calculation method, namely, the all-electron local orbital FPLO 6.00-24 code [29] in the fully relativistic mode, where the Dirac-Kohn-Sham equations including the spin-orbit coupling in all orders are solved [201]. It uses the LSDA [202].

4.4 Elemental clusters

Bulk cubic transition metals exhibit very small value of MAE due to the high symmetry. Hence it is expected that the MAE decreases for the perfect icosahedral clusters. With the breaking of symmetry, for example by tetragonal distortion, the MAE increases considerably [203]. Such an enhancement of MAE may also occur for the relaxed clusters. Therefore, we have calculated the MAE for both ideal

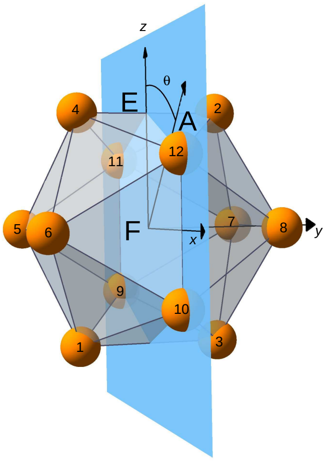

Figure 4.3: The perfect icosahedral cluster showing the *x*-*z* plane, where the angle θ is varied for the MAE calculations. E, F, and A abbreviate the directions from the center to the middle of an edge, the middle of a facet, and an outer atom, respectively.

and relaxed M_{13} clusters. Each of them will be discussed categorically in the following.

4.4.1 MAE of perfect clusters

Figure 4.3 shows the perfect icosahedral cluster with the definition of (x, z)-plane and the angle θ for the magnetization directions. For $\theta = 0$, the magnetization is directed parallel to an axis passing through the central atom and the center of a bond connecting two outer atoms; with increasing θ, the magnetization direction passes through the center of a triangular facet, through an outer atom and finally arrives again at a bond center for $\theta = \pi/2$.

In order to calculate the MAE of the perfect icosahedral clusters, the minimum-energy center-shell distances for each of the perfect icosahedral M_{13} clusters are calculated, which are found to be 2.39 Å, 2.33 Å and 2.32 Å for Fe_{13}, Co_{13} and Ni_{13}, respectively with total magnetic moments 44 μ_B (Fe_{13}), 31 μ_B (Co_{13}), and 8 μ_B (Ni_{13}). For Fe_{13} with magnetic moment 44 μ_B, there are difficulties in achieving convergence in the calculation of MAE at low smearing of 0.01 eV due to the dense energy levels near the Fermi level. Therefore, a perfect icosahedron with total magnetic moment 46 μ_B, which has a center-shell distance of 2.57 Å is considered. Figure 4.4 shows the comparison of θ-dependent energy differences ($\Delta E(\theta)$) of perfect Fe_{13} ICO (with total magnetic moment 46 μ_B) obtained from *ab initio* calculations with the Néel model. The global minima is obtained for the magnetization directed parallel to the line from the central atom to the circumcenter of the triangular facets and the global maxima is obtained for the magnetization parallel to the line from center atom to one of the surface atoms. The magnitude of $\Delta E(\theta)$ for Fe_{13} cluster is found to be 1.7 μeV/atom, which is comparable to that of the bulk bcc Fe. The MAE of perfect Co_{13} and Ni_{13} are found to be 0.31 μeV/atom, and 0.77

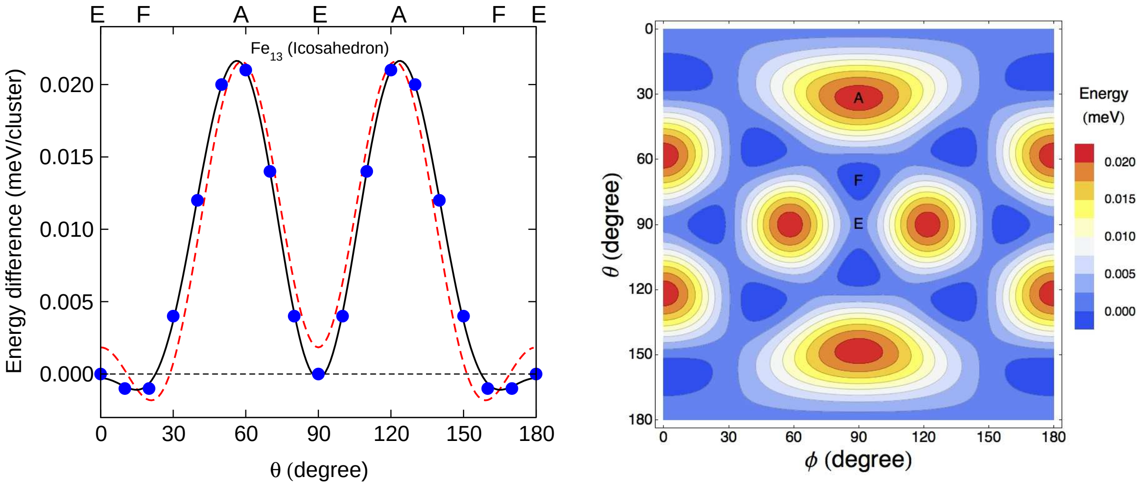

Figure 4.4: Left: The energy difference ΔE = E (θ) - E(0) in meV/cluster as a function of θ for a perfect Fe$_{13}$ icosahedral cluster, which shows a comparison between the *ab initio* data (filled circles connected by solid line as guide to the eyes) and the fit to the anisotropy term of Néel model (the dashed line). The letters A, E, and F refer to the positions defined in Fig. 4.3 Right: the (θ, ϕ) for the MAE of the perfect Fe$_{13}$ cluster.

μeV/atom, respectively. The $\Delta E(\theta)$ shows a similar qualitative trend for Co$_{13}$ and Ni$_{13}$ as obtained for perfect Fe$_{13}$. The total energy obtained as a function of θ from the *ab initio* calculations for Fe$_{13}$ are fitted to the anisotropy expansion of the Néel surface anisotropy model [204, 205] for a nearly spherical cluster, which is defined as

$$\Delta E_{\text{Néel}} = \sum_n E_n = -\sum_n \sum_{i=1}^{N} D_n(\mathbf{e}_i \cdot \mathbf{S}_i)^n. \tag{4.3}$$

where, D_n is the anisotropy constant of order n (an even integer), $\mathbf{e}_i$ the normalized position vector of atom i along the radial directions and $\mathbf{S}_i$ are their magnetic moments. D$_n$ are assumed to be θ-independent. From the symmetry considerations of perfect ICO, the second and fourth order contributions have no θ-dependence. The major contribution to anisotropy energy is from the next order contribution, i.e., the sixth order. Still higher order contributions are negligible and the $\Delta E(\theta)$ could be successfully fitted to the sixth order fit.

4.4.2 Structural distortion of relaxed clusters

In order to calculate the MAE of relaxed clusters, we have transformed the perfect ICO in two different paths, namely, the Jahn-Teller distortion (JT) and the distortion along the Mackay path, the mackay transformation (MT). The JT and the Mackay distortions reduce the I$_h$ symmetry of a perfect icosahedron in two different ways, lifting the (quasi-) degeneracy of the highest occupied molecular orbitals and gaining in energy from their splitting. The JT distortion [14] maintains the five-fold ro-

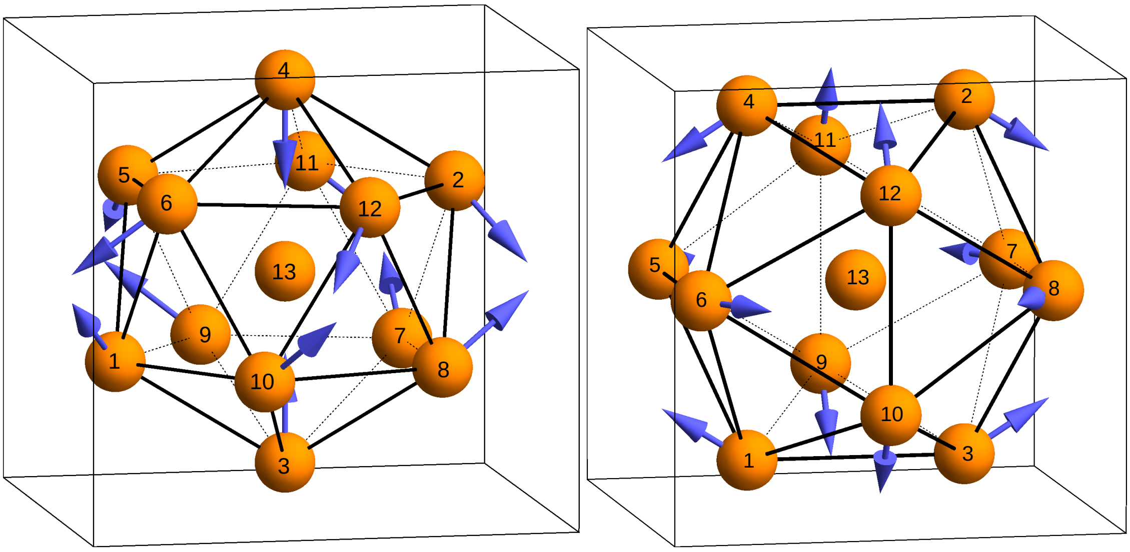

Figure 4.5: The JT-distorted and MT Fe_{13} clusters in the left and right panels, respectively. Arrows indicate the direction of relative shift of atoms with respect to the ideal positions. The arrows have been scaled up by a factor of 20 and 30 for the JT and MT Fe_{13} cluster. The box is only guide to the eyes. The actual simulation box size is 15^3 Å^3 [18].

tational symmetry, with a compression of the cluster along the corresponding axis. It also involves a mutual opposite rotation of the two pentagonal rings pierced by the axis in consideration. The JT distortion can be characterized by parameter r, defined as $r = |\boldsymbol{r}_3 - \boldsymbol{r}_4|/|\boldsymbol{r}_1 - \boldsymbol{r}_2|$ (see left panel of Fig. 4.5 for the labeling of atoms). The MT can be characterized by parameter s, which is the square of the ratio of the stretched to the unstretched edges (see Fig. 4.5, right panel) being equal to 1 and 2 for the perfect icosahedron and cuboctahedron, respectively [206]. That is, $s = |\boldsymbol{r}_4 - \boldsymbol{r}_2|^2/|\boldsymbol{r}_4 - \boldsymbol{r}_{12}|^2$.

Figure 4.6 shows the variation of energy as a function of the JT-parameter r and of the Mackay parameter s for M_{13} clusters. As the starting geometries, the minimum energy center-shell distances for the perfect ICO of Fe_{13}, Co_{13} and Ni_{13} are considered, which are 2.39 Å, 2.33 Åand 2.32 Å, respectively. The minimum energy structural parameters are reported in Table 4.1. It should be noted that for the JT-distorted clusters, two of the axial atoms have different center-shell distances compared to the other atoms, while for the Mackay transformed clusters, the center-shell distances remains independent of s.

For Fe_{13} cluster, the JT-distorted structure is by 125 meV/cluster, the MT cluster by 61 meV/cluster lower in energy compared to the energy of perfect ICO. For Co_{13}, the JT relaxation is by 7 meV/cluster and the MT relaxation is by 27 meV lower in energy with respect to the perfect ICO, whereas for Ni_{13} the energy differences are nearly the same (16 meV/cluster) for both JT and MT clusters, respectively.

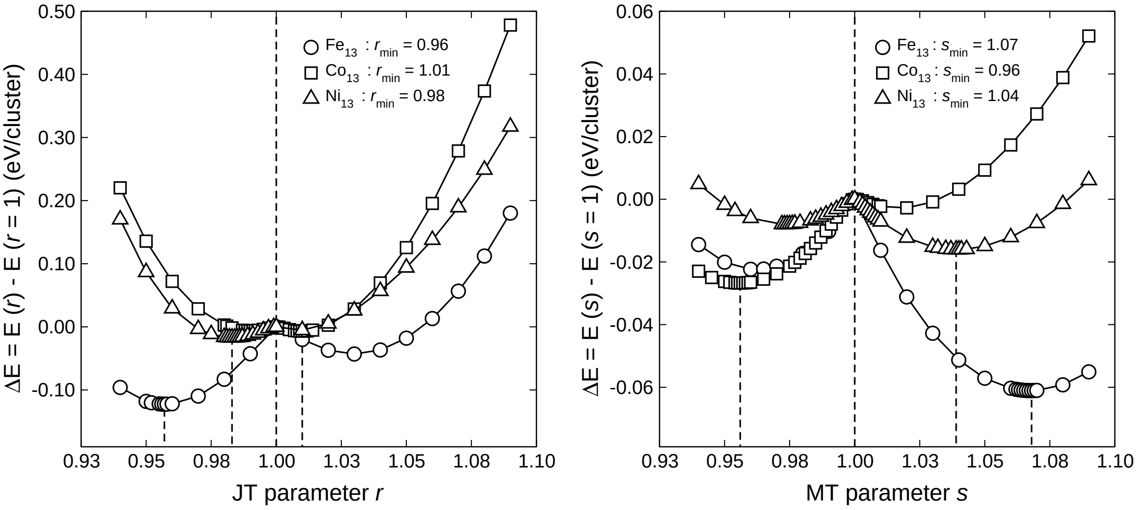

Figure 4.6: The values of the *r* and *s* obtained for M_{13} clusters. The dashed lines indicate the minimum points for both cases. For each case, *s* = 1 and *r* = 1 represent the perfect ICO.

Table 4.1: The bond lengths (Å) for the minimum energy JT-distorted (r = 0.965 for Fe_{13}, 1.01 for Co_{13}, 0.98 for Ni_{13}) and MT (s = 1.07 for Fe_{13}, 0.96 for Co_{13}, 1.04 for Ni_{13}) M_{13} clusters.

Bonds	Fe_{13} (JT)	Co_{13} (JT)	Ni_{13} (JT)
2 × center-shell	2.34	2.35	2.28
10 × center-shell	2.42	2.32	2.33
Bonds	Fe_{13} (MT)	Co_{13} (MT)	Ni_{13} (MT)
Center-shell	2.39	2.33	2.32
24 × bond length (surface)	2.50	2.46	2.43
6 × bond length (surface)	2.58	2.41	2.47

4.4.3 Spin and orbital magnetic moments of relaxed clusters

Table 4.2: The average orbital moment $\langle \mathrm{L} \rangle = \frac{1}{13}\sum_{i=1}^{13}|\mathbf{L}_i|$ and the average spin moment $\langle \mathrm{S} \rangle = \frac{1}{13}\sum_{i=1}^{13}|\mathbf{S}_i|$ for MT M_{13} clusters in units of μ_B/atom, compared to the corresponding calculated bulk values for bcc Fe, fcc Co and Ni.

Cluster	$\langle \mathrm{L} \rangle$	$\langle \mathrm{S} \rangle$	$\langle |\mathbf{L}| \rangle_{\mathrm{bulk}}$	$\langle |\mathbf{S}| \rangle_{\mathrm{bulk}}$
Fe_{13} (MT)	0.08	3.05	0.06	2.25
Co_{13} (MT)	0.12	2.05	0.08	1.67
Ni_{13} (MT)	0.06	0.66	0.05	0.65

The average orbital moments $\langle L \rangle$ and the average spin moments $\langle S \rangle$ for the Mackay-distorted M_{13} clusters are compared with related bulk values in Tab. 4.2. The orbital and spin moments are obtained for the bulk systems at the equilibrium lattice parameters of 2.83 Å (bcc Fe), 3.52 Å (fcc Co) and 3.523 Å (fcc Ni). We observe larger values of spin moments for clusters as compared to that of the corresponding bulk, which is expected in small clusters. For Ni_{13}, the spin moment is approximately the same as the corresponding bulk value. On the other hand, the orbital moments for M_{13} clusters are found to be larger by factors of $\sim$ 1.2 to 1.5 than in the bulk. For Co_{13} and Ni_{13}, the orbital magnetic moments are observed to be more sensitive towards the geometry than spin magnetic moments. Previous study based on tight-binding technique [207], has shown that in Ni clusters of up to 13 atoms, the average orbital moment $\langle L \rangle$ per atom is about 4 to 8 times larger than the bulk value and with increase in cluster sizes, $\langle L \rangle$ was shown to approach the bulk value. Table 4.3 shows a comparison of the on-site magnetic moments for Mackay-distorted M_{13} clusters, obtained with VASP and SIESTA. The relaxed MT coordinates obtained with VASP have been used in the calculation with SIESTA, in order to compare the spin and orbital moments, and the non-collinearity. For both methods, the spin moments are aligned parallel (the x- and the y-components of the spin vectors amount to at most 0.001 μ_B and are not shown in Tab. 4.3). The orbital moments slightly deviate from the z-axis, but these deviations are not significantly above the numerical noise level. While comparing the numerical results for spin and orbital magnetic moments from these two calculation methods, one must take into account the difference in their definitions. In VASP, the properties (spin and orbital moments) are extracted as projection onto an atomic sphere, While in SIESTA, the magnetic moments are computed in terms of the decomposition by projection onto localized, numerical orbitals, known as Mulliken population analysis. It is known that the local magnetic moments as well as the atomic charges in heterogeneous systems are often very different, when estimated according to these two different schemes. In order to illustrate this effect, we give in the last column of Tab. 4.3 (in parentheses), the values of spin moment, extracted from the SIESTA results by summing up the spatial spin density over atom-centered spheres with a radius of 1.302 Å. The fluctuations of the magnetic moments over equivalent atoms are observed, which occur due to the sparseness of the spatial grid with steps of 0.078 Å, on which the spin density summation has been done. While the results of the Mulliken population analysis by definition add up to the total moments, the added values of the spatial summations are smaller than the total moments by about 10%.

4.4.4 MAE of relaxed clusters

The MAE is calculated both for the JT and MT M_{13} clusters, for the structural parameters compiled in Table 4.1. The relaxation pattern for both transformations is shown in Fig. 4.5. In order to underline the remaining symmetry, the spatial orientation of both clusters is different. According to these different orientations, the θ-path for the calculation of MAE is, therefore different for both distortions. For the JT case, the $\theta = [0, \pi]$ path is roughly A-E-A-F-E-F-A (see Fig. 4.5, left panel), while for the

MT case, it follows the path as discussed for the perfect icosahedron, E-F-A-E for $\theta = [0, \pi/2]$.
The θ-dependent energy differences for the relaxed M_{13} clusters are depicted in Fig. 4.7. For the JT-distorted M_{13} clusters, a large second order contribution to the MAE (see Fig. 4.7, left panel) is obtained, as is a consequence of symmetry breaking. All higher order terms are significantly small and hence can be neglected. On the other hand, due to the cubic symmetry of the MT clusters, the lowest order contribution is only the fourth order, D_4. No second order anisotropy is found in this case. The higher orders can be neglected. The corresponding values are listed in Table 4.4. For all cases, the MAE of the JT-clusters are found to have larger values as compared to that of the MT clusters. For example, in the case of Fe_{13}, the MAE of the JT-distorted cluster is calculated to be 322 μeV/atom, which is approximately six times larger as compared to the MT Fe_{13} cluster (55 μeV/atom). Similarly, for Co_{13}, the MAE of the JT-distorted cluster has a value of 147 μeV/atom and this is approximately 100 times larger than the MT-distorted (1.42 μeV/atom) cluster. However, among all M_{13} clusters, the JT-distorted Ni_{13} cluster has the largest value (688 μeV/atom), which is about 30 times larger than that of the MT-distorted ones. The reason behind such large values of MAE for the JT-distorted clusters compared to the MT ones is the symmetry breaking in the former case. Concerning the comparision of MAE with respect to bulk, a large value of MAE per atom for JT- and MT-distorted Fe_{13} and Ni_{13} clusters are obtained relative to the corresponding bulk, which is 1.4 μeV/atom for bcc Fe, 2.7 μeV/atom for fcc Ni as obtained from LSDA calculations [208]. For Co_{13}, a different trend is observed. Though the JT-distorted Co_{13} has a large MAE value $\sim$100 times larger than that of the value of bulk (1.3 μeV/atom for fcc Co), for MT Co_{13}, it is approximately similar to the bulk.

4.4.5 Pt capped clusters: $(Fe, Co, Ni)_{13}Pt_n$

Binary clusters show a larger diversity compared to the elemental systems. For example, the intermixing of Co with Rh results in large magnetic moments of the binary systems [196]. Also, both free FePt clusters and Co clusters supported by a Pt substrate show enhanced spin and orbital moments with respect to corresponding bulk values [209]. Hence, it is interesting to study how the magnetic properties including the MAE of M_{13} clusters change as they are capped with Pt atoms. The important point is to investigate the evolution of spin and orbital moments as well as the MAE in more ”asymmetric” clusters as obtained by adatoms. Therefore, we have added different number of Pt atoms on the top of M_{13} clusters and studied the resulting properties. We considered three high-symmetry positions (A, E, and F in Fig. 4.3) to cap the M_{13} clusters by a single Pt atom and found that a Pt position above the middle point of a facet is most favorable in all three cases, M = Fe, Co, Ni. In the following, we used this finding as a guideline for initial geometries of $M_{13}Pt_n$ clusters (n = 3, 5, 20). In all cases, the Pt atoms were initially placed above the facet centers at a distance found in the single-Pt capping case. After relaxation, optimized geometries were obtained as shown in Fig. 4.8 for $Co_{13}Pt_3$ (left) and for $Co_{13}Pt_5$ (right). Since atom projected quantities like spin and orbital moments depend on the specific code, we compared for the particular case of $Ni_{13}Pt_3$ related data obtained by VASP and FPLO. The structure optimization was carried out by VASP, and the same geometry was used to evaluate the

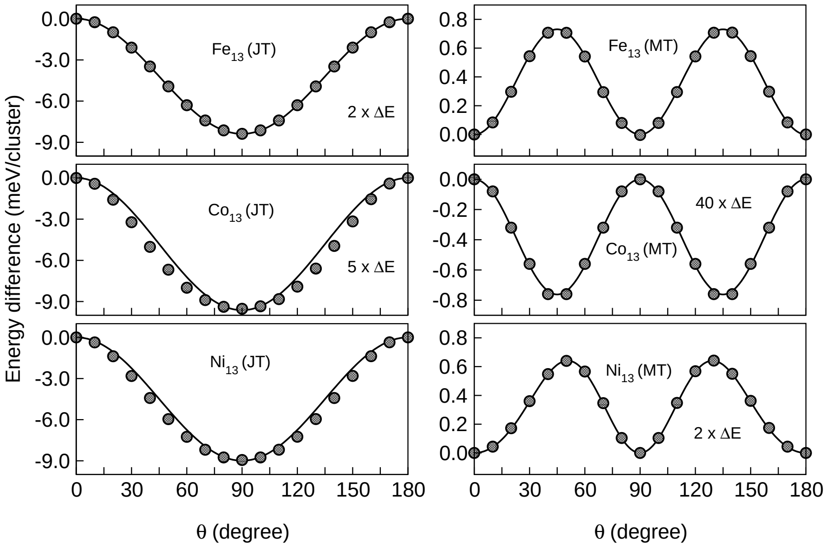

Figure 4.7: The energy differences ΔE = E (θ) - E(0) in meV/cluster as a function of θ for the JT-(left) and Mackay-distorted (right) M_{13} clusters. The magnetization direction varies in the $x-z$ plane. For the JT case, the $x-z$ plane passes through atoms 3, 4, 12 and middle of the bond 8-10 (see left panel of Fig. 4.5). For the MT case θ varies through all atoms shown in Fig. 4.3. For the JT-distorted clusters, the energy difference for the Co_{13} and Fe_{13} clusters is multiplied by factors of 5 and 2, respectively, whereas for the MT-distorted clusters, the energy difference for Co_{13} and Ni_{13} is multiplied by factors of 40 and 2, respectively.

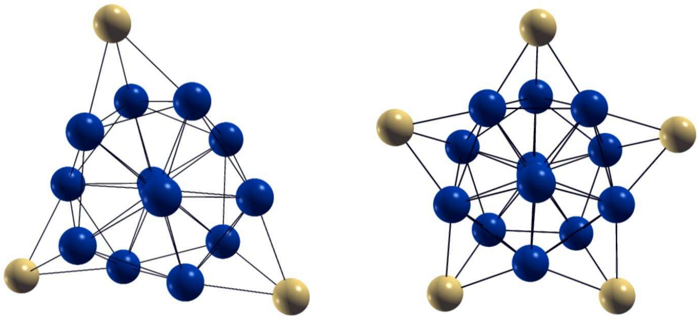

Figure 4.8: The low energy isomers of $Co_{13}Pt_3$ (left) and $Co_{13}Pt_5$ (right) clusters. Blue and yellow spheres represent Co atoms and Pt atoms, respectively.

magnetic moments by both codes. In FPLO, the magnetic moments are calculated through Mulliken population analysis. Fig. 4.9 shows the absolute value of orbital moment per atom $|\mathbf{L}_i|$ (left) and the absolute value of spin moment per atom $|\mathbf{S}_i|$ (right) on each atomic site. It is obvious that both codes give results which are in good agreement with each other. Therefore, the calculations which are discussed in the following are done with VASP only.

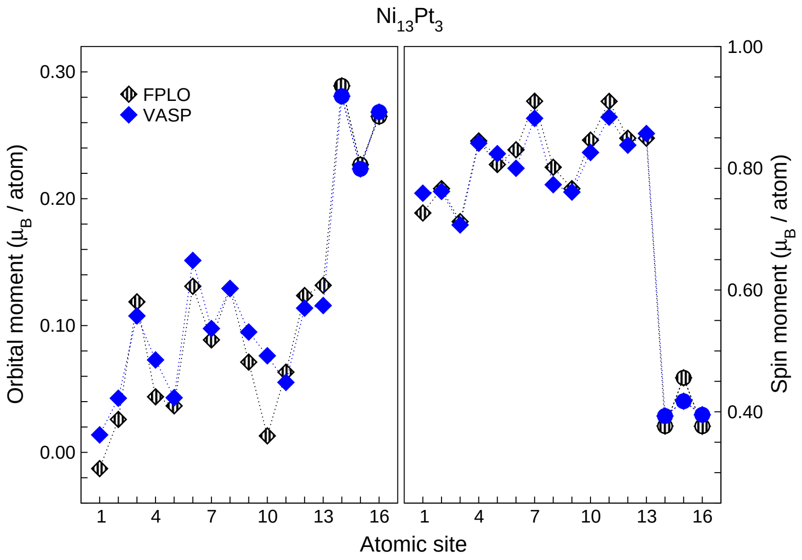

Figure 4.9: A comparison of the magnetic moments for $Ni_{13}Pt_3$ obtained by VASP (filled symbols) and FPLO (dashed symbols). The left and right panel shows the onsite orbital moments $|\mathbf{L}_i|$ and spin moments $|\mathbf{S}_i|$ for the $Ni_{13}Pt_3$ cluster, respectively. The diamonds and circles show the magnetic moments on Ni and Pt atoms. Atomic site 1 is the center atom. The results obtained using FPLO are calculated by D. Fritsch and M. Richter.

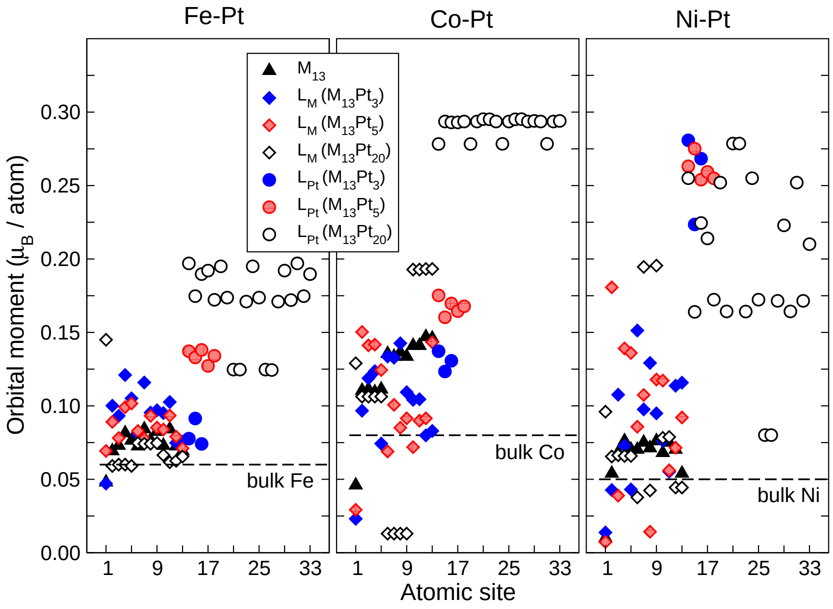

Figure 4.10: The onsite orbital moment $|\mathbf{L}_i|$ of $Fe_{13}Pt_n$ (left), $Co_{13}Pt_n$ (middle) and $Ni_{13}Pt_n$ (right) clusters. The dashed lines show the calculated orbital moments of bulk bcc Fe, fcc Co, and fcc Ni, respectively.

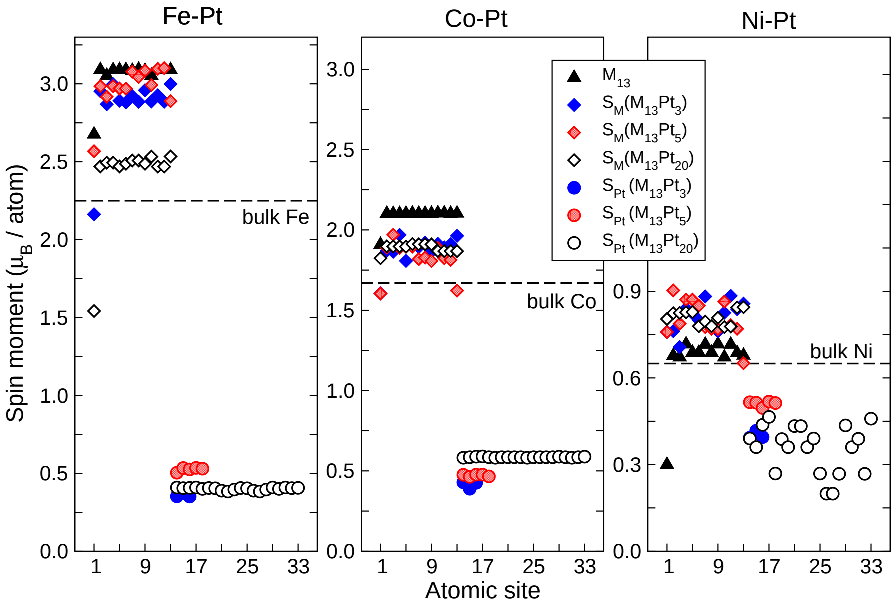

Figure 4.11: The onsite spin moment $|\mathbf{S}_i|$ of $Fe_{13}Pt_n$ (left), $Co_{13}Pt_n$ (middle) and $Ni_{13}Pt_n$ (right) clusters. The dashed lines show the calculated spin moments of bulk bcc Fe, fcc Co, and fcc Ni, respectively The same symbols as in Fig. 4.10 are used.

Figures 4.10 and 4.11 show the variation of $|\mathbf{L}_i|$ and the variation of $|\mathbf{S}_i|$ on each atomic site of $M_{13}Pt_n$ clusters are shown, respectively (the symbols are kept consistent for both figures and the center atom is placed at 1). Fig. 4.10 shows that the orbital moments of such few-atom systems, which in general depend sensitively on the particular chemical composition and geometry. The resulting electronic structure can be very individual (e.g., the nature of the highest occupied level depends on the electron number and on the spin moment), and is hard to be predicted without a detailed calculation. It is found that the $|\mathbf{L}_i|$ of Fe_{13} clusters approach the corresponding bulk value of bcc Fe (see Table 4.5), with increasing number of Pt atoms. This trend is absent in the related Co and Ni systems (see Table 4.5). The orbital moment on Pt atoms is found to be very sensitive with respect to the core atomic species. For Fe and Co cores, it grows with the number n of Pt atoms, but for Ni cores it slightly decreases with growing n.

In Fig. 4.11, the site-specific spin moments of the capped clusters are shown. Different trends are found for the core atoms: While the Fe and the Co spin moments are reduced by the capping, the Ni moments are relatively enhanced. The spin moment on Pt atoms does not show any clear trend. One intriguing point is the difference between the trends of Pt orbital and spin moments for the $M_{13}Pt_3$/$M_{13}Pt_5$ clusters, as M varies from Fe to Ni. Here, the Pt orbital moments increase by a factor of two, while the Pt spin moments are merely unchanged. We assume that the hybridization between Ni and Pt is weaker than between Fe and Pt due to the different extension of the atomic orbitals.

Weaker hybridization in general yields larger orbital moments, since the hybridization mixes different *m*-states. An approximate conservation of spin moments of the Pt atoms while passing from Fe to Ni may be due to the fact that in each case the maximum induced spin moment on Pt is already reached, close to a value of 0.5 μ_B which is comparable to the spin moment of the isoelectronic Ni. We have checked this by additional calculations in which we placed one Pt atom on the top of triangular Fe_3 (Co_3, Ni_3) clusters, which shows a similar variation of $|\mathbf{L}_i|$ and $|\mathbf{S}_i|$ as in the cluster calculations of $M_{13}Pt_3/M_{13}Pt_5$.

In the following, quantitative discussions have been presented for the capped clusters. Table 4.5 compiles the values of average orbital moment and average spin moment for each atomic species of $M_{13}Pt_n$ clusters with the total orbital moment L_{tot} and total spin moment S_{tot}.

4.4.6 $Fe_{13}Pt_n$

It is observed that, the addition of Pt atoms on the Fe_{13} cluster leads to considerably enhanced values of L_{tot}, and reduced value of S_{tot} if the Pt-overlayer is completed. This is due to a considerable reduction of the Fe spin moment in comparison with the bare Fe_{13} cluster. The average orbital moment $\langle L_M \rangle$ on Fe_{13} decreases with increasing number of Pt atoms. Regarding the MAE of capped $M_{13}Pt_n$ clusters, we observe that the symmetry of the cluster determines the magnitude of the effect similar to the case in the M_{13} systems. For example, four Pt atoms are capped onto Fe_{13} with the Mackay orientation, to get the $Fe_{13}Pt_4$ cluster shown on the left panel of Fig. 4.12, and, after optimizing the structure, the MAE is calculated. The θ-dependent energy is shown in the right panel of Fig. 4.12. As a consequence of reduced symmetry, we obtain a second-order type anisotropy for this cluster, which is quite large, exceeding by a factor of 10 ($\sim$7 meV/cluster) that of the MT-distorted Fe_{13} and by a factor of 2 that of the JT-distorted Fe_{13}.

4.4.7 $Co_{13}Pt_n$

For $Co_{13}Pt_n$ clusters, a ferromagnetic ground state is found to be stable for all compositions. L_{tot} increases monotonically with *n*. $\langle L_M \rangle$ and $\langle L_{Pt} \rangle$ for $Co_{13}Pt_n$ clusters show a trend similar to $Fe_{13}Pt_n$, i.e. with increasing number of Pt atoms, $\langle L_M \rangle$ (as defined in Table 4.5) decreases and $\langle L_{Pt} \rangle$ increases. $\langle S_M \rangle$ on Co_{13} is merely constant, while the Pt-spin moment increases monotonically with the number of Pt atoms on the cluster surface. This yields a high spin moment of the completely Pt-covered Co_{13}.

4.4.8 $Ni_{13}Pt_n$

Both L_{tot} and S_{tot} vary monotonically with increasing number of Pt atoms for $Ni_{13}Pt_n$ clusters. $\langle L_M \rangle$ and $\langle L_{Pt} \rangle$ for this cluster do not much depend on the number of Pt atoms. However, a decrease of $\langle L_{Pt} \rangle$ and $\langle S_{Pt} \rangle$ from $Ni_{13}Pt_5$ to $Ni_{13}Pt_{20}$ is also observed, which is the consequence of structural

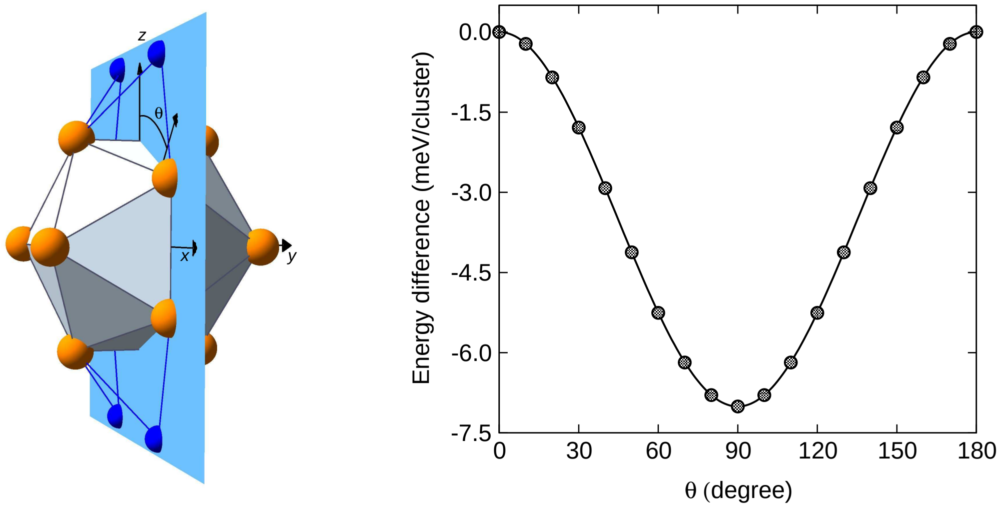

Figure 4.12: Left: The $Fe_{13}Pt_4$ cluster with the x-z plane, where the angle θ is varied. The orange and blue spheres denote the Fe and Pt atoms, respectively. For the optimized $Fe_{13}Pt_4$ cluster, two opposite edges (those adjacent to the Pt atoms) of the Fe_{13} cluster moved towards each other. Right: The θ-dependent energy differences for the relaxed $Fe_{13}Pt_4$ cluster. The solid curve is simply a cubic spline fit to data obtained from the GGA calculations.

instability occurring for the latter composition upon relaxation. The geometry optimization of this cluster converges to a structure with different symmetry, where the Ni atoms are placed closer to the surface of the cluster. The reason for the segregation of Ni atoms towards the surface may be due to its lower surface energy compared to Pt [139]. Another related aspect may be observed in the right panels of Figs. 4.10 and 4.11 showing the variation of onsite orbital and spin moments. The large variations in orbital and spin moments just occur because of the structural distortion for this cluster composition. Comparing all three cases of capped clusters, we find that the presence of Pt atoms on M_{13} affects the orientation of core orbital moments in such a way that they always prefer to be in non-collinear alignment for the $M_{13}Pt_n$ clusters, which is not the case in the uncapped M_{13} clusters. On the other hand, directions of individual spin moments remain always collinear for the same clusters indicating that they are less affected by the Pt atoms.

Table 4.3: Spin and orbital moments in μ_B/atom for the Mackay-distorted M_{13} clusters as calculated by VASP and SIESTA, for an initial [001] setting of the spin direction. The x and y-components of the spin moment are < 0.001 μ_B (not shown). For VASP calculations, the spin moments are calculated over atom-centered spheres of 1.302 Å for Fe_{13}, Co_{13} and 1.286 Å for Ni_{13}, respectively. For SIESTA calculations, the values of spin moments are given in terms of Mulliken populations and over atom-centered spheres (shown in parenthesis). The same values of atomic radius are used for the SIESTA calculations.

				Fe_{13} (MT)				
	VASP				SIESTA			
Atom No.	L_x	L_y	L_z	S_z	L_x	L_y	L_z	S_z
1	0.00	-0.02	0.11	3.06	0.00	-0.01	0.09	3.43 (3.14)
2	0.00	0.02	0.12	3.06	0.00	0.01	0.09	3.43 (3.12)
3	-0.01	0.00	0.08	3.08	-0.01	0.00	0.08	3.43 (3.16)
4	0.01	0.00	0.08	3.08	0.01	0.00	0.08	3.44 (3.12)
5	0.00	0.00	0.07	3.10	0.00	0.00	0.06	3.44 (3.18)
6	0.00	0.00	0.07	3.10	0.00	0.00	0.06	3.44 (3.15)
7	0.00	0.00	0.07	3.10	0.00	0.00	0.06	3.44 (3.16)
8	0.00	0.00	0.07	3.10	0.00	0.00	0.06	3.44 (3.13)
9	0.01	0.00	0.08	3.08	0.01	0.00	0.08	3.44 (3.18)
10	-0.01	0.00	0.08	3.08	-0.01	0.00	0.08	3.44 (3.15)
11	0.00	0.02	0.11	3.05	0.00	0.01	0.09	3.43 (3.18)
12	0.00	-0.02	0.11	3.06	0.00	-0.01	0.09	3.43 (3.16)
13	0.00	0.00	0.05	2.70	0.00	0.00	0.03	2.75 (2.61)
				Co_{13} (MT)				
1	0.00	0.02	0.10	2.06	0.00	0.00	0.08	2.42 (2.16)
2	0.00	-0.02	0.10	2.06	0.00	0.00	0.08	2.42 (2.14)
3	0.02	0.00	0.12	2.05	0.01	0.00	0.10	2.42 (2.17)
4	-0.02	0.00	0.12	2.05	-0.01	0.00	0.10	2.42 (2.14)
5	0.00	0.00	0.15	2.05	0.00	0.00	0.12	2.42 (2.17)
6	0.00	0.00	0.15	2.05	0.00	0.00	0.12	2.42 (2.14)
7	0.00	0.00	0.15	2.05	0.00	0.00	0.12	2.42 (2.19)
8	0.00	0.00	0.15	2.05	0.00	0.00	0.12	2.42 (2.16)
9	-0.02	0.00	0.12	2.05	-0.01	0.00	0.10	2.42 (2.19)
10	0.02	0.00	0.12	2.05	0.01	0.00	0.10	2.42 (2.16)
11	0.00	0.02	0.10	2.06	0.00	0.00	0.08	2.42 (2.17)
12	0.00	-0.02	0.10	2.06	0.00	0.00	0.08	2.42 (2.19)
13	0.00	0.00	0.04	1.97	0.00	0.00	0.04	1.96 (1.88)
				Ni_{13} (MT)				
1	0.00	-0.02	0.06	0.66	0.00	0.01	0.07	0.64 (0.68)
2	0.00	0.02	0.06	0.66	0.00	-0.01	0.07	0.64 (0.68)
3	0.00	0.00	0.07	0.70	-0.01	0.00	0.06	0.64 (0.68)
4	0.00	0.00	0.07	0.70	0.01	0.00	0.06	0.64 (0.67)
5	0.00	0.00	0.06	0.70	0.00	0.00	0.05	0.64 (0.68)
6	0.00	0.00	0.06	0.70	0.00	0.00	0.05	0.64 (0.67)
7	0.00	0.00	0.06	0.70	0.00	0.00	0.05	0.64 (0.68)
8	0.00	0.00	0.06	0.70	0.00	0.00	0.05	0.64 (0.68)
9	0.00	0.00	0.07	0.70	0.01	0.00	0.06	0.64 (0.68)
10	0.00	0.00	0.07	0.70	-0.01	0.00	0.07	0.64 (0.68)
11	0.00	-0.02	0.06	0.66	0.00	0.01	0.07	0.64 (0.68)
12	0.00	0.02	0.06	0.66	0.00	0.01	0.07	0.64 (0.68)
13	0.00	0.00	0.02	0.38	0.00	0.00	0.00	0.30 (0.27)

Table 4.4: Anisotropy constants D_n for the perfect and relaxed M_{13} clusters obtained by fitting the GGA results. For the icosahedral symmetry, second- and fourth-order contributions do not depend on θ for any value of $D_{2,4}$. Thus, the related data are omitted. The same holds for the second-order terms in cubic symmetry (MT clusters). In all cases, only the leading order terms are essential and all higher order terms can be neglected. r and s are parameters describing the JT and the Mackay-transformation, respectively. The last column shows the energy differences obtained from the GGA calculations.

Cluster		D_2 (meV)	D_4(meV)	D_6(meV)	$r-1$	$s-1$	ΔE^{DFT} (meV)
Fe_{13} (ICO)	46 μ_B			-0.04	0	0	0.02
Co_{13} (ICO)	31 μ_B			-0.01	0	0	0.004
Ni_{13} (ICO)	8 μ_B			-0.02	0	0	0.01
Fe_{13} (JT)	44 μ_B	15.0			-0.04		4.20
Co_{13} (JT)	31 μ_B	-16.0			0.01		1.90
Ni_{13} (JT)	8 μ_B	44.1			-0.02		8.90
Fe_{13} (MT)	44 μ_B		-11.5			0.07	0.71
Co_{13} (MT)	31 μ_B		-0.4			-0.04	0.02
Ni_{13} (MT)	8 μ_B		-10.1			0.04	0.32

Table 4.5: The orbital and spin moments in μ_B/atom for the binary $M_{13}Pt_n$ clusters. The average cluster magnetic moments are defined by $\langle L_M \rangle = \frac{1}{13}\sum_{i=1}^{13} |\mathbf{L}_{i,M}|$ and $\langle S_M \rangle = \frac{1}{13}\sum_{i=1}^{13} |\mathbf{S}_{i,M}|$ (M denotes the 13-atom Fe, Co and Ni clusters), $\langle L_{Pt} \rangle = \frac{1}{n}\sum_{i=1}^{n} |\mathbf{L}_{i,Pt}|$ and $\langle S_{Pt} \rangle = \frac{1}{n}\sum_{i=1}^{n} |\mathbf{S}_{i,Pt}|$ (the number of Pt atoms n = 3, 4, 5, 20) $|\mathbf{L_{tot}}|$ and $|\mathbf{S_{tot}}|$ are the corresponding absolute values of the total orbital and total spin moment for every cluster.

Cluster	$\langle L_M \rangle$	$\langle L_{Pt} \rangle$	$\langle S_M \rangle$	$\langle S_{Pt} \rangle$	$\lvert\mathbf{L_{tot}}\rvert$	$\lvert\mathbf{S_{tot}}\rvert$
Fe_{13}	0.08		3.05		1.09	39.64
$Fe_{13}Pt_3$	0.09	0.08	2.86	0.36	1.43	38.30
$Fe_{13}Pt_4$	0.10	0.14	2.87	0.32	1.74	38.60
$Fe_{13}Pt_5$	0.08	0.13	2.97	0.53	1.76	41.30
$Fe_{13}Pt_{20}$	0.05	0.17	2.18	0.40	2.74	36.40
Co_{13}	0.12		2.05		1.52	26.60
$Co_{13}Pt_3$	0.10	0.13	1.87	0.42	1.68	25.60
$Co_{13}Pt_5$	0.09	0.16	1.83	0.47	2.06	26.10
$Co_{13}Pt_{20}$	0.07	0.30	1.88	0.60	4.90	36.20
Ni_{13}	0.06		0.66		0.80	8.65
$Ni_{13}Pt_3$	0.06	0.20	0.81	0.40	1.61	11.70
$Ni_{13}Pt_5$	0.05	0.26	0.80	0.51	2.01	13.00
$Ni_{13}Pt_{20}$	0.08	0.20	0.81	0.36	3.55	17.60

5 Structure and magnetism of clusters on Pt surfaces

5.1 Introduction

Metal clusters show electronic structures which change completely with the slight change in the number of atoms in the cluster. Similar size-dependencies have been found in the magnetism of clusters [54, 56, 79]. In order to realize the practical applications of such properties, a prerequisite is to deposit the cluster on a substrate. Due to the interaction with the substrate, it is expected that the cluster may either emerge into the substrate or show a wetting behavior by spreading over it. Such tendencies have been earlier observed experimentally for nanoparticles [210] and thin films [211, 212]. For example, Co nanoparticles ($\approx$ 10 nm diameter) when deposited on Cu(100) and Ag(100) substrates show burrowing effects at 600K [210]. Similar effects have been observed theoretically based on molecular dynamics simulations for Ni clusters on Au substrates, where Ni clusters exchange few of the Au atoms and form the subsurface wetting layers [213].

With change in the morphology, it is evident that clusters deposited on substrate show magnetic properties different from the freestanding clusters and the bulk [178, 181, 214–217]. To study the magnetic properties of deposited clusters, several experimental techniques have been employed, such as X-ray magnetic circular dichroism, Magneto-optic kerr effect or Scanning tunnelling microscopy measurements, where large MAE, orbital moment as well as spin moment for clusters can be obtained [3, 218–221]. XMCD measurements for supported Fe clusters indicate enhanced spin and orbital magnetic moments with respect to bulk Fe [220, 221]. Using scanning tunneling spectroscopy, the size dependence MAE for small Co and Fe clusters on Pt(111) surface have been studied, where for a single Co and Fe atom, the MAEs of 10.25 meV/atom and 6.53 meV/atom are measured, respectively [177]. Theoretically, large spin and orbital moments have been calculated for supported clusters relative to bulk [180–182, 184, 209, 214–217, 222]. Using Kohn-Korringa-Rostoker (KKR) Green's function formalism in the framework of DFT, Šipr *et al.* [215] have studied the size dependence spin and orbital moments for free and supported small Fe and Co clusters on different substrates, where the magnetic moments decrease with increasing cluster size though it is always larger than the respective bulk values. Using the same method, Mavropoulos *et al.* [223] have studied the size dependence of the spin moments of Fe clusters on Ni and Cu substrates, where a linear decrease of spin moments with cluster size is reported due to the increase in the hybridization of *d*-orbitals with the higher coordination of

Fe atoms. Studies based on tight-binding technique [178] for Co clusters on Pd(111) surface have reported large spin and orbital moments as well as MAE for Co clusters where the significant role of substrate behind the enhanced the magnetic properties has been reported. The above theoretical studies have neglected the effect of structural optimization of clusters. It is evident that relaxation effects play an important part in determining the properties of deposited clusters [181, 182, 216]. For example, as a consequence of atomic relaxation, it has been observed that Ni dimers on Cu(001) surface lead to vanishing magnetic moments [216]. For Fe clusters on Pd(001), the relaxation effects lead to reduced magnetic moments for Fe clusters and enhanced induced magnetization on the Pd substrate [182]. Studies of deposited clusters considering the effects of atomic relaxation are still limited.

In the present chapter, we have studied the structural stability and magnetic properties such as spin moments, orbital moments and MAE of closed shell $M_{13,55}$ (M = Fe, Co, Ni) clusters supported on Pt(001) and Pt(111) surfaces considering the effects of structural relaxation of both clusters and substrates. Pt is considered as a substrate due to its large spin-orbit coupling. Though the orbital moment is quenched in 3*d* TM systems, still they are magnetic. Therefore, the combined effect of large spin-orbit coupling strength of Pt and 3*d* TM may give rise novel magnetic properties. This has been observed for free standing Pt-capped Fe_{13} clusters, where a large second order MAE has been obtained [18]. Along with the elemental clusters, the structural and magnetic properties of binary $(Fe\text{-}Pt)_{13,55}$ clusters on Pt(001) and Pt(111) will be discussed.

To deposit the clusters on Pt surfaces, three and four substrate layers are considered for Pt(001) and Pt(111), respectively. The periodic boundary condition is imposed along the directions parallel to the surfaces. The structural relaxation for the cluster/substrate complex is performed using the conjugate gradient algorithm. In order to mimic the bulk behavior, only the bottom layer is kept fixed for Pt(001) and for Pt(111) the bottom two layers are kept fixed. Sufficiently extended surface layer and large vacuum space is created along the perpendicular direction to the substrate to minimize the interaction between the periodic images of cluster. The integration over the Brillouin-zone is performed at the Γ point. The Pt(001) surface is constructed with the experimental value of lattice constant 3.92 Å, while for Pt(111), the equilibrium value of lattice constant 3.99 Å calculated from GGA are taken into account.

5.2 Deposited elemental clusters

5.2.1 Structural stability of M_{13} and M_{55} clusters on Pt(001) and Pt(111)

The perfect icosahedrons [18] with equilibrium center-shell distances 2.39 Å, 2.33 Å and 2.32 Å are considered as the starting geometries for Fe_{13}, Co_{13} and Ni_{13}, respectively for deposition on Pt surfaces. The structural relaxation of M_{13} clusters on Pt(001) surface shows a deformation of icosahedral geometry, where the M_{13} clusters emerge into the Pt(001) substrate by substituting few of the Pt atoms. Fig. 5.1 for instance, illustrates the starting (top panel) and the optimized (bottom panel)

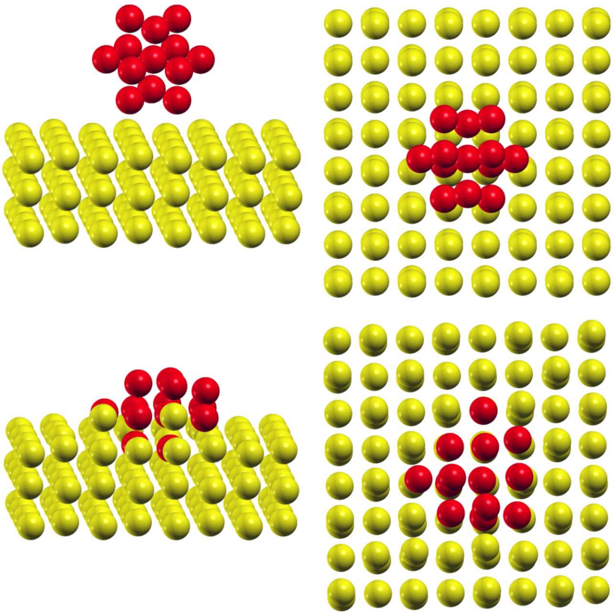

Figure 5.1: The initial and relaxed structures of Co_{13} on Pt(001) surface are shown in the top and bottom panel, respectively with different side views. The red and yellow balls are marked by Co and Pt atoms, respectively. The optimized structure for Co_{13} on Pt(001) shows the substitution of Pt atoms by few Co atoms.

structure of Co_{13} on Pt(001). For the optimized structure, the Co atoms substitute few Pt atoms in the substrate and occupy exactly the lattice sites in the substrate indicating a hint for the surface alloy formation. The reason behind the cluster deformation and emergence of cluster into substrate is be due to the large mismatch of nearest neighbour bond lengths in bulk Pt and the cluster species, which is $\sim$ 28%. The intermixing tendency of M_{13} clusters on Pt(001) substrate is confirmed by molecular dynamics simulations at 300K for supported Fe_{13} and Co_{13}. Experimentally, such tendency has been observed for Fe and Co thin films on Pt surfaces [211, 212, 224]. In addition to Co thin films, Zimmermann *et al.* [210] have observed such effect for supported Co nanoparticles with diameter $\sim$ 10nm, where the Co atoms burrow into the Ag(100) and Cu(100) at finite temperature, which they attribute is due to the large capillary forces on the nanoparticles and the low surface energy of the substrate. With increase in cluster size, for M_{55} on Pt(001), the intermixing tendency persists for Co_{55} and Ni_{55}, while for Fe_{55}, the cluster spreads over the substrate. To see this effect, the optimized structures of Fe_{55} and Co_{55} clusters on Pt(001) are displayed in Fig. 5.2 in the left and right panel, respectively. Like M_{13}/Pt(001), all supported clusters are geometrically deformed.

Deposition of M_{13} and M_{55} clusters on Pt(111) substrate shows structural trends different from those on Pt(001). Due to the closed packing, the clusters on Pt(111) do not show any sign of surface alloying, rather they spread over the surface showing a strong deviation from icosahedron geometry. However, Fe_{13} on Pt(111) does not fall in the same trend. For this system, the icosahedral structure is

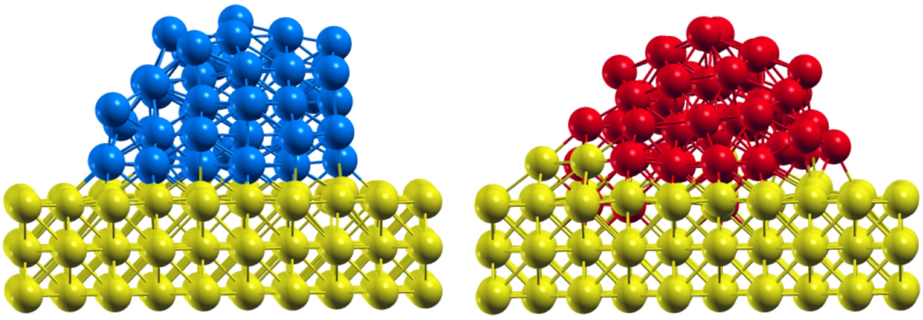

Figure 5.2: Relaxed structures of Fe_{55} (left) and Co_{55} on Pt(001) surface (right). The later case shows the substitution of substrate atoms by few Co atoms. The blue, red and yellow balls are marked as Fe, Co and Pt atoms, respectively.

still preserved.

5.2.2 Spin and orbital moments of deposited elemental clusters

Previous studies have shown a strong dependency of cluster magnetization on the local environment [178]. Due to the change in the number of nearest neighbor bonds and hybridization processes, the magnetic moments of clusters are strongly affected. Similar tendencies are observed in our calculations. The average spin and average orbital moments for M_{13} and M_{55} clusters on different Pt surfaces are reported in Table 5.1. For the sake of comparison, the spin and orbital moments of free clusters and bulk are listed. It is observed that the spin and orbital moments for the deposited clusters are enhanced with respect to the bulk while they are found to be reduced as compared to the corresponding free clusters. Calculations based on KKR formalism report such enhancements with respect to bulk for the spin and orbital moments of small Co clusters on Pt(111) surface [209]. For M_{13}/Pt(001), the reduction of total spin moments can be quantified approximately by 6 μ_B for Fe_{13} and Co_{13} relative to their corresponding free clusters (44 μ_B and 31 μ_B for Fe_{13} and Co_{13}, respectively). For Ni_{13}, such reduction is found to be relatively weak. The reduction of cluster magnetic moments on Pt(001) is due to the substitution of Pt atoms by cluster atoms, which results in strong hybridization among the 3*d* orbitals of cluster atoms and 5*d* orbitals of Pt atoms. On the other hand, M_{13} clusters deposited on Pt(111) exhibit both spin and orbital moments larger than those on Pt(001) surface. Since clusters spread over the Pt(111) surface, the nearest neighbour coordination for the cluster atoms with the substrate are less compared to that of on Pt(001) surface. As a result there is a weak hybridization among the cluster and Pt substrate. Therefore both spin and orbital magnetic moments are enhanced on Pt(111). This can also be marked from the electronic density of states (DOS) plotted in Fig. 5.3, which shows a comparison of the DOS for both free and deposited M_{13} clusters. This shows that clusters supported on Pt(111) surface have highly localized peaks with the exchange splitting at the Fermi level in both spin channels, while for clusters on Pt(001), as a consequence of

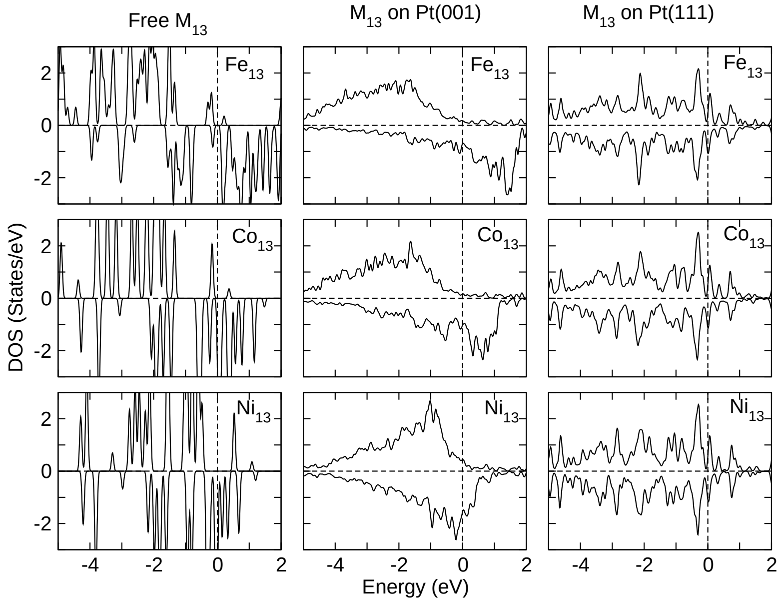

Figure 5.3: Left: The DOS of free standing M_{13} clusters. Middle and right panel indicates DOS of M_{13} clusters on Pt(001) and Pt(111) surfaces. The vertical dashed line indicates the Fermi level fixed at zero.

strong hybridization with Pt, the broadened peaks show the exchange splitting only in the minority spin channel at the Fermi level. With increase in cluster size, i.e., for deposited M_{55} clusters, the spin and orbital moment does not show any significant change for both surfaces of Pt, in spite of the fact that the relaxation patterns are different, which is due to the fact that with increasing number of atoms in the cluster, the number of nearest-neighbour bonds between the cluster and substrate in the interface decreases. Thus the clusters almost retain the magnetic moments like the corresponding free ones. The deposition of clusters leads to some induced magnetic moments on Pt surfaces.

Table 5.1: The average spin moment per atom $\langle S\rangle = \frac{1}{N}\sum_{i=1}^{N}|\mathbf{S}_i|$ (where N = 13, 55)and average orbital moment per atom $\langle L\rangle = \frac{1}{N}\sum_{i=1}^{N}|\mathbf{L}_i|$ for deposited $M_{(13,55)}$ clusters in μ_B/atom, compared to that of the corresponding unsupported clusters and for bulk bcc Fe, fcc Co and Ni as obtained from our calculations.

Cluster	$\langle S\rangle_{M/Pt(001)}$	$\langle S\rangle_{M/Pt(111)}$	$\langle\lvert\mathbf{S}\rvert\rangle_{free}$	$\langle\lvert\mathbf{S}\rvert\rangle_{bulk}$	$\langle L\rangle_{M/Pt(001)}$	$\langle L\rangle_{M/Pt(111)}$	$\langle\lvert\mathbf{L}\rvert\rangle_{free}$	$\langle\lvert\mathbf{L}\rvert\rangle_{bulk}$
Fe_{13}	2.88	2.74	3.05	2.25	0.07	0.08	0.08	0.06
Co_{13}	1.81	3.18	2.05	1.67	0.08	0.12	0.12	0.08
Ni_{13}	0.62	0.64	0.66	0.65	0.06	0.07	0.06	0.05
Fe_{55}	2.72	2.62	2.65	2.25	0.07	0.08	0.08	0.06
Co_{55}	1.78	1.75	1.87	1.67	0.09	0.10	0.10	0.08
Ni_{55}	0.63	0.62	0.74	0.65	0.06	0.06	0.09	0.05

In addition to spin and orbital moments, the magnetic anisotropy is calculated for the optimized

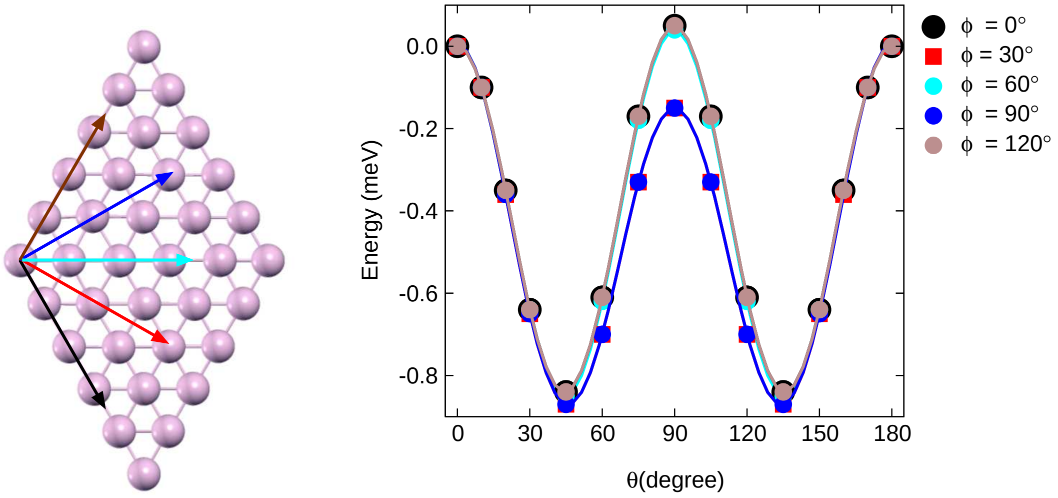

Figure 5.4: Left: Monolayer of Ni(111), where the colored arrows indicate the different ϕ values. Right: The θ-dependent MAE for the corresponding ϕ values for Ni(111) surface.

structure of Fe_{13} on Pt(111). In order to check the correct variation of total energy according to the symmetry of the surface, a single layer of Ni(111) surface is considered and the magnetization direction is varied in terms of θ for several values of ϕ as shown in the left panel of Fig 5.4. According to the symmetry of the surface, the energy as a function of θ should show similar qualitative and quantitative trends for $\phi = 0^\circ, 60^\circ, 120^\circ$. Also the θ-dependent energies for $\phi = 30^\circ$ should match with $\phi = 90^\circ$. Similar trends are obtained form the present calculations as illustrated in the right panel of Fig 5.4. The θ-dependent energies for different ϕ values show a fourth order contribution to the anisotropy.

The θ-dependent energy differences is studied for the relaxed structure of Fe_{13} on Pt(111) (shown in the left panel of Fig. 5.5). The total energy as a function of θ for the several ϕ values ($\phi = 0^\circ, 30^\circ, 60^\circ, 90^\circ, 120^\circ$) are plotted in the right panel of Fig. 5.5. It must be noted that the energy difference plotted in Fig. 5.5 is scaled with respect to the corresponding energy at $\theta = 0^\circ$. As a consequence of atomic relaxation, there is lowering of symmetry. This leads to a large second order anisotropy for such system. The MAE is defined as the energy difference between the maximum and the minimum total energy obtained from various θ at particular ϕ. The MAE for $\phi = 0^\circ$ is observed to be approximately 165 times larger than the MAE of bulk Fe with bcc structure (1.4 μeV/atom) [43]. The enhanced MAE for deposited Fe_{13} clusters relative to bulk indicates the role of structural relaxation effects. The dominant role of atomic relaxation on the magnetic anisotropy has been previously reported for Fe films [225] and clusters [226] supported on Pt surfaces.

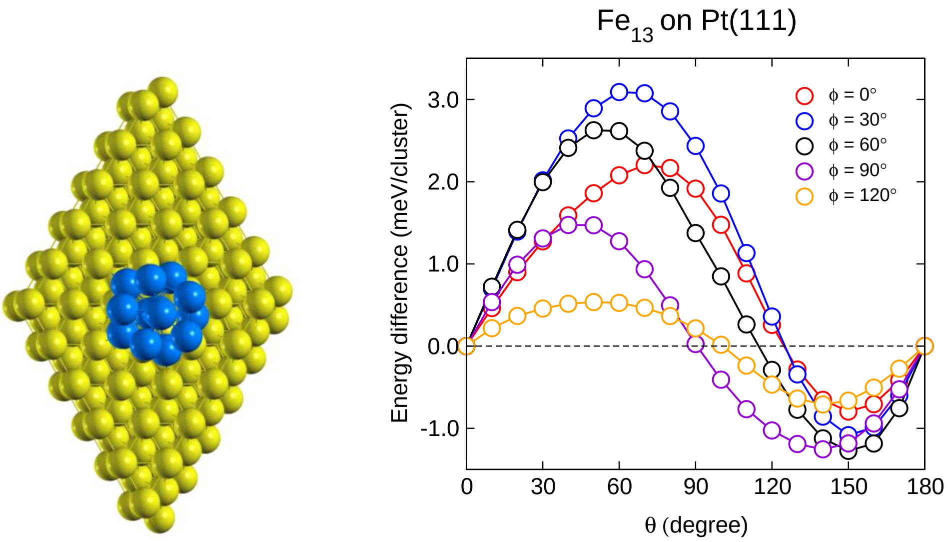

Figure 5.5: Left: Optimized structure of Fe_{13} on Pt(111). The blue and yellow balls are Fe and Pt atoms, respectively. Right: The MAE as a function of θ for relaxed Fe_{13} on Pt(111) surface.

5.3 Deposited binary clusters: $L1_0$ $(FePt)_{55}$ on Pt surfaces

One of the most discussed materials for magnetic data storage devices is a near-stoichiometric $L1_0$ Fe-Pt phase, where the Fe and Pt atoms are stacked alternatingly in [001] direction. Similar layered arrangement in Fe-Pt nanoparticles is envisaged as medium for high-density magnetic data storage devices, which are also observed to be thermodynamically stable [17]. The magnetic anisotropy constant for the $L1_0$ Fe-Pt nanoparticles is an order larger in magnitude than that of the materials being used in present day technology (bulk) [227]. As a result it is easier to overcome the super-paramagnetic limit which posses a lower bound limit for the particle sizes above which the magnetization of a grain can withstand the thermal relaxation processes for relatively longer time. This has however not been achieved experimentally [228] and it is understood that other morphologies of Fe-Pt nanoparticles at similar sizes also occur which do not posses hard magnetic properties as discussed for Fe-Pt $L1_0$ nanoparticles. Few theoretical studies regarding the growth and stability of free and supported Fe-Pt $L1_0$ nanoparticles exist in the literature [229]. This chapter discusses the morphological stability and magnetic properties of binary $L1_0$ cuboctahedral and the corresponding icosahedral Fe-Pt clusters (generated by the Mackay transformation, explained in chapter 6) supported on (001) and (111) surfaces of Pt. The $L1_0$ ordered cuboctahedron has an alternate layered stacking of two atomic species (Fe and Pt, in the present case) in the (001) direction, illustrated in the right panel of Fig. 5.6. Since theoretical studies on $L1_0$ free Fe-Pt clusters show a cuboctahedral geometry with Pt terminating layers to be more stable relative to the Fe terminating compositions [230], we have considered the $L1_0$ structure with terminating Pt layers. In order to construct a 55-atom perfect $L1_0$ Fe-Pt cluster with Pt-

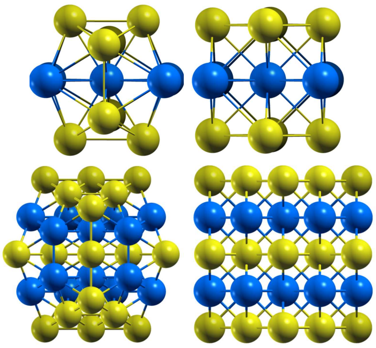

Figure 5.6: The Fe_5Pt_8 (upper panel) and $Fe_{24}Pt_{31}$ (bottom panel) clusters. For both cluster sizes, the icosahedron and $L1_0$ cuboctahedron geometries are shown in the left and right panels, respectively. Blue balls: Fe and Yellow balls: Pt.

terminating layers, the structure should have 24 Fe atoms and 31 Pt atoms. For instance, Fig. 5.6 shows the layered structures for 13- and 55-atom Fe-Pt clusters with the corresponding icosahedrons. The equilibrium geometries for free standing 13-, 55- atom icosahedron and $L1_0$ cuboctahedron are found to show slight structural deformations with respect to their regular clusters. For both cluster sizes, the distorted icosahedral Fe-Pt is energetically more preferable relative to the distorted $L1_0$ cuboctahedral structure. This is in agreement with previous theoretical studies [230], where the Fe-Pt clusters upto 561 atoms ($\sim$ 2.5 nm size range) show enhanced stability for ordered or core shell icosahedral structures compared to $L1_0$ ordered cuboctahedrons. A ferromagnetic ordering of magnetic moments is preferred for both geometries. With increasing cluster size, previous theoretical calculation [230] suggest the existence of layered antiferromagnetic-like ordering which mimics the magnetic behavior in bulk $L1_0$ Fe-Pt. When the 13- and 55-atom Fe-Pt clusters (illustrated in Fig. 5.6) are deposited on Pt(001) and Pt(111) surfaces, after relaxation, the equilibrium geometries for deposited clusters are found to be all deformed relative to the their regular geometries. Neither of the icosahedral nor the cuboctahedral morphology are found to be stable on both Pt surfaces. They show wetting tendencies by spreading over the Pt surfaces. The energetics for the supported as well as free clusters are reported in Table 5.2. It is observed that the cluster with a starting geometry as icosahedron shows enhanced stability for both deposited and free Fe-Pt clusters. However, Fe_5Pt_8/Pt(001) is an exception to such trend, where the cluster with a starting geometry as a cuboctahedron shows the higher stability.

Table 5.2: The energetics for the deposited and free Fe-$Pt_{13,55}$ clusters. $\Delta E : E_{\mathrm{ico}} - E_{\mathrm{cubo}}$: The energy difference between ico and cubo.

	Pt(001)		Pt(111)		Free cluster	
	ΔE (eV/atom)	Stable	ΔE (eV/atom)	Stable	ΔE (eV/atom)	Stable
Fe_5Pt_8	0.005	$L1_0$	-0.005	ICO	-0.04	ICO
$Fe_{24}Pt_{32}$	-0.031	ICO	-0.006	ICO	-0.05	ICO

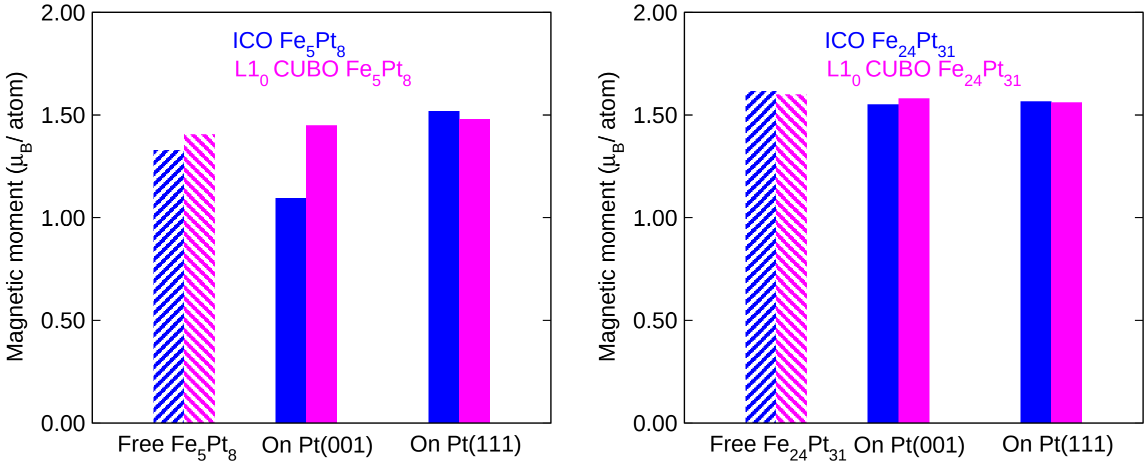

Figure 5.7: The magnetic moments for free and deposited Fe_5Pt_8 and $Fe_{24}Pt_{31}$ in the left and right panel, respectively. The hatched histograms for both clusters represent the magnetic moments for free clusters and the solid histograms show the moments on deposited clusters. The blue and magenta denote the moments for the icosahedral and $L1_0$ cuboctahedral clusters.

Table 5.3: The magnetic moments for Fe_5Pt_8 and $Fe_{24}Pt_{31}$. μ_{Fe} and μ_{Pt} are the magnetic moments in units of μ_B/atom for Fe and Pt sites. μ_{Total} is the total magnetic moment for cluster and substrate.

Cluster	μ_{Fe}	μ_{Pt}	μ_{Total}
Fe_5Pt_8 ico	3.05	0.284	18.0
Fe_5Pt_8 ico on Pt(001)	2.48	0.200	19.0
Fe_5Pt_8 ico on Pt(111)	3.21	0.323	15.0
Fe_5Pt_8 $L1_0$ cubo	3.08	0.351	19.3
Fe_5Pt_8 $L1_0$ cubo on Pt(001)	3.22	0.323	30.3
Fe_5Pt_8 $L1_0$ cubo on Pt(111)	3.23	0.375	13.0
$Fe_{24}Pt_{31}$ ico	3.08	0.46	93.0
$Fe_{24}Pt_{31}$ ico on Pt(001)	3.08	0.37	98.0
$Fe_{24}Pt_{31}$ ico on Pt(111)	3.10	0.38	109.0
$Fe_{24}Pt_{31}$ $L1_0$ cubo	3.07	0.45	92.0
$Fe_{24}Pt_{31}$ $L1_0$ cubo on Pt(001)	3.09	0.41	101.0
$Fe_{24}Pt_{31}$ $L1_0$ cubo on Pt(111)	3.08	0.39	119.0

Figure 5.7 shows a comparison of the average magnetic moments (μ_B/atom) for free and deposited Fe_8Pt_5 (left panel), and $Fe_{24}Pt_{31}$ (right panel). It is observed that the average magnetic moment of icosahedral Fe_8Pt_5 cluster shows a large fluctuation depending on the type of Pt surfaces. The icosahedral Fe_8Pt_5 on Pt(001) has a lower average magnetic moment compared to the free cluster as well as that of the cluster deposited on Pt(111). On the other hand, the average magnetic moment for de-

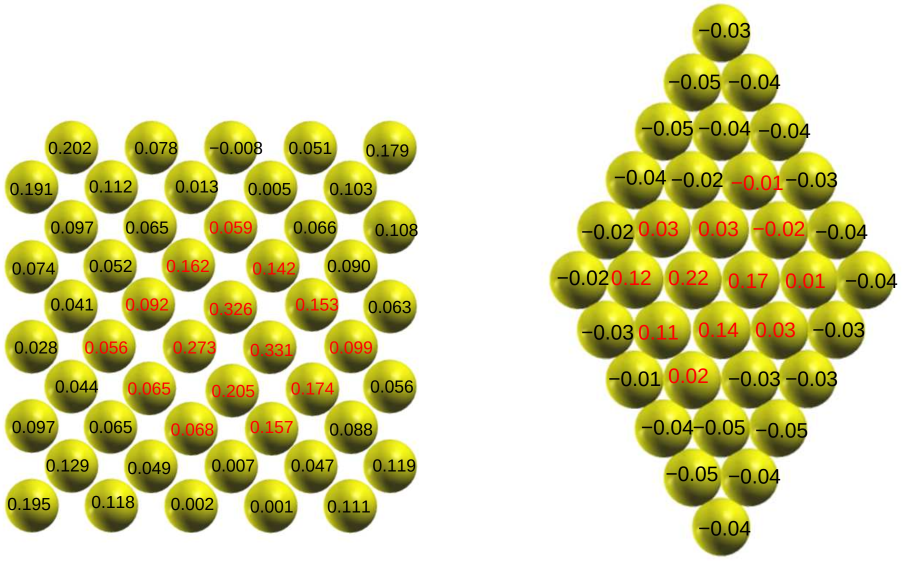

Figure 5.8: The induced magnetic moments on Pt(001) and Pt(111) surfaces in the left and right panel, respectively. The moments are shown for the layer close to the cluster (here, $L1_0$ Fe_5Pt_8 cuboctahedron). The red colored numbers are the magnetic moment of substrate atoms which are directly bonded to the cluster.

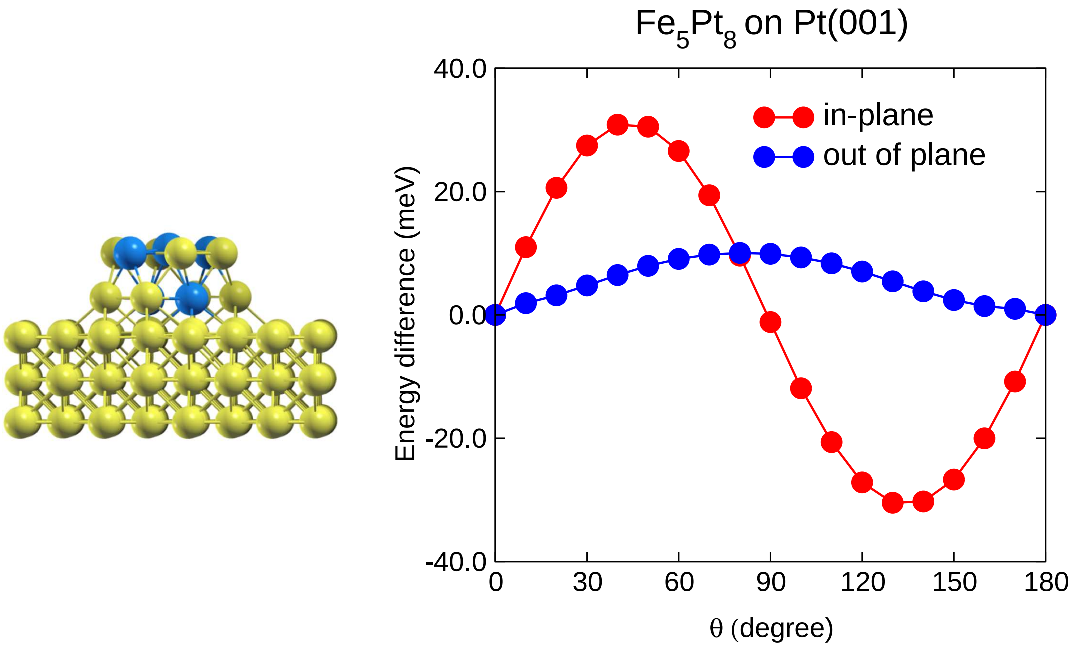

Figure 5.9: Left: Relaxed Fe_5Pt_8 cluster on Pt(001) surface. Blue and yellow balls represent the Fe and Pt atoms, respectively. Right: The in-plane (red circles) and out of plane (blue circles) magnetic anisotropies for relaxed Fe_5Pt_8 on Pt(001) surface.

posited L1_0 Fe_8Pt_5 cluster on Pt surfaces remains almost unchanged with respect to the corresponding unsupported ones. With increasing cluster size (right panel of Fig. 5.7), the average magnetic moment remains nearly constant with respect to the corresponding free clusters irrespective of the type of Pt surfaces. In Table 5.3, the average magnetic moments on Fe (μ_{Fe}) and Pt (μ_{Pt}) atoms of the deposited clusters along with the total magnetic moment of cluster/substrate complex are listed. As a consequence of cluster-substrate interaction and the intermixing of Fe 3*d* and Pt 5*d* orbitals, μ_{Fe} for deposited clusters is enhanced with respect to the μ_{Fe} of free ones. However, icosahedral Fe_8Pt_5 is an exception to the such behavior, where both μ_{Fe} and μ_{Fe} decrease compared to that of free cluster. Such behavior is reflected with the decreasing average moment for the same cluster on Pt(001), as shown in the left panel of Fig. 5.7. Due to the presence of Fe atoms, some magnetic moment is induced on the Pt surfaces, shown in Fig. 5.8. The Pt layer close to the cluster exhibits larger induced magnetization compared to other layers. The induced moments on the Pt layer close to the cluster are depicted in Figure 5.8 for Pt(001) and Pt(111) surface in the left and right panel, respectively. Especially, the Pt atoms bonded with cluster atoms show large magnetic magnetic moments shown as red digits in Fig. 5.8. Figure 5.9 (left panel) shows the relaxed structure of Fe_5Pt_8 on Pt(001) for which we have calculated the angle-dependent energies (right panel). The angle θ is varied in the $z-x$ (out of plane) and $x-y$ plane (in-plane). Due to the structural deformation, the symmetry is lowered, as a result a second order contribution to the anisotropy is obtained. The MAE is defined as the energy difference between the maximum and the minimum total energy obtained from various θ. The in-pane MAE is found to be larger ($\sim$ 58 meV/atom) compared to the out of plane anisotropy ($\sim$ 10 meV/atom). The reason behind obtaining a large in-plane MAE is the lower symmetry of the cluster/substrate complex arising due to the effect of structrual relaxation and the large spin-orbit coupling of Pt substrate.

6 Transition metal clusters on graphene

6.1 Introduction

Graphene, a one-atom thick carbon layer arranged in a honeycomb lattice, is one of the most prominent materials to be studied as substrate due to high surface area, inertness [231], and high conductivity [232, 233]. It is a zero-band gap semiconductor with a linear dispersion at the Fermi level. Figure 6.1 shows the band structure of graphene obtained from the tight-binding calculations, where the Dirac points are found at the symmetry points of the Brillouin zone [234]. Because of its two dimensional confinement with a point-like Fermi surface and a linear dispersion at the Fermi level, it is a suitable material for studying anomalous quantum Hall effects and ballistic transport [235].

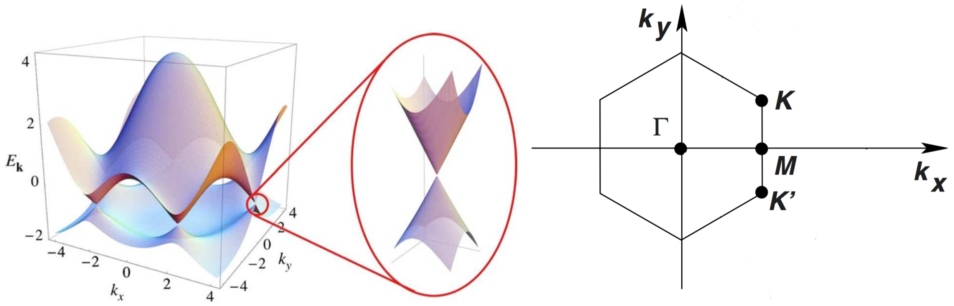

Figure 6.1: Band dispersions of graphene (left panel) showing the Dirac points (the zoom in part) at K and K$'$ of the Brillouin zone in the right panel. Figure is taken from Ref. [250].

Graphene-supported transition metal catalysis has drawn much attention [20, 21]. Experimentally, Yoo *et al.* have observed very high catalytic activity of small Pt clusters for CO oxidation while supported on graphene. Similar observation is confirmed theoretically by Zhou and Yamamoto *et al.* [236, 237]. However, the origin of such high catalytic reactivity is still to be solved. Theoretical calculations by Lu *et al.* [122] predicts high catalytic activity for Au-embedded graphene for the CO oxidation reaction, which they attribute due to the partially occupied *d* orbital localized in the vicinity of the Fermi level because of the interaction between the Au atom with graphene. Theoretically, using DFT, Li *et al.* [238] have found good catalytic activity for CO oxidation reaction on Fe-embedded graphene. Using different carbon supports, experimentally, the changes in the chemical activity for clusters of Ni [239], Co [240], Pt [241–245], Pd [246], and Rh [247] have been studied. Theoretically, DFT calculations have been performed to investigate the catalytic activity for small clusters on graphene. For example, Duca *et al.* [248] have studied the stability and electronic properties of Pd clusters adsorbed on graphene. Okamoto *et al.* [249] have studied the stability and catalytic activity of Pt_{13} and Au_{13} clusters on graphene sheet and flakes. From the above studies, it is evident that graphene can act as an attractive support as compared to the traditional supports.

The present chapter deals with the studies of the geometric, magnetic and electronic properties of Fe, Co, Ni and Pt clusters consisting of 13-atoms adsorbed on two types of graphene supports, namely the defect-free (pristine) graphene and five-membered ring graphene flake. In addition, the catalytic activity of free-standing and graphene supported clusters are studied by the adsorption of CO molecule on the surface of clusters.

6.2 Computational details

Our calculations are based on DFT within PBE exchange correlation functional [251]. The projector augmented wave method is used for the treatment of core electrons [27]. The TM clusters are adsorbed on a pristine (defect free) and a five-member ring graphene flake. For the pristine (defect free) graphene sheet, a (6×4) supercell consisting of 96 atoms have been used. The periodic boundary condition is applied along the graphene plane. A (3×3×1) k-mesh is used for the integration over the Brillouin zone. While, for the five member ring graphene flake which is a hydrocarbon cluster: $C_{45}H_{15}$, the integration over Brillouin zone are performed at the Γ point only. A large supercell of size (23×23×15) Å^3 has been used, which sufficiently minimizes the interaction between the cluster with the periodic image. For constructing the substrate, a calculated C-C bond length of 1.427 Å has been used which is close to the experimental value of 1.42 Å. The structural relaxations of the cluster-substrate complex are performed using the conjugate gradient method. The self-consistent calculations are performed with a convergence criterion of 10^{-6} eV. In order to check the binding strength between the cluster and graphene, the adsorption energy (E_{ads}) is calculated, which is defined in the following.

$$E_{ads}^{cluster} = E_{tot}(cluster) + E_{tot}(graphene) - E_{tot}(cluster + graphene) \tag{6.1}$$

where, $E_{tot}(cluster)$ is the total energy of metal cluster. $E_{tot}(graphene)$: The total energy of graphene. $E_{tot}(cluster + graphene)$: The total energy of cluster on graphene.

6.3 Clusters on defect free graphene sheet

The icosahedral clusters of M_{13} (M = Fe, Co, Ni and Pt) are adsorbed on the on the hollow site of the pristine graphene sheet where the center atom of the cluster lies over the middle of the hollow site with one the triangular facets of the cluster being oriented parallel to the graphene surface. The equilibrium geometries of M_{13} clusters on graphene results in distorted icosahedral clusters from their corresponding regular geometry. This is marked from the deviation of average bond lengths for the deposited clusters as compared to the free standing ones, shown in Table 6.1. The adsorption energies (E_{ads}) for these deposited clusters are presented in Table 6.2. It is observed that the E_{ads} for Co_{13} on graphene has a larger value compared to that of Fe_{13} and Ni_{13} indicating a strong binding strength for Co_{13} with graphene. Previous studies based on DFT have shown a similar tendency for dimers of Fe, Co and Ni, where Co dimer on graphene shows larger E_{ads} compared to that of Fe and Ni dimers on graphene [252].

Table 6.3 shows a comparison of the magnetic moments for the deposited clusters with respect to the corresponding free ones. It is observed that the deposited M_{13} clusters have reduced total magnetic moments as compared to their corresponding free clusters. For instance, the total moment for deposited Fe_{13} on graphene decreases by 8 μ_B compared to that of the free Fe_{13} cluster (44 μ_B). For Co_{13}, the decrease in total moment is even more($\sim$ 10 μ_B). On the other hand for Ni_{13}, the moment is slightly enhanced unlike Fe_{13} or Co_{13}. This can be seen from Fig. 6.4, which shows the electronic density of states of deposited M_{13} clusters. For Ni_{13}/graphene, the large exchange splitting in the spin-down channel near the Fermi level explains this fact. For graphene supported TM dimers, previous studies report different trend of magnetic moments where, the Fe, Co or Ni dimers on graphene posses total moments comparable to the free dimers [252], which is not observed for 13-atom clusters. This may be due to the fact that with increase in cluster size, there is an increase in the coordination numbers for each atom as a consequence the total magnetic moment is reduced.

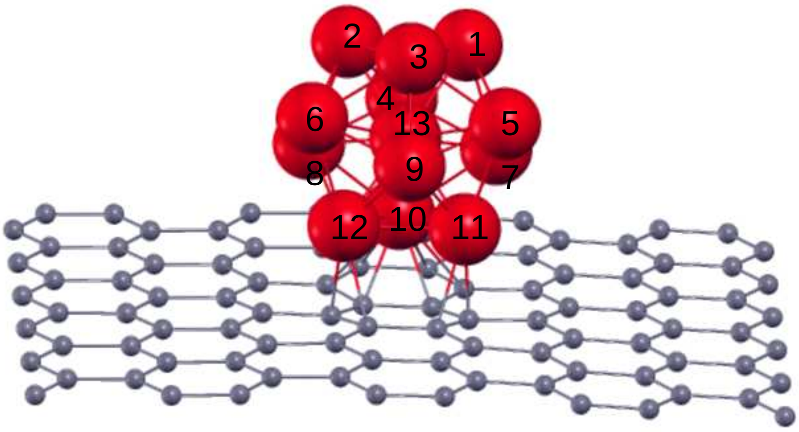

Figure 6.2: Relaxed structure of Co_{13} (with labeling of atoms) on defect free graphene sheet. The red and black balls denote the Co and C atoms, respectively.

The onsite spin moments for M_{13} clusters are listed in Table 6.4, which shows that, the cluster atoms bonded with graphene (indices 10, 11 and 12 shown in Fig. 6.2) show reduced moments relative to the other atoms (indices 1-9 in Fig. 6.2). The reduction of magnetic moments on TM atoms is counterbalanced by the slight induced magnetization on graphene. This can be quantified as 0.23 μ_B for

Fe_{13}/graphene, 0.12 μ_B for Co_{13}/graphene and 0.05 μ_B for Ni_{13}/graphene. Such induced magnetization on C atoms for graphene supported TM has been observed theoretically [252]. The carbon atoms bonded with cluster atoms show more induced moments compared to the those away from clusters.

Table 6.1: The average bond lengths in Å for M_{13} and Pt_{13} clusters on pristine and five-member ring graphene.

Bond length	Fe_{13}	Co_{13}	Ni_{13}	Pt_{13}(ico)	Pt_{13}(layered)
Free Cluster	2.48	2.42	2.41	2.63	2.57
On pristine	2.49	2.42	2.43	2.72	2.65
On five member	2.49	2.41	2.42	2.64	2.65

Figure 6.4 (top left panel) shows the total electronic density of states (DOS) for pure graphene and M_{13} clusters on graphene (top right and the bottom panel). The DOS shows a non magnetic behavior of pure graphene. When M_{13} clusters are deposited on it, as a consequence of induced magnetization on C-atoms, the Fermi level for the graphene supported clusters shows a shift towards the conduction band. For all cases the Fermi level shows the exchange splittings in the minority spin channel, which indicates the half-metallic behavior of graphene. Theoretically, such a trend has been observed for the adsorption of Fe and Co adatoms on graphene [252].

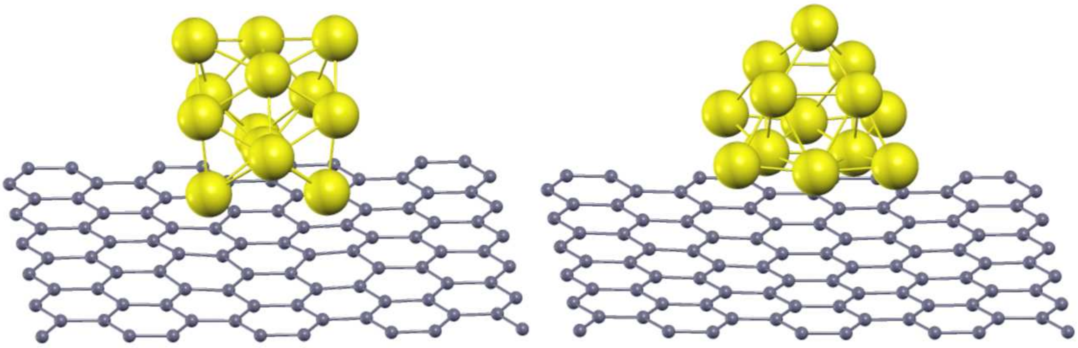

Figure 6.3: The optimized geometry of deposited layered Pt_{13} (left) and distorted icosahedral Pt_{13} (right) on pristine graphene. Yellow and black balls are marked by Pt and C atoms respectively.

Since previous studies on free standing Pt_{13} shows an enhanced stability for a layered-like geometry [253–255] relative to the icosahedral one, thus along with the icosahedron, a layered-like Pt_{13} clusters is adsorbed on graphene. Our calculations on free Pt_{13} clusters suggests that the layered structure is energetically lowered by approximately 3 eV with respect to the icosahedral structure. This is more or less in agreement with Ref. [253], where the authors have reported an energy difference of more than 1 eV between the icosahedron and the layered structure. Due to such a large energy difference between the icosahedral and the layered structure of Pt_{13}, the optimized structure of Pt_{13} with the starting geometry as icosahedron is found to be not stable on graphene as shown in the left panel of Fig. 6.3. Our results are not in good agreement with Previous calculations, where it was reported that the optimized geometry of Pt_{13} is a slightly distorted icosahedron on graphene [249]. The reason behind such a discrepancy might be related to the initial height of cluster from the substrate. On the other hand, the layered morphology of Pt_{13} on graphene is found to be preserved, which is shown in Fig. 6.4, right panel. As a consequence of structural deformation of Pt_{13} with icosahedron as the starting structure, a large value of E_{ads} is found (5.42 eV) as compared to that of the layered Pt_{13} on graphene (2.11 eV).

Table 6.2: Adsorption energy of M_{13} clusters on pristine and five-member ring graphene.

Clusters	Pristine	Five-member
Fe_{13}	1.86	2.47
Co_{13}	2.78	3.24
Ni_{13}	2.33	3.05
Pt_{13}(ico)	5.42	5.16
Pt_{13}(layered)	2.11	2.17

Table 6.3: The magnetic moments of clusters on pristine and five member ring graphene.

Clusters	μ_{Pristine}	$\mu_{\text{Five member}}$	$\mu_{\text{Cluster+Pristine}}$	$\mu_{\text{Cluster+five member}}$	$\mu_{\text{Free cluster}}$
Fe_{13}	36.0	34.33	36.00	36.0	44.0
Co_{13}	22.0	23.00	21.00	23.0	31.0
Ni_{13}	9.0	9.30	8.50	9.1	8.0
Pt_{13}(ico)	1.68	0.88	1.83	1.0	2.1
Pt_{13}(layered)	2.00	0.92	2.27	1.0	2.0

6.4 Clusters on five-member ring graphene

It has been observed earlier that for graphene-supported TM clusters, presence of a defect in graphene substrate enhances the adsorption energy of cluster. For example, calculations based on DFT by Okamoto *et al.* show large adsorption energies for Pt and Au clusters adsorbed on a defective graphene sheet as compared to that of on a pristine graphene sheet [249]. Therefore, in the present calculation, to study the effect of C vacancy on the structural stability and magnetic properties of clusters the TM clusters are adsorbed on a five-member ring graphene flake, which is expressed as a hydrocarbon cluster: $C_{45}H_{15}$. Such topological disorders are quite well-known in graphene sheets [256]. The relaxed structures of M_{13} clusters on five-member ring graphene are shown in Fig. 6.5. As observed for TM clusters on pristine graphene, the adsorption of M_{13} clusters on five-member graphene results in distorted structures with respect to their regular geometries. The average bond lengths for the de-

Table 6.4: The atomic magnetic moments for M_{13} clusters on pristine graphene. The labeling of atoms are illustrated in Fig. 6.2. Atom index 13 is the center atom and 10, 11, 12 metal atoms are bonded with the C atoms, which show reduced moments compared to the rest ones.

Atomic sites	Fe_{13}	Co_{13}	Ni_{13}	Pt_{13}
1	2.84	1.79	0.81	0.17
2	2.85	1.79	0.81	0.18
3	2.85	1.79	0.81	0.29
4	2.95	1.83	0.76	0.22
5	2.94	1.77	0.74	0.12
6	2.95	1.77	0.73	0.12
7	2.98	1.80	0.72	0.08
8	2.98	1.80	0.72	0.08
9	2.92	1.79	0.72	0.23
10	2.26	0.87	0.34	0.04
11	2.59	1.44	0.37	0.08
12	2.59	1.44	0.37	0.08
13	2.22	1.41	0.57	0.00

posited clusters are listed in Table 6.1. With the cluster deformation, different bending tendencies of the substrate is observed. For supported Fe_{13}, the five-membered ring graphene flake shows a bending towards the cluster for Fe_{13}/graphene, while it bends oppositely for supported Co_{13} and Ni_{13}. The different bending behavior of the five-membered ring graphene is found to be very sensitive towards the starting structures of M_{13} clusters. For all three clusters, as starting structures the perfect icosahedral clusters with the center to shell distances of 2.39 Å (Fe_{13}), 2.33 Å (Co_{13}) and 2.32 Å (Ni_{13}), respectively are considered, which are the minimum energy center-shell distances [18]. A slight variation in the center-shell distance results in different bending tendencies. The bending trend is also found to be dependent on the morphology of cluster. This can be understood from the Pt_{13}/graphene system, where the graphene substrate for Pt_{13} with a layer structure as the starting geometry bends towards the cluster, while Pt_{13} with the starting structure as icosahedron, graphene shows an opposite bending behavior. The adsorption energies of M_{13} and Pt_{13} clusters on five-member graphene sheet are listed in Table 6.2. Comparing the adsorption energies for clusters on defected graphene with the clusters on defect free graphene, it is observed that clusters on a defected graphene flake are more stable relative the clusters adsorbed on a pristine one.

Table 6.3 (fifth column) shows the total magnetic moment for supported clusters on five-member ring graphene are tabulated. Like clusters on Pristine graphene sheet, an almost same quantitative reduction of magnetic moment is observed for clusters on five-member ring graphene. The Co_{13} and Ni_{13} clusters on five-member ring graphene show slightly enhanced values of magnetic moments on five-member ring graphene compared to those on pristine graphene. The reason may be due to the weak hybridization between the d-orbitals of cluster and π-orbitals of C for the cluster-graphene

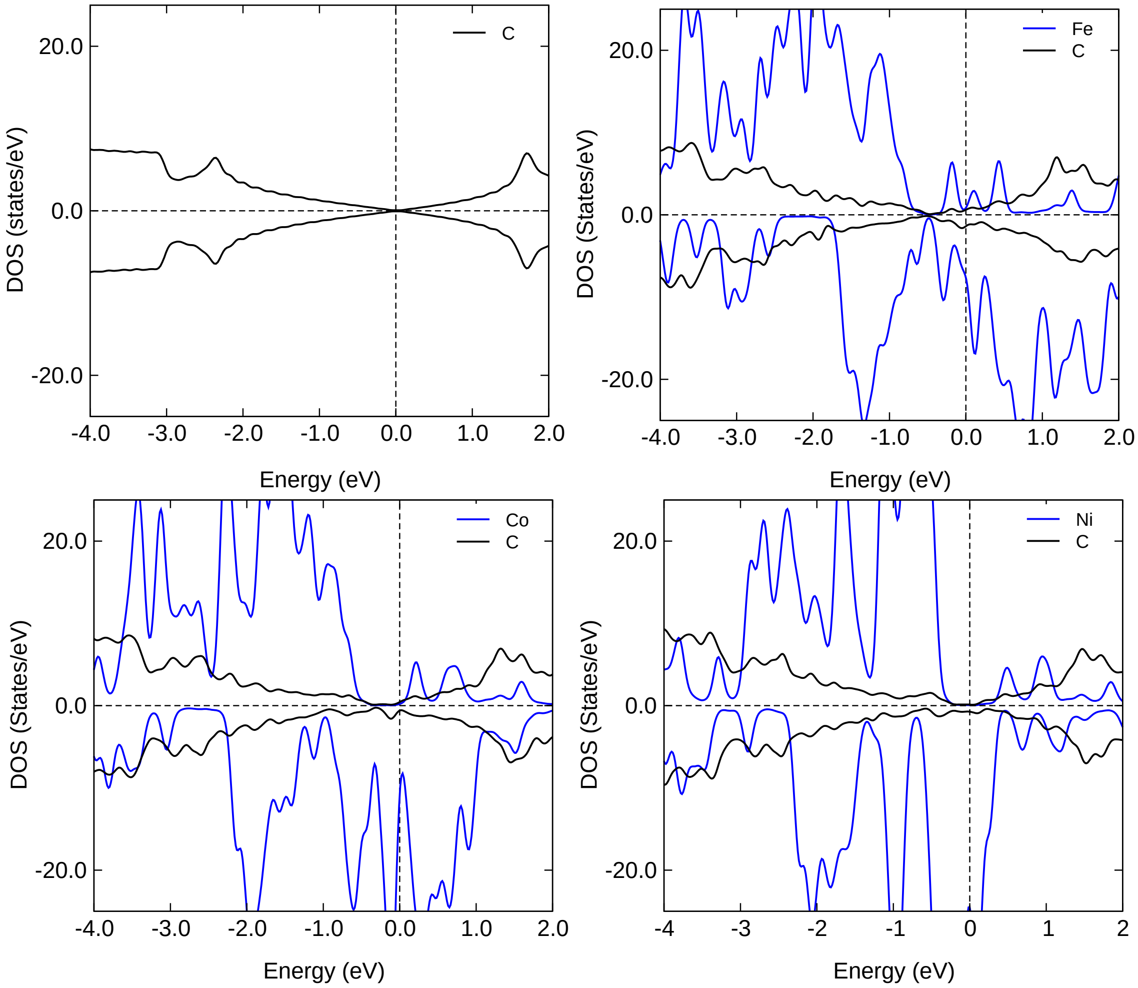

Figure 6.4: The site projected electronic density of states for pristine graphene and deposited M_{13} clusters on pristine graphene. A Gaussian broadening parameter $\sigma = 0.05$ eV has been used to calculate the DOS. The Fermi level is shifted to zero for each case. (a) Pristine graphene, (b) Fe_{13} on graphene, (c) Co_{13} on graphene, (d) Ni_{13} on graphene.

system. On the other hand, for Fe_{13} on five-member graphene, due to the bending of five-member ring graphene towards the cluster leads to a decrease of total moment form 23 μ_B (Fe_{13} on pristine graphene) to 21 μ_B (Fe_{13} on defected graphene). The metal atoms close to graphene have a reduced moment and some amount of magnetic moment is induced to the substrate (mainly C atoms close to cluster) for Fe_{13} and Co_{13}. A different situation appears for adsorption of Ni_{13} on graphene. Here, like the case of Ni_{13} on defect free graphene, there is no change in total moment of the cluster relative to the free ones. As a result, there is no induced magnetization on C atoms of the substrate. Such a behavior is due to the weak hybridization between the Ni *d*-orbitals and the C π-orbitals.

In addition to 13 atom clusters, the deposition of larger icosahedral clusters consisting of 55 atoms are also deposited on five-membered ring graphene. For the deposition of M_{55} clusters, the five member

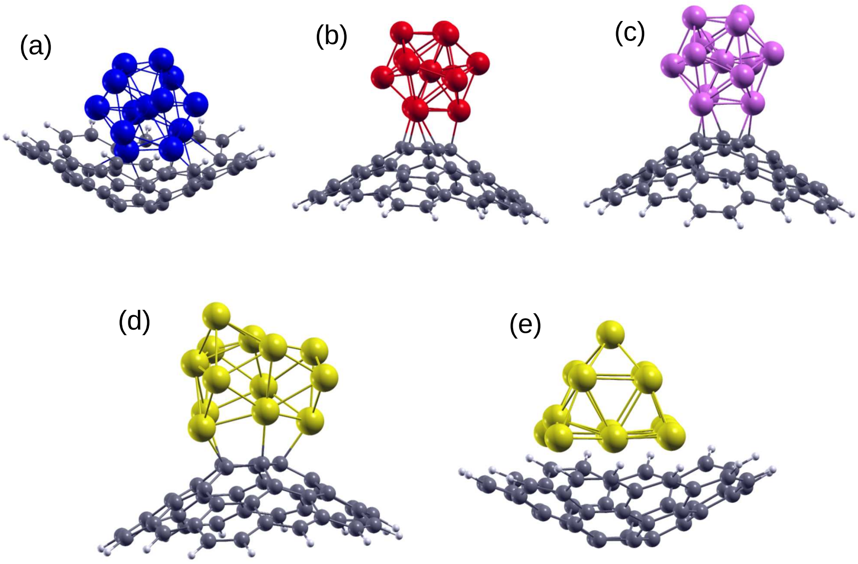

Figure 6.5: Optimized structures of 13-atom clusters on five-member ring graphene. Blue: Fe, red: Co, magenta: Ni, yellow: Pt, black: C and white: H

ring graphene consists of 80 C atoms and 20 H atoms. Unlike the M_{13} clusters, the deposited M_{55} clusters show same bending tendencies of five-membered ring graphene, where the defected graphene always shows a bending towards the cluster. Unlike deposited M_{13} clusters, the magnetic moments of adsorbed M_{55} clusters almost retain the magnetic moments like the corresponding free clusters.

6.5 CO adsorption on clusters deposited on five member ring graphene

Nanoclusters exhibit unique active sites like facets, vertices or edges, which can show varying catalytic activities [257]. Therefore a proper understanding of favorable adsorption sites of CO molecule on clusters is essential. In order to study the role of carbon support on catalytic activity of 13 atom clusters, we have adsorbed the CO molecule on clusters deposited on five-member ring graphene. As a substrate, the five-member graphene is chosen because we obtain large adsorption energy for M_{13} clusters compared to that of the clusters on pristine graphene. The CO molecule is adsorbed on several sites of the clusters. For instance, the most probable adsorption sites of CO molecule on an icosahedron are: On the middle of a triangular face (facet), middle of a bond (edge) and on the top of an atom (vertex). Among these possibilities, we have looked for the suitable adsorption site of CO for each cluster. Figure 6.6 shows the optimized structures with favorable adsorption sites of CO on free and graphene supported clusters. It is found that due to the adsorption of CO, the free clusters are distorted from the ideal structure. However, for Pt_{13}, the icosahedral geometry is no more preserved. It might be due to the fact that the ground state of Pt_{13} is a layered-like [253]

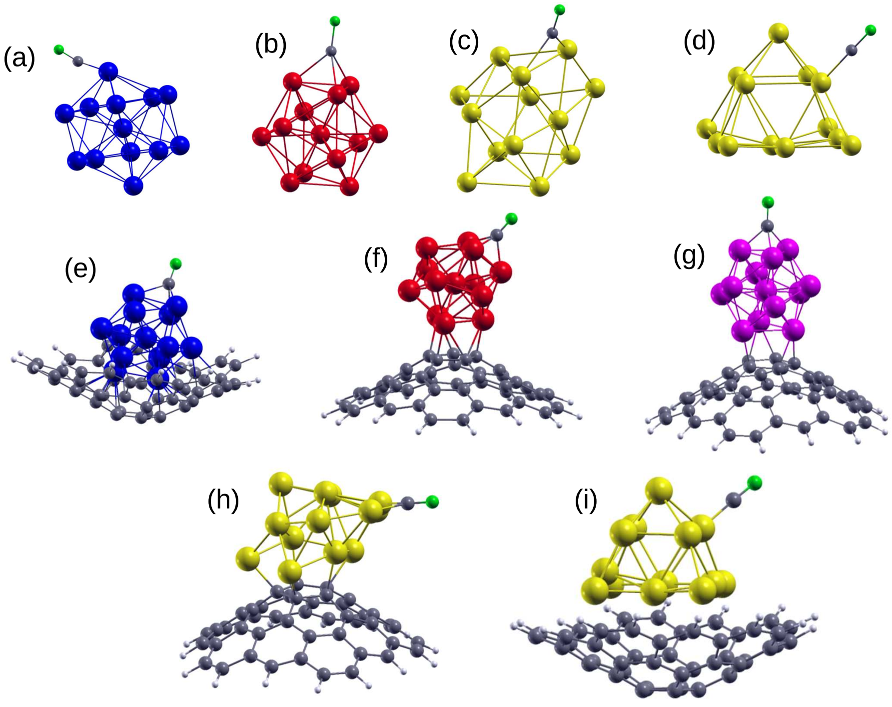

Figure 6.6: The favorable adsorption sites for CO on metal clusters without and with the five-member graphene flake. Blue: Fe, red: Co, magenta: Ni, yellow: Pt, black: C, white: H, green: O.

Table 6.5: Adsorption energy of CO on Fe_{13}, Co_{13}, Ni_{13} and Pt_{13} clusters with and without five-member ring graphene.

Clusters	with graphene	without graphene
Fe_{13}	2.26	1.75
Co_{13}	2.09	2.23
Ni_{13}	2.27	2.20
$Pt_{13}(ico)$	2.82	5.49
$Pt_{13}(layered)$	2.48	2.19

structure instead of an icosahedron. The favorable adsorption site of CO on Fe_{13} and layered Pt_{13} are found to be the vertices, whereas For Co_{13} and Ni_{13} CO preferably adsorbs on the facets. For Pt_{13} (starting structure as icosahedron), the edge is the stable adsorption site. Our findings for Pt_{13} cluster is consistent with the DFT calculations (through hybrid functional B3LYP) for Pt_{10} and Pt_{11} clusters by Monteiro *etal*. [258]. On the other hand, for Fe and Co clusters, the same authors have predicted the edge and the top positions as the preferential adsorption sites of CO for Fe_{11} and Co_{10} clusters. The difference in adsorption sites for Fe and Co clusters compared to ours may be related to the different exchange-correlations functionals (LDA and BPW91) and basis sets.

Adsorbing these clusters on graphene flake does not change the adsorption sites except for Fe_{13}+graphene+CO, where CO prefers to be adsorbed on the facet. In the presence of graphene, the strong interaction between the cluster and substrate and the distortion of cluster, the CO is adsorbed on the facet instead of the vertex of the cluster as found for free Fe_{13}. The adsorption energies for the free clusters with and without graphene are listed in Table 6.5. This suggests that CO is strongly adsorbed on the metal clusters in the presence of five member ring graphene with a large adsorption energy. The enhanced adsorption energy indicates a high reactivity of metal clusters in the presence of graphene leading to enhanced catalytic activity for reactions such as CO oxidation or CO_2 dissociation, which is beyond the scope of this thesis.

6.6 CO oxidation on pristine graphene

It has been observed that presence of graphene decreases the energy barrier for the CO oxidation reactions on Pt clusters [236]. The authors have reported the energy vs. reaction coordinate curves and few transition states, which are shown in Fig. 6.7. This motivates us to study the CO oxidation on pristine graphene, where we have studied the Langmuir-Hinselwood type reaction followed by (CO + O_2 –> CO_2 + O). The transition states for the catalytic reaction are determined by using the nudged elastic band method [22], where the total energies of the intermediate states along the reaction path connecting the initial (reactant) and final (product) states are simultaneously minimized in constraint of atomic motions restricted only along the hyperplane perpendicular to the reaction path. More about the method is described in Refs [22, 23].

As reactant, both CO and O_2 molecules are adsorbed on graphene in the hexagonal hollow site, where the CO molecule is adsorbed such that C-O bond (bond length = 1.14 Å) is perpendicular to the substrate and O_2 molecule with bond length 1.26 Åis coadsorbed (aligned parallel). The product is characterized by the free CO_2 molecule and a single oxygen atom adsorbed on the substrate at the favorable site of hexagonal hollow. We have taken four intermediatory states between the reactant and the product, which is as a first approximation, is a linear interpolation from the reactant and the product coordinates at equal intervals. It may be stated that the reaction path observed in nature could be different than the first approximation we have used. In fact, a through study of different reaction path would eventually lead to a reaction path which can be directly compared with the real reactions. This can be achieved by identifying the reaction path with the minimum activation barrier. In the present study however, we are concerned with the methods used to study reaction. For instance, Eichler *et al.* [23] have studied the CO oxidation on Pt(111) surface through a variety of reaction paths and reported their activation barriers. Fig. 6.8 (data taken from stated reference) shows the energy profile with respect to the reaction coordinates along the reaction path (shown in schematics) for the CO oxidation with reaction path having the minimum activation barrier.

Fig. 6.9 shows the calculated energy profile along the reaction coordinates for the CO oxidation and the initial state, transition state and final state. The reaction coordinates are given by the distance between carbon atom of CO molecule and the oxygen of O_2 molecule, which are kept fixed during the reaction. From our calculation, the activation energy barrier is calculated to be 1.19 eV, which is relatively larger as compared to the CO oxidation on graphene in presence of Pt cluster [236]. This shows that Pt clusters help in reducing the activation barrier of CO reaction, which will be the next step in this direction of research.

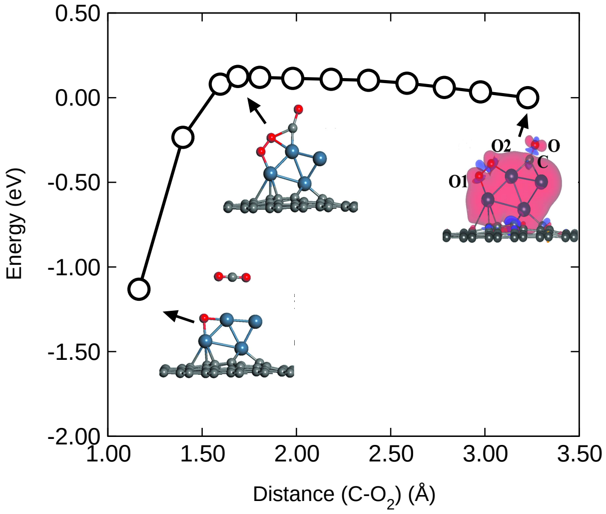

Figure 6.7: The energy profile as a function of reaction coordinates for the CO oxidation on graphene supported Pt cluster. The reaction coordinate is taken as the distance between the carbon atom of CO and the nearest oxygen atom of the O_2 molecule. The green, black and red balls represent the Pt, C and O atoms, respectively. Figure is adopted from Ref. [236].

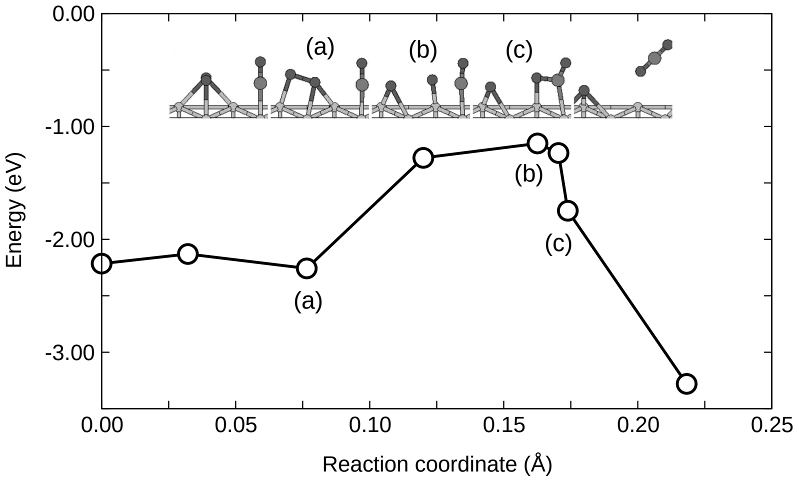

Figure 6.8: The energy profile as a function of reaction coordinate for Langmuir-Hinselwood type CO oxidation reaction on Pt(111) surface. The optimized states along the reaction path are also shown. (a-c) represent the transition states. The black and gray balls are marked by C and O atoms, respectively. The figure is adopted from Ref. [23].

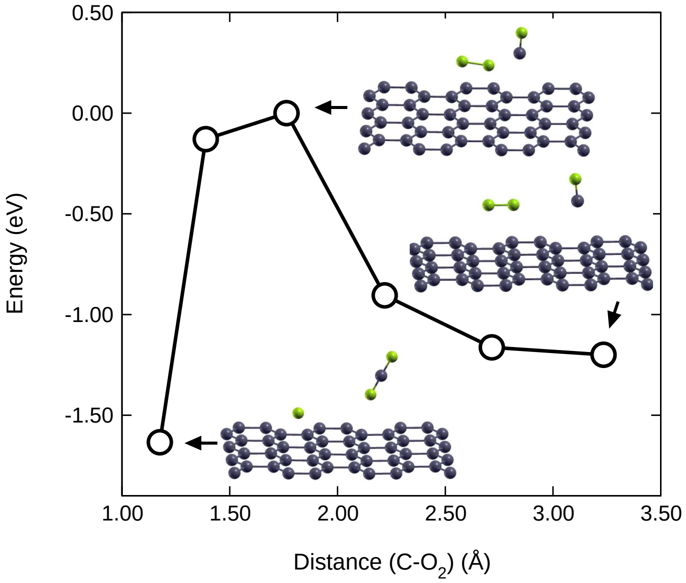

Figure 6.9: The energy profile as a function of reaction coordinate for the Langmuir-Hinselwood type CO oxidation on a defect free graphene. The reaction coordinates are taken as the distance between the carbon atom of CO and the nearest oxygen atom of the O_2 molecule. Black and green balls represent the C and O atoms, respectively.

7 Exact diagonalization and thermodynamics of clusters

7.1 Introduction

In the previous, the ground state properties of TM clusters are exclusively discussed using DFT, which is based on variational principle, i.e., a system has a lower bound in energy, known as the ground state energy, which can be obtained by minimizing the total energy of a system. However, such a treatment completely barrs from estimating any properties at non-zero temperature. Thermodynamics of some of the exactly solvable models are already well established [259]. In this chapter, the nearest-neighbour Heisenberg spin model is adopted to study the magnetic and thermodynamic properties of finite systems through exact diagonalization technique [31]. Besides the exact diagonalization method, several other techniques such as the density matrix renormalization group [260], cluster expansions [261], spin-wave expansions [262–264] and quantum Monte Carlo techniques [265–267], which can be used to study the magnetic systems. However, some of these techniques have limitations, for instance quantum Monte Carlo technique has limitations in describing the systems with geometric frustration. In this regard, exact diagonalization method has the advantage, where it is possible to obtain all energy levels with their spectroscopic classification (useful for the electron paramagnetic resonance or nuclear magnetic resonance spectra).

It is well known that frustration in low dimensional magnetic systems leads to many nontrivial features, like plateaus and jumps in magnetization with the variation of external magnetic field and occurrence of low-lying singlets [30, 268–277] in the energy spectra. For example, through exact diagonalization of the antiferromagnetic Heisenberg model, Konstantinidis *et al.* [268] have calculated the ground state magnetization for a dodecahedron and icosahedron symmetry for $s = \frac{1}{2}$ and 1, where they have found discontinuity in the field-dependent magnetization and double peaks in the temperature-dependent specific heat arising due to the frustrations. The same authors have applied the full diagonalization technique to a series of clusters with size ranging from 24 to 32, where they have shown the effect of frustration and connectivity on the low lying energy spectrum. For a 28-site cluster, they obtain the most pronounced plateaus in the field-dependent magnetization compared to other cluster sizes [278]. Using perturbation theory, Coffey *et al.* [269] have studied the effect of frustration and connectivity on the magnetic properties of a 60-site cluster [279]. Schnalle *et al.* [270] have applied an approximation of diagonalization scheme to a cuboctahedron for $s = 1$ and $\frac{3}{2}$ in order to obtain the energy spectra. In addition to ground state magnetic properties, several studies also exist for the thermodynamical properties. Honecker *et al.* [280] have computed several magneto-thermal properties such as the magnetic susceptibility, specific heat and magnetic cooling rate for a cuboctahedron with different spin quantum numbers using the antiferromagnetic Heisenberg model, where they have observed significant deviations from the classical behavior for the corresponding properties of the cuboctahedron with $s \leq 5$. Studies on the effect of dipolar interaction and radial anisotropy on properties of nano clusters is still limited [238, 281, 282]. In the present chapter, the exact diagonalization method is applied to small clusters consisting of 13 and 4-atoms with spin-$\frac{1}{2}$ and 1 and a systematic study of the magnetic and thermodynamic properties has been performed. The main focus is showing the effect of dipolar interaction and uniaxial anisotropy on the magnetization behavior in the presence of magnetic field. The ground state and the temperature-dependent spin-spin correlation functions are also calculated for these clusters.

7.2 Theoretical method

The Heisenberg spin Hamiltonian for a set of nearest neighbour interacting spins $\boldsymbol{s}_i$ has the following form,

$$H = -\sum_{i<j} J_{ij} \boldsymbol{s}_i \cdot \boldsymbol{s}_j, \tag{7.1}$$

where, the sum is over all pairs. $\boldsymbol{s}_i$ is the spin operator on site i having total spin s and $s_i^z = -s, -s+1, \ldots, s$; J_{ij} is the exchange coupling. For a ferromagnetic and antiferromagnetic interaction, $J_{ij} > 0$ and $J_{ij} < 0$, respectively. Though, for one dimensional nearest-neighbour couplings $J_{ij} = J$, the Heisenberg model has been solved analytically by means of the Bethe-Ansatz [283], for higher dimensions, other approximation methods are highly required. However, for small spin systems, the problem is solved by employing the exact diagonalization technique [284]. In order to study the model Hamiltonian numerically (defined in Eq. 7.1), the straightforward way is to obtain the matrix elements of H in a basis of $|s_1^z, s_2^z, \ldots, s_n^z\rangle$, with the z-axis taken as quantization direction, where n is the total number of spins in the system, and then diagonalize the Hamiltonian matrix. For instance, for the $s = \frac{1}{2}$ Heisenberg model, we can construct the basis states,

$$\begin{aligned}
|1\rangle &= |\uparrow\uparrow \ldots \uparrow\uparrow\rangle, \\
|2\rangle &= |\uparrow\uparrow \ldots \uparrow\downarrow\rangle, \\
|3\rangle &= |\uparrow\uparrow \ldots \downarrow\uparrow\rangle, \\
&\vdots \\
|2^n\rangle &= |\downarrow\downarrow \ldots \downarrow\downarrow\rangle,
\end{aligned}$$

where ↑ and ↓ represents $s_i^z = \frac{1}{2}$ and -$\frac{1}{2}$ state, respectively. In terms of these basis states, the dimension of the Hamiltonian matrix will be $2^n \times 2^n$. For $s = 1$ systems, s^z has three basis states (-1, 0, 1) leading to the dimension of Hamiltonian matrix $3^n \times 3^n$. In general for a spin system of size n, the number of basis states to represent the Hilbert space is $(2s+1)^n$. Therefore, with increase of the system size, the dimension of the matrix grows exponentially and becomes intractable. There are conserved quantities corresponding to the symmetry of the systems. In such cases, the basis states with different eigenvalues of the symmetry operators do not mix together on the application of Hamiltonian on the basis. Then, the Hamiltonian matrix can be expressed as a direct product of several small matrices. It has been observed that the Heisenberg Hamiltonian commutes with the square of the total spin of the system $\boldsymbol{S}^2$ and the z component of the total spin S^z. Though it is straightforward to work in an S^z subspace, there is no efficient method to construct symmetry adopted eigenstates of $\boldsymbol{S}^2$. In addition, the Hamiltonian is symmetric under combination of permutation of spins that respect the connectivity of the small size cluster considered in the present case. Furthermore, the model also possesses time reversal symmetry in the absence of external magnetic field. While the symmetries of the system is taken into account, S^z basis states can be projected into states that transform under specific irreducible representation of the symmetry group. In this way, the Hamiltonian is block diagonalized into small matrices and the maximum dimension is dramatically reduced compared to full Hilbert space size.

In the presence of an external magnetic field the Heisenberg Hamiltonian is modified to the following form,

$$H = -\sum_{i<j} J_{ij}\,\boldsymbol{s}_i \cdot \boldsymbol{s}_j - B^z S^z, \tag{7.2}$$

where B^z is the external magnetic field along z-direction, and $S^z = \sum_i s_i^z$ is the z-component of the total spin. The value of S^z can vary from $-S$ to $+S$ in unit steps, with S being the maximum total spin of the system. Note that B^z measures the field energy, i.e., the factor μ_{B} is absorbed into B^z. In the presence of a magnetic field, the time reversal symmetry is broken, as a result, the eigenvalues of the Hamiltonian within the positive S^z sector and negative S^z sector will be different. However, one can obtain the eigenvalues of the system in the presence of magnetic field directly from the eigenvalues of the pure Heisenberg model for $B^z = 0$, Eq. (7.1), by shifting the eigenvalues by $B^z S^z$, as S^z commutes with H.

Now the Hamiltonian matrix is constructed in terms of eigenstates of the total S^z operator by expressing the Hamiltonian in the form

$$\mathcal{H} = -\sum_{i<j} J_{ij}\left[\frac{1}{2}\left(s_i^+ s_j^- + s_i^- s_j^+\right) + s_i^z s_j^z\right] - B^z S^z, \tag{7.3}$$

where $s_i^{\pm} = s_i^x \pm i s_i^y$ are the raising and lowering operators. When s_i^+ and s_i^- operates on the eigenstates of s_i^z, we have

$$s_i^{\pm}|s_i^z\rangle = \sqrt{s(s+1) - s_i^z(s_i^z \pm 1)}\,|s_i^z \pm 1\rangle. \tag{7.4}$$

For example, for a spin-$\frac{1}{2}$ particle,

$$\begin{aligned}
s_i^+|\uparrow_i\rangle &= 0, \\
s_i^+|\downarrow_i\rangle &= |\uparrow_i\rangle, \\
s_i^-|\uparrow_i\rangle &= |\downarrow_i\rangle, \\
s_i^-|\downarrow_i\rangle &= 0,
\end{aligned}$$

and for a spin-1 particle,

$$\begin{aligned}
s_i^+|\uparrow_i\rangle &= 0, \\
s_i^+|0_i\rangle &= \sqrt{2}|\uparrow_i\rangle, \\
s_i^+|\downarrow_i\rangle &= \sqrt{2}|0_i\rangle, \\
s_i^-|\uparrow_i\rangle &= \sqrt{2}|0_i\rangle, \\
s_i^-|0_i\rangle &= \sqrt{2}|\downarrow_i\rangle, \\
s_i^-|\downarrow_i\rangle &= 0,
\end{aligned}$$

where in the latter case $\downarrow, 0, \uparrow$ denote the three possible values of $s_i^z = -1, 0, 1$. We have adopted the block diagonalization procedure in order to obtain the eigenvalue spectra of 13- and 4-atom clusters, where the total Hamiltonian matrix is written in terms of smaller matrices with the zero off diagonal elements. For instance, in case of a 13-atom cluster with $s = \frac{1}{2}$, the dimension of the Hamiltonian matrix is $2^{13} \times 2^{13}$. Because of the block diagonalization, the whole matrix is divided into blocks with dimension $\binom{13}{k} \times \binom{13}{k}$, with $k = 0, \ldots, 13$. 14 such block matrices have to be solved and the largest block matrix has $\binom{13}{6} = 1716$ rows. In addition, the effect of uniaxial anisotropy for 13- and 4-atom clusters with $s = 1$ has been studied, as the anisotropy does not have any contribution for $s = \frac{1}{2}$. For a spin-1 system, the total Hamiltonian in the presence of local uniaxial anisotropy axes $\boldsymbol{e}_i$ can be written as

$$H = -\sum_{i<j} J_{ij}\boldsymbol{s}_i \cdot \boldsymbol{s}_j - B^z S^z - \sum_i D_i\,(\boldsymbol{e_i} \cdot \boldsymbol{s_i})^2, \tag{7.5}$$

where D_i are the local uniaxial anisotropy constants and $\boldsymbol{e_i}$ are the easy axes compatible with the symmetry of the system [18]. The results obtained for 13- and 4-atom clusters are discussed in the following sections.

7.3 13-atom clusters with spin-$\frac{1}{2}$

In order to study the properties of 13-atom clusters, we have considered two geometries: The icosahedron (ICO) and the cuboctahedron (CUBO). Both geometries are shown in Fig. 7.1. The ICO having a connectivity like fullerene [285, 286], exhibits 12 vertices, 20 triangular facets and 30 edges with a symmetry group I_h. The CUBO has 12 vertices with 8 triangular and 6 square faces, 24 edges, which belongs to a symmetry group O_h. In spite of same number of vertices (12), both geometries exhibit different number of nearest neighbors, i.e., the ICO and CUBO posses 5 and 4 nearest neighbors, respectively.

The total Hamiltonian for a 13-atom cluster has the following form

$$H = -J \sum_{\substack{i,j>0 \\ \langle ij \rangle}} \boldsymbol{s}_i \cdot \boldsymbol{s}_j - J' \sum_{i>0} \boldsymbol{s}_0 \cdot \boldsymbol{s}_i - B^z \sum_i s_i^z, \tag{7.6}$$

where $\boldsymbol{s}_0$ is the spin of the center atom, and the first sum runs over nearest-neighbor pairs $\langle ij \rangle$ in the surface shell. J is the exchange coupling between atoms in the surface shell and J' is the exchange coupling between central and surface spins.

The Hamiltonian matrix of dimension 8192×8192 has to be diagonalized for 13-atom spin-$\frac{1}{2}$ cluster. Because of symmetries of the system, the Hamiltonian matrix is divided into 14 sub-matrices with block diagonalization dimensions $\binom{13}{k}$ with $k = 0, 1, \ldots, 6$ for the positive and negative S^z sectors. The block diagonalization of the total Hamiltonian matrix leads to the eigenvalues of the system. The ground state energy is obtained by taking the minimum of the energy eigenvalues from each magnetization sector. We have obtained the energies for four different exchange couplings defined by (i) all spins ferromagnetic ($J = J' = 1$); (ii) all spins antiferromagnetic ($J = J' = -1$); (iii) central spin is reversed with respect to the ferromagnetic surface spins ($J = 1$ and $J' = -1$), (iv) antiferromagnetic surface spins with ferromagnetic central spin ($J = -1$ and $J' = 1$). Note that all energies are measured in units of $|J|$, where $|J|$ is fixed to the one.

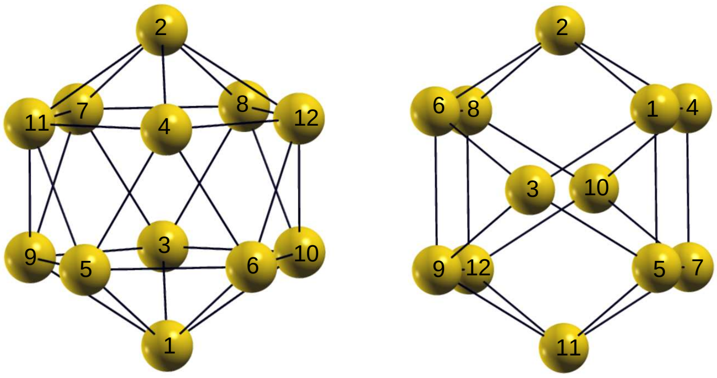

Figure 7.1: Skematic picture of 13-atom ICO (left) and CUBO (right) with labeling of each atomic site. Both structures have 12 vertices with one atom at center. The center atom for both cases are not shown here.

The minimum energies for AFM case of 13-atom clusters (ICO and CUBO) corresponding to each S^z sector are listed in Tab. 7.1, which suggests a two-fold degeneracy for AFM case i.e., the minimum energy for each positive S^z sector has similar value like that of the corresponding negative S^z sector.

Table 7.1: Low energy eigenvalues in the units of $\mid J \mid$ and the corresponding S^z for 13-atom ICO and CUBO for AFM interaction.

S^z	Energy (ICO)	Energy (CUBO)
6.5	10.5000	9.0000
5.5	4.0000	2.5000
4.5	0.8819	0.0000
3.5	-1.8342	-2.5000
2.5	-3.9669	-4.6313
1.5	-5.4198	-5.8687
0.5	-6.2880	-6.0622

Figure 7.2 illustrates the complete eigenvalue spectrum for the FM and AFM interactions of ICO (top panel) and CUBO (bottom panel). The ground state energies are marked in red. For the FM interaction, the degenerate minimum energies are obtained, which is due to the fact that the Hamiltonian has spin rotational invariance, as a result, turning the total spin in another direction, does not change the energy. For the AFM interaction, the minimum energies are found to be nondegenerate for each S^z sector and the energy gaps are different between the consecutive S^z sectors for both ICO and CUBO geometries (see Table 7.1,

The variation of magnetization as a function of external magnetic field for the four cases of interactions of the ICO are shown in the left panel of Fig. 7.3. It is observed that for the AFM case ($J = J' = -1$), the presence of external magnetic field leads to the appearance of plateaus, marked by solid curve in Fig. 7.3, left panel. This occurs due to the inequivalent energy gaps between the consecutive S^z sectors. On the other hand, for the FM case with $J = J' = 1$, only a single energy minimum state exists at $S^z = 6.5$, due to the degeneracy of the ground state energy (see the dashed curve in Fig. 7.3). The right panel of Fig. 7.3 illustrates the variation of magnetization as a function of magnetic field for the four interactions of the CUBO geometry. As observed in the case of ICO, we obtain a similar behavior for the variation of magnetization with respect to magnetic field for the FM interaction. However, for the AFM interactions of CUBO, the plateaus appearing in the magnetization have different sizes compared to the ICO, which can be marked from the solid curve in the right panel of Fig. 7.3. This occurs as the consequence of structural symmetries. Figure 7.4 illustrates the variation of the minimum energy (in units of $|J|$) as a function of magnetic field for each S^z for the AFM and FM interactions of ICO (left panel) and CUBO (right panel). The inequivalent energy gaps at several B^z values for the ICO and CUBO clearly shows the reason behind the different plateaus sizes for the AFM. On the other hand due to the degenerate energies for each S^z sector, all energies meet at one point for FM interaction at zero external magnetic field B^z.

The influence of dipolar interaction on the magnetization of 13-atom ICO with $s = 1/2$ has been studied in the presence of a magnetic field. The dipole-dipole coupling is useful in the studies of molecular structures as it depends only on known physical constants and the inverse cube of interatomic distance.

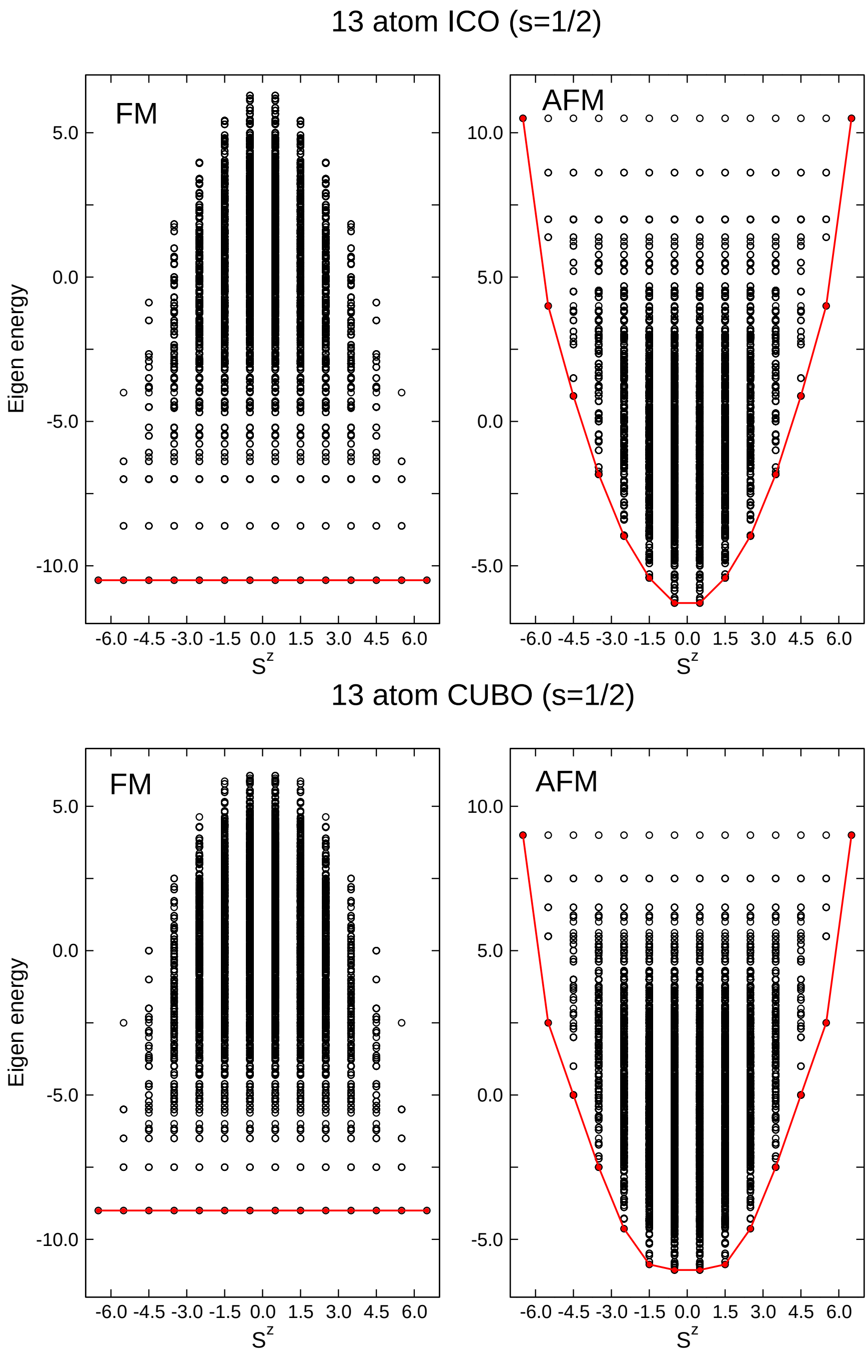

Figure 7.2: All eigenvalues (N= 8192) for FM and AFM interactions of ICO (top two columns) and CUBO (bottom two columns) with spin-$\frac{1}{2}$. The solid line is a guide to eye, which indicates the minimum eigenenergies. For AFM interaction, there exists a $\pm S^z$ degeneracy for both symmetries.

The dipolar coupling Hamiltonian can be expressed through the following form,

$$H_{\text{dipole}} = \omega \sum_{i<j} \frac{\boldsymbol{s}_i \cdot \boldsymbol{s}_j - 3(\boldsymbol{s}_i \cdot \hat{\boldsymbol{r}}_{ij})(\hat{\boldsymbol{r}}_{ij} \cdot \boldsymbol{s}_j)}{|\boldsymbol{r}_{ij}|^3}, \tag{7.7}$$

where $\hat{\boldsymbol{r}}_{ij} = \boldsymbol{r}_{ij}/|\boldsymbol{r}_{ij}|$ is the unit vector along the line joining the two spins, and $\omega = g^2\mu_B^2\mu_0/4\pi$ is the dipolar coupling strength, measured in units of $|J|$. Figure 7.5 shows the variation of magnetization as a function of the magnetic field for several dipolar interaction strengths with ω = 0, 0.025, 0.05 and 0.1 for the AFM case (we have set the shell radius to one).

For ω = 0, a reversed central spin $\boldsymbol{s}_0$ with negative hysteresis is observed, as for $B^z/|J'| \leq 6.5$ the exchange coupling is stronger than the field. For larger magnetic fields the central spin flips along the field direction. At finite values of ω, the magnetization of center atom (the blue curve in Fig. 7.5) and surface atoms (solid curve in Fig. 7.5) behave differently depending on their position indicating the strong impact of dipolar interaction on the magnetization of surface spins of the cluster. For finite values of ω, the spins of the top and bottom atoms of the cluster (left panel of Fig. 7.1) show a different magnetization behavior compared to the other surface spins. The magnetization of the center atom remains nearly unaffected by the change in ω values. On the other hand, for the FM case, ω has no influence on the magnetization for the center or surface spins, since the dipolar interactions cancel with each other. Only one step appears for the field-dependence of magnetization, not shown here. Table 7.2 compiles the values of center s_0^z and surface spin s_i^z magnetizations for $\omega = 0$ at different

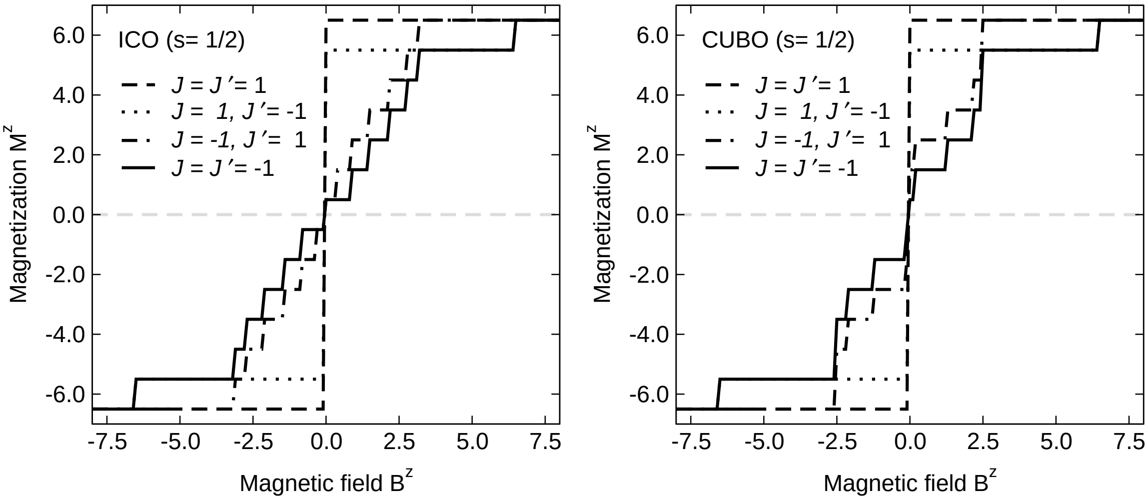

Figure 7.3: Variation of magnetization as a function of magnetic field for different interactions of 13-atom ICO (left panel) and CUBO (right panel). J and J' are the exchange couplings between the surface spins and center-surface spins, respectively. The external magnetic field is measured in units of $|J|$.

Table 7.2: The ground state expectation values of center and surface spins at $\omega = 0$ for the AFM case of ICO and the corresponding S^z. Note that for $S^z = 6.5$ the central spin is parallel.

S^z	$\langle s_0^z \rangle$	$\langle s_i^z \rangle$
6.5	0.5	0.5
5.5	-0.4231	0.4936
4.5	-0.4091	0.4091
3.5	-0.3889	0.3241
2.5	-0.3571	0.2381
1.5	-0.3	0.15
0.5	-0.1667	0.0556

values of S^z, given by

$$\langle s_0^z \rangle = -\frac{S^z}{2(S^z+1)}, \qquad \langle s_i^z \rangle = \frac{S^z - \langle s_0^z \rangle}{12}. \tag{7.8}$$

In addition the ground state spin-spin correlation functions are calculated for the ICO and CUBO, which has the following form

$$\langle \mathbf{s}_i \cdot \mathbf{s}_j \rangle = \frac{\mathrm{Tr}\, e^{-\beta H} \mathbf{s}_i \cdot \mathbf{s}_j}{\mathrm{Tr}\, e^{-\beta H}}. \tag{7.9}$$

Table 7.3 and 7.4 lists the ground state correlation functions for several distances between the spins, which are calculated in terms of the eigenvectors obtained from the exact diagonalization of the Hamiltonian obtained from Eq. 7.6. The correlations for the FM case are found to be same for both geometries, while for the AFM interactions, different correlation functions are obtained, which show

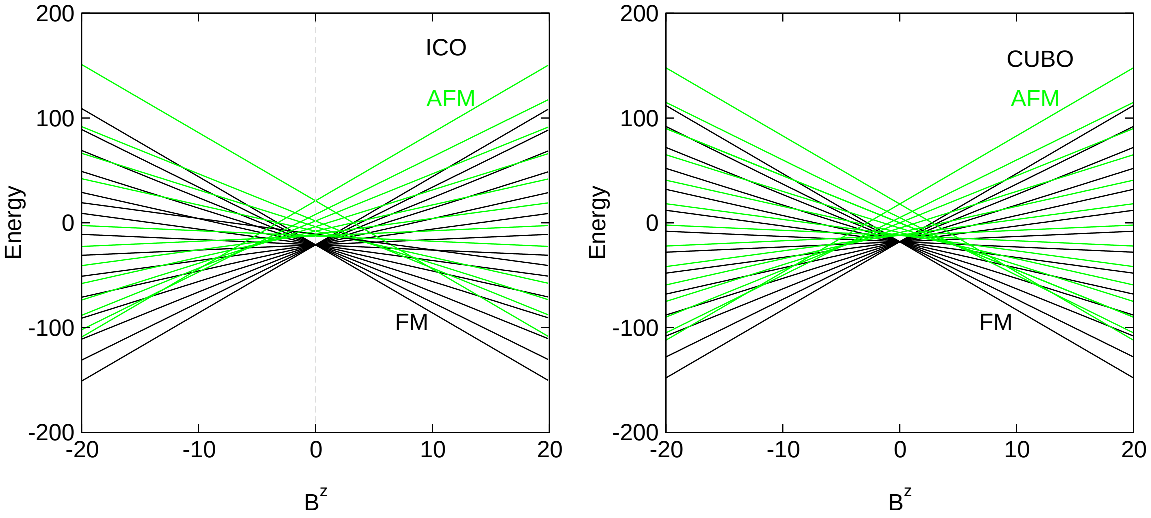

Figure 7.4: The magnetic field dependence of minimum eigenenergy for ICO (left panel) and CUBO (right panel). The black and green lines for both symmetries represent the energy variation with respect to the external magnetic field for FM and AFM cases, respectively.

Table 7.3: Ground state spin-spin correlation functions for ICO with FM and AFM interactions. See left panel of Fig. 7.1 for the labeling of atomic sites. Here, index “zero” is the center atom.

Correlation function	FM	AFM
$\langle \mathbf{s}_0 \cdot \mathbf{s}_2 \rangle$	0.25	-0.083
$\langle \mathbf{s}_2 \cdot \mathbf{s}_4 \rangle$	0.25	-0.176
$\langle \mathbf{s}_2 \cdot \mathbf{s}_6 \rangle$	0.25	0.085
$\langle \mathbf{s}_2 \cdot \mathbf{s}_1 \rangle$	0.25	-0.127

Table 7.4: Spin correlation functions for CUBO for FM and AFM interactions. See right panel of Fig. 7.1 for the labeling of atomic sites. Here, also index “zero” is the center atom.

Correlation function	FM	AFM
$\langle \mathbf{s}_0 \cdot \mathbf{s}_2 \rangle$	0.25	-0.083
$\langle \mathbf{s}_2 \cdot \mathbf{s}_1 \rangle$	0.25	-0.127
$\langle \mathbf{s}_2 \cdot \mathbf{s}_3 \rangle$	0.25	0.085
$\langle \mathbf{s}_2 \cdot \mathbf{s}_5 \rangle$	0.25	0.085
$\langle \mathbf{s}_2 \cdot \mathbf{s}_7 \rangle$	0.25	-0.176
$\langle \mathbf{s}_2 \cdot \mathbf{s}_{11} \rangle$	0.25	-0.176

a tendency towards the antiferromagnetic order. The ICO appears to be less frustrated with respect to the CUBO. Compared to the ICO, the CUBO shows much smaller and irregular correlations in the 3rd and 4th neighbour shell.

The thermodynamic quantities such as entropy, specific heat and susceptibility (defined in Eqs. 7.10, 7.11 and 7.12, respectively) as a function of magnetic field at several temperatures are calculated for ICO and CUBO for the AFM (see Fig. 7.6, 7.7) and FM interactions (see Fig. 7.8). The top and bottom panel of Figure 7.6 shows the variation of entropy as a function of external magnetic field for the AFM case of ICO and CUBO, respectively. This shows sharp peaks for the field-dependent entropy at low temperature, which is due to the fact that at low temperatures only the minimum energies

$$\text{Entropy } S = k_B \left(logZ + \frac{\langle E \rangle}{k_B T} \right) \tag{7.10}$$

$$\text{Specific heat } C = \frac{\partial \langle E \rangle}{\partial T} = \frac{1}{k_B T^2} \left(\langle E^2 \rangle - \langle E \rangle^2 \right) \tag{7.11}$$

where, $\langle E \rangle = \frac{\sum_n \varepsilon_n e^{-\varepsilon_n / k_B T}}{Z}$

$$\text{Susceptibility } \chi = \frac{\partial \langle M \rangle}{\partial T} = \frac{(g\mu_B)^2}{k_B T} \left[\frac{1}{Z} \sum_n S_n^{Z^2} e^{-\varepsilon_n / k_B T} - \left(\frac{1}{Z} \sum S_n^Z e^{-\varepsilon_n / k_B T} \right)^2 \right] \tag{7.12}$$

of each S^z sector are more decisive. With the variation in the magnetic field, the absolute minimum eigenstates shift from S^z= 0.5 to higher S^z values. However, as the temperature increases more number

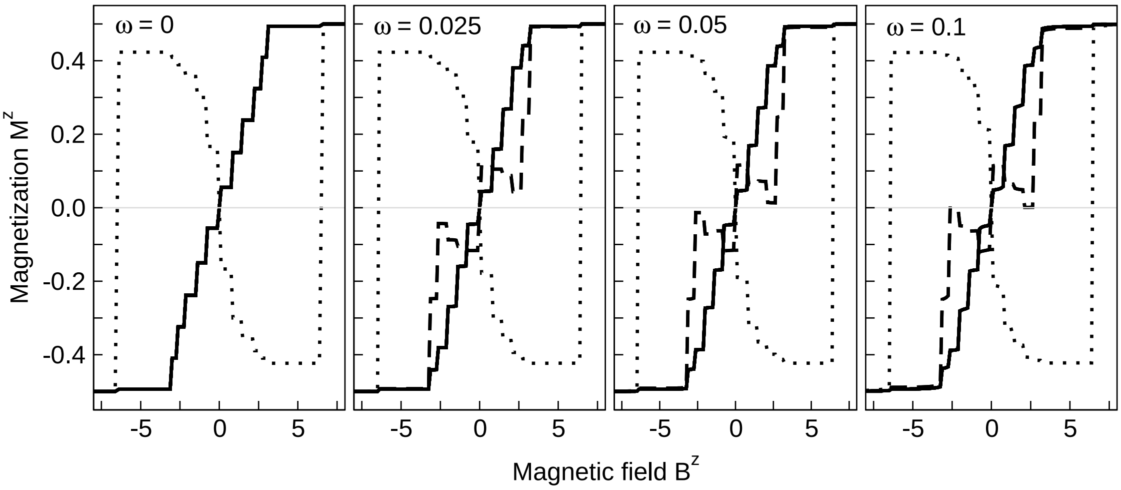

Figure 7.5: Variation of magnetization $\langle s_i^z \rangle$ as a function of magnetic field (in units of $|J|$) for the AFM case of 13-atom ICO at several values of dipole coupling strengths ω. The dotted lines in all plots show the field-dependence of magnetization for the center spin $\langle s_0^z \rangle$. The dashed and the solid lines show the same quantity for the top-bottom atoms and remaining 10 atoms on the surface, respectively. It depicts that the magnetization of the central spin remains almost unaffected by the strength of the dipolar interaction.

of states from S^z sector contribute to the thermodynamics, as a result the peaks for field-dependent entropy are smeared out. Similar explanation can be given to the behavior of specific heat and susceptibility with respect to magnetic field at several temperatures, which are shown in Fig. 7.7. On the other hand, for the FM case (Fig. 7.8), however, only the maximum S^z block matrix has the lowest energy for all magnetic fields, which means that all eigenvalues are simply scaled with magnetic field and therefore no non-trivial features are observed for the thermodynamic quantities such as entropy, specific heat and susceptibility.

Figure 7.9 shows the variation entropy (top panel) and specific heat as a function of temperature at different external magnetic fields for the AFM interaction. The results for the ICO and CUBO are shown in the left and right panels, respectively. The peaks in the temperature-dependent specific heat at low temperatures (T $\approx$ 1) indicate the classical excitations in the system. However, the additional peaks in the temperature-dependent specific heat and plateaus in the entropy appear due to the quantum excitations from the low lying energy levels at low temperatures. In Fig. 7.10 the temperature-dependent entropy, specific heat and susceptibility are displayed for the FM case of both clusters, which shows the trivial behavior.

Figure 7.11 shows the field-dependence of magnetization at different temperatures for AFM (left) and FM (right) interactions of ICO, respectively. It shows that with increasing temperature, the magnetization is smeared out for both interactions. A similar magnetization behavior with increasing temperature is also observed for the CUBO case, which is not shown in the thesis.

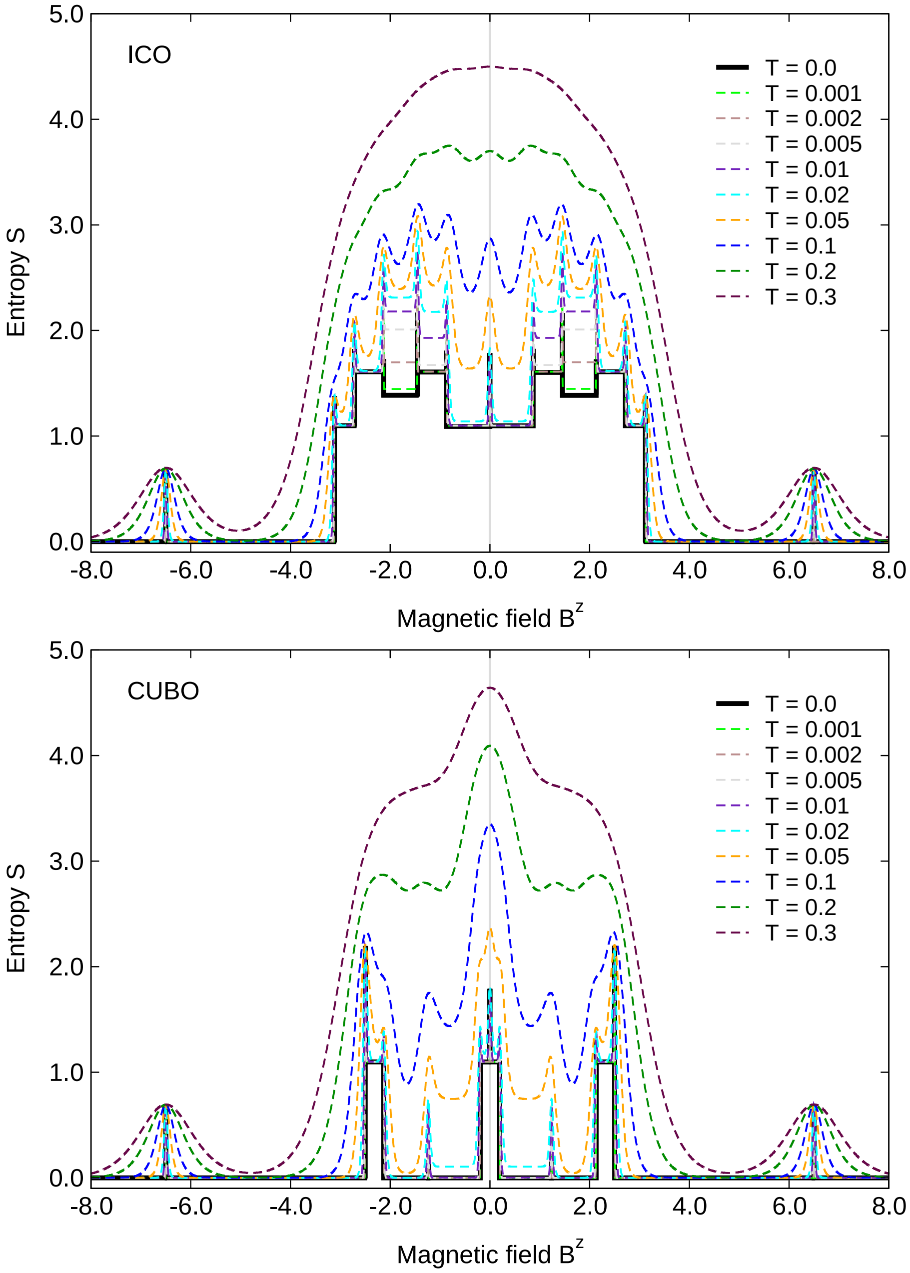

Figure 7.6: Variation of entropy as a function of external magnetic field for the AFM case of 13-atom ICO (top panel) and CUBO (bottom panel) with spin-$\frac{1}{2}$. The several colors denote the behavior of these quantities at several temperatures. The opposite ordinate represents the degeneracy of the minimum energy eigenvalues.

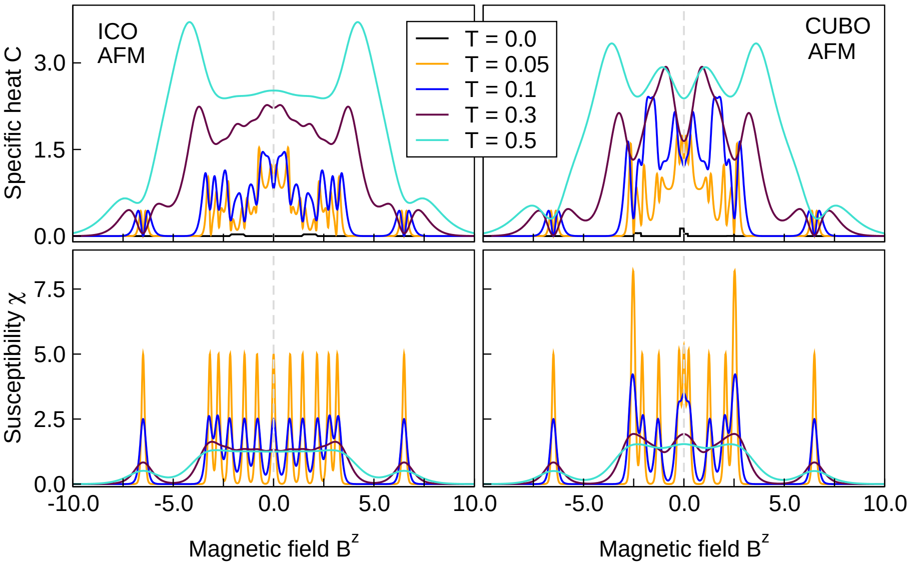

Figure 7.7: Variation of thermodynamical entities as a function of external magnetic field for 13-atom ICO (left column) and CUBO (right column) with spin-$\frac{1}{2}$. The top and bottom panels indicate the field-dependent specific heat and field-dependent susceptibility for the AFM case, respectively. The several colors denote the behavior of these quantities at several temperatures.

7.4 4-atom cluster: Tetrahedron and square

Previously, we have studied the structural and magnetic properties of small transition metal clusters with more emphasis on the magnetic anisotropy using the density functional theory (DFT) [18], where the energies obtained from DFT calculations were fitted by using a classical Heisenberg Hamiltonian. The investigations presented here can be viewed as a continuation of the previous work in the sense that we perform exact diagonalization of a corresponding quantum spin Hamiltonian to study the system. The effect of uniaxial anisotropy has been studied for a tetrahedron and a square geometry (shown in Fig. 7.12) with $s = 1$. As the uniaxial anisotropy gives a constant value for $s = \frac{1}{2}$. In the presence of the uniaxial anisotropies, the Hamiltonian has a form as shown in Eq. 7.5. A regular tetrahedron has four triangular faces with the equilateral triangles of tetrahedron meeting at each vertex. It has a symmetry group T_d, whereas a square is a regular quadrilateral with D_4 symmetry. We begin our discussion with the case of spin-$\frac{1}{2}$ square.

7.4.1 Square (s = $\frac{1}{2}$)

For a 4-atom system with spin-$\frac{1}{2}$system, a Hamiltonian matrix of dimension (16×16) has to be solved. Because of the block diagonalization method, the whole Hamiltonian matrix is divided into 5 sub-matrices each corresponding to a definite S^z value. The 5 sub-matrices have dimensions 1, 4, 6, 4, 1

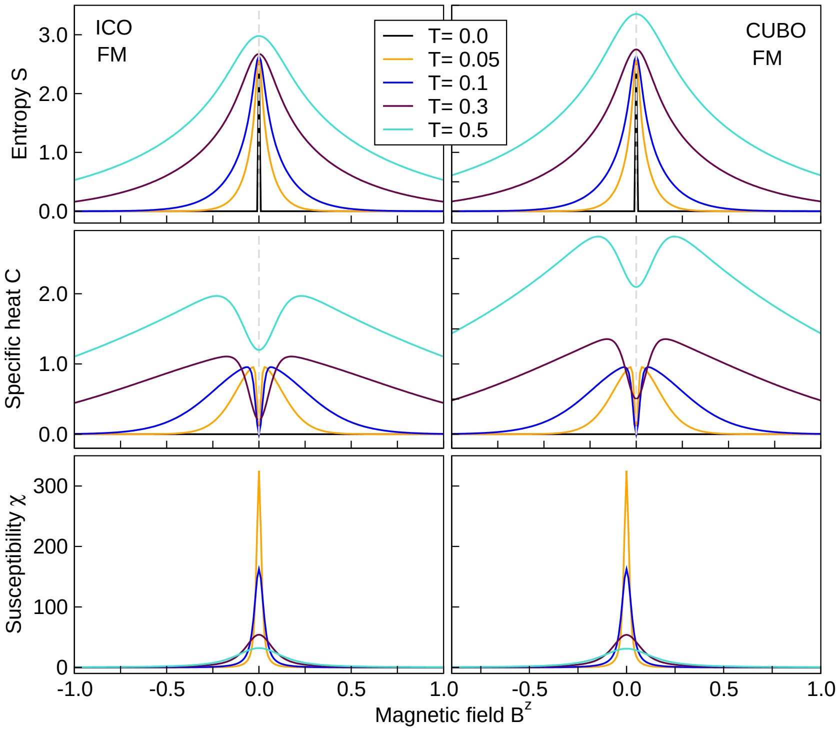

Figure 7.8: Variation of thermodynamical entities as a function of external magnetic field for 13-atom ICO (left column) and CUBO (right column) with spin-$\frac{1}{2}$. The top, middle and bottom rows indicate the variation of Entropy, specific heat and susceptibility with respect to magnetic field for the FM case. The several colors denote the behavior of these quantities at several temperatures.

in positive and negative S^z sectors. In the present case, S^z= -2, -1,...2. The ground state energies, for the square are found to be all degenerate for FM interaction, while they are non-degenerate for the AFM interaction, as observed in the case of 13-atom clusters. The reason behind such trend is similar as discussed previously. The variation of magnetization with respect to external magnetic field has been shown in Figure 7.13. We found that with increase in magnetic field, for $J_{ij}>0$, magnetization does not change and always has a value of 2.0 in the positive S^z (dashed curve in Fig. 7.13), while for $J_{ij}<0$, a number of plateaus occur for each S^z (solid curve in Fig. 7.13). The reason is similar like for 13-atom clusters, which is described in Sec. III.

7.4.2 Tetrahedron and square with s = 1

Several studies have been performed for the magnetic and thermodynamic properties for spin-1 clusters [282, 287] using Heisenberg model. Studies including the influence of radial anisotropy on various properties of clusters are still limited. In the present work, we have investigated the influence of anisotropy on the magnetic properties and temperature-dependent correlation functions for the spin-1

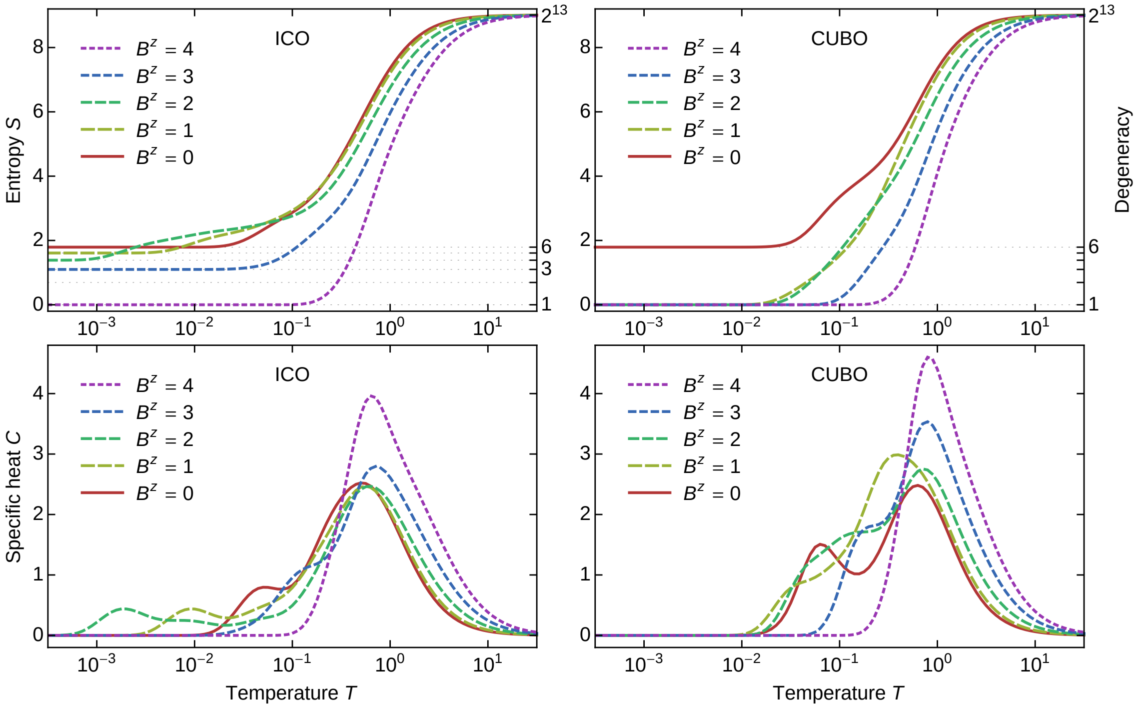

Figure 7.9: Variation of entropy (top panel) and specific heat (bottom panel) as a function of temperature for 13-atom ICO (left column) and CUBO (right column) with spin-$\frac{1}{2}$ for the AFM case. The colors indicate the variations of same quantities at several magnetic fields.

tetrahedron and square. The Hamiltonian is modified to a form as represented in Eq. (7.5) in the presence of local uniaxial anisotropies, where $D_i = D$ is the anisotropy constant and $\boldsymbol{e}_i$ are the easy axes which may differ for each spin. Figure 7.12 shows the anisotropy axes (double arrows) pointing in the radial directions for the square and tetrahedron. For the 4-atom spin-1 cluster, the Hamiltonian matrix is of dimension $3^4 \times 3^4$. The total number of block matrices is 9 in this case with $S^z = -4, -3, \ldots, 4$. Taking the minimum energy from each S^z sector results in 9 eigenenergies. The presence of anisotropy D shows different qualitative behavior of field-dependent magnetization as depicted in Fig. 7.14 for the case of tetrahedron (a-b) and the square (c-d). For $D = 0$, we obtain a single step in the magnetization for FM case and plateaus for the AFM case of both geometries. The presence of anisotropy leads to the smearing of magnetization with respect to magnetic field for FM and AFM interactions (see the squares and diamonds) of square and tetrahedron. In particular, for tetrahedron geometry, differences in the magnetization for positive and negative values of D are observed, whereas for the square geometry, the change of sign in the anisotropy does not affect the magnetization significantly. This indicates the dependence of anisotropy on the structural symmetry, which has been observed earlier for 13-atom clusters through Monte Carlo simulations [281].

7.15 shows the nearest-neighbour correlation functions with respect to temperature at different values of anisotropy constants for FM and AFM interactions of tetrahedron and square with spin-1. We

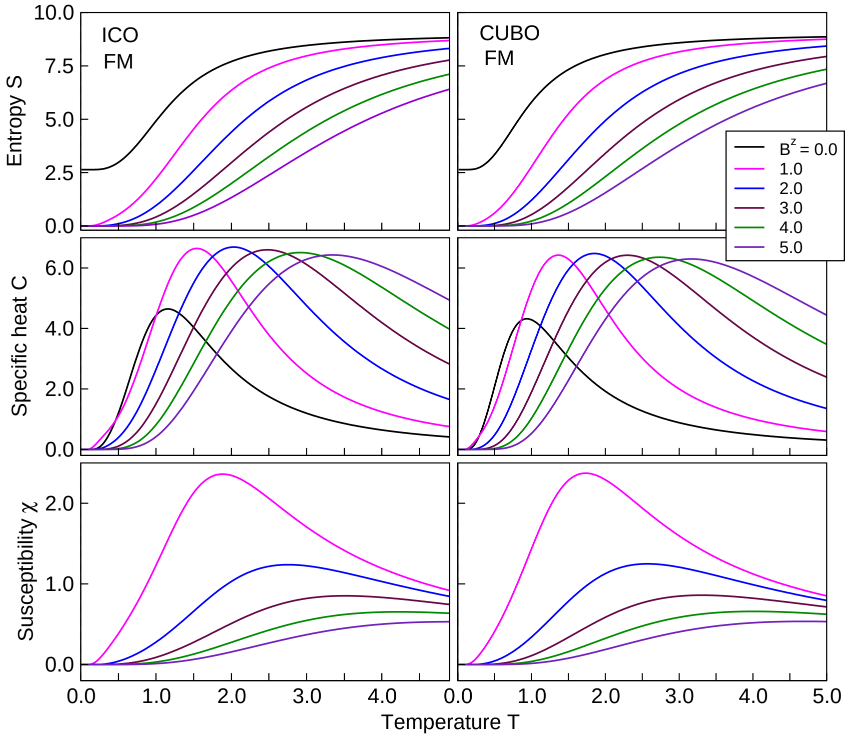

Figure 7.10: Variation of thermodynamical entities as a function of temperature for 13-atom ICO (left column) and CUBO (right column) with spin-$\frac{1}{2}$. The top, middle and bottom rows indicate the temperature-dependent entropy, specific heat and susceptibility for the FM case at different external magnetic fields (shown in several colors).

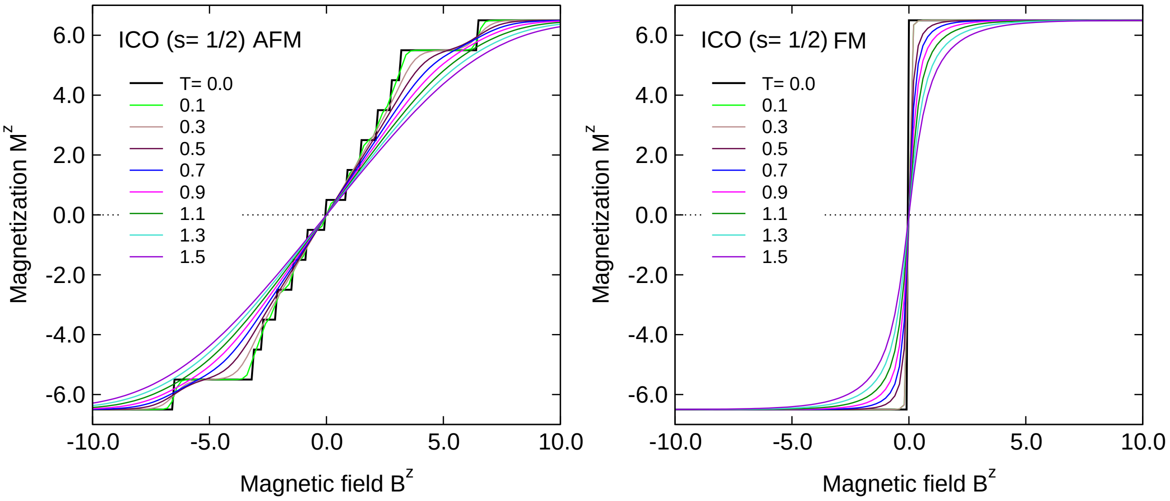

Figure 7.11: Magnetization as a function of magnetic field at various temperatures. With increase in temperature, the plateaus vanish for AFM case of 13-atom ICO.

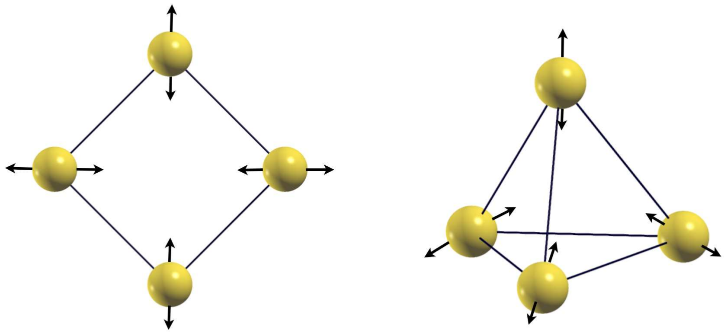

Figure 7.12: Skematic picture of a planar square (left panel) and a three dimensional tetrahedron (right panel) with 4 lattice sites. The arrows indicate the radial spin orientations taken into account to study the effect of anisotropy for s = 1.

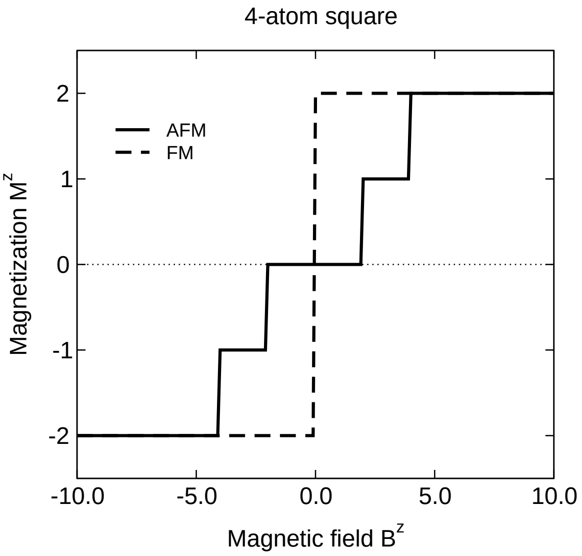

Figure 7.13: Variation of magnetization as a function of external magnetic field for $s=\frac{1}{2}$ case of 4-atom square. The dashed and solid curve show the magnetic field dependence of magnetization for FM and AFM cases.

observe that the anisotropy has significant effect on correlation function at low temperature regions for both FM and AFM interactions. For the FM case, they are positive, while they have negative sign for AFM case. For $D \geq 0$, with increasing temperature, the correlations between spins gradually decreases for both cases as expected. For negative value of D, the correlations are reduced, which might be due to some quantum fluctuations. Such effect can be marked for the square geometry, where, the classical ground state would be in the direction perpendicular to the plane, as all couplings are satisfied and the spin directions are all perpendicular to the anisotropy axes. Hence, the reduction of correlation functions at low temperature occur due to the quantum effects. However, this reduction

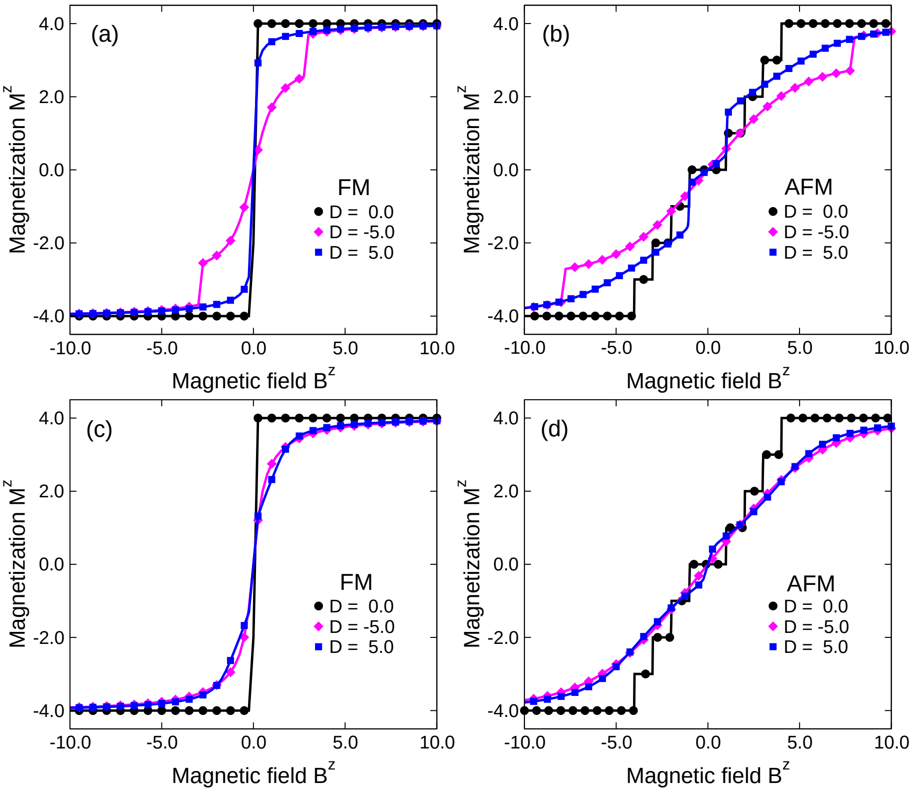

Figure 7.14: Magnetization as a function of magnetic field for different anisotropy constants for spin-one 4-atom tetrahedron (a-b)and square (c-d). The results for FM and AFM are shown in left and right side, respectively. The black curve for FM and AFM shows the variation of field-dependent magnetization in the absence of anisotropy constant D. The magenta and blue curves show the variation of the same at positive and negative D.

in correlation function becomes negligible in the high temperature regime, as a result the correlations show a decreasing trend as usual.

7.5 13-atom icosahedron with spin-1

For the spin-1 icosahedron (the Hamiltonian is shown in Eq. 9.6), the Hamiltonian matrix has a dimension $(3^{13} \times 3^{13})$, which can be decomposed into block matrices with sizes represented as trinomial numbers $\binom{13}{k}_2$ for $-13 \leq k \leq 13$, shown in Table 7.5 together with the lowest eigenvalues of each S^z block. The variation of magnetization as a function of magnetic field for $D = 0$ shows a similar behavior like spin-$\frac{1}{2}$ case, as the magnetization has a constant step size from -11 to 11 for $|B^z| \leq 6$ (see Fig. 7.16, black line). The plateaus at $M^z = \pm 11$ indicate the saturated outer shell, where only the central spin points antiparallel to the external field. In addition, the effect of radial uniaxial anisotropy is studied for this geometry, with the Hamiltonian shown in Eq. 9.5. For such studies, the whole Hamil-

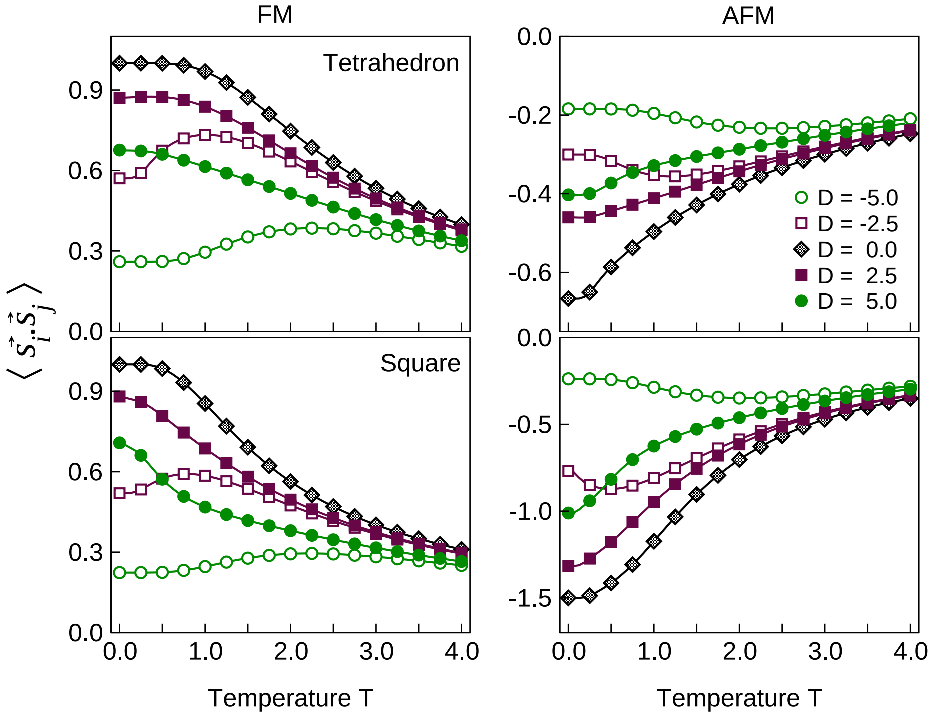

Figure 7.15: The variation of spin-spin correlation function with respect to temperature for spin-1 tetrahedron (top) and square (bottom) for several anisotropy constants.

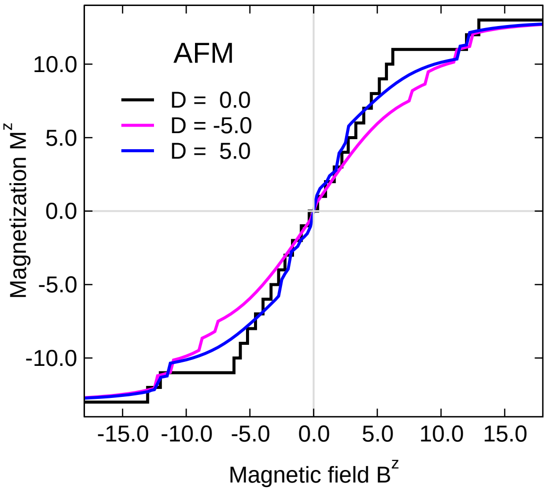

Figure 7.16: Variation of magnetization as a function of the external magnetic field (measured in units of $|J|$) for the spin-1 AFM icosahedron.

tonian matrix is considered, since the anisotropy term does not commute with the interaction term and hence destroys the block structure of the H. In the present case, we have calculated the minimum eigenvalues and eigenvectors using the Lanczos scheme. The resulting field-dependent magnetiza-

Table 7.5: Size of matrices, lowest energy eigenvalues E_0 and degeneracy K_0 for different S^z for 13-atom AFM ICO with spin-1.

$\|S^z\|$	Matrix size	$E_0/\|J\|$	K_0
13	1	$+42$	1
12	13	$+29$	1
11	91	$+17$	1
10	442	$+10.763932$	3
9	1651	$+5.034063$	5
8	5005	-0.131753	4
7	12727	-4.663902	4
6	27742	-8.608201	3
5	52624	-11.932667	4
4	87802	-14.679508	5
3	129844	-16.920343	5
2	171106	-18.566489	3
1	201643	-19.506298	5
0	212941	-19.839976	3

Table 7.6: Ground state spin-spin correlation functions for the spin-1 ICO with FM and AFM interactions. See left panel of Fig. 7.1 for the labeling of atomic sites. $\boldsymbol{s}_0$ is the center atom.

Neighbor	Correlation function	FM	AFM
1	$\langle \boldsymbol{s}_2 \cdot \boldsymbol{s}_0 \rangle$	$+1$	-0.166667
1	$\langle \boldsymbol{s}_2 \cdot \boldsymbol{s}_4 \rangle$	$+1$	-0.594666
2	$\langle \boldsymbol{s}_2 \cdot \boldsymbol{s}_6 \rangle$	$+1$	$+0.382099$
3	$\langle \boldsymbol{s}_2 \cdot \boldsymbol{s}_1 \rangle$	$+1$	-0.770497

tions are plotted in Fig. 7.16 for several anisotropy constants with magenta curve for negative value of D and blue curve for positive value of D.

Table 7.6 shows the ground state spin correlations of the FM and AFM spin-1 ICO without anisotropy, which are also similar to that of spin-$\frac{1}{2}$ case. They show AFM-like ordering for the AFM case with a larger anti-correlation between opposite sites 2 and 1 (see Fig. 7.1) as compared to the nearest neighbour value, which approaches towards the classical limit -1.

8 Summary and outlook

8.1 Summary

This thesis deals with the study of structural, magnetic and electronic properties of elemental and binary transition metal clusters. We have considered especially the closed shell clusters of Fe, Co, Ni and Pt. We have used the density functional theory for studying the electronic structure and the total energy. As the exchange-correlation potential we have adopted the generalized gradient approximation, which is successful in describing the properties of metals. The cluster geometries are structurally optimized by applying the conjugate gradient energy minimization procedure. We have explored various essential properties of clusters like the ground-state structure, structure dependent magnetic moment, possible distribution of atoms in binary clusters through segregation and mixing. Magnetic anisotropy properties has been studied for various free and supported clusters. We have used the exact-diagonalization procedure to study the thermodynamics of clusters.

The studies of the ground-state structural properties of small elemental clusters of Ni and Fe with upto 16 atoms suggest that the small clusters are slightly distorted from perfect geometry. The distortion is identified as the Jahn-Teller distortion which arises because of the inherent property of a system to avoid degeneracy of states at the Fermi level. The magnetic moments of clusters are larger than bulk due to the uncompensated bonding of atoms. The magnetic moment as a function of cluster size shows an oscillatory (non-monotonous) behavior. The convergence of magnetic moment towards the corresponding bulk value is much faster for Ni clusters than that of Fe, which is in agreement with experimental results. We observe existence of two spin states for the icosahedral Fe_{13} from the fixed spin moment calculations The two spin states are: (i) the high-spin state with magnetic moment 44 μ_B, where all spins are parallel to each other, (ii) the low spin state with magnetic moment 34 μ_B, where the central spin is aligned oppositely with respect to the surrounding surface atoms. We find that the high-spin state has a lower energy than the low-spin state.

Our studies on binary icosahedral Fe-(Co, Ni, Pt) and Co-(Pt, Mn) clusters show a competition between the alloy components which finally leads to chemical ordering and segregation. In order to achieve this, the energetically preferable configuration of the binary clusters are found for several compositions. Using the lowest energy structure of the compositions, the mixing energy is calculated. We observe a qualitative resemblance for composition-dependent mixing energy for $Fe_{13-n}Ni_n$ clusters as compared to that of the bulk alloy. For Fe-Ni clusters, it is found that Ni atoms show the occupancy at the surface of the icosahedron for all compositions studied. For 55-atom binary clusters, however, owing to the large number of configurations that can be possible, we have studied selective compositions in the extreme composition regions to compare the trends of 13-atom cluster. Our studies on 55-atom binary clusters showed similar tendencies as that of the 13-atom binary clusters. From the segregation properties as observed for Fe-Ni, Fe-Pt and Co-Pt, we could generalize the trend that in a binary cluster the component with larger atomic number segregate towards the surface of the cluster. In the TM-Pt binary clusters we find induced magnetic moment on Pt due to the TM component, which is otherwise non magnetic in bulk.

Our studies on 13- and 55-atom icosahedral binary Fe, Co, Ni and Pt clusters show that there is a competition between the alloy components which finally leads to chemical ordering and segregation. We have calculated the mixing energy at all compositions for the energetically most favorable configuration of component atoms in the cluster. The trend in the mixing energy gives the chemical ordering and the corresponding cluster configuration is used to study the segregation property. We observe a qualitative resemblance of composition-dependent mixing energy for $Fe_{13-n}Ni_n$ clusters as compared to that of the bulk alloy. For 55-atom binary clusters, however, owing to the large number of configurations that can be possible, we have studied selective compositions in the extreme composition regions to compare the trends of 13-atom cluster. Our studies on 55-atom binary clusters showed similar tendencies as that of the 13-atom binary cluster. From the segregation properties as observed for Fe-Ni, Fe-Pt and Co-Pt, we could generalize the trend that in a binary cluster the component with larger atomic number segregate towards the surface of the cluster. In the TM-Pt binary clusters we find induced magnetic moment on Pt due to the TM component, which is otherwise non magnetic in bulk.

One of the main part of the thesis is the magnetic anisotropy studies of clusters. Usually the computational demand for magnetic anisotropy studies is more because of inclusion of spin-orbit part into the Hamiltonian. Since the energy differences we are dealing with magnetic anisotropy studies are relatively smaller, this needs more accurate calculations with large energy cut-off and Fourier transformation grids. Our studies show that both spin and orbital moments of clusters are larger compared to the corresponding bulk values. The MAE for perfect icosahedral clusters has been obtained from our calculations and compared with the Néel anisotropy model, which are in good qualitative agreement. We have studied the MAE of relaxed Fe_{13}, Co_{13} and Ni_{13} clusters through two competing structural transformation paths, namely, the Jahn Teller and the Mackay transformation. As already mentioned, JT-distortion in clusters is a natural way to structural deviations. In the present controlled structural transformation with separate transformations paths show that Fe_{13} prefers JT-distortion, while Co_{13} prefers MT-distortion. For Ni_{13} we find that both JT- and MT- distortions are almost degenerate. It is found that the MAE of clusters is larger as compared to their bulk values. Since MAE is related to the structure through the position vectors of all the atoms, symmetry of clusters play an important role. The relaxed clusters have a large MAE than the perfect clusters as a consequence of symmetry lowering for the relaxed clusters. It is peculiar that this trend was not observed for Co_{13} cluster, where the MAE values were similar to that of bulk values. Our studies on Pt-capped Fe_{13} cluster ($Fe_{13}Pt_4$)

show that the MAE is further enhanced as compared to the elemental clusters.

In addition to free clusters, we have studied clusters deposited on surface by modeling the system with 13- and 55-atom Fe, Co and Ni clusters and the surface as (001) and (111) surfaces of Pt. As expected, the deposited clusters show the structural and magnetic properties different from that of free clusters. The role of the surface-type is quite important for the properties of cluster-substrate interaction. For example, we find that the closed shell 13 and 55-atom Fe, Co, Ni clusters are completely deformed while deposited on Pt(001) surface with the cluster atoms penetrating the surface with tendency of forming surface-alloy. On Pt(111), however, the icosahedral geometry of Fe_{13} cluster is preserved, while Co_{13} and Ni_{13} shows a tendency of spreading on the surface. From magnetic properties point of view, we find that clusters deposited on Pt(001) have lower values of spin and orbital magnetic moment, while clusters deposited on Pt(111) have higher values of spin and orbital magnetic moment, as compared to their corresponding free clusters. Our studies on the magnetic anisotropy of Pt-supported Fe_{13} show an enhanced MAE which is several orders of magnitude larger with respect to the free Fe_{13} cluster (as well as bulk). The enhancement of MAE is a consequence of reduction of structural symmetry (relaxation effect) and due to the large spin-orbit coupling of Pt substrate, which develops induced magnetic moment.

We have studied icosahedral 13-atom Fe, Co, Ni and Pt clusters deposited on both pristine and five-membered ring graphene. Our purpose is to investigate the stability of metal cluster and graphene interfaces, which is important from the perspective of catalytic activity of metal clusters. Our calculations suggest that the interface stability is enhanced for clusters/five-membered ring graphene as compared to those adsorbed on pristine graphene. We observe significant reduction in the total magnetic moment for the adsorbed Fe and Co clusters as compared to the corresponding free clusters. We have attempted to study the catalytic reaction, where a CO molecule is adsorbed on 13-atom cluster both for free clusters and for graphene supported clusters. We observe that, the adsorption of CO on metal clusters show a strong dependence on the atomic species and the cluster geometry, for example, CO molecule prefers to be adsorbed on Fe_{13} and Pt_{13} on the top of the atom, while for Co_{13} and Ni_{13}, it prefers the middle of the facet. The adsorption sites of CO remain unchanged for the graphene supported metals clusters. It must be mentioned that DFT-GGA has short-comings in predicting the correct adsorption sites on surfaces which can be overcome by a van-der Waal's correction.

We have studied the ground-state magnetic properties and thermodynamics of clusters by the exact diagonalization technique. This technique is useful in studying the magnetic properties dependent on temperature and magnetic field, the informations of which is not directly accessible from the DFT calculations. We have modeled the cluster by the Heisenberg model with nearest-neighbour interaction for 13- (icosahedron and cuboctahedron) and 4-atom (tetrahedron and square) clusters with both spin-$\frac{1}{2}$ and spin-1. Our studies reveal that in the absence of external magnetic field, the ground state is degenerate for the FM interaction, while for the antiferromagnetic case, they are non-degenerate. In the presence of external magnetic field the variation of magnetization shows discontinuities with appearance of plateaus for the antiferromagnetic interaction, while for the FM interaction it shows

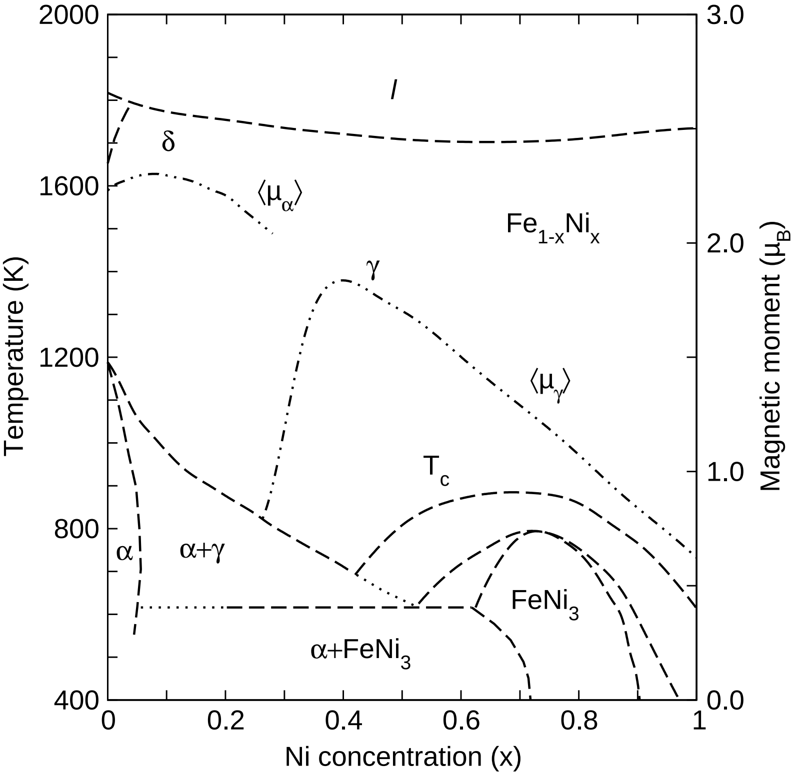

Figure 8.1: The structural and magnetic phase diagram of Fe_{1-x}-Ni_x bulk alloy [137, 138].

a single step. With inclusion of dipolar interaction in the Hamiltonian for spin-$\frac{1}{2}$ particles for the 13-atom icosahedron we find that the central atom has different field-dependent magnetization as compared to the extreme atoms (top and bottom atoms), which in turn different from the rest of atoms in the cluster. By including a radial anisotropy term in the Hamiltonian, we could differentiate the field-dependent magnetization for square and tetrahedron with spin-1 particles. This is also reflected in the temperature-dependent correlation function. The Hamiltonian for the 13-atom spin-1 icosahedron with dimension of the Hamiltonian matrix is $3^{13} \times 3^{13}$ has been solved by using Lanczos method and the hysteresis for the icosahedron with radial uniaxial anisotropy is calculated.

8.2 Outlook

There are many scopes of clusters studies, which still need to be understood. As an outlook mostly two important phenomena are focussed which will be persued if similar studies are continued.

Firstly about the binary clusters, which give a scope of manipulating the clusters properties through its compositional arrangements. We have already seen from our studies that the segregation tendencies in Fe-Ni clusters depend on the geometry of the clusters and the concentration of the components. It is interesting to study the structural phase diagram of binary clusters, and to find whether there

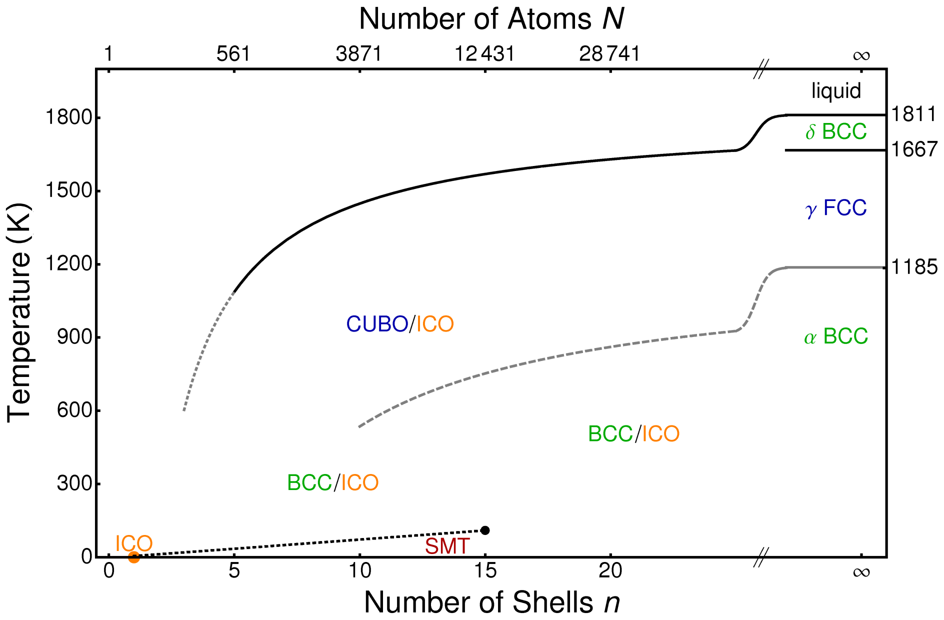

Figure 8.2: Phase diagram from nano to bulk for Fe taken from [288].

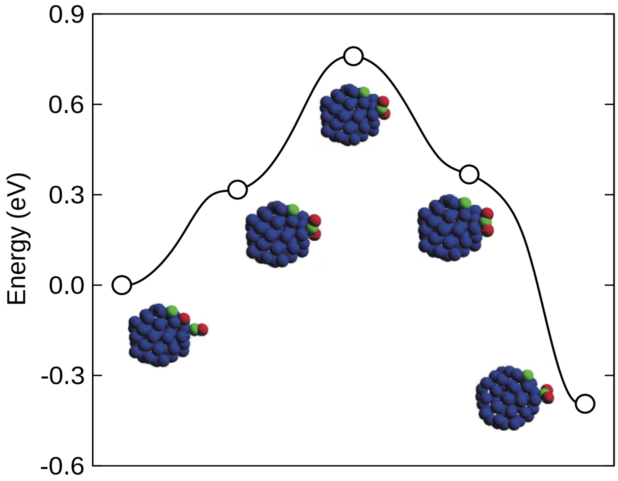

Figure 8.3: Minimum energy paths for CO_2 formation on Fe_{55} starting from CO and co-adsorbed atomic C/O [257]. Several intermediate structures along the path are shown.A, E and F abbreviate the top of the atom, edge and facet of the cluster, where the molecules are adsorbed. Blue, green and red balls denote the Fe, C and O atoms, respectively.

is any similarity to the bulk binary alloys (for example in Fe-Ni binary system). Figure 8.1 shows the phase-diagram of Fe-Ni bulk alloy [137, 138]. It must be noated that the studies would need many different types of cluster geometry and thus the task is an enormous one. Experimentally, it has been shown that as the system size is decreased from bulk to clusters, the phase formations, such as eutectic composition and the transition temperature differs [289, 290]. This will nevertheless help us to address questions like, what are the properties of a desired configuration of clusters and how they can be synthesized by understanding the stability of the desired configuration from the phase diagram. The studies will lead the scope of extending the traditional phase transition theories to low dimensions. Since experimentally the studies on nano-phases can be a challenge, so theoretical studies based on DFT may provide the right insight into the problem. Fig. 8.2 shows the cluster to bulk phase diagram for Fe [288] (studied through molecular dynamics simulations using embedded atom potentials) which predicts a stability for the icosahedral and shell wise Mackay transformed structures up to cluster sizes with 15 closed atomic shells. Wang *et al.* have studied the size-dependent surface reconstruction and layerwise relasation of icosahedron FePt nanoparticles and propose that the structural results can be understood if the atomic distribution in the nanoparticle is assumed to have radial composition gradient with a Pt-rich shell and a Fe-rich core [140]. It is understood that empirical studies can be quick from computational aspects, but approaching the problem in fundamental way through *ab initio* formalism will be useful for building better empirical potentials and directly approaching the problem from *ab initio* will lead to unchallenged results.

A second scope of the outlook is the studies on catalysis properties of transition metal clusters. While catalysis is an active technological application of transition metal nanoparticles, there are relatively few theoretical studies attempted to understand how transition metal atom act as a catalyst for chemical reaction. Catalytic reactions can be studied by comparing the energy-barrier of reaction paths thus predicting the most favourable reaction path. Figure 8.3 shows the several states of CO_2 formation on Fe_{55} cluster [257]. The energy barrier is comparable to the experimental values. Treating this problem may sound easy, but comparing to the number of configurations of reactants and products, the task is challenging. These studies will contribute to desigining catalysts for efficient reactions, for example, for efficient combustion of hydrogarbons or gasolins in industries and automobiles.

Appendix

Extension of cluster magnetism to finite temperatures

DFT being a variational theory has shortcoming in predicting the excited state properties of materials. A direct extention to temperature dependence of properties is not straightforward. One of the ways to deal with finite temperature properties especially for the magnetic properties can be easily conceivable. It is a rather indirect method of calculating the distance-dependent exchange integrals $J_{ij}(r)$ of magnetic atoms by *ab initio* methods and thereby simulating the thermodynamics by the Monte Carlo approach through the construction of classical Heisenberg Hamiltonian,

$$H_{eff} = -\sum_{i \neq j} J_{ij}\, \boldsymbol{s}_i \cdot \boldsymbol{s}_j \tag{8.1}$$

where, $\boldsymbol{s}_i$ is the spin magnetic moment on the atomic site.

We have attempted to extent the zero-temperature *ab initio* calculations of the magnetic properties of small clusters to finite temperatures. The exchange integrals can be calculated from the Green's function formalism adopted in the SPR-KKR code [291] from the group of Prof. Ebert at LMU-Munich. The essential theory behind the method is derived by Lichtenstein *et al.* [292] through frozen-magnon approximation. The exchange integral is thus given by the energy integration of the imaginary part of combination of t-matrix and τ-matrix integrated from the bottom of the valency band (theoretically $-\infty$) up to the Fermi-energy [293].

$$J_{ij} = -\frac{1}{4\pi}\mathrm{Im}\int^{E_\mathrm{F}} dE\ \mathrm{Tr}\left[\delta_i(E) G_{ij}^{\uparrow\uparrow}(E) \delta_j(E) G_{ji}^{\downarrow\downarrow}(E)\right] \tag{8.2}$$

where, $G_{ij}^{\sigma\sigma}$ is the propagator of electrons with spin σ between sites i and j in the ferromagnetic configuration. The quantity $\delta_i(E)$ is the energy-dependent local exchange splitting at site i. The trace is over the orbital index.

It must be stressed that the mean-field estimation of the magnetic transition temperature from the J_{ij}s itself is overestimated. This is already well known for the bulk magnetic materials. Especially in clusters, because of the large number of surface atoms which are under-coordinated, the mean-field prediction can be still misleading. Thus Monte-Carlo simulations are must. One must be aware that for finite systems the statistics has to be closely monitored, and the transition point can be estimated by suitably scaling the physical quantities (magnetization for example) by appropriate critical exponents. There has already been some attempts of studies in literature. For example, the left panel of Fig 8.4

shows the distance-dependent exchange parameters for Fe clusters. In the right panel of Fig 8.4, the variation of J_{ij} with respect to the cluster size is shown [222]. Typical results obtained by the magnetic properties by using the J_{ij} in the Heisenberg model with classical spins are, for example, shown in Fig 8.5, where the variation of average magnetization as a function of temperature is plotted as for Fe_{59} and Fe_{89} clusters.

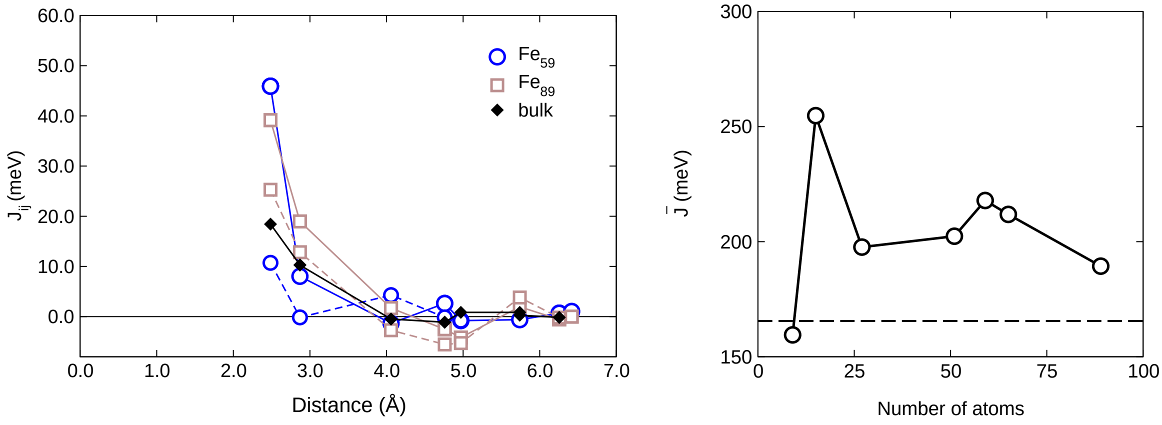

Figure 8.4: Left: The distance-dependent exchange parameter (J_{ij}) for Fe clusters consisting of 59 (circles) and 89 (squares) atoms. The J_{ij} for bulk Fe is represented by black diamond. The dashed and solid lines indicate the exchange interactions between center to other atoms and the surface to other atoms. The black solid line at zero along y-axis is just guide to the eye. Both figures are replotted from Ref [222]. $\bar{J}$ in the right panel is the average exchange parameter, defined as $\bar{J} = \frac{1}{N}\sum_i \sum_{j\neq i} J_{ij}$.

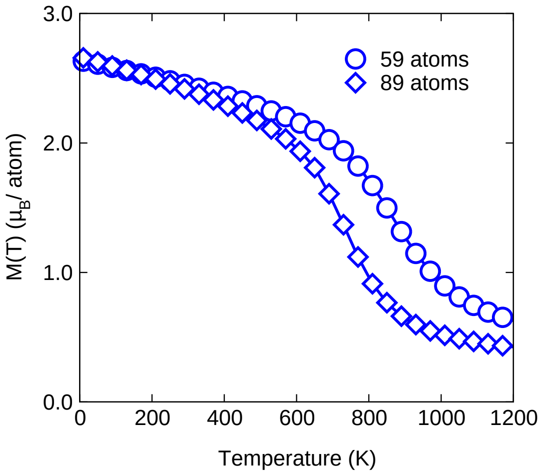

Figure 8.5: The variation of magnetization with respect to temperature for Fe_{59} and Fe_{89} clusters [222]. The circle and square shows the temperature-dependent magnetizations for Fe_{59} and Fe_{89} clusters.

We have, so far, carried out few calculations of J_{ij} for small clusters of Fe_2 and Fe_{13} using the Juelich SKKR code [294, 295]. But since the cluster calculations have already been published mainly by the group of Prof. Hubert Ebert (LMU Munich) for tiny Fe and Fe-Pt clusters, we discuss here the published results.

Bibliography

[1] J. Kübler, *Theory of Itinerant Electron Magnetism*, (Oxford University Press, Oxford, 2000).

[2] W. E. Stephens, *A pulsed mass spectrometer with time dispersion*, Phys. Rev. **69**, 691 (1964).

[3] P. Gambardella, S. Rusponi, M. Veronese, S. S. Dhesi, C. Grazioli, A. Dallmeyer, I. Cabria, R. Zeller, P. H. Dederichs, K. Kern, C. Carbone, and H. Brune, *Giant magnetic anisotropy of single cobalt atoms*, Science **300**, 1130 (2003).

[4] J. A. Alonso, *Structure and properties of atomic nanoclusters*, Imperial college press, London (2005).

[5] P. Crespo, R. Litrán, T. C. Rojas, M. Multigner, J. M. de la Fuente, J. C. Sánchez-López, M. A. García, A. Hernando, S. Penadés, and A. Fernández, *Permanent magnetism, magnetic anisotropy, and hysteresis of thiol-capped gold nanoparticles*, Phys. Rev. Lett. **93**, 087204 (2004).

[6] F. Baletto and R. Ferrando, *Structural properties of nanoclusters: Energetic, thermodynamic, and kinetic effects*, Rev. Mod. Phys. **77**, 371 (2005).

[7] M. E. Gruner and P. Entel, *Simulating functional magnetic materials on supercomputers*, J. Phys.: Condens. Matter, **21**, 293201 (2009).

[8] S. Blundell, *Magnetism in Condensed Matter*, (Oxford University Press, Oxford, 2001).

[9] R. Skomski, *Simple Models of Magnetism*, (Oxford University Press, Oxford, 2008).

[10] J. Stöhr and H. C. Siegmann, *Magnetism from Fundamentals to Nanoscale Dynamics*, (Springer, Berlin, 2006).

[11] M. A. Ruderman and C. Kittel, *Indirect exchange coupling of nuclear magnetic moments by conduction electrons*, Phys. Rev. **96**, 99 (1954).

[12] T. Kasuya, *A theory of metallic ferro- and antiferromagnetism on Zener's model*, Prog. Theor. Phys. **16**, 45 (1956).

[13] K. Yoshida, *Magnetic Properties of Cu-Mn Alloys*, Phys. Rev. **106**, 893 (1957).

[14] H. A. Jahn and E. Teller, *Stability of polyatomic molecules in degenerate electronic states. I. Orbital degeneracy*, Proc. R. Soc. London A **161**, 220 (1937).

[15] W. D. Knight, K. Clemenger, W. A. de Heer, W. A. Saunders, M. Y. Chou, and M. L. Cohen, *Electronic shell structure and abundances of sodium clusters*, Phys. Rev. Lett. **52**, 2141 (1984).

[16] F.E. Kruis, H. Fissan, and A. Peled, *Synthesis of nanoparticles in the gas phase for electronic, optical and magnetic applications-a review*, J. Aerosol Sci. **29**, 511 (1998).

[17] M. L. Plumer, E. J. Van, and D. Weller, *The Physics of Ultra-high-density Magnetic Recording*, (Springer, Berlin, 2001)

[18] S. Sahoo, A. Hucht, M. E. Gruner, G. Rollmann, and P. Entel, A. Postnikov, J. Ferrer, L. Fernández-Seivane, M. Richter, D. Fritsch, and S. Sil, *Magnetic properties of small Pt-capped Fe, Co, and Ni clusters: A density functional theory study*, Phys. Rev. B **82**, 054418 (2010).

[19] A. Zangwill, *Physics at Surfaces*, (Cambridge University Press, Cambridge, 1988).

[20] E. Yoo, T. Okata, T. Akita, M. Kohyama, J. Nakamura, and I. Honma, *Enhanced electrocatalytic activity of Pt subnanoclusters on graphene nanosheet surface*, Nano Lett. **9**, 2255 (2009).

[21] G. M. Scheuermann, L. Rumi, P. Steurer, W. Bannwarth, and R. Mulhaupt, *Palladium nanoparticles on graphite oxide and its functionalized graphene derivatives as highly active catalysts for the Suzuki-Miyaura coupling reaction*, J. Am. Chem. Soc. **131**, 8262 (2009).

[22] H. Jonsson, G. Mills, and K. W. Jacobsen, *Classical and Quantum Dynamics in Condensed Phase Simulations*, edited by B. J. Berne, G. Ciccotti, and D. F. Coker (World Scientific, 1998).

[23] A. Eichler and J. Hafner, *Reaction channels for the catalytic oxidation of CO on Pt(111)*, Phys. Rev. B **59**, 5960 (1999).

[24] P. Lazić, M. Alaei, N. Atodiresei, V. Caciuc, R. Brako, and S .Blügel, *Density functional theory with nonlocal correlation: A key to the solution of the CO adsorption puzzle*, Phys. Rev. B, **81** 045401 (2010).

[25] G. Kresse and J. Furthmüller, *Efficiency of ab initio total energy calculations for metals and semiconductors using a plane-wave basis set*, Comput. Mater. Sci. **6**, 15 (1996).

[26] G. Kresse and D. Joubert, *From ultrasoft pseudopotentials to the projector augmented-wave method*, Phys. Rev. B **59**, 1758 (1999).

[27] P. E. Blöchl, *Projector augmented-wave method*, Phys. Rev. B **50**, 17953 (1994).

[28] J. M. Soler, E. Artacho, J. D. Gale, A. Gracía, J. Junquera, P. Ordejón, and D. Sánchez-Portal, *The SIESTA method for ab initio order-N materials simulation*, J. Phys.: Condens. Matter **14**, 2745 (2002).

[29] K. Koepernik and H. Eschrig, *Full-potential nonorthogonal local-orbital minimum-basis band-structure scheme*, Phys. Rev. B **59**, 1743 (1999).

[30] J. Schnack, *Effects of frustration on magnetic molecules: a survey from Olivier Kahn until today*, Dalton Trans. **39**, 4677 (2010).

[31] A. Hucht, S, Sahoo, S. Sil, and P. Entel, *Effect of anisotropy on small magnetic clusters,* Accepted in Phys. Rev. B. (2011).

[32] P. Hohenberg and W. Kohn, *Inhomogeneous electron gas*, Phys. Rev. **136**, B864 (1964).

[33] W. Kohn and L. J. Sham, *Self-Consistent equations including exchange and correlation effects*, Phys. Rev. **140**, A1133 (1965).

[34] R. M. Martin, *Electronic Structure: Basic Theory and Practical Methods*, (Cambridge University Press, Cambridge, 2004).

[35] L. H. Thomas, *The calculation of atomic fields*, Proc. Cambridge Phil. Roy. Soc. **23**, 542 (1927).

[36] E. Fermi, *Un metodo statistico per la determinazione di alcune priorieta dell atome*, Rend. Accad. Naz. Lincei **26**, 376 (1930).

[37] F. J. Jensen, *Introduction to Computational Chemistry*, Wiley, Chichester (1999).

[38] J. S. Blakemore, *Solid State Physics*, (Cambrige University Press, Cambridge, 1985).

[39] M. C. Payne, M. P. Teter, D. C. Allan, T. A. Arias, and J. D. Joannopoulos, *Iterative minimization techniques for ab initio total-energy calculations: Molecular dynamics and conjugate gradients,* Rev. Mod. Phys **64**, 1045 (1992).

[40] Per Söderlind, J. M. Wills, B. Johansson, and O. Eriksson, *Structural properties of plutonium from first-principles theory*, Phys. Rev. B **55**, 1997 (1997).

[41] U. von Barth and L. Hedin, *A local exchange-correlation potential for the spin polarized case:I*, J. Phys. C **5**, 1629 (1972).

[42] R. Q. Wu and A. J. Freeman, *Spin-orbit induced magnetic phenomena in bulk metals and their surfaces and interfaces.*, J. Magn. Mag. mater. **200**, 498 (1999).

[43] G.H.O. Daalderop, P. J. Kelly, and M. F. H. Schuurman, *First-principles calculation of the magnetocrystalline anisotropy energy of iron, cobalt and nickel*, Phys. Rev. B **42**, 11919 (1990).

[44] X. D. Wang, D. S. Wang, R. Q. Wu and A. J. Freeman, *Validity of the force theorem for magnetocrystalline anisotropy*, J. Magn. Mag. mater. **159**, 337 (1996).

[45] *Handbook of Magnetism and Advanced Magnetic Materials, Vol. 1* edited by H. Kronmüller and S. Parkin (Wiley, 2007).

[46] O. Eriksson, *Band-Ferromagnetism*, edited by K. Baberschke, M. Donath and W. Nolting, (Springer, Berlin, 2001).

[47] X. Wang, R. Wu, D. Wang, and A. J. Freeman, *Torque method for the theoretical determination of magnetocrystalline anisotropy*, Phys. Rev. B **54**, 61 (1996).

[48] M. P. Teter, M. C. Payne, and D. C. Allan, *Solution of Schrödinger's equation for large systems* Phys. Rev. B **40**, 12255 (1989).

[49] W. H. Press, B. P. Flannery, S. A. Teukolsky, and W. T. Vetterling, *Numerical Recipies*, (Cambridge University Press, 1992).

[50] R. P. Feynman, *Forces in molecules*, Phys. Rev. **56**, 340 (1939).

[51] P. Pulay, *Ab initio calculation of force constants and equilibrium geometries. I. theory*, Mol. Phys. **17**, 197 (1969).

[52] I. M. L. Billas, A. Châtelain, and W. A. de Heer, *Magnetism of Fe, Co and Ni clusters in molecular beams*, JMMM **168**, 64 (1997).

[53] I. M. L. Billas, A. Châtelain, and W. A. de Heer, *Magnetism from the Atom to the Bulk in iron, cobalt, and nickel clusters*, Science **265**, 1682 (1994).

[54] S. E. Apsel, J. W. Emmert, J. Deng, and L. A. Bloomfield, *Surface-enhanced magnetism in nickel clusters*, Phys. Rev. Lett., **76** 1441 (1996).

[55] Isabelle M. L. Billas, J. A. Becker, A. Châtelain, and Walt A. de Heer, *Magnetic moments of iron clusters with 25 to 700 atoms and their dependence on temperature*, Phys. Rev. Lett. **71**, 4067 (1993).

[56] M. Castro, C. Jamorski, and D. R. Salahub, *Structure, bonding, and magnetism of small* Fe_n, Co_n *and* Ni_n *clusters*, $n \leq 5$, Chem. Phys. Lett. **271** 133 (1997).

[57] R. Singh and P. Kroll, *Structural, electronic, and magnetic properties of 13-, 55-, and 147-atom clusters of Fe, Co, and Ni: A spin-polarized density functional study*, Phys. Rev. B **78**, 245404 (2008).

[58] H. M. Duan, X. G. Gong, Q. Q. Zheng, and H. Q. Lin, *Electronic and magnetic properties of Ni clusters*, J. Appl. Phys. **89** 7308 (2001).

[59] J. Guevara, F. Parisi, A. M. Llois, and M. Weissmann, *Electronic properties of transition-metal clusters: Consideration of the spillover in a bulk parametrization*, Phys. Rev. B **55** 13283 (1997).

[60] G. M. Pastor, J. Dorantes-Dávila, and K. H. Bennemann, *Size and structural dependence of the magnetic properties of small 3d-transition-metal clusters*, Phys. Rev. B **40** 7642 (1989).

[61] E. K. Parks, L. Zhu, J. Ho and S.J. Riley, *The structure of small nickel clusters. I.* Ni_3-Ni_{15}, J. Chem. Phys. **100** 7206 (1994).

[62] E. K. Parks, L. Zhu, J. Ho and S. J. Riley, *The structure of small nickel clusters. II.* $Ni_1$6-Ni_{28}, J. Chem. Phys. **100** 7377 (1995).

[63] B. V. Reddy, S. K. Nayak, S. N. Khanna, B. K. Rao, and P. Jena, *Physics of nickel clusters, electronic structure and magnetic properties*, J. Phys. Chem. A **102**, 1748 (1998).

[64] F. Aguilera-Granja, S. Bouarab, M. J. López, A. Vega, J. M. Montejano-Carrizales, M. P. Iniguez, and J. A. Alonso, *Magnetic moments of Ni clusters*, Phys. Rev. B **57** 12469 (1998).

[65] F. A. Reuse, and S. N. Khanna, *Geometry, electronic structure, and magnetism of small* Ni_n *(n=2-6,8,13)clusters*, Chem. Phys. Lett. **234** 77 (1995).

[66] T. Futschek, J. Hafner, and M. Marsman, *Stable structural and magnetic isomers of small transition-metal clusters from the Ni group: an ab initio density-functional study*, J. Phys.: Condens. Matter, **18**, 9703 (2006).

[67] H. Purdum, P. A. Montano, G. K. Shenoy, and T. Morrison, *Extended-x-ray-absorption-fine-structure study of small Fe molecules isolated in solid neon*, Phys. Rev. B **25**, 4412 (1982).

[68] P. A. Montano, and G. K. Shenoy, *EXAFS study of iron monomers and dimers isolated in solid argon*, Solid state Commun. **35**, 53 (1980).

[69] E. K. Parks, B. H. Weiller, P. S. Bechthold, W. F. Hoffman, G. C. Nieman, L. G. Pobo, and S. J. Riley, *Chemical probes of metal cluster structure: Reactions of iron clusters with hydrogen, ammonia, and water*, J. Chem. Phys. **88**, 1622 (1988).

[70] T. L. Haslett, K. A. Bosnick, S. Fedrigo, and M. Moskovits, *Resonance Raman spectroscopy of matrix-isolated mass-selected* Fe_3 *and* Ag_3, J. Chem. Phys. **111**, 6456 (1999).

[71] E. A. Rohlfing, D. M. Cox, A. Kaldor, and K. H. Johnson, *Photoionization spectra and electronic structure of small iron clusters*, J. Chem. Phys. **81**, 3846 (1984).

[72] S. Yang and M. B. Knickelbein, *Photoionization studies of transition metal clusters: Ionization potentials for* Fe_n *and* Co_n, J. Chem. Phys. **93**, 1533 (1990).

[73] L. Wang, H. Cheng, and J. Fan, *Photoelectron spectroscopy of size-selected transition metal clusters:* Fe_n^-*, n=3-24*, J. Chem. Phys. **102**, 9480 (1995).

[74] L. Wang, X. Li, and H. Zhang, *Probing the electronic structure of iron clusters using photoelectron spectroscopy*, Chem. Phys. **262**, 53 (2000).

[75] A. Andriotis and M. Menon, *Tight-binding molecular-dynamics study of ferromagnetic clusters*, Phys. Rev. B **57**, 10069 (1998).

[76] J. L. Chen, C. S. Wang, K. A. Jackson, and M. R. Pederson, *Theory of magnetic and structural ordering in iron clusters*, Phys. Rev. B **44**, 6558 (1991).

[77] M. Castro and D. R. Salahub, *Theoretical study of the structure and binding of iron clusters:* Fe_n $n \leq 5$, Phys. Rev. B **47** 10955 (1993).

[78] P. Ballone and R. O. Jones, *Structure and spin in small iron clusters*, Chem. Phys. Lett. **233**, 632 (1995).

[79] O. Diéguez, M. M. G. Alemany, C. Rey, P. Ordejón, and L. J. Gallego, *Density-functional calculations of the structures, binding energies, and magnetic moments of Fe clusters with 2 to 17 atoms*, Phys. Rev. B **63**, 205407 (2001).

[80] P. Bobadova-Parvanova, K. A. Jackson, S. Srinivas, M. Horoi, C. Köhler and G. Seifert, *Scanning the potential energy surface of iron clusters: A novel search strategy*, J. Chem. Phys. **116**, 3576 (2002).

[81] M. Castro and D. R. Salahub, *Density-functional calculations for small iron clusters:* Fe_n, Fe_n^+, *and* Fe_n^- *for* $n \leq 5$, Phys. Rev. B **49** 11842 (1994).

[82] O N Mryasov, A I Liechtenstein, L M Sandratskii and V A Gubanov, *Magnetic structure of FCC iron*, J. Phys.: Condens. Matter **3**, 7683 (1991).

[83] T. Oda, A. Pasquarello, and R. Car, *Fully unconstrained approach to noncollinear magnetism: Application to small Fe clusters*, Phys. Rev. Lett. **80**, 3622 (1998).

[84] D. Hobbs, G. Kresse, and J. Hafner, *Fully unconstrained noncollinear magnetism within the projector augmented-wave method*, Phys. Rev. B **62** 11556 (2000).

[85] M. Zelený, M. Sob and J. Hafner, *Noncollinear magnetism in manganese nanostructures*, Phys. Rev. B **80** 144414 (2009).

[86] C. J. Barden, J. C. Rienstra-Kiracofe, and H. F. Schaefer III *Homonuclear 3d transition-metal diatomics: A systematic density functional theory study*, J. Chem. Phys. **113** 690 (2000).

[87] J. C. Pinegar, J. D. Langenberg, C. A. Arrington, E. M. Spain, and M. D. Morse, Ni_2 *revisited: Reassignment of the ground electronic state*, J. Chem. Phys. **102** 666 (1994).

[88] M. Bienati, V. Bonacic-Koutecky, and P. Fantucci, *The electronic structre and magnetic properties of the nickel tetramer and its partially carbonylated forms*, Eur. Phys. J. D **9** 467 (1999).

[89] M. C. Michelini, R. P. Diez, and A. H. Joubert, *Density functional calculations of* Ni_5 *and* Ni_6 *clusters*, Journal of Molecular Structure, **490** 181 (1999).

[90] M. Böyükata, Z. B. Güvenc, S. Özcelik, P. Durmus, and J. Jillinek, *Structure and reactivity of* Ni_n *(n = 7-14, 19) clusters*, Int. J. Quant. Chem. **84**, 208 (2001).

[91] S. K. Nayak, S. N. Khanna, B. K. Rao, and P. Jena, *Physics of Nickel Clusters: Energetics and Equilibrium Geometries*, J. Phys. Chem. A **101**, 1072 (1997).

[92] N. Desmarais, C. Jamorski, F. A. Reuse, and S. N. Khanna, *Atomic arrangements in* Ni_7 *and* Ni_8 *clusters*, Chem. Phys. Lett. **294**, 480 (1998).

[93] D. M. Cox, D. J. Trevor, R. L. Whetten, E. A. Rohlfing, and A. Kaldor, *Magnetic behavior of free-iron and iron oxide clusters*, Phys. Rev. B **32** 7290 (1985).

[94] G. Rollmann, P. Entel, and S. Sahoo, *Competing structural and magnetic effects in small iron clusters*, Comput. Matter. Sci. **35**, 275 (2006).

[95] G. Rollmann, S. Sahoo, and P. Entel, *Structural and magnetic properties of Fe-Ni clusters*, Phys. Status Solidi A, **201** 3263 (2004).

[96] B. I. Dunlap, *Symmetry and cluster magnetism*, Phys. Rev. A **41**, 5691 (1990).

[97] P. Bobadova-Parvanova, K. A. Jackson, S. Srinivas, and M. Horoi, *Density-functional investigations of the spin ordering in* Fe_{13} *clusters*, Phys. Rev. B **66** 195402 (2002).

[98] M. B. Knickelbein, *Adsorbate-induced enhancement of the magnetic moments of iron clusters*, Chem. Phys. Lett. **353**, 221 (2002).

[99] V. L. Moruzzi, P. M. Marcus, K. Schwarz, and P. Mohn, *Ferromagnetic phases of bcc and fcc Fe, Co, and Ni*, Phys. Rev. B **34**, 1784 (1986).

[100] G. Rollmann, M. E. Gruner, A. Hucht, R. Meyer, P. Entel, M. L. Tiago, and J. R. Chelikowsky, *Shellwise Mackay Transformation in Iron Nanoclusters*, Phys. Rev. Lett. bf 99, 083402 (2007).

[101] H. C. Herper, E. Hoffmann, and P. Entel, *Ab initio full-potential study of the structural and magnetic phase stability of iron*, Phys. Rev. B, **60**, 3839 (1999).

[102] L. Favre, V. Dupuis, E. Bernstein, P. Mélinon, A. Pérez, S. Stanescu, T. Epicier, J. -P. Simon, D. Babonneau, J. -M. Tonnerre, and J. -L. Hodeau, *Structural and magnetic properties of CoPt mixed clusters*, Phys. Rev. B **74**, 014439 (2006).

[103] R. Ferrando A. Fortunelli, and G. Rossi, *Quantum effects on the structure of pure and binary metallic nanoclusters*, Phys. Rev. B. **72**, 085449 (2005).

[104] J. Vrijen and S. Radelaar, *Sigmalike phase and nanoscale segregation in polycrystalline* Fe_xCr_{1-x} *films: An element-resolved magnetic and structural study*, Phys. Rev. B **61** 64 (2000).

[105] S. Heinrichs, W. Dieterich, and P. Maass *Modeling epitaxial growth of binary alloy nanostructures on a weakly interacting substrate*, Phys. Rev. B. **75**, 085437 (2007).

[106] F. R. Negreiros, Z. Kuntová, G. Barcaro, G. Rossi, R. Ferrando, and A. Fortunelli, *Structures of gas-phase Ag-Pd nanoclusters: A computational study*, J. Chem. Phys. **132**, 234703 (2010).

[107] G. Rossi, R. Ferrando and C. Mottet, *Structure and chemical ordering in CoPt nanoalloys*, Faraday Discuss. **138**, 193 (2008).

[108] M. Gruner and P. Entel, *Structural and magnetic properties of ternary* $Fe_{1-x}Mn_xPt$ *nanoalloys from first principles*, Bailstein J. Nanotechnol. **2**, 162 (2011).

[109] N. T. Wilson and R. L. Johnston, *A theoretical study of atom ordering in copper-gold nanoalloy clusters*, J. Mater. Chem. **12** 2913 (2002).

[110] L. D. Lloyd, R. L. Johnston, S. Salhi, and N. T. Wilson, *Theoretical investigation of isomer stability in platinum-palladium nanoalloy clusters*, J. Mater. Chem. **14** 1691 (2004).

[111] C. Mottet, G. Tréglia and B. Legrand, *Theoretical investigation of chemical and morphological ordering in* Pd_cCu_{1-c} *clusters*, Phys. Rev. B **66** 045413 (2002).

[112] S. Darby, T. V. Mortimer-Jones, R. L. Johnston, C. Roberts, *Theoretical study of Cu-Au nanoalloy clusters using a genetic algorithm*, J. Chem. Phys. **116** 1536 (2002).

[113] M.S. Bailey, N.T. Wilson, C. Roberts, and R. L. Johnston, *Structures, stabilities and ordering in Ni-Al nanoalloy clusters*, Eur. Phys. J. D **25** 41 (2003).

[114] E.B. Krissinel and J. Jellinek, *13-atom Ni-Al alloy clusters: Structures and dynamics*, Int. J. Quant. Chem. **62** 185 (1996).

[115] J. L. Rousset, A. M. Cadrot, F. J. Cadete Santos Aires, A. Renouprez, P. Mélinon, A. Perez, M. Pellarin, J. L. Vialle, and M. Broyer, *Study of bimetallic Pd-Pt clusters in both free and supported phases*, J. Chem. Phys. **102** 8574 (1995).

[116] H. Yasuda and K. Furuya, *Spontaneous alloying of tin atoms into nanometer-sized gold clusters and phase stability in the resultant alloy clusters* Eur. Phys. J. D **10** 279 (2000).

[117] J.M. Montejano-Carrizales, M. P. Iñiguez, and J. A. Alonso, *Embedded-atom method applied to bimetallic clusters: The Cu-Ni and Cu-Pd systems*, Phys. Rev. B **49** 16649 (1994).

[118] F. Baletto, C. Mottet and R. Ferrando, *Growth simulations of silver shells on copper and palladium nanoclusters*, Phys. Rev. B **66** 155420 (2002).

[119] J. Bansmann, S. H. Baker, C. Binns, J. A. Blackman, J.-P. Bucher, J. Dorantes-Dávila, V. Dupuis, L. Favre, D. Kechrakos, A. Kleibert, K.-H. Meiwes-Broer, G. M. Pastor, A. Perez, O. Toulemonde, K. N. Trohidou, J. Tuaillon, and Y. Xie, *Magnetic and structural properties of isolated and assembled clusters*, Surf. Sci. Rep. **56**, 189 (2005).

[120] D. Zitoun, M. Respaud, M. Fromen, M. J. Casanove, P. Lecante, C. Amiens, and B. Chaudret, *Magnetic enhancement in nanoscale CoRh particles*, Phys. Rev. Lett. **89**, 037203 (2002).

[121] N. Nunomura, H. Hori, T. Teranish, M. Miyake, and S. Yamada, *Magnetic properties of nanoparticles in Pd/Ni alloys*, Phys. Lett. A **249** 524 (1998).

[122] Y. H. Lu, M. Zhou, C. Zhang, Y. P. Feng, *Metal-embedded Graphene: A possible catalyst with high activity*, J. Phys. Chem. C **113** 20156 (2009).

[123] G. Mpourmpakis, G. E. Froudakis, A. N. Andriotis, and A. Menon, *Role of Co in enhancing the magnetism of small Fe clusters*, Phys. Rev. B **72** 104417 (2005).

[124] B.K. Rao, S.R. de Debiaggi and P. Jena, *Structure and magnetic properties of Fe-Ni clusters*, Phys. Rev. B **64** 024418 (2001).

[125] N. Nunomura, H. Hori, T. Teranish, M. Miyake, and S. Yamada, *Structural and magnetic properties of CoRh nanoparticles*, Phys. Rev. B **70** 014410 (2004).

[126] S. Dennler, J. L. Ricardo-Chavez, J. Morillo, and G. M. Pastor, *Density functional calculations on small bimetallic magnetic clusters*, Eur. Phys. J. D **24** 237 (2003).

[127] T. Sondón, J. Guevara, and A. Saúl, *Study of the structure, segregation, and magnetic properties of Ni-Rh clusters*, Phys. Rev. B **75** 104426 (2007).

[128] G. Rollmann, *Ab initio simulationen eisenhaltiger systeme: vom Festkörper zum cluster*, PhD Thesis, University of Duisburg-Essen (2007).

[129] V. Crisan, P. Entel, H. Ebert, H. Akai, D. D. Johnson, and J. B. Staunton, *Magnetochemical origin for Invar anomalies in iron-nickel alloys*, Phys. Rev. B **66** 014416 (2002).

[130] K. Kadau, M. E. Gruner, P. Entel, and M. Kreth, *Modeling structural and magnetic phase transitions in iron-nickel nanoparticles*, Phase Trans. **76** 355 (2003).

[131] S. Sahoo, G. Rollmann and P. Entel, *Segregation and ordering in binary transition metal clusters*, Phase Trans. **79** 693 (2006).

[132] S. Sahoo, G. Rollmann and P. Entel, *First-principles calculation of cluster geometries and magnetization of pure Ni and Fe-Ni clusters*, Phase Trans. **78** 723 (2005).

[133] J. Kaspar, and D. R. Salahub, *Explanation of the Invar Anomalies from Molecular-Orbital Cluster Calculations*, Phys. Rev. Lett. **47** 54 (1981).

[134] H.C. Herper, *Ab initio untersuchung magnetischer und struktureller Eigenschaften von 3d-Übergangsmetallen und ihren Legierungen*, PhD thesis, University of Duisburg-Essen (2000).

[135] F. Aguilera-Granja and A. Vega, *Stability, magnetic behavior, and chemical order of* $(CoxFe1\text{-}x)_N$ *(N = 5, 13) nanoalloys*, Phys. Rev. B **79**, 144423 (2009).

[136] M. Pratzer and H. J. Elmers, *Magnetic and electronic properties of binary alloy monolayers:* Fe_xMn_{1-x} *and* $Co_{1-x}Fe_x$ *on W(110)*, Phys. Rev. B **69**, 134418 (2004).

[137] W. Pepperhoff, M. Acet, *Constitution and Magnetism of Iron and its Alloys*, Engineering Materials Vol. III, (Springer, Berlin, 2001).

[138] O. Kubaschewski, *Iron Binary Phase Diagrams* (Springer, Berlin, 1982). H. Masumoto, K. Watanabe, Japan Inst. Met. **42**, 256 (1978). J. Crangle, G. C. Hallam, Proc. Roy. Soc. London **A272**, 119 (1963).

[139] J. A. Alonso and N. H. March, *Electrons in Metals and Alloys* (Academic, London, 1989).

[140] R. M. Wang, O. Dmitrieva, M. Farle, G. Dumpich, H. Q. Ye, H. Poppa, R. Kilaas, and C. Kisielowski, *Layer resolved structural relaxation at the surface of magnetic FePt icosahedral nanoparticles*, Phys. Rev. Lett., **100** 017205 (2008).

[141] G. Rollmann, S. Sahoo, A. Hucht, and P. Entel, *Magnetism and chemical ordering in binary transition metal clusters*, Phys. Rev. B **78**, 134404 (2008).

[142] S. Yin, R. Moro, X. Xu, and W. A. de Heer, *Magnetic enhancement in cobalt-manganese alloy clusters*, Phys. Rev. Lett. **98**, 113401 (2007).

[143] M. B. Knickelbein, *Magnetic moments of small bimetallic clusters:* Co_nMn_m, Phys. Rev. B **75**, 014401 (2007).

[144] J. Crangle, *The magnetization of cobalt-manganese and cobalt-chromium alloys*, Philos. Mag. **2**, 659 (1957).

[145] G. L. Gutsev, M. D. Mochena, and C. W. Bauschlicher, *Structure and Properties of* Mn_n, Mn_n^-, *and* Mn_n^+ *Clusters (n = 3-10)*, J. Phys. Chem. A **110**, 9758 (2006).

[146] Z. Q. Qiu, J. Pearson, and S. D. Bader, *Asymmetry of the spin reorientation transition in ultra-thin Fe films and wedges grown on Ag(100)*, Phys. Rev. Lett. **70**, 1006 (1993).

[147] R. K. Kawakami, E. J. Escorcia-Aparicio, and Z. Q. Qiu, *Symmetry-induced magnetic anisotropy in Fe films grown on stepped Ag(001)*, Phys. Rev. Lett. **77**, 2570 (1996).

[148] M. Farle, B. Mirwald-Schulz, A. N. Anisimov, W. Platow, and K. Baberschke, *Higher-order magnetic anisotropies and the nature of the spin-reorientation transition in face-centered tetragonal Ni(001)/Cu(001)*, Phys. Rev. B, **55**, 3708 (1997).

[149] J. S. Hong and R. Q. Wu, *Magnetic properties of Co nanochains*, Phys. Rev. B **70**, 060406 (2004).

[150] P. Weinberger and L. Szunyogh, *Perpendicular magnetism in magnetic multilayer systems*, Comp. Mater. Sci. **17**, 414 (2000).

[151] D. D. Koelling and B. N. Harmon, *A technique for relativistic spin-polarised calculations*, J. Phys. C: Solid State Phys. **10**, 3107 (1977).

[152] O. Hjortstam, K. Baberschke, J. M. Wills, B. Johansson and O. Eriksson, *Magnetic anisotropy and magnetostriction in tetragonal and cubic Ni*, Phys. Rev. B., **55**, 15026 (1997).

[153] K. Baberschke,*The magnetism of nickel monolayers*, Appl. Phys. A **62**, 417 (1996).

[154] I. G. Baek, H. G. Lee, H. K. Kim, and E. Vescovo, *Spin reorientation transition in Fe(110) thin films: the role of surface anisotropy*, Phys. Rev. B **67**, 075401 (2003).

[155] R. Vollmer, and J. Kirschner, *Influence of* H_2 *adsorption on magnetic properties of Fe films on Cu(001).*, Phys. Rev. B, **61**, 4146 (2000).

[156] R. Vollmer, Th. Gutjahr-Löser and J. Kirschner, S. van Dijken, and B. Poelsema, *Spin-reorientation transition in Ni films on Cu(001): the influence of* H_2 *adsorption.*, Phys. Rev. B, **60**, 6277 (1999)

[157] D. Matsumura, T. Yokoyama, K. Amemiya, S. Kitagawa, and T. Ohta, *X-ray magnetic circular dichroism study of spin reorientation transitions of magnetic thin films induced by surface chemisorption*, Phys. Rev. B, **66**, 024402 (2002).

[158] D. Sander, W. Pan, S. Ouazi, J. Kirschner, W. Meyer, M. Krause, S. MÃŒller, L. Hammer, and K. Hein, *Reversible H-induced switching of the magnetic easy axis in Ni=Cu(001) thin films.*, Phys. Rev. Lett., **93**, 247203 (2004).

[159] P. Gambardella, A. Dallmeyer, K. Maiti, M. C. Malagoli, W. Eberhardt, K. Kern, and C. Carbone, *Ferromagnetism in one-dimensional monatomic metal chains*, Nature **416**, 301 (2002).

[160] N. Nilius, T. N. Wallis, and W. Ho, *Development of one-dimensional band structure in artificial gold chains*, Science **297**, 1853 (2002).

[161] S. Bedanta and W. Kleemann,*Superparamagnetism*, J. Phys. D: Appl. Phys., **42**, 013001 (2009).

[162] A. L. Barra, *Single-molecule magnet behavior of a tetranuclear iron(III) complex. The origin of slow magnetic relaxation in iron(III) clusters*, Journal of the American Chemical Society **121**, 5302 (1999).

[163] M. Jamet, W. Wernsdorfer, C. Thirion, D. Mailly, V. Dupuis, P. Mélinon, and A. Pérez, *Magnetic anisotropy of a single cobalt nanocluster*, Phys. Rev. Lett. **86**, 4676 (2001).

[164] M. Jamet, W. Wernsdorfer, C. Thirion, V. Dupuis, P. Mélinon, and A. Pérez, *Magnetic anisotropy in single clusters*, Phys. Rev. B **69**, 024401 (2004).

[165] P. Gambardella, A. Dallmeyer, K. Maiti, M. C. Malagoli, S. Rusponi, P. Ohresser, W. Eberhardt, C. Carbon, and K. Kern, *Oscillatory magnetic anisotropy in one-dimensional atomic wires*, Phys. Rev. Lett. **93**, 077203 (2004).

[166] S. Rusponi, T. Cren, N. Weiss, M. Epple, P. Buluschek, L. Claude, and H. Brune, *The remarkable difference between surface and step atoms in the magnetic anisotropy of two-dimensional nanostructures*, Nat. Mat. **2**, 546 (2003).

[167] M. Pratzer, H. J. Elmers, M. Bode, O. Pietzsch, A. Kubetzka, and R. Wiesendanger, *Atomic-scale magnetic domain walls in quasi-one-dimensional Fe nanostripes*, Phys. Rev. Lett. **87**, 127201 (2001).

[168] M. Pratzer and H. J. Elmers, *Domain wall energy in quasi-one dimensional Fe/W(110) nanostripes*, Phys. Rev. B **67**, 094416 (2003).

[169] J. S. Hong and R. Q. Wu, *First principles calculations of magnetic anisotropy energy of Co monatomic wires*, Phys. Rev. B **67**, 020406 (2003).

[170] B. Lazarovits, L. Szunyogh, and P. Weinberger, *Magnetic properties of finite Co chains on Pt(111)*, Phys. Rev. B **67**, 024415 (2003).

[171] A. B Shick, Y. N. Gornostyrev, and A. J. Freeman, *Magnetoelastic mechanism of spin reorientation transitions at step edges*, Phys. Rev. B **60**, 3029 (1999).

[172] A. B Shick, F. Maca, and P. M. Oppeneer, *Anomalous ferromagnetism of a monatomic Co wire at the Pt(111) surface step edge*, Phys. Rev. B **69**, 212410 (2004).

[173] C. Ederer, M. Komelj, and M. Fahnle, *Magnetism in systems with various dimensionalities: a comparison between Fe and Co*, Phys. Rev. B **68**, 052402 (2003).

[174] Y. Mokrousov, G. Bihlmayer, S. Heinze, and S. Blügel, *Giant magnetocrystalline anisotropies of 4d transition-metal monowires*, Phys. Rev. Lett. **96**, 147201 (2006).

[175] L. M. Sandratskii, *Noncollinear magnetism in itinerant-electron systems: Theory and applications* Adv. Phys. **47**, 91 (1998).

[176] L. M. Sandratskii and J. Kübler, *Noncollinear magnetism: Effects of symmetry and relativity*, Mod. Phys. Lett. B **10**, 189 (1996).

[177] T. Balashov, T. Schuh, A. F. Takács, A. Ernst, S. Ostanin, J. Henk, I. Mertig, P. Bruno, T. Miyamachi, S. Suga, and W. Wulfhekel, *Magnetic anisotropy and magnetization dynamics of individual atoms and clusters of Fe and Co on Pt(111)*, Phys. Rev. Lett. **102**, 257203 (2009).

[178] R. Félix-Medina, J. Dorantes-Dávila, and G. M. Pastor, *Ground-state magnetic properties of Co_N clusters on Pd(111): Spin moments, orbital moments, and magnetic anisotropy*, Phys. Rev. B **67**, 094430 (2003).

[179] S. Rohart, C. Raufast, L. Favre, E. Bernstein, E. Bonet, and V. Dupuis, *Magnetic anisotropy of $CoxPt1-x$ clusters embedded in a matrix: Influences of the cluster chemical composition and the matrix nature*, Phys. Rev. B **74**, 104408 (2006).

[180] A. N. Andriotis and M. Menon, *Orbital Magnetism: Pros and Cons for Enhancing the Cluster Magnetism*, Phys. Rev. Lett. **93**, 026402 (2004).

[181] Š. Pick, V. S. Stepanyuk, A. L. Klavsyuk, L. Niebergall, W. Hergert, J. Kirschner, and P. Bruno, *Magnetism and structure on the atomic scale: Small cobalt clusters in Cu(001)*, Phys. Rev. B **70**, 224419 (2004).

[182] J. Hafner and D. Spišák, *Morphology and magnetism of Fe_n clusters $(n=1-9)$ supported on a Pd(001) substrate*, Phys. Rev. B **76**, 094420 (2007).

[183] S. Bornemann, J. Minár, J. B. Staunton, J. Honolka, A. Enders, K. Kern, and H. Ebert, *Magnetic anisotropy of deposited transition metal clusters*, Eur. Phys. J. D **45**, 529 (2007).

[184] B. Nonas, I. Cabria, R. Zeller, P. H. Dederichs, T. Huhne and H. Ebert, *Strongly enhanced orbital moments and anisotropies of adatoms on the Ag(001) surface*, Phys. Rev. Lett. **86**, 2146 (2001).

[185] G. M. Pastor, J. Dorantes-Dávila, S. Pick, and H. Dreyssé, *Magnetic anisotropy of 3d transition-metal clusters*, Phys. Rev. Lett. **75**, 326 (1995).

[186] R. A. Guirado-López and J. M. Montejano-Carrizales, *Orbital magnetism and magnetic anisotropy energy of Co nanoparticles: Role of polytetrahedral packing, polycrystallinity, and internal defects*, Phys. Rev. B **75**, 184435 (2007).

[187] L. Fernández-Seivane and J. Ferrer, *Magnetic anisotropies of late transition metal atomic clusters*, Phys. Rev. Lett. **99**, 183401 (2007).

[188] P. Błoński and J. Hafner, *Magnetic anisotropy of transition-metal dimers: Density functional calculations*, Phys. Rev. B **79**, 224418 (2009).

[189] Y. Xie and J. A. Blackman, *Magnetic anisotropy of nanoscale cobalt particles*, J. Phys.: Condens. Matter **16**, 3163 (2004).

[190] T. O. Strandberg, C. M. Canali, and A. H. MacDonald, *Transition-metal dimers and physical limits on magnetic anisotropy*, Nature Mater. **6**, 648 (2007).

[191] D. Fritsch, K. Koepernik, M. Richter, and H. Eschrig, *Transition metal dimers as potential molecular magnets: A challenge to computational chemistry*, J. Comp. Chem. **29**, 2210 (2008).

[192] J. Kortus, T. Baruah, and M. R. Pederson, *Magnetic moment and anisotropy in* Fe_nCo_m *clusters*, Appl. Phys. Lett. **80**, 4193 (2002).

[193] J. Hong, and R. Q. Wu, *First principles determinations of magnetic anisotropy energy of Co nanoclusters*, J. Appl. Phys. **93**, 8764 (2003).

[194] F. Luis, J. Bartolomé, F. Bartolomé, M. J. Martínez, L. M. García, F. Petroff, C. Deranlot, F. Wilhelm, and A. Rogalev, *Enhancement of the magnetic anisotropy of Co clusters by Au capping*, J. Appl. Phys. **99**, 08G705 (2006).

[195] S. Dennler, J. Morillo, and G. M. Pastor, *First-principles study of binary transition-metal clusters and alloys*, J. Phys.: Condens. Matter. **16**, S2263 (2004).

[196] M. Muñoz-Navia, J. Dorantes-Dávila, and G. M. Pastor, *Calculation of the orbital magnetic moments in fcc 3d-4d binary clusters: Co-Rh and Co-Pd*, J. Phys.: Condens. Matter. **16**, S2251 (2004).

[197] J. P. Perdew, in *Electronic Structure of Solids'91*, edited by P. Ziesche and H. Eschrig (Berlin, Akademie Verlag, 1991), pp. 11-20.

[198] J. Junquera, Ó. Paz, D. Sánchez-Portal, and E. Artacho, *Numerical atomic orbitals for linear-scaling calculations*, Phys. Rev. B **64**, 235111 (2001).

[199] N. Troullier and J. L. Martins, *Efficient pseudopotentials for plane-wave calculations*, Phys. Rev. B **43**, 1993 (1991).

[200] L Fernández-Seivane, M. A. Oliveira, S. Sanvito, and J. Ferrer, *On-site approximation for spin-orbit coupling in linear combination of atomic orbitals density functional methods*, J. Phys.: Condens. Matter **18**, 7999 (2006).

[201] H. Eschrig, M. Richter, and I. Opahle, in: *Relativistic Solid State Calculations. Relativistic Electronic Structure Theory – Part II: Applications*, edited by P. Schwerdtfeger (Amsterdam: Elsevier, 2004), pp. 723-776.

[202] J. P. Perdew and Y. Wang, *Accurate and simple analytic representation of the electron-gas correlation energy*, Phys. Rev. B **45**, 13244 (1992).

[203] M. E. Gruner, P. Entel, I. Opahle, and M. Richter, *Ab initio investigation of twin boundary motion in the magnetic shape memory Heusler alloy* Ni_2MnGa, J. Mater. Sci. **43**, 3825 (2008).

[204] L. Néel, C. R. Acad. Sci. Paris **237**, 1468 (1953).

[205] L. Néel, *Anisotropie magnétique superficielle et surstructures d'orientation*, J. Phys. Radium. **15**, 225 (1954).

[206] A. L. Mackay, *A dense non-crystallographic packing of equal spheres*, Acta Cryst. **15**, 916 (1962).

[207] R. A. Guirado-López, J. Dorantes-Dávila, and G. M. Pastor, *Orbital Magnetism in Transition-Metal Clusters: From Hund's Rules to Bulk quenching*, Phys. Rev. Lett. **90**, 226402 (2003).

[208] S. V. Halilov, A. Ya. Perlov, P. M. Oppeneer, A. N. Yaresko, and V. N. Antonov, *Magnetocrystalline anisotropy energy in cubic Fe, Co, and Ni: Applicability of local-spin-density theory reexamined*, Phys. Rev. B **57**, 9557 (1998).

[209] H. Ebert, S. Bornemann, J. Minár, P. H. Dederichs, R. Zeller, and I. Cabria, *Magnetic properties of Co- and FePt-clusters*, Comput. Mater. Sci. **35**, 279 (2006).

[210] C. G. Zimmermann, M. Yeadon, K. Nordlund, J. M. Gibson, and R. S. Averback, *Burrowing of Co nanoparticles on clean Cu and Ag surfaces*, Phys. Rev. Lett. **83**, 1163 (1999).

[211] J. Honolka, T. Y. Lee, K. Kuhnke, A. Enders, R. Skomski, S. Bornemann, S. Mankovsky, and J. Minár *Magnetism of FePt Surface Alloys*, Phys. Rev. Lett., **92**, 147202 (2004).

[212] J. S. Tsay and C. S. Shern, *Diffusion and alloy formation of Co ultrathin films on Pt(111)*, J. Appl. Phys., **80**, 3777 (1996).

[213] D. N. Tafen and L. J. Lewis, *Structure and energetics of Ni and Au nanoclusters deposited on the (001), (110), and (111) surfaces of Au and Ni: A molecular dynamics study*, Phys. Rev. B **77**, 075429 (2008).

[214] Y. Xie and J. A. Blackman, *Theory of enhanced magnetic anisotropy induced by Pt adatoms on two-dimensional Co clusters supported on a Pt(111) substrate*, Phys. Rev. B **74** 054401 (2006).

[215] O. Šipr, J. Minár and H. Ebert, *Magnetism of free and supported clusters: a comparative study*, Cent. Eur. J. Phys. **7** 257 (2009).

[216] S. K. Nayak, P. Jena, V. S. Stepanyuk and W. Hergert, *Effect of atomic relaxation on the magnetic moment of Fe, Co and Ni dimers supported on Cu(001)*, Surf. Sci., **491** 219 (2001).

[217] L. Tang, X. Zhang, and Q. Guo, *Organizing C_{60} molecules on a nanostructured Au(111) surface*, surf. Sci. **604** 1310 (2010).

[218] J. Chen, M. Drakaki, C. A. Ballentine, and J. L. Erskine, Bull. Am. Phys. Soc. **35**, 199 (1989).

[219] K. von Bergmann, M. Bode, and R. Wiesendanger *Magnetism of iron on tungsten (001) studied by spin-resolved scanning tunneling microscopy and spectroscopy*, Phys. Rev. B **70**, 174455 (2004).

[220] J. T. Lau, A. Föhlisch, M. Martins, R. Nietubyc, M. Reif and W. Wurth, *Spin and orbital magnetic moments of deposited small iron clusters studied by x-ray magnetic circular dichroism spectroscopy*, New J. Phys. **4**, 98 (2002).

[221] K. W. Edmonds, C. Binns, S. H. Baker, S. C. Thornton, C. Norris, J. B. Goedkoop, M. Finazzi, and N. B. Brookes, *Doubling of the orbital magnetic moment in nanoscale Fe clusters*, Phys. Rev. B **60**, 472 (1999).

[222] S. Polesya, O. Šipr, S. Bornemann, J. Minár, and H. Ebert, *Magnetic properties of free Fe clusters at finite temperatures from first principles*, Europhys. Lett. **74**, 1074 (2006).

[223] P. Mavropoulos, S. Lounis, R. Zeller and S. Blügel *Fe clusters on Ni and Cu: size and shape dependence of the spin moment*, Appl. Phys. A **82** 103 (2006).

[224] T. I. Fu, P. C. Liao, and C. S. Shern, *Growth mechanism and surface alloy formation of Ni on Pt(110) surface*, J. Vac. Sci. Technol. A, **11**, 2407 (1993).

[225] M. Tsujikawa, A. Hosokawa, and T. Oda, *Magnetic anisotropy of Fe/Pt(001) and Pt/Fe/Pt(001) using a first-principles approach*, Phys. Rev. B **77**, 054413 (2008).

[226] M. Tsujikawa, A. Hosokawa, and T. Oda, *Magnetism of free Fe clusters and islands on Pt surfaces*, Appl. Phys. A **82**, 109 (2006).

[227] D. Weller and A. Moser, *Thermal effect limits in ultrahigh-density magnetic recording*, IEEE Trans. Magn, **35** 4423 (1999).

[228] U. Wiedwald, L. Han, J. Biskupek, U. Kaiser, P. Ziemann, *Preparation and characterization of supported magnetic nanoparticles prepared by reverse micelles*, Beilstein J. Nanotechnol. **1**, 24 (2010).

[229] M. Müller and K. Albe, *Kinetic Monte-Carlo simulations on the ordering kinetics of free and supported FePt $L1_0$-nanoparticles*, Bailstein J. Nanotechnol. **2**, 40 (2011).

[230] M. E. Gruner, G. Rollmann, P. Entel, and M. Farle, *Multiply twinned morphologies of FePt and CoPt nanoparticles*, Phys. Rev. Lett. **100**, 087203 (2008).

[231] A. B. Stiles, *Catalysts Supports and Supported Catalysts*, Butter-worths: Boston, MA, (1987).

[232] A. V. Melechko, V. I. Merkulov, T. E. McKnight, M. A. Guillorn, K. L. Klein, D. H. Lowndes, and M. L. Simpson, *Vertically aligned carbon nanofibers and related structures: Controlled synthesis and directed assembly*, J. Appl. Phys. **97** 041301 (2005).

[233] E. Auer, A. Freund, J. Pietsch, and T. Tacke, *Carbons as supports for industrial precious metal catalysts*, Appl. Catal. A **173** 259 (1998).

[234] P. R. Wallace, *The band theory of graphite*, Phys. Rev. **71** 622 (1947).

[235] A. K. Geim and K. S. Novoselov, *The rise of graphene*, Nat. Mater. **6**, 183 (2007).

[236] M. Zhou, A. Zhang, Z. Dai, C. Zhang, and Y. P. Feng, *Greatly enhanced adsorption and catalytic activity of Au and Pt clusters on defective graphene* J. Chem. Phys. **132**, 194704 (2010).

[237] K. Yamamoto, T. Imaoka, W-J Chun, O. Enoki, H. Katoh, M. Takenaga, and A. Sonoi, *Size-specific catalytic activity of platinum clusters enhances oxygen reduction reactions* Nat. Chem. **1**, 397 (2009).

[238] Y. Li, T. Wang, and Y. X. Li, *The influence of dipolar interaction on magnetic properties in nanomagnets with different shapes*, Phys. Status Solidi, **247** 1237 (2010).

[239] E. Ochoa-Fernández, D. Chen, Z. Yu, B. Totdal, M. Ronning, and A. Holmen, *Effect of carbon nanofiber-induced microstrain on the catalytic activity of Ni crystals*, Surf. Sci. **554**, L107 (2004)

[240] Z. J. Liu, Z. Xu, Z. Y. Yuan, D. Y. Lu, W. X. Chen, and W. Z. Zhou, *Cyclohexanol dehydrogenation over Co/carbon nanotube catalysts and the effect of promoter K on performance*, Chem. Lett. **72**, 203 (2001).

[241] H. Kim, W. Lee, D. Yoo, *Functionalized carbon support with sulfonated polymer for direct methanol fuel cells*, Electrochim. Acta **52**, 2620 (2007).

[242] C. Bessel, K. Laubernds, N. M. Rodriguez, R. T. K. J. Baker, *Graphite nanofibers as an electrode for fuel cell applications*, J. Phys. Chem. B **105** 1115 (2001).

[243] Z. L. Liu, X. Y. L. XY, B. Guo, L. Hong, J. Y. Lee, *Pt and PtRu nanoparticles deposited on single-wall carbon nanotubes for methanol electro-oxidation*, J. Power sources **167**, 272, (2007).

[244] V. Selvaraj, and M. Alagar, *Pt and Pt-Ru nanoparticles decorated polypyrrole/multiwalled carbon nanotubes and their catalytic activity towards methanol oxidation*,Electrochem. Commun. **9**, 1145, (2009).

[245] S. Kim, and S. J. Park, *Preparation and electrochemical behaviors of platinum nanoparticles impregnated on binary carbon supports as catalyst electrodes of direct methanol fuel cells*, J. Solid State Electrochem. **11**, 821, (2007).

[246] J. -S. Zhenga, X. -S. Zhang, P. Lia, J. Zhua, X. -G. Zhoua, W. -K. Yuana, *Effect of carbon nanofiber microstructure on oxygen reduction activity of supported palladium electrocatalyst*, Electrochem. Commun. **9**, 895 (2007).

[247] R. Giordano, P. Serp, P. Kalck, Y. Kihn, J. Schreiber, C. Marhic, and J. -L. Duvail, *Preparation of Rh catalysts supported on carbon nanotubes by a surface mediated organometallic reaction*, Eur. J. Inorg. Chem. 610, (2003).

[248] D. Duca, F. Ferrante, and G. L. Manna, *Theoretical study of palladium cluster structures on carbonaceous supports*, J. Phys. Chem. C **111**, 5402 (2007).

[249] Y. Okamoto, *Density-functional calculations of icosahedral M13 (M = Pt and Au) clusters on graphene sheets and flakes*, Chem. Phys. Lett. **420**, 382 (2006).

[250] A. H. Castro Neto, F. Guinea, N. M. R. Peres, K. S. Novoselov, and A. K. Geim, *The electronic properties of graphene*, Rev. Mod. Phys. **81** 109 (2009).

[251] J. P. Perdew, K. Burke, and M. Ernzerhof, *Generalized gradient approximation made simple*, Phys. Rev. Lett. **77**, 3865 (1996).

[252] C. Cao, M. Wu, J. Jiang, and H. Cheng, *Transition metal adatom and dimer adsorbed on graphene: Induced magnetization and electronic structures*, Phys. Rev. B **81** 205424 (2010).

[253] M. Zhang and R. Fournier, *Density-functional-theory study of 13-atom metal clusters* M_{13}, *M = Ta - Pt*, Phys. Rev. A, **79** 043203 (2009).

[254] L. Xiao and L. Wang, *Structure of platinum clusters: Planar or spherical?*, J. Phys. Chem. A, **108** 8605 (2004).

[255] L-L. Wang and D. D. Johnson, *Density functional study of structural trends for late-transition-metal 13-atom clusters*, Phys. Rev. B **75** 235405 (2007).

[256] P. Kim, *Graphene: Across the border*, Nat. Mat. **9** 792 (2010).

[257] G. Lanzani, A. G. Nasibulin, K. Laasonen, and E. I. Kauppinen, *CO dissociation and CO + O reactions on a nanosized iron cluster*, Nano Res., **2**, 660 (2009).

[258] R. S. Monteiro, L. W. C. Paes, J. W. M. Carneiro, and D. A. G. Aranda, *Modeling the adsorption of CO on small Pt, Fe and Co clusters for the Fischer-Tropsch synthesis*, J. clust. Sci. **19** 601 (2008).

[259] P. Fazekas, *Lecture Notes on Electron Correlation and Magnetism*, World scientific, Singapore (1999).

[260] S. R. White, *Density-matrix algorithms for quantum renormalization groups*, Phys. Rev. B **48**, 10345 (1993).

[261] M. P. Gelfand, R. R. P. Singh, and D. A. Huse, *Perturbation expansions for quantum many-body systems*, J. Stat. Phys. **59**, 1093 (1990).

[262] D. C. Mattis, *The Theory of Magnetism I: Statics and Dynamics* (Springer, New York, 1988).

[263] Q. F. Zhong and S. Sorella, *Spin-wave theory on finite lattices: Application to the J1-J2 Heisenberg model*, Europhys. Lett. **21**, 629 (1993).

[264] A. E. Trumper, L. Capriotti, and S. Sorella, *Finite-size spin-wave theory of the triangular Heisenberg model*, Phys. Rev. B **61**, 11529 (2000).

[265] A. W. Sandvik and J. Kurkijärvi, *Quantum Monte Carlo simulation method for spin systems*, Phys. Rev. B **43**, 5950 (1991).

[266] A. W. Sandvik, *Stochastic series expansion method with operator-loop update*, Phys. Rev. B **59**, R14157 (1999).

[267] L. Engelhardt and M. Luban, *Low-temperature magnetization and the excitation spectrum of antiferromagnetic Heisenberg spin rings*, Phys. Rev. B **73**, 054430 (2006).

[268] N. P. Konstantinidis, *Antiferromagnetic Heisenberg model on clusters with icosahedral symmetry*, Phys. Rev. B **72**, 064453 (2005).

[269] D. Coffey, and S. A. Trugman, *Correlations for the S = 1/2 antiferromagnet on a truncated tetrahedron* Phys. Rev. B **46**, 12717 (1992).

[270] R. Schnalle, A. Laeuchli, and J. Schnack, *Approximate eigenvalue determination of geometrically frustrated magnetic molecules*, Condens. Matter Phys. **12**, 331 (2009).

[271] N. P. Konstantinidis, and D. Coffey, *Accurate results from perturbation theory for strongly frustrated S = 1/2 Heisenberg spin clusters*, Phys. Rev. B **63**, 184436 (2001).

[272] I. Rousochatzakis, A. M. Läuchli, and F. Mila, *Highly frustrated magnetic clusters: The kagomé on a sphere*, Phys. Rev. B **77**, 094420 (2008).

[273] N. P. Konstantinidis, *Unconventional magnetic properties of the icosahedral symmetry antiferromagnetic Heisenberg model*, Phys. Rev. B **76**, 104434 (2007).

[274] J. Schulenburg, A. Honecker, J. Schnack, and H.-J. Schmidt, *Macroscopic magnetization jumps due to independent magnons in frustrated quantum spin lattices* Phys. Rev. Lett. **88**, 167207 (2002).

[275] C. Schröder, H.-J. Schmidt, J. Schnack, and M. Luban, *Metamagnetic phase transition of the antiferromagnetic heisenberg icosahedron* Phys. Rev. Lett. **94**, 207203 (2005).

[276] J. Schnack, R. Schmidt, and J. Richter, *Enhanced magnetocaloric effect in frustrated magnetic molecules with icosahedral symmetry*, Phys. Rev. B **76**, 054413 (2007).

[277] J. Schnack, *Properties of highly frustrated magnetic molecules studied by the finite-temperature Lanczos method*, Eur. Phys. J. B **78**, 535 (2010).

[278] N. P. Konstantinidis, *$s = 1/2$ antiferromagnetic Heisenberg model on fullerene-type symmetry clusters*, Phys. Rev. B **80**, 134427 (2009).

[279] D. Coffey, and S. A. Trugman, *Magnetic properties of undoped C_{60}*, Phys. Rev. Lett. **69**, 176 (1992).

[280] A. Honecker and M. E. Zhitomirsky, *Magneto-thermal properties of the spin-s Heisenberg antiferromagnet on the cuboctahedron*, J. Phys. Conference series **145**, 012082 (2009).

[281] L. Hernández and C. Pinettes, *Study of the influence of surface anisotropy and lattice structure on the behaviour of a small magnetic cluster*, J. Magn. Magn. Mater. **295**, 82 (2005).

[282] Z. B. Li, K. L. Yao, and Z. L. Liu, *Thermodynamic properties of a spin-1 tetrahedron as a model for a molecule-based compound $[Mo_{12}O_{30}(\mu_2\text{-}OH)_{10}H_2\{Ni(H_2O)_3\}_4]$Â·$14H_2O$* J. Magn. Magn. Mater. **320**, 1759 (2008).

[283] F. Bonechi, E. Celeghini, R. Giachetti, E. Sorace, and M. Tarlini, *Heisenberg XXZ model and quantum Galilei group* J. Phys. A: Math. Gen. **25**, L939-L943 (1992).

[284] H. Q. Lin and J. E. Gubernatis, *Exact diagonalization methods for quantum systems*, Computers in Physics **7**, 400 (1993).

[285] H. W. Kroto, J. R. Heath, S. C. OB́rien, R. F. Curl, and R. E. Smalley, *C60: Buckminsterfullerene*, Nature **318**, 162 (1985).

[286] P. W. Fowler and D. E. Manolopoulos, *An Atlas of Fullerenes*, (Oxford University Press, London, 1995).

[287] G. Kamieniarz, R. W. Gerling, L. S. Campana, A. C. DÁuria, F. Esposito, and U. Esposito, *Thermodynamic properties of some $S = 1$ soliton-bearing and Haldane-like systems* J. Magn. Magn. Mater. **104**, 865 (1992).

[288] D. Comtesse, A. Hucht, R. Meyer, and P. Entel, unpublished.

[289] W. A. Jesser, G. L. Shiflet, G. L. Allen, and J. L. Crawford, *Equilibrium phase diagrams of isolated nano-phases*, Mat. Res. Innovat. **2**, 211 (1999).

[290] H. Mori and H. Yasuda, *Alloy phase formation in nanometer-sized particles*, Mater. Sci. Eng. A **312**, 99 (2001).

[291] *Electronic Structure and Physical Properties of Solids*, edited by H. Dreyssé (Springer, Berlin, 2000).

[292] A. I. Liechtenstein, M. I. Katsnelson, V. P. Antropov, and A. V. Gubanov *Local spin density functional approach to the theory of exchange interactions in ferromagnetic metals and alloys*, J. Magn. Mag. Mater. **67**, 65 (1987).

[293] S. Frota-Pessôa, R. B. Muniz, and J. Kudrnovský, *Exchange coupling in transition-metal ferromagnets*, Phys. Rev. B **62**, 5293 (2000).

[294] N. Papanikolaou, R. Zeller and P. H. Dederichs, *Conceptual improvements of the KKR method*, J. Phys.: Condens. Matter **14** 2799 (2002).

[295] N. Papanikolaou, R. Zeller and P. H. Dederichs, *Computational Nanoscience: Do it Yourself*, edited by J. Grotendorst, S. Blügel, and D. Marx, NIC Series **31**, Jülich (2006).

Acknowledgments

This thesis has been possible out of the active and passive contributions from colleagues and collaborators. I would extend my heartly thanks to all the people who have been very cooperative and participated with patience all throughout my PhD work.

My ernest thanks to Prof. Dr. Peter Entel for his supervision as a guide and his constant concern and encouragement during my work that has helped me in many ways. I specially thank my colleagues Dr. Alfred Hucht, Dr. Markus E. Gruner, Dr. Georg Rollmann and Dr. Heike Herper who have been cooperative and from whom I learnt a lot. I additionally thank Dr. Gruner for suggesting improvements and translating the abstract of this thesis form English to German. I extend my thanks to all present colleagues, Anna Grünebohm, Mario Siewert, Denis Comtesse, Antje Dannenberg, and ex-colleagues Dr. Ralf Meyer, Dr. Alexei Zayak, Dr. Waheed A. Adeagbo, Sergej Schmidt, Stephan Buschmann and the group members of Prof. Jürgen König, whose welcoming gestures and helpful attitude certainly helped me in having a pleasant time.

I also extend my thanks to collaborators, Dr. Manuel Richter, IFW Dresden, Germany and Dr. Sreekantha Sil, Viswabharati University, India and Dr. Andrei Postnikov, University of Metz, France, with whom I had very fruitful discussions. Especially, Dr. Richter and Dr. Postnikov has helped me in magnetic anisotropy studies and Dr. Sil and Dr. Hucht have helped me for studies in exact-diagonalization techniques. I also thank collaborators Dr. Phivos Mavropoulos, Forschungszentrum Jülich and Prof. Stefan Müller, University of Hamburg, for my studies on exchange integrals of transition metal clusters and cluster expansion methods (studies not included in this thesis), respectively.

I would also like to thank our experimental colleague Dr. Marina Spasova for helpful discussions.

I express my gratitude to Prof. Surjo N. Behera, ex-director of the Institute of Physics, Bhubaneswar, India and Prof. Gouri S. Tripathi, Berhampur University, India for their constant encouragement throughout my research work. I thank Prof. Behera for going through my thesis and suggesting improvements.

I would like to express my thanks to Ms. Dagmar Thiele, our secretary, and the university administration in general which has been impressive in managing students of foreign origin, like me, to have a pleasant working atmosphere.

Some efforts from everybody in my family and my friends have collectively played a positive role in my work and credit of my success also goes to all my family members and friends.

List of own publications

1. G. Rollmann, S. Sahoo, and P. Entel, *Structural and magnetic properties of Fe-Ni clusters*, Phys. Status Solidi A, **201** 3263 (2004).
2. S. Sahoo, G. Rollmann and P. Entel, *First-principles calculation of cluster geometries and magnetization of pure Ni and Fe-Ni clusters*, Phase Transitions **78**, 723 (2005).
3. S. Sahoo, G. Rollmann, and P. Entel, *Segregation and ordering in binary transition metal clusters*, Phase Transitions **79**, 693 (2006).
4. G. Rollmann, P. Entel, and S. Sahoo, *Competing structural and magnetic effects in small iron clusters*, Comput. Matter. Sci. **35**, 275 (2006).
5. G. Rollmann, S. Sahoo, and P. Entel, *Structure and magnetism in iron clusters*, in: Nanoscale Materials: From Science to Technology, edited by S. N. Sahu, R. K. Choudhury, and P. Jena (Nova Science, New York, 2006).
6. M. E. Gruner, G. Rollmann, S. Sahoo, and P. Entel, *Magnetism of close packed* Fe_{147} *clusters*, Phase Transitions **79**, 701 (2006).
7. P. Entel, M. E. Gruner, A. Hucht, R. Meyer, G. Rollmann, S. Sahoo, and S. K. Nayak, *Simulating structure, magnetism and electronic properties of monoatomic, binary and ternary transition metal nanoclusters* in: Proceedings of the International Workshop on Mesoscopic, Nanoscopic and Macroscopic Materials (IWMNMM-2008), edited by S. M. Bose, S. N. Behera and B. K. Roul, AIP Conference Proceedings **1063**, 3 (2008).
8. P. Entel, M. E. Gruner, G. Rollmann, A. Hucht, S. Sahoo, A. T. Zayak, H. C. Herper, and A. Dannenberg, *First-principles investigations of multimetallic transition metal clusters*, Phil. Mag. **88**, 2725 (2008).
9. G. Rollmann, S. Sahoo, A. Hucht, and P. Entel, *Magnetism and chemical ordering in binary transition metal clusters*, Phys. Rev. B **78**, 134404 (2008).
10. S. Sahoo, A. Hucht, M. E. Gruner, G. Rollmann, and P. Entel, A. Postnikov, J. Ferrer, L. Fernández-Seivane, M. Richter and D. Fritsch and S. Sil, *Magnetic properties of small Pt-capped Fe, Co, and Ni clusters: A density functional theory study*, Phys. Rev. B **82**, 054418 (2010).

11. P. Entel, S. Sahoo, A. Hucht, and M. E. Gruner, *From tiny magnetic clusters to functional materials*, Proceedings of the Internal Conference on Advances in Condensed and Nano Materials (ICACNM), February 22-26, Chandigarh, India, AIP Conference Proceedings, edited by S. K. Tripathi (2011), in print.

12. A. Hucht, S, Sahoo, S. Sil, and P. Entel, *Effect of anisotropy on small magnetic clusters*, accepted in Phys. Rev. B (2011).